

**THE INSTITUTE OF CHEMISTRY
OF THE ACADEMY OF SCIENCES OF MOLDOVA**

With manuscript title

UDC: 546.7:546.5:546.4(043.3)+541.13(043.3)+544.174.2(043.3)

SÎRBU DUMITRU

**SYNTHESIS, STUDY OF FERROCENE AND PORPHYRIN
DERIVATIVES AND THEIR COMPLEXES WITH TRANSITION
METALS (Fe, Co, Ni, Cu, Zn, Ru and Pd)**

141.01. INORGANIC CHEMISTRY

Doctoral thesis in chemical sciences

Scientific supervisor:

Turtă Constantin

Doctor Habilitatus, Univ. Professor, Academician

Inorganic Chemistry

Scientific co-supervisor:



Benniston Andrew

PhD, Professor, Photonic Energy Sciences

Author:



Sîrbu Dumitru

CHIȘINĂU – 2015

**INSTITUTUL DE CHIMIE
AL ACADEMIEI DE ȘTIINTE A MOLDOVEI**

Cu titlu de manuscris

CZU: 546.7:546.5:546.4(043.3)+541.13(043.3)+544.174.2(043.3)

SÎRBU DUMITRU

**SINTEZA, STUDIUL DERIVAȚILOR FEROCENULUI ȘI
PORFIRINEI ȘI A COMBINAȚIILOR COORDINATIVE ALE
ACESTORA CU METALELE DE TRANZIȚIE
(Fe, Co, Ni, Cu, Zn, Ru și Pd)**

141.01. CHIMIE ANORGANICĂ

Teză de doctor în științe chimice

Conducător științific:

Turtă Constantin

Doctor Habilitat, Profesor, Academician

Chimie anorganică

Conducător științific:



Benniston Andrew

(Cotutelă)

Doctor, Profesor, Științe fotonice

Autor:



Sîrbu Dumitru

CHIȘINĂU – 2015

© Sîrbu Dumitru, 2015

TABLE OF CONTENTS

Annotation (Romanian, Russian, English)	6
List of abbreviations	9
Introduction	11
 1. DERIVATIVES OF FERROCENE AND PORPHYRIN – A LITERATURE REVIEW ON THE STRUCTURE, PHYSICO-CHEMICAL PROPERTIES AND APPLICATIONS	
1.1. The structure and general properties of porphyrins	18
1.2. The synthesis of porphyrins	20
1.3. Porphyrin based dyes for Dye Sensitised Solar Cells	23
1.4. Light induced processes in ferrocene - [Ru-polypyridyl] ⁿ⁺ derivatives	28
1.5. Light induced processes in ferrocene - porphyrin derivatives	30
1.6. Light induced processes in other ferrocene containing systems	35
1.7. Photodriven H ₂ evolution using ferrocene containing systems	40
1.8. Ferrocene in Dye Sensitised Solar Cells	41
1.9. Ferrocene in other solar cell technologies	43
1.10. Conclusions to Chapter 1	45
 2. DERIVATIVES OF 1,1'-DISUBSTITUTED FERROCENE	
2.1. New pathway to asymmetrical ferrocenes via oxidation of 1,1'-ferrocene dicarboxaldehyde	46
2.1.1. Oxidation of 1,1'-ferrocenedicarboxaldehyde	46
2.1.2. Ferrocene – terpyridine complexes	48
2.1.3. Michael addition products	53
2.1.4. Temperature dependence of ⁵⁷ Fe-Mössbauer spectra for ferrocene-terpyridine systems	59
2.2. Synthesis, molecular structure and properties of a ferrocene-based difluoropyrrolo-oxaborole derivative	64
2.2.1. Synthesis of 1,1'-ferrocene bis(2-(4-ethyl-3,5-dimethylpyrro)methanone borondifluoride)	65
2.2.2. X-ray Crystallography	67
2.2.3. Temperature dependence of ⁵⁷ Fe-Mössbauer spectra	69
2.2.4. DFT molecular modelling	71
2.2.5. Electrochemistry and absorption spectroscopy	73
2.2.6. UV-Vis spectroelectrochemistry	75
2.3. Conclusions to Chapter 2	77

3. FERROCENE-PORPHYRIN CONJUGATES	
3.1. Synthesis, properties of a <i>meso</i>-tris-ferrocene appended zinc(II) porphyrin and evaluation of its dye sensitised solar cell performance	78
3.1.1. Synthesis of Zn(II) 5,10,15-trisferrocenyl-20-(4-carboxyphenyl) porphyrin	79
3.1.2. DFT molecular orbital calculations	81
3.1.3. Electrochemistry and absorption spectroscopy	83
3.1.4. ⁵⁷ Fe Mössbauer spectroscopy	86
3.1.5. Dye sensitised solar cell performance	87
3.1.6. Pump-probe spectroscopy	88
3.1.7. Evaluation of excited state deactivation for DSSC application	91
3.2. Electrocatalytic hydrogen production using Palladium(II) and Copper(II) <i>meso</i>-tetraferrocenyl porphyrin complexes	92
3.2.1. Synthesis of Palladium(II) and Copper(II) <i>meso</i> -tetraferrocenyl porphyrin	93
3.2.2. ⁵⁷ Fe Mössbauer spectroscopy	94
3.2.3. Electrochemistry and absorption spectroscopy	95
3.2.4. UV-Vis spectroelectrochemistry	98
3.2.5. Electrocatalytic proton reduction	100
3.3. Conclusions to Chapter 3	104
4. EXPERIMENTAL METHODS AND PROCEDURES	
4.1. Physical methods of investigation	106
4.2. Solar cell preparation	108
4.3. Electrocatalysis cell and GC analysis	109
4.4. Synthetic procedures for compounds discussed in Chapters 2 and 3	110
4.5. Conclusions to Chapter 4	126
OVERALL CONCLUSIONS AND RECOMMENDATIONS	127
REFERENCES	129
ANEXES 1-14	144
DECLARATION ON THE ASSUMPTION OF RESPONSIBILITY	162
AUTHOR'S CV	163

ADNOTARE

Sîrbu Dumitru, „Sinteza, studiul derivaților ferocenului și porfirinei și a combinațiilor coordinative ale acestora cu metalele de tranziție (Fe, Co, Ni, Cu, Zn, Ru și Pd)”. Teză de doctor în științe chimice, specialitatea 141.01 - chimia anorganică. Chișinău, 2015. Teza constă din introducere, patru capitole, concluzii generale și recomandări, bibliografie din 223 referințe și 14 anexe care conțin 24 figuri. 128 pagini text de bază conțin 90 figuri, 11 tabele și 2 ecuații. Rezultatele descrise în teză au fost publicate în 13 lucrări științifice: patru articole în reviste cu factor de impact și un articol în revistă națională de categoria B (fără coautori), un fragment al capitolului dintr-o monografie internațională, o prezentare orală și șapte abstracte (trei fără coautori) la conferințe.

Cuvinte cheie: ferocen, porfirină, complecși, metale, tranziție, celulă solară, reducerea protonilor, UV-Vis.

Scopul acestei lucrări este studiul relațiilor structură-proprietate ce ar permite înțelegerea mai profundă a mecanismelor care determină procesele fotofizice și electrochimice, în sistemele în baza porfirinei și ferocenului, pentru evidențierea potențialului aplicativ al materialelor obținute. Pentru îndeplinirea **obiectivelor** propuse au fost utilizate diferite metode contemporane, inclusiv spectroscopiile de masă, IR, RMN, absorbția atomică, analiza elementală și difracția razelor X – pentru determinarea compoziției și caracterizarea structurală a compușilor. Studiul fotofizic, electrochimic și al potențialului aplicativ a fost efectuat prin utilizarea unui șir de metode: absorbție electronică și spectroelectrochimie UV-Vis, absorbție tranzientă „pump-probe”, spectroscopie Mössbauer, voltametrie ciclică și modelare moleculară DFT.

Originalitatea științifică. Au fost obținuți 27 compuși, inclusiv 14 derivați noi ai ferocenului și porfirinei, utilizând procedeele sintetice elaborate și au fost propuse mecanisme reacțiilor. Trebuie subliniată sinteza produsului nou, derivat bis-cetopirolic al ferocenului și al complexului său cu BF_2 , precum și procedeul nou pentru desimetrizarea oxidativă a moleculei de ferocen. Pentru prima dată un colorant ferocen-porfirinic a fost utilizat în calitate de sensibilizator al suprafeței de TiO_2 în celulă Grätzel și au fost analizate procesele-cheie ce determină eficacitatea sistemului. A fost propus mecanismul producerii electrochimice a hidrogenului în baza intermediarului florinic, catalizat de *mezo*-tetraferocenil porfirinatul de Pd(II) și Cu(II), și a fost explicat rolul unităților ferocenice.

Această lucrare oferă unele răspunsuri și concluzii cu **semnificație teoretică și o valoare aplicativă** pentru procesul de cercetare atât în echipa noastră, cât și în alte grupe ce lucrează în domenii similare sau înrudite. Metoda simplă fără cromatografie, elaborată pentru desimetrizarea moleculei de ferocen oferă o cale alternativă de obținere a derivaților 1,1'-asimetric disubstituiți ai ferocenului ce prezintă potențial de aplicare în procesele catalitice industriale. Proprietățile redox ale derivatului bis-cetopirolic al ferocenului permit aplicarea acestui material în calitate de sensibilizator redox al prezenței nucleofililor. Studiul proceselor fotoinduse în colorantul ferocen-porfirinic adsorbit pe suprafața TiO_2 prezintă o încercare de a găsi factorii limită ai DSSC, iar concluziile făcute în această lucrare vor ghida optimizarea ulterioară a celulelor solare sensibilizate cu porfirine. Complecșii *mezo*-tetraferocenil porfirinici au prezentat activitate catalitică înaltă în obținerea electrochimică a hidrogenului, oferind informație valoroasă pentru generarea materialelor alternative în reducerea electrocatalitică a protonilor.

Problema științifică soluționată constă în elucidarea relației structură-proprietate în sistemele moleculare în baza ferocenului și porfirinei, contribuind la înțelegerea mai profundă a proceselor fizice și chimice în materialele studiate, întru optimizarea ulterioară a eficienței lor aplicative.

АННОТАЦИЯ

Сырбу Думитру, "Синтез, исследование производных ферроцена и порфирина и их комплексов с переходными металлами (Fe, Co, Ni, Cu, Zn, Ru и Pd)". Диссертация доктора химических наук, специальность 141.01 - неорганическая химия. Кишинэу, 2015. Диссертация состоит из введения, четырех глав, общих выводов и рекомендаций, библиографии из 223 ссылок и 14 приложений, состоящих из 24 фигур. 128 страниц основного текста содержат 90 рисунков, 11 таблиц и два уравнения. Результаты, описанные в диссертации были опубликованы в 13 научных работах: четыре статьи в журналах с импакт-фактором, одна в журнале Б-класса (без соавторов), отрывок в главе монографии, устный доклад и семь тезисов (три без соавторов) на научных конференциях. Ключевые слова: ферроцен, порфирин, комплекс, солнечная ячейка, восстановление протонов, УФ-Вид.

Целью данной работы является исследование соотношений структура-свойство которые позволили бы лучше понять механизмы, регулирующие фотофизические и электрохимические процессы, в системах на основе порфирина и ферроцена, для выявления их практического потенциала. Разнообразие современных методов (ИК, ЯМР, масс спектроскопии, атомная абсорбция, элементный и рентгено-дифракционный анализ) были использованы для описания состава и структуры соединений, в то время как УФ-Вид поглощение и спектроскопия, "pump-probe" нестационарное поглощение, мессбауэровская спектроскопия, циклическая вольтамперометрия и молекулярное моделирование методом ДФТ были использованы для изучения фотофизических, электрохимических свойств и прикладного потенциала полученных материалов.

Оригинальность результатов. Были получены 14 новых производных порфирина и ферроцена и предложены механизмы реакций. Следует отметить синтез нового, трудно выделяемого кетопирольного производного ферроцена и его BF_2 хелата, а также новый простой путь для десимметризации молекулы ферроцена. Впервые ферроцен-порфириновый краситель был использован в качестве сенсibiliзирующего пигмента поверхности TiO_2 в ячейке Грәцель и были проанализированы основные процессы определяющие производительность системы. Предложен механизм электрохимического получения водорода основанный на формировании мезо-тетра-ферроценил флоринового промежуточного продукта и было предложено объяснение роли ферроцена.

Эта работа дает некоторые ответы и выводы с *теоретическим и прикладным значением*, которые, как ожидается, будут полезны для дальнейших исследований как в нашей, так и в других группах, работающих в аналогичных или смежных областях. Простой метод исключая хроматографию, разработанный для десимметризации молекулы ферроцена, является альтернативным маршрутом для получения 1,1'-асимметричных ферроценов, потенциально полезных в промышленных каталитических процессах. Циклическая вольтамперометрия бис-кетопирольного ферроцена показала потенциал для редокс зондирования нуклеофилов. Исследование фотоиндуцированных процессов в ферроцен-порфириновом красителе, закрепленном на поверхности TiO_2 , будет полезно для дальнейшей разработки солнечных батарей сенсibiliзированных порфиринами. мезо-Тетраферроценил порфириновые комплексы были использованы в электрохимическом получении молекулярного водорода, предоставляя ценную информацию для разработки новых альтернативных материалов для электрокаталитического восстановления протонов.

Решенная научная проблема состоит в выяснении взаимосвязи структура-свойство в молекулярных системах на основе ферроцена / порфирина, способствуя более глубокому пониманию физических и химических процессов в исследованных материалах, для дальнейшей оптимизации их практической эффективности.

ANNOTATION

Sîrbu Dumitru, „Synthesis, study of ferrocene and porphyrin derivatives and their complexes with transition metals (Fe, Co, Ni, Cu, Zn, Ru and Pd)”. PhD thesis in chemistry, speciality 141.01 - inorganic chemistry. Chişinău, 2015. Thesis consists of introduction, four chapters, overall conclusions and recommendations, bibliography of 223 references and 14 annexes comprising of 24 figures. 128 pages of main text contain 90 figures, 11 tables and two equations. The results described within this dissertation were published in 13 scientific papers: four articles in journals with impact factor and one in journal of B grade (without co-authors), part of a chapter from international book, one oral and seven poster presentations (three without co-authors) at scientific conferences.

Keywords: ferrocene, porphyrin, transition metal complexes, solar cell, protons reduction, UV-Vis.

The aim of this work is the study of structure-property relationships that would allow a better understanding of the mechanisms governing the photophysical and electrochemical processes, in the porphyrin and ferrocene based systems, in order to identify their practical potential. A variety of contemporary methods, including IR, NMR and mass spectrometries, atomic absorption, elemental and X-ray diffraction analyses, were used for molecular composition and structural characterisation of the compounds, while UV-Vis absorption and spectroelectrochemistry, pump-probe transient absorption, Mössbauer spectrometry, cyclic voltammetry and DFT molecular modelling were employed in order to study the photophysical, electrochemical and applicative properties.

The originality of results. 14 new derivatives of ferrocene and porphyrin were obtained using elaborated synthetic protocols and the reaction mechanisms were proposed. It should be emphasized the synthesis of the new, rarely isolated ketopyrrole halfway product in the BODIPY synthesis, and its BF_2 chelate, as well as the novel simple route for oxidative desymmetrization of ferrocene molecule. For the first time a ferrocene-porphyrin dye was employed as sensitizer for TiO_2 surface in a Grätzel cell and the key processes governing the system efficiency were analysed. The mechanism for Pd(II) and Cu(II) porphyrin ring centred electrochemical hydrogen production was proposed consisting of a phlorin mediated pathway and a feasible explanation of ferrocene units role was suggested.

This work is giving some answers and conclusions with ***fundamental and applicative*** value, that are expected to be useful in the further research both in our and other teams working in similar or related area. The simple chromatography-free method elaborated for desymmetrizing ferrocene molecule is an alternative route to 1,1'-asymmetrical ferrocenes that could find practical applications in industrial catalytic processes. The cyclic voltammetry of bis-ketopyrrolic derivative of ferrocene proved the material to be useful for nucleophiles redox sensing. The study of photoinduced processes in ferrocene-porphyrin dye anchored on the TiO_2 surface is a trial to find the “bottleneck” of DSSCs and the conclusions made within this work will guide further design of porphyrin-sensitized solar cells. The *meso*-tetraferrocenyl porphyrin metal complexes showed catalytic activity in electrochemical generation of molecular hydrogen, giving some valuable information for generation of alternative materials for the electrocatalytic reduction of protons.

The ***solved scientific problem*** consists of elucidating the structure-property relationship in the molecular systems based on ferrocene/porphyrin, contributing to a deeper understanding of the physical and chemical processes in the materials studied for further optimisation of their practical efficiency.

SHORTCUTS

AM1.5 – Air Mass coefficient (1.5 atmosphere thickness)

APCI – Atmospheric-Pressure Chemical Ionization

ASAP – Atmospheric Solids Analysis Probe

BF₂ – the complexed BF₂⁺ unit

BODIPY – Boron-dipyrromethene

bpy – 2,2'-bipyridine

Carbz-PAHTDIT – 3-(5-6-[5-(2-{4-[Bis-(4-carbazol-9-yl-phenyl)-amino]-phenyl}-vinyl)-3-hexyl-thien-2-yl]-dithieno[3,2-b;2',3'-d]thiophen-2-yl}-4-hexyl-thien-2-yl)-2-cyano-acrylic acid

Chl-*a* – Chlorophyll *a*

Cp – Cyclopentadienide rings

CR – Charge Recombination

CS – Charge Separated, Charge Separation

CV – Cyclic Voltammetry

DAF – 1,1'-Diacetylferrocene

DBF – 1,1'-Dibenzoylferrocene

DCM – DiChloroMethane

DDQ – 2,3-Dichloro-5,6-Dicyanobenzo Quinone

DFT – Density Functional Theory

DMF – Dimethylformamide

DMSO – Dimethyl Sulfoxide

DNA – DeoxyRibonucleic Acid

DSSC – Dye-Sensitized Solar Cell

EN – Energy Transfer

EPR – Electron Paramagnetic Resonance

ESI – ElectroSpray Ionisation

ET – Electron Transfer

EtOH - Ethanol

f' – Recoil-free Absorption

Fc – Ferrocene

FF – Fill Factor

GC – Gas Chromatography

HOMO – Highest Occupied Molecular Orbital

HREI – Accurate mass Electron Ionisation

i_c – current response of the catalytic wave

i_p – current response of the sample in the absence of acid

IPCE – Incident Photon-to-Current Efficiencies

IR – Infra Red

IS – Isomer Shift

ITO – Indium Tin Oxide

J_{SC} – Short Circuit Current Density

LBCN – Laboratory of Bioinorganic Chemistry and Nanocomposites

LUMO – Lowest Unoccupied Molecular Orbital

MALDI – Matrix-Assisted Laser Desorption/Ionization

MeOH - Methanol

MPL – Molecular Photonics Laboratory

MS – Mass Spectroscopy	SAM – Self-Assembled Monolayers
MS – Mössbauer Spectrum	SCE – Saturated Calomel Electrode
MV – Methyl-Viologen	SubPc – Boron Subphthalocyanine
N00 buffer = 7.5 mM NaH ₂ PO ₄ , 1 mM EDTA, pH 7.0	tap – Bis-(1,4,5,8-tetraazaphenanthrene)
N-719 – Di-tetrabutylammonium cis-bis(isothiocyanato) bis(2,2'-bipyridyl-4,4'-dicarboxylato) Ru(II)	TBABF ₄ – Tetrabutylammonium Tetrafluoroborate
NDI – Naphthalenediimide	TEAHCl – Triethylamine Hydrochloride
NHE – Normal Hydrogen Electrode	TFA – Trifluoroacetic Acid
NMI – Naphthalene Monoimide	TFPH ⁻ – <i>meso</i> -Tetraferrocenyl Phlorin Anion
NMR – Nuclear Magnetic Resonance	THF – Tetrahydrofuran
nT – Oligothiophene	TOF – Time-Of-Flight
OTE – Optically Transparent Electrode	TOF – Turnover Frequency
OTTLE – Optically Transparent Thin-Layer Electrode	TON – Turn Over Number
P – Porphyrin	TPP – TetraPhenylPorphyrin
PBI – Perylenetetracarboxylic Diimide	tpy, terpy – 2,2':6',2''-terpyridine
<i>p</i> -Chloranil – Tetrachloro-1,4-benzoquinone	TsOH – <i>p</i> -Toluenesulfonic Acid
Ph ₃ N – Triphenylamine	TTF – Tetrathiafulvalene
PhCN – Benzonitrile	UP – 2-Ureido-4(1H)-Pyrimidinone
phen – 1,10-Phenanthroline	UV-Vis – Ultraviolet Visible
PhNBu ₂ – 4-N,N-Dibutylaminophenyl	V _{OC} – Open Circuit Voltage
PhNMe ₂ – 4-N,N-Dimethylaminophenyl	Y123 – 3-{6-{4-[Bis(2',4'-dihexyloxybiphenyl-4-yl)amino-]phenyl}-4,4-dihexyl-cyclopenta-[2,1-b:3,4-b]dithiophene-2-yl}}-2-cyanoacrylic acid
PhOC ₁₂ H ₂₅ – Dodecyl Phenyl Ether	θ_D – Debye Temperature
pp – 3-Methyl-1-(2'-pyridine)pyrazole	Γ – Line Width
QS – Quadrupole Splitting	η – Energy Conversion Efficiency
RT – Room Temperature	

INTRODUCTION

Actuality and importance of the addressed issue within the research area

The first reports in 1951 by Kealy and Pauson [1] and 1952 by Miller et al. [2] on the new organo-iron compound with chemical formula $\text{FeC}_{10}\text{H}_{10}$ opened a new area of chemistry, and in 1973 the Nobel Prize in Chemistry was awarded jointly to Ernst Otto Fischer and Geoffrey Wilkinson "for their pioneering work, performed independently, on the chemistry of the organometallic, so called sandwich compounds". The initially proposed structures were wrong, but the unusual stability, diamagnetic nature, single C-H stretching mode in IR spectrum and nonpolar character of the compound, permitted to deduce the sandwich structure (the generally accepted representations of ferrocene (Fc) are shown in Figure 1), later confirmed by X-ray crystallographic analysis [3]. The molecule showed aromatic behaviour and therefore in analogy to benzene the name ferrocene was suggested. It was later expanded to compounds of the general composition $\text{M}(\text{C}_5\text{H}_5)_2$ named metallocenes. Representation IV of ferrocene molecule from Figure 1 was chosen to be used within this work.

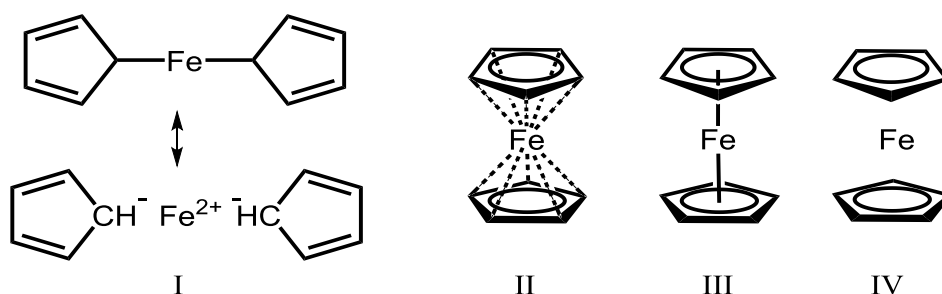


Fig. 1. The structural illustration of $\text{Fe}(\text{C}_5\text{H}_5)_2$ (I) proposed by Kealy and Pauson, and (II-IV) showing generally accepted representations of ferrocene sandwich structure.

The ferrocene undergoes typical for aromatic systems reactions, such as Friedel-Crafts acetylation, alkylation, formylation, sulfonation, metalation with butyllithium etc. [3] thus opening access to a wide variety of derivatives. It was found to be substantially more reactive than benzene towards electrophilic reagents [4]. The central Fe^{II} can be oxidized to Fe^{III} by treating with FeCl_3 [5], *p*-benzoquinone [6] and other oxidizing agents generating respective ferrocenium Fc^+ salts. Fc^+ / Fc redox couple is used as internal standard in electrochemistry, showing a clean one-electron oxidation at a low potential, around 0.5 V vs. saturated calomel electrode (SCE). Decamethylferrocene is easier oxidised than Fc, so it can be used instead of it when overlapping is to be avoided. Fc and its numerous derivatives found multiple applications in the field of materials, molecular engineering and catalysis, molecular ferromagnets, sensors, non-linear optical materials, medicine etc [7, 8].

Pyrrole based macrocycles, such as porphyrins, chlorins, bacteriochlorins, corroles and corrins are widely used in nature, particularly in their metallated forms, for various purposes including light-harvesting [9], small molecules transportation [10], catalysis [11] etc. The most abundant iron protoporphyrin from heme proteins serves many biological roles as small molecules / electron transport and storage (hemoglobin, myoglobin), electron transfer and biocatalysis (cytochromes, catalase, peroxidase, lignin peroxidase, cytochrome P450). Chlorophylls and phaeophytins play key-roles in harvesting the solar light and initiation of energy / electron transfer cascade in the photosynthetic machine, to finally store the chemical energy in sugars. In the attempt to understand and “copy” Nature, a large and continuously increasing number of artificial systems were created in order to reproduce the performance of parent natural analogues. As result, during the last decades numerous examples of porphyrin applications in chemistry, materials science, physics, biology and medicine have been reported [12], a special attention being given to the solar energy conversion [13].

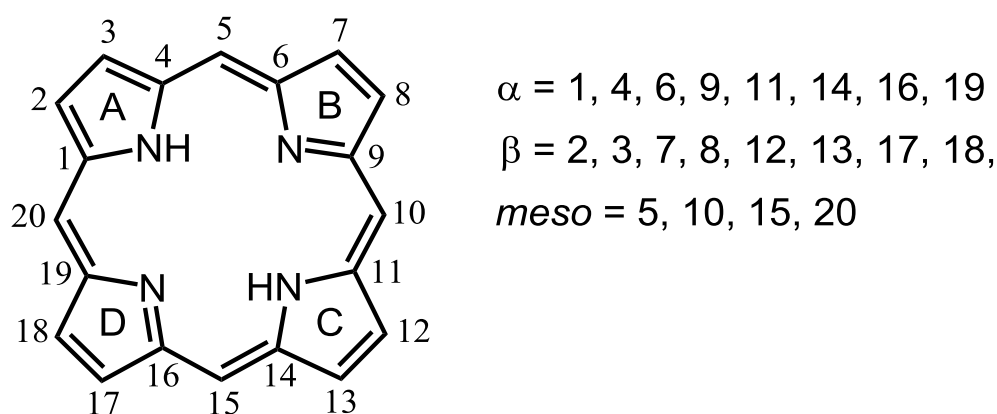


Fig. 2. Structure of porphyrin macrocycle showing the numbering and functionalization sites.

A large delocalized aromatic system of porphyrin macrocycle (Figure 2) formed by the fully conjugated 22 π electrons is responsible for its typical UV-Vis absorption pattern, usually consisting of two distinguishable signatures – B (also called Soret) and Q bands. The Soret band at maximum wavelength $\lambda_{\text{max}} \sim 400$ nm (absorption coefficient $\epsilon \sim 10^5 \text{ M}^{-1} \text{ cm}^{-1}$) is the most pronounced porphyrin electronic absorption characteristic for metal-free, diprotonated and metalated forms. Other up to four less intense Q bands are found at lower energies in the region 450 – 700 nm. Taking into account the strong absorption of visible light by porphyrins and porphyrin related macrocycles it is not surprising to see a constantly increasing number of publications employing porphyrin based systems for light harvesting. As described below, the porphyrins proved to be a good alternative to classical Ru-polypyridyl dyes for Dye Sensitised Solar Cells (DSSCs), also known as Grätzel cells [14].

The increasingly high demand of power is constantly motivating the research of new energy resources. The ecological issues generated by the greenhouse emissions have attracted much attention during the last years [15] and either removal of the formed gases from atmosphere or the shift from fossil fuels to carbon neutral renewable energy sources are required. Solar energy is so far the largest accessible renewable energy resource, providing in one hour to the Earth more energy than the humans could consume in a year. Furthermore, the solar energy resource exceeds any prognostics on human society consumption levels. Still, for a major contribution to the global energy production, the solar energy must be harvested, converted into a useful form (chemical or electrical energy) and stored in an efficient and low cost process. In order to achieve this, a substantial improvement of knowledge about the systems discussed herein and generation of new materials created to capture and store light energy are needed.

The aim of this work is the study of structure-property relationships that would allow a better understanding of the mechanisms governing the photophysical and electrochemical processes, in the porphyrin and ferrocene based systems, in order to identify their practical potential.

The main objectives aiming to achieve the purpose of this work were the following:

- Design and synthesis of molecular systems based on ferrocene and porphyrin;
- Composition determination and structural characterisation of the obtained compounds by using physico-chemical methods (IR, NMR, Atomic Absorption, Mass Spectrometries, Elemental Analysis and X-ray crystallography);
- Study of the photophysical and electrochemical properties of the materials by various methods (Mössbauer, UV-Vis absorption spectrometries, cyclic voltammetry, UV-Vis spectroelectrochemistry, Ultrafast Transient Absorption Pump-Probe spectrometry);
- Revealing the structure-property relationships determining physico-chemical properties by using the information obtained from previous objectives;
- Study of the applicative potential for the examined materials.

The originality of results:

- A new simple route for desymmetrizing ferrocene was found based on selective oxidation of only one aldehyde unit in 1,1'-ferrocenedicarboxaldehyde to give 1'-formyl-ferrocenecarboxylic acid.
- Since no similar route was described by far, a tentative mechanism was proposed to explain the formation of 3-methyl-5-oxocyclohex-3-enyl ring, consisting of a cascade of stepwise

reactions starting with Michael addition of diethyl malonate molecule to 1'-((E)-3-oxo-but-1-enyl)-ferrocenecarboxylic acid.

- The new, rarely isolated halfway product in the BODIPY synthesis, namely 1,1'-ferrocene-bis[2-(4-ethyl-3,5-dimethylpyrro)methanone], was found to be stable and reacted with $\text{BF}_3 \cdot \text{Et}_2\text{O}$ to produce the bis(difluoropyrrolo-oxaborole) compound. Though the formation of a five-membered ring facilitates the formation of BF_2 chelate, surprisingly only two examples of ketopyrrole- BF_2 complexes were found in the literature. Interestingly, the redox behaviour of the 2-ketopyrrole intermediate is strongly influenced by nucleophiles as exemplified with cyclic voltammetry experiments.
- The synthetic routes to ferrocene-porphyrin conjugates were elaborated and applied in order to obtain a porphyrin macrocycle with a single ferrocene group appended at three of the *meso* positions, with the fourth *meso* position containing a *p*-benzoic acid unit designed to be an anchoring moiety to a semiconductor surface.
- For the first time a ferrocene-porphyrin dye was employed as a sensitizer for TiO_2 surface in a Grätzel solar cell and the key processes governing the system were analysed using cyclic voltammetry and UV-Vis transient absorption spectroscopy.
- The mechanism for electrochemical hydrogen production, catalysed by Pd(II) and Cu(II) *meso*-tetraferrocenyl porphyrin complexes, was proposed consisting of phlorin mediated pathway and a feasible explanation of ferrocene units role was suggested.

Thesis overview

This work is devoted to a number of research topics, which are followed within its sections. In Chapter 1 an overview is given on the work done by various research groups worldwide on the synthesis, study and applications of molecular systems based on ferrocene and porphyrin, highlighting the processes associated and inspired by natural photosynthesis. A brief introduction to the porphyrins structure and general properties is followed by the summary on the main synthetic routes to construct the porphyrin molecule. The next section is giving a short analysis of the modified chlorophyll and synthetic porphyrin dyes for sensitisation of TiO_2 surface in DSSCs, aiming to illustrate the structure-property relationships determining the device efficiency. The last section is dealing with the ferrocene containing molecular systems, including ferrocene-porphyrin conjugates, focusing on description of light induced processes and the role of ferrocene unit.

The achievement of thesis objectives is fully described in Chapters 2 – 4 that comprise the experimental work done mainly in the Molecular Photonics Laboratory (MPL), Newcastle

University and the Laboratory of Bioinorganic Chemistry and Nanocomposites (LBCN), Institute of Chemistry of ASM. Chapter 2 describes the synthesis and study of 1,1'- disubstituted products comprising two distinct topics. In the first section, a new route to access asymmetrically substituted ferrocenes is addressed and the two products obtained by partial oxidation of 1,1'-dicarboxaldehyde were used to obtain five new asymmetrical derivatives. The second part comprises the synthesis and thorough description of ferrocene-based difluoropyrrolo-oxaborole derivative, obtained from the halfway product in the boron-dipyrromethene synthesis. A potential application as a dark-state energy transfer quencher, or redox reporter for the non-chelated intermediate, is proposed.

In Chapter 3, the structure, redox, photophysical and electrocatalytical properties of ferrocene-porphyrin conjugates are discussed. The section is divided into two discrete topics, the first being addressed to the design and study of a *meso*-tris-ferrocene appended zinc(II) porphyrin and a critical evaluation of its performance in a TiO₂ based DSSC. Mössbauer, cyclic voltammetry, UV-Vis, pump-probe spectroscopies and DFT calculations were employed in order to characterize the Zn(II)-5,10,15-trisferrocenyl-20-(4-carboxyphenyl)porphyrin, which was further used as a sensitizer for TiO₂ surface. The second part is focused upon the study of transition metal *meso*-tetraferrocenyl porphyrin complexes as alternative electrocatalyst candidates for molecular hydrogen production and a mechanism pathway is proposed. Cyclic voltammetry and UV-Vis spectroelectrochemistry were used to describe the catalytic process, followed by bulk electrolysis with a concomitant analysis of the resulted gases using continuous flow rig with in-line GC analysis.

The final chapter gives detailed information on the methods, software and instruments (IR, NMR, Mössbauer, Atomic and Electronic (UV-Vis) absorption spectrometries, X-ray crystallography, cyclic voltammetry and UV-Vis spectroelectrochemistry, Ultrafast Transient Absorption (Pump-Probe experiment) spectrometry, Elemental Analysis, Gas Chromatography (GC) and Mass Spectrometry, e.g. Electrospray Ionisation (ESI), Matrix-Assisted Laser Desorption / Ionization Time-Of-Flight (MALDI-TOF), Atmospheric-Pressure Chemical Ionization Atmospheric Solids Analysis Probe (APCI-ASAP) techniques) used during and required by the research process, the solar cell and electrocatalysis cell preparation, as well as the synthetic routes employed to obtain the target materials. In total, twenty six compounds were synthesized including starting materials, intermediate and target products. It is to be emphasized that the synthesis procedures described herein and especially the new method for desymmetrization of ferrocene molecule are expected to be incorporated by current and future LBCN and MPL members into their synthetic protocols.

The solved scientific problem consists of elucidating the structure-property relationship in the molecular systems based on ferrocene / porphyrin, contributing to a deeper understanding of the physical and chemical processes in the materials studied for further optimisation of their practical efficiency.

Fundamental and applicative aspects of the results:

Following the aspiration to enrich the understanding of processes chosen and refined by the genius of Nature, this work is giving some answers and conclusions that are expected to be useful for further research both in our and any other teams working in similar or related area. The very quick citation of our work is encouraging our fair attempt.

As it was shown by engaging the both oxidation products of 1,1'-ferrocenedicarboxaldehyde into classical organic reactions and further complexation (Fe(II), Ru(II)), the simple chromatography-free method elaborated for desymmetrizing ferrocene molecule is an alternative route to 1,1'-asymmetrical ferrocenes that could find practical applications in industrial catalytic processes [16]. At the same time the unusual route of 3-methyl-5-oxocyclohex-3-enyl ring formation in one pot reaction starting from Michael addition to but-3-en-2-one is showing the “unlimited” possibilities of organic synthesis. The study into the insights of light induced instability of ferrocene – terpyridine couple is a modest contribution to the actively developing prodigious organometallic world. The 1'-(3,5-dihydroxy-2-picolinoyl)-3,5-di(pyridin-2-yl)cyclohexyl)-ferrocene-carboxylic acid is a promising candidate in the exploration of host-guest interactions in aqueous media with small molecules like aminoacids.

The new unusually stable ketopyrrole derivative is a rarely isolated halfway intermediate in the BODIPY synthesis, while the bis(difluoropyrrolo-oxaborole) ferrocene is only the third example of ketopyrrole-BF₂ chelate described in the literature. Beside the fundamental interest, it was found that the reactivity of electrochemically generated ferrocenium ion could be used for nucleophiles redox sensing by 1,1'-ferrocene-bis[2-(4-ethyl-3,5-dimethylpyrro)methanone], while its bis-BF₂ complex may potentially be applied as a dark-state energy transfer quencher for fluorophores which emit between 500 and 600 nm.

The study of photoinduced processes in ferrocene-porphyrin dye anchored on the TiO₂ surface is a trial to find the “bottleneck” of DSSCs and the conclusions made in this work will guide further design of porphyrin-sensitized solar cells.

The study of *meso*-tetraferrocenyl porphyrin metal complexes showed electrocatalytical activity for generation of energetically useful products, i.e. molecular hydrogen. The proposed mechanism pathway is giving some valuable information for the construction of alternative materials for the electrocatalysis of proton reduction reaction.

Dissemination and publication of the research findings

The research results described in this thesis were presented in poster (seven abstracts) and one oral sessions at national and international scientific conferences, symposiums, summer schools: International Conference of Young Researchers, IXth edition (11 November 2011, Chişinău, Republic of Moldova); The V International Conference-Symposium “ECOLOGICAL CHEMISTRY 2012” (2 – 3 March 2012, Chişinău, Republic of Moldova); The XVII-th Conference "Physical Methods in Coordination and Supramolecular Chemistry" (24 – 26 October 2012, Chişinău, Republic of Moldova); The VIIth National conference on chemistry and nanomaterials of young scientists, PhD and students with the international participation "Mendeleev-2013" (2 - 5 April 2013, St. Petersburg, Russian Federation); Integration through research and innovation (26 - 28 September 2013, Chişinău, Republic of Moldova); Symposium & Young-Researcher-Meeting: Current Challenges in Supramolecular Artificial Photosynthesis (09 – 13 March 2014, Jena, Germany); The International Conference dedicated to the 55th anniversary from foundation of the Institute of Chemistry of the ASM (28 – 30 May 2014, Chişinău, Moldova). Some aspects of the research process were disseminated at scientific TV show: “Ştiinţă şi inovare”, TeleRadioMoldova, 28th December 2013 and 11th of January 2014.

This thesis is based on the following papers (four in journals with impact factor and one without co-authors in journal of B grade):

1. Sirbu D., Turta C., Benniston A.C., Abou-Chahine F., Lemmetyinen H., Tkachenko N.V., Wood C., Gibson E. Synthesis and properties of a meso tris-ferrocene appended zinc(II) porphyrin and a critical evaluation of its dye sensitised solar cell (DSSC) performance. In: *RSC Advances*, 2014, 4 (43), p. 22733-22742. DOI: 10.1039/c4ra03105a. (IF 3.84).
2. Benniston A.C., Sirbu D., Turta C., Probert M.R., Clegg W. Synthesis, molecular structure and properties of a ferrocene-based difluoropyrrolo-oxaborole derivative. In: *Eur. J. Inorg. Chem.*, 2014, 36, p. 6212–6219. DOI:10.1002/ejic.201402752. (IF 2.942).
3. Benniston A.C., Sirbu D., Turta C., Probert M.R., Clegg W. A simple method for desymmetrizing 1,1'-ferrocenedicarboxaldehyde. In: *Tetrahedron Letters*, 2014, 55 (28), p. 3777-3780. DOI: 10.1016/j.tetlet.2014.05.040. (IF 2.379).
4. Sirbu D. Temperature dependence of ⁵⁷Fe-mössbauer spectra for a $Fe^{II}_{Fc} - Fe^{II}_{t_{py}} - Fe^{II}_{Fc}$ trinuclear system. In: *Chemistry Journal of Moldova. General, Industrial and Ecological Chemistry*, 2015, 10 (1), p. 84-88. (B-grade journal, UIF 0.135)
5. Sirbu D., Turta C., Gibson E.A., Benniston A.C. The ferrocene effect: enhanced electrocatalytic hydrogen production using meso-tetraferrocenyl porphyrin palladium (II) and copper (II) complexes. In: *Dalton Trans.*, 2015, Advance Article. (IF 4.197)

Additionally, a review material related and partially used in this thesis was published in the series of *Water Science and Technology Library*, Chapter 3: *Electrochemical Solar Cells Based on Pigments* of book *Management of Water Quality in Moldova* (Springer, 2014, pages 48-59).

1. DERIVATIVES OF FERROCENE AND PORPHYRIN – A LITERATURE REVIEW ON THE STRUCTURE, PHYSICO-CHEMICAL PROPERTIES AND APPLICATIONS

1.1. The structure and general properties of porphyrins

The properties of porphyrin molecule result from its structure (shown previously in Figure 2). Four pyrrole units connected by methine bridges form the planar porphyrin ring, fully conjugated by the mean of 22 π electrons, of which 18 form the delocalized aromatic system ($4n+2$, where $n = 4$). The porphyrin ring current causes deshielding of meso-protons (8 to 10 ppm) and shielding of NH signals (-1 to -4 ppm) as it can be seen by NMR spectroscopy, proving its aromatic character. Reducing one peripheral double bond on the pyrrole unit to form chlorin, or two bonds on opposite pyrroles for bacteriochlorin does not break the aromaticity because of the remaining nine unsaturated bonds (Figure 1.1). At the same time the porphyrinogen (intermediate in the porphyrin synthesis), with 3 reduced double bonds, does not fulfil the Huckel's rule, resulting in much weaker electronic absorption. Some other reduced species are known as bacteriochlorin isomers, namely isobacteriochlorin, porphomethenes, and chlorin isomers namely *trans* / *cis*-porphodimethenes and phlorins (Figure 1.1).

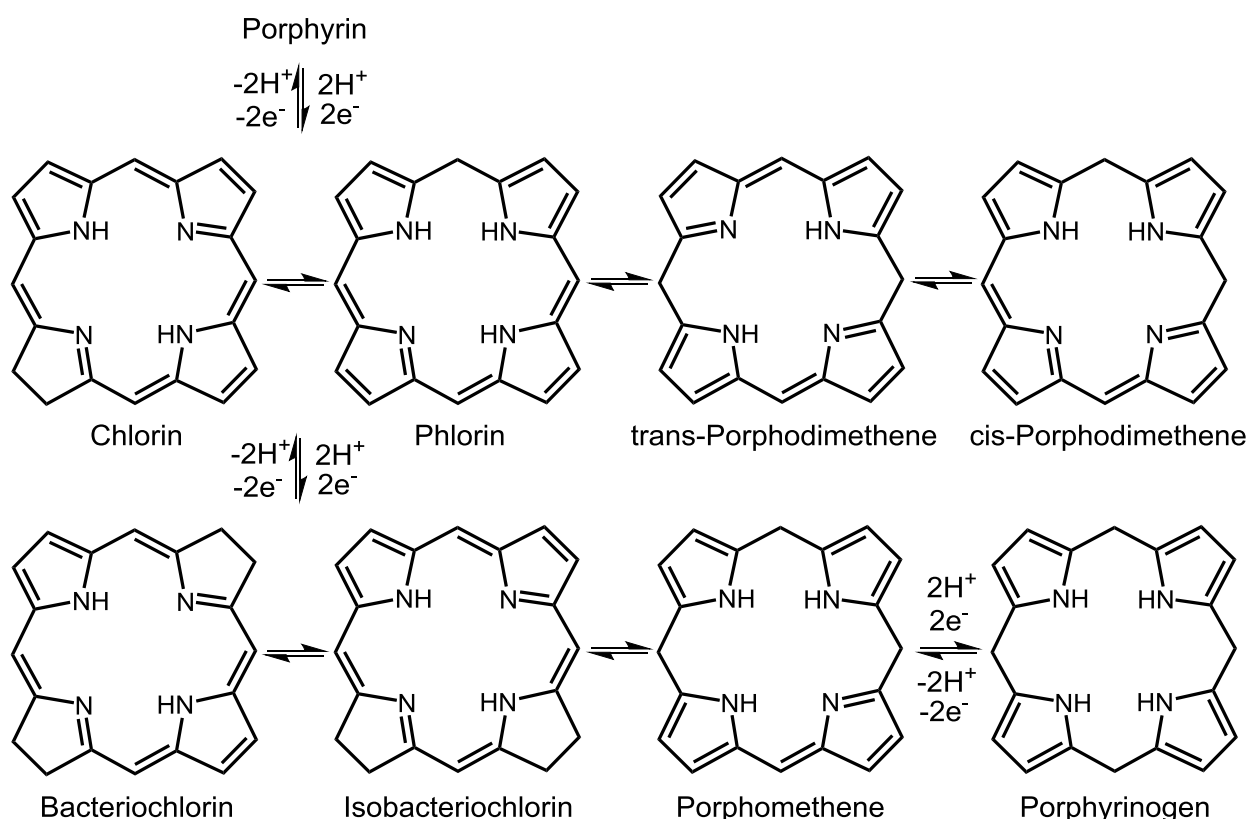


Fig. 1.1. Structure of hydroporphyrins and redox relationships between them.

The porphyrin ring can act as both a base and an acid. The protonation of “free” nitrogen atoms is easily achieved in acids, while strong bases remove the two nitrogen protons to form a dianion. Although porphyrins can react primarily by electrophilic or radical substitution, as expected for aromatic compounds, still the B and D pyrrole rings (Figure 2) can react differently on the double bond which is not directly involved in aromatic system [17]. Performing reactions on the macrocycle ring, and the use of various starting materials combined with different synthesis methods led to a vast number of porphyrins, the first example being reported by Fisher in 1920 [18].

The large delocalized aromatic system of the porphyrin ring is responsible for its typical UV-Vis absorption. The Soret band at $\lambda_{\text{max}} \sim 400 \text{ nm}$ (absorption coefficient $\epsilon \sim 10^5$) is the most pronounced porphyrin macrocycle electronic absorption characteristic for metal-free, diprotonated and metalated forms. Other four less intense Q bands are found at lower energies in the region 450 – 700 nm ($\epsilon \sim 10^4$). Their maximum wavelength and relative intensities were found to be dependent on the nature and position of the porphyrin substituents. As proposed by Gauterman, the perturbation of porphyrin π orbitals by the peripheral substituents electronic effect [19] gives the four general types of Q bands absorption, classified by their relative intensity: etio – rel. int. $\text{IV} > \text{III} > \text{II} > \text{I}$, rhodo – $\text{III} > \text{IV} > \text{II} > \text{I}$, oxorhodo – $\text{III} > \text{II} > \text{IV} > \text{I}$, phyllo – $\text{IV} > \text{II} > \text{III} > \text{I}$, where the wavelength increases in the order $\text{IV} < \text{III} < \text{II} < \text{I}$. Coordination to divalent metal ions simplifies the absorption spectrum which usually consists of only one Q band with two shoulders and the Soret band, due to the increase of the molecule symmetry from D_{2h} to D_{4h} . The electronic structure of coordinated metal influences the absorption so that first row transition metals with no partially filled d-orbitals like Zn(II) and Ti(IV) have little impact on the π system of porphyrins (called regular), while metals like Cu(II), Ni(II), Co(II) etc with partially filled d-orbitals significantly affect both the absorption and emission spectra (called irregular) by strong mixing with porphyrin π orbitals.

Changes in conjugation of the macrocycle ring affect the absorption spectrum as well, so that reducing one peripheral bond to give chlorin is characterized by a long wavelength band at $\sim 660 \text{ nm}$, while reducing two double bonds to give bacteriochlorin shows strong absorption at $\sim 750 \text{ nm}$ and a split of Soret band of comparable intensity. The formation of phlorins is accompanied by broadening and considerable decrease of absorption. The red absorption is found at $\sim 650 \text{ nm}$ for free-base phlorins, while the metallophlorin anions show a strongly red shifted band at $\sim 900 \text{ nm}$.

1.2. The synthesis of porphyrins

The construction of porphyrin macrocycle can be achieved through three main pathways, depending on starting materials [20]:

- monopyrroles;
- dippyroles;
- and linear tetrapyrroles.

The first pathway is based on the higher reactivity of pyrrole α -position compared to β -position. The most used method consists of condensation of α -unsubstituted pyrroles and aliphatic or aromatic aldehydes. This leads to *meso*-tetrasubstituted porphyrins, symmetrical if only one type of aldehyde and pyrrole are used or a mixture of products if two or more aldehydes / pyrroles are used. Rothmund was the first who prepared unsubstituted [21] and later *meso*-tetrasubstituted porphyrins by heating pyrrole and an aldehyde in pyridine in a sealed tube at 150 °C for 24 h [22] (Figure 1.2). The reported yields were very low, but further improved to 9 % for tetraphenyl porphyrin [23]. The final product is usually contaminated with chlorin derivative. Adler and Longo made a major improvement in synthesis of *meso*-tetraphenyl porphyrin by reacting benzaldehyde and pyrrole in refluxing propionic acid open to the air [24]. Many other substituted benzaldehydes were converted into respective porphyrins in yields of up to 20 % [25]. The products crystallize on cooling the reaction mixture, thus simplifying the purification procedure. As mentioned previously, the porphyrins were contaminated with not fully oxidized species but treatment with 2,3-dichloro-5,6-dicyanobenzoquinone (DDQ) converted the chlorin into porphyrin, thus giving better yields. The weak side of the Adler-Longo method is the failure to obtain porphyrins from benzaldehydes bearing sensitive functional groups, because of the harsh reaction conditions.

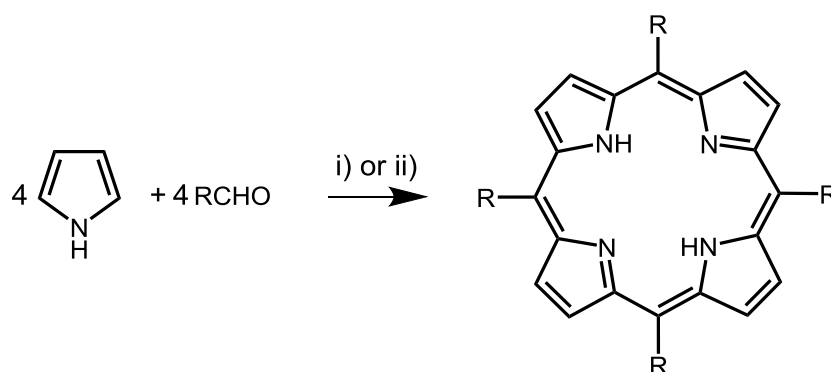


Fig. 1.2. The scheme of the Rothmund porphyrin synthesis: i) MeOH / Pyridine, 150-220 °C, 24-48 h in sealed vessel, R = H, CH₃, C₄H₉, C₆H₅ and Adler-Longo porphyrin synthesis; ii) propionic acid, 141 °C, 30 min in air, R = substituted aryl rings.

Lindsey et al. developed another synthetic approach by separating the cyclization and oxidation steps [26]. As it can be seen in Figure 1.3, the two-step one-pot procedure takes into consideration that under equilibrium conditions the acid catalysed condensation (usually trifluoroacetic acid TFA or $\text{BF}_3 \cdot \text{OEt}_2$) forms porphyrinogens, which are further oxidised with quinone derivatives (usually tetrachloro-1,4-benzoquinone (p-chloranil) or DDQ). A detailed study of the reaction mechanisms showed that the yield (average of 30 - 40%) is very sensitive to the concentration of reagents (usually 10^{-2} M) and acid (usually 10^{-3} M), as well as the time of reaction [27, 28]. Milder conditions used in this approach allowed the use of sensitive aldehydes, but the low concentration of reagents is a problem for large-scale production.

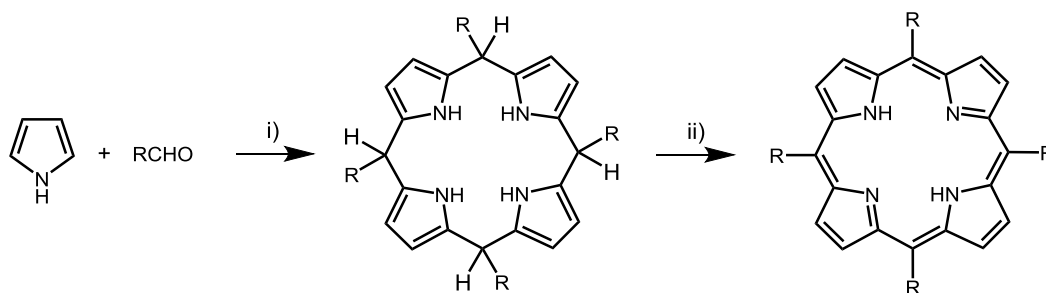


Fig. 1.3. The scheme of the two-step, one-pot Lindsey porphyrin synthesis i) DCM, RT, TFA or $\text{BF}_3 \cdot \text{OEt}_2$, 30-60 min in inert atmosphere ii) DDQ or p-chloranil, RT, 1-2 h.

The mixed aldehydes condensation results in the formation of a statistical mixture of porphyrins which have to be separated in order to obtain the desired product. Condensation of an aldehyde with unsymmetrically substituted pyrroles yields isomer mixtures, while the head-to-tail self-condensation of 2-substituted pyrroles allows targeted synthesis of porphyrins with different β -substituents (Figure 1.4) [29]. The stability and reactivity of the intermediate carbocation, produced by the removal of leaving group L, is essential for the reaction efficiency. Nature uses this method for the construction of the uroporphyrinogen.

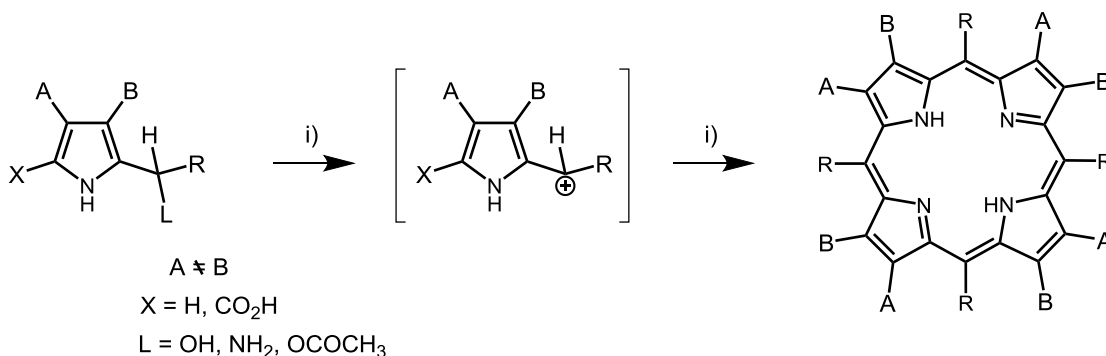


Fig. 1.4. The scheme of the porphyrin synthesis by self-condensation of 2-substituted pyrroles i) reflux.

The use of dipyrrolic intermediates for the unsymmetrical porphyrin synthesis (commonly called “2+2 synthesis”) was extensively studied as well. The access to both β and *meso* unsymmetrical porphyrins is the main reason for this. Dipyrromethene based synthesis is the backbone of the Fisher’s method [18]. An alternative 2+2 synthesis was developed by MacDonald by using the dipyrromethane intermediates [30]. This method involves either the condensation of 5,5'-diformyldipyrromethanes with 5,5'-diunsubstituted dipyrromethanes or self-condensation of 5'-unsubstituted 5-formyldipyrromethanes under mild acid catalysis [31]. Lindsey showed that condensation of dipyrromethanes with aldehydes can be efficiently used for construction of *trans*-A₂B₂-porphyrins (Figure 1.5), but the scrambling processes that leads to a mixture of porphyrins is the main issue for any type of 2+2 synthesis [32].

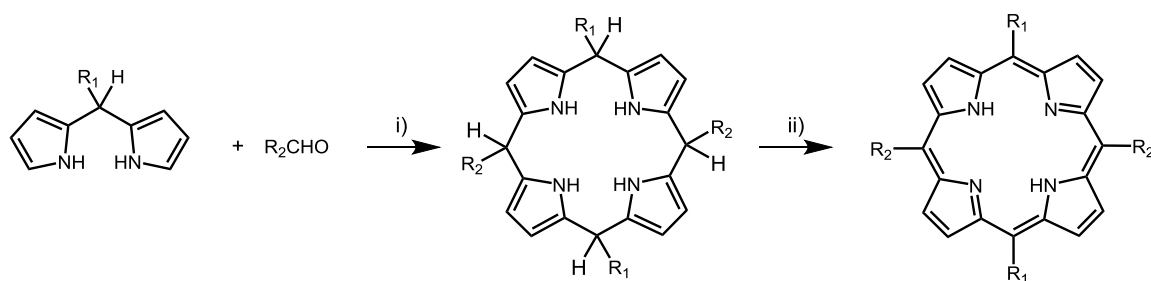


Fig. 1.5. The scheme of modified Lindsey synthesis of *trans*-A₂B₂-porphyrins starting with dipyrromethanes i) DCM, RT, TFA or BF₃·OEt₂, 30-60 min in inert atmosphere ii) DDQ or *p*-chloranil, RT, 1-2 h.

If fully unsymmetrical porphyrin is required, then stepwise coupling of individual pyrroles is performed to give linear tetrapyrroles, cyclization of which ends with desired product [33] (Figure 1.6). Bilenes *b* and Biladienes *ac* are the most frequently used tetrapyrrole precursors by cyclization of which, in the presence of Cu(II) salts, the copper complexes of porphyrin are obtained. Copper is later removed with strong acids to form the metal-free porphyrins.

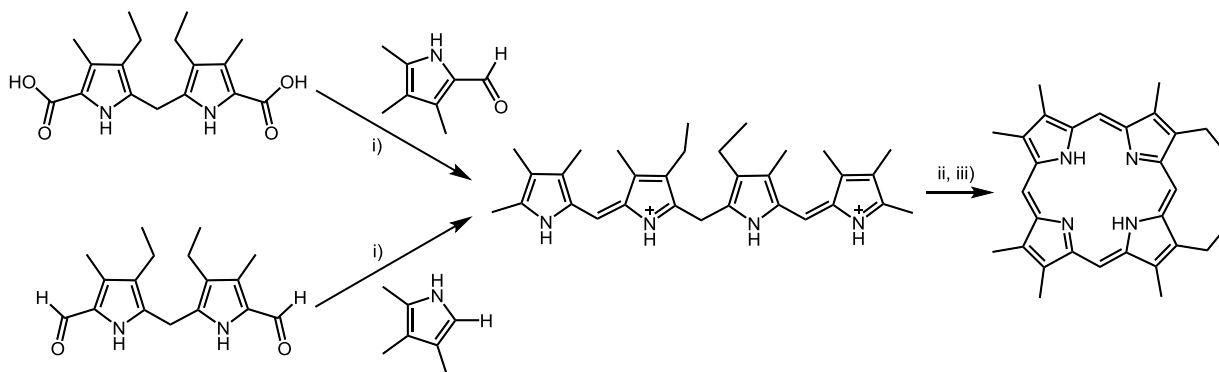


Fig. 1.6. The scheme of porphyrin synthesis through Biladiene *ac* i) MeOH, HCl, RT ii) MeOH, Cu(OAc)₂, reflux, 48 h iii) H₂SO₄.

1.3. Porphyrin based dyes for Dye Sensitised Solar Cells [34]

The use of porphyrins as light harvesters in various solar energy conversion systems is quite reasonable because of an intense absorption in the Soret band at high energy region, as well as in the Q bands at low energy. The numerous reports on the use of natural and synthetically obtained porphyrins in conversion of solar energy into chemical or electrical energy represent an attempt to mimic the photosynthetic systems found in plants and some bacteria. The DSSCs are one of the multiple examples employing porphyrins for light absorption and subsequent photoinduced processes.

In 1993 was reported for the first time the incorporation of the chlorophyll *a* (Chl-*a*), depicted in Figure 1.7, into a TiO₂ based DSSC [35]. Using Chl-*a* and compounds obtained by its chemical modification (pheophorbide *a*, Mg-chlorin *e*₆, H₂-chlorin *e*₆, Cu-chlorin *e*₆ and Cu-2-*a*-oxymesoisochochlorin *e*₄), Incident Photon-to-Current Efficiencies (IPCEs) of up to 70 % were obtained. Maximum overall energy conversion efficiency (η) of 2.6 % (under simulated sunlight illumination) was obtained for unmodified Chl-*a*.

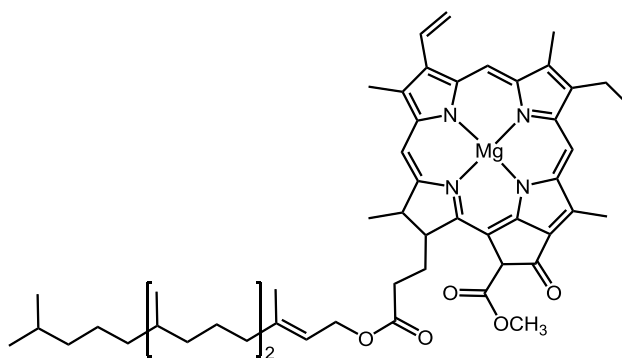


Fig. 1.7. Structure of chlorophyll *a*.

Using a derivative of Chl-*a* (Figure 1.8) another group has obtained an improved overall energy conversion efficiency of 3.1 % [36]. Employing carotenoids as redox spacer they achieved optimisation of the η up to 4.2 % (for β -carotene) [37].

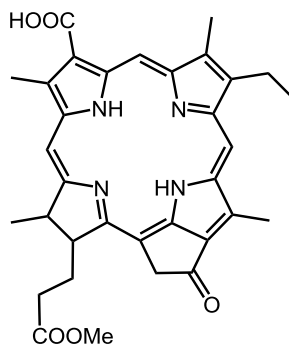


Fig. 1.8. Structure of methyl 3-carboxy-3-devinyl pyropheophorbide *a*.

The influence of carotenoid moiety was further investigated by the same group [38]. The authors concluded that introduction of a carotenoid unit to the pheophorbide molecule may result in an electron transfer and singlet-energy transfer from the carotenoid to the chlorin moiety and suppression of the singlet–triplet annihilation reaction. As a result, the performance of the cell was improved from 1.4 to 1.8 %. The maximum overall energy conversion efficiency was greatly improved to 6.5 % by extension of π -conjugation length along the Q_y axis (Figure 1.9) [39]. This improvement can be explained by concentration of the electron density in the Q_y direction with an efficient LUMO +2 for electron injection and enhanced Q_y absorption band together with a smaller E_{ox} value for light-harvesting. Moreover the HOMO and HOMO-1 are mainly distributed far from TiO_2 surface allowing efficient electron transfer from I^-/I_3^- electrolyte.

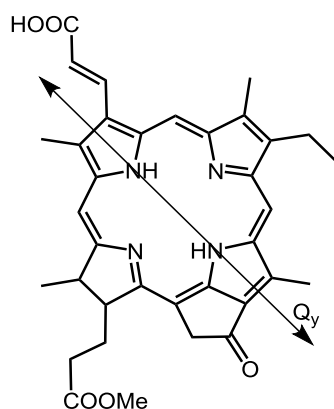


Fig. 1.9. Structure of methyl trans-3²-carboxypyropheophorbide *a*.

Using the knowledge accumulated during last years a series of new chlorin based compounds was obtained by Wang et al [40]. The overall energy conversion efficiencies for all DSSCs sensitized with chlorin-based dyes exceeded 6 % and reach 8 % for dodecyl trans-3²-carboxypyropheophorbide *a* (Figure 1.10). This is the highest η value among chlorophyll sensitized solar cells published to date.

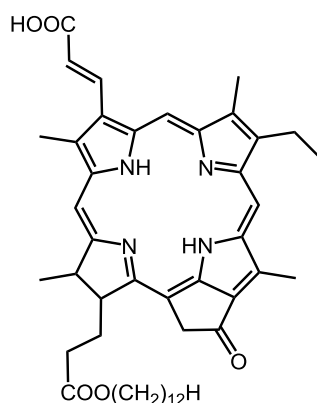


Fig. 1.10. Structure of dodecyl trans-3²-carboxypyropheophorbide *a*.

Another approach to the cyclic tetrapyrrole molecules for DSSCs sensitizing is the use of synthetic porphyrins. The porphyrin based sensitizer with the highest overall energy conversion efficiency ($\eta = 3.0\%$) until 2004 was the easily accessible tetra(4-carboxyphenyl)porphyrin (Figure 1.11) [41]. The relatively low η value of the sensitizer was explained by the highly symmetrical structure and the aggregation of porphyrin molecules on the TiO_2 surface.

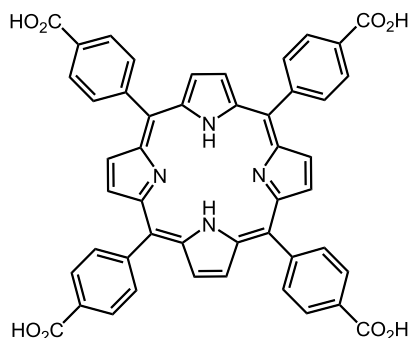


Fig. 1.11. Structure of tetra(4-carboxyphenyl)porphyrin.

Substitution at the porphyrin β -pyrrole position with surface anchoring π -extending moieties proved to be a useful tool in obtaining efficient porphyrin based sensitizers. Nazeeruddin and coworkers have designed a series of β -substituted porphyrins for sensitization of TiO_2 surfaces [42]. The Zn porphyrins β -substituted with ethenylbenzoic acid as anchoring moiety (Figure 1.12) gave highest overall energy conversion efficiency of up to 4.8 %, while using Cu porphyrins or phosphonic acid as anchoring group showed much lower η values. It is to be emphasized that the introduction of methyl substituents in the *meso*-position of phenyl groups give 16 % rise of η (4.11 to 4.8 %), probably by preventing π - π stacking between porphyrin molecules on the semiconductor surface and thereby inhibiting exciton annihilation.

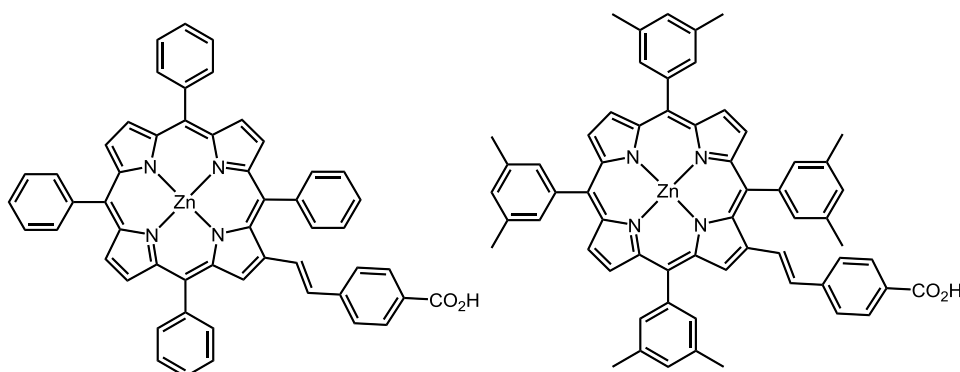


Fig. 1.12. Structures of 4-(*trans*-2'-(2''-(5'',10'',15'',20''-tetraphenylporphyrinato zinc(II)-yl)ethen-1'-yl)-1-benzoic acid (left) and 4-(*trans*-2'-(2''-(5'',10'',15'',20''-tetra(4-methylphenyl)porphyrinato zinc(II)-yl)ethen-1'-yl)-1-benzoic acid (right).

In order to further improve the above discussed design, other surface anchoring linkers were employed by the same group [43]. The cyanoacrylic acid modified porphyrin (Figure 1.13) showed best results of $\eta = 5.6\%$, compared to acrylic acid ($\eta = 4.0\%$), 2-cyanopenta-2,4-dienoic acid ($\eta = 4.0\%$), 3-(4-ethenyl-phenyl)-cyanoacrylic acid ($\eta = 3.7\%$) or 1,2-benzenedicarboxylic acid ($\eta = 2.4\%$). The IPCEs of the obtained porphyrins are very high reaching 85 %. The additional withdrawing CN group showed a stabilizing effect on the LUMO and LUMO+1 which degeneracy is broken and the LUMO is extended out onto the β -substituent, beneficial for electron injection into the TiO_2 conduction band.

In the following work [44] the same group has modified the phenyl units of a Zn porphyrin β -substituted by malonic acid (Figure 1.13) in order to determine its influence on the solar cell performance. From the series of obtained dyes the *p*-methyl phenyl substituted porphyrin showed the best $\eta = 7.1\%$ under standard global AM 1.5 solar conditions. However, all of the dyes exhibit efficiencies $\geq 5\%$. It is indicating that the nature of the substituents of the phenyl group is not the critical factor in determining photosensing properties of dyes. At the same time a very good performance of $\eta = 3.6\%$ was achieved by incorporation of this dye into a solid state DSSC.

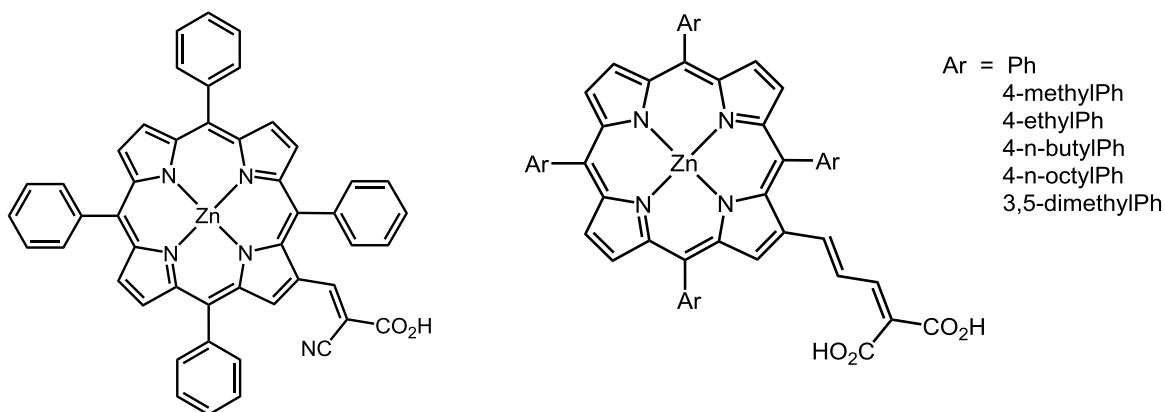


Fig. 1.13. Structure of cyano-3-(2'-(5',10',15',20'-tetraphenylporphyrinato zinc(II))yl)-acrylic acid (left) and 2-carboxy-5-(2'-(5',10',15',20'-tetra(4''-aryl)porphyrinato zinc(II))yl)penta-2,4-dienoic acids.

An interesting approach was reported by Japanese researchers [45]. It consists in unsymmetrical π -system elongation of the porphyrin *via* connection of the linker moiety by meso, β – ring fusion of Zn porphyrin and carboxy-naphthyl unit (Figure 1.14), which resulted in conversion efficiency of 4.1 % (50 % higher in comparison to the unfused porphyrin reference). It illustrates the benefit of porphyrin desymmetrization and π -system elongation in harvesting of solar light in the visible and near infrared regions, giving enhanced cell performance.

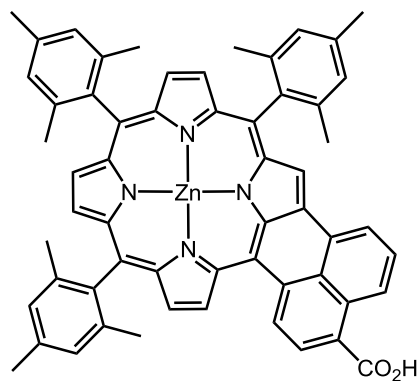


Fig. 1.14. Structure of 5-(4-carboxynaphth-1-yl)-10,15,20-tris(2,4,6-trimethylphenyl)porphyrinato zinc(II).

The best design of porphyrin based DSSC dyes proved to be the donor- π -acceptor configuration by efficient removal of the positive charge from the semiconductor surface and charge recombination inhibition. A research group from Taiwan synthesized a Zn(II) porphyrin with bis(4-tert-butylphenyl)amino and 4-carboxylphenylethynyl substituents on the opposite meso sites (Figure 1.15) with best on that moment efficiency for porphyrin dyes [46]. This was improved later by incorporating two octyloxy groups in the ortho positions of each *meso*-phenyl ring as pictured in Figure 1.15 in combination with Co^(II/III)tris(bipyridyl) redox electrolyte [47]. The use of alkoxy chains provides a very effective barrier to recombination of the electrons in the titania and holes in the Co electrolyte. A record efficiency of 11.9 % was achieved, further improved to 12.3 %, by cosensitization with an earlier published organic dye 3-{6-[4-[bis(2',4'-dihexyloxybiphenyl-4-yl)amino-]phenyl]-4,4-dihexyl-cyclopenta-[2,1-b:3,4-b]dithiophene-2-yl]}-2-cyanoacrylic acid, compared with previous Ru based dye record of 11.1 % [48].

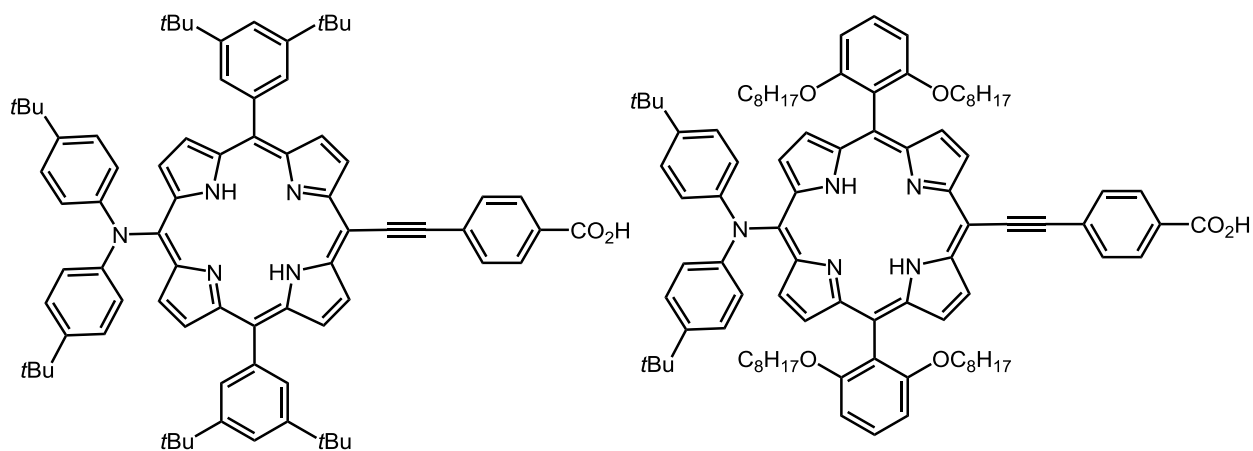


Fig. 1.15. Structures of 5,15-bis(3,5-di-tert-butylphenyl)-10-(bis(4-tert-butylphenyl)amino)-20-(4-carboxylphenylethynyl) porphyrin (left) and its *ortho*-dioctyloxyphenyl analogue (right).

1.4. Light induced processes in ferrocene - [Ru-polypyridyl]ⁿ⁺ derivatives

Ferrocene is one of the most widely exploited compounds in the chemical literature, and it is frequently used as a starting material in both organometallic and organic chemistry transformations [49]. This sandwich-type compound consists of an iron(II) atom bonded in an η^5 fashion to two cyclopentadienyl rings (Cp). Redox cycling between the $\text{Fe}^{2+} / \text{Fe}^{3+}$ states is both chemically and electrochemically reversible. Certainly this final point is one main reason why ferrocene has been so popular as a redox reporter in supramolecular structures [50]. Fc molecule is largely used in supramolecular systems as active unit in both intra and intermolecular photoinduced processes. Wrighton and Lee [51] studied for the first time the nature of ruthenium polypyridyls excited state quenching by Fc derivatives in acetonitrile. Benniston et al. [52] reported the first example of $\text{Fc}^+ - [\text{Ru}(\text{bpy})_3]^+$ Charge Separated (CS) state (left picture of Figure 1.16), formed in a polyene-bridged binuclear Fc-Ru system. The Fc was found to efficiently quench the $[\text{Ru}(\text{bpy})_3]^{2+}$ and $[\text{Ru}(\text{bpy})_2(\text{phen})]^{2+}$ [53] luminescence but no indication of reduced species was found (within experiment resolution) in transient absorption spectra for ethane and ethene linkers, while the use of 3,8-dimethyl-1,3,5,7,9-decapentene afforded spectral signature of CS state with a lifetime of (430 ± 50) ps. The use of ornithine amino acid to connect ferrocene carboxylic acid and bpy-carboxylic acid via peptide bonding in analogous $[\text{Ru}(\text{bpy})_3]^{2+}$ complex showed similar luminescence quenching, but no lifetime measurements were done [54]. The fluorescence of $[\text{Ru}(\text{bpy})_2\text{pp}]^{2+}$ and $[\text{Ru}(\text{tap})_2\text{pp}]^{2+}$ (tap = bis-(1,4,5,8-tetraazaphenanthrene, pp = 3-methyl-1-(2'-pyridine)pyrazole) was quenched as well with insertion of one ferrocene moiety by direct linking to pp unit [55]. Still, no clear results were obtained from transient absorption, but a long lived (5 μs) species was found in water solution for $\text{Ru}(\text{bpy})_2(\text{ppFc})^{2+}$, which is not present in CH_3CN .

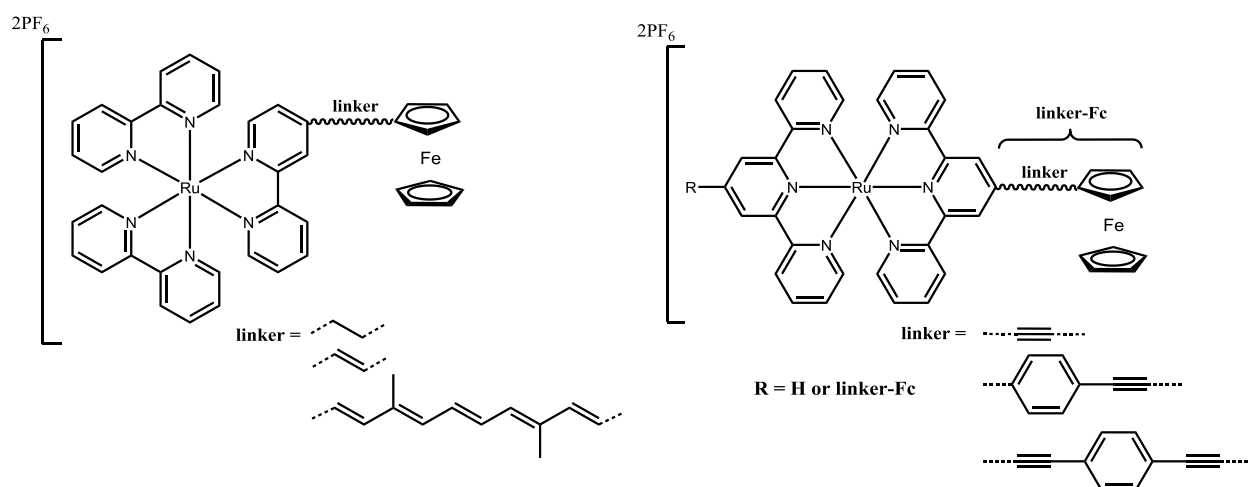


Figure 1.16. Examples of ferrocene – Ru(II) polypyridyl designs.

Intramolecular $[\text{Ru}(\text{tpy})_2]^{2+}$ luminescence quenching by Fc was shown to be possible to control by changing the terminal atom of peptide bridge that connects the Fc to tpy moiety [56]. The complexes with C-bound Fc were much less luminescent compared to analogues with N-bound Fc. As expected Fc directly linked to C₄ on tpy in $[\text{Ru}(\text{tpy})(\text{Fc-tpy})]^{2+}$ and $[\text{Ru}(\text{Fc-tpy})_2]^{2+}$ quenches the excited state of $[\text{Ru}(\text{tpy})_2]^{2+}$ and shortens the lifetimes to <25 ns (the resolution limit of experimental setup) compared with 11 μs for “Fc-free” complex in EtOH / MeOH solvent mixture [57]. The insertion of an ethynyl spacer into the binuclear Ru-Fc-Fc-Ru analogue results in partial restore of luminescence with a lifetime of 67 ns [58].

Siemeling et al. [59] studied the influence of the Fc-tpy spacer on the excited state dynamics of $[\text{Ru}(\text{tpy})(\text{Fc-tpy})]^{2+}$ and $[\text{Ru}(\text{Fc-tpy})_2]^{2+}$ complexes (right picture of Figure 1.16). Although no certain intramolecular quenching mechanisms were recognized, certainly the excited state lifetimes (260 ns for $[\text{Ru}(\text{tpy})(\text{Fc-C}\equiv\text{C-tpy})]^{2+}$) are the longest compared to other Fc-Ru dyads or triads. It was noticed that the use of octamethyl-ferrocene showed shorter lifetimes compared to parent Fc, no room temperature luminescence and only weak emission at 77 K. The oxidation of Fc unit partially restored the luminescence, but did not show major influence on the lifetimes of long lived species so that no obvious conclusions were made.

One explanation is based on the research by A. Harriman et al. [60], who showed that the triplet lifetimes of the $[\text{Ru}(\text{Fc-tpy})_2]^{2+}$ after introduction of acetylenic substituents on the tpy are significantly longer than that of the parent complex. The proposed explanation consisted of electron delocalisation over the extended π^* orbital, while introduction of an additional phenyl ring into the π -electron system lead to an opposite effect.

An interesting case is the use of Ru(II) for Fc-C₆₀ linking by formation of ruthenocene-like Ru-C₆₀ direct bond, in the C₆₀-Ru-Fc triads [61]. Competition between photoinduced charge separation and intersystem crossing due to a heavy-atom effect was noticed by the authors. From the UV-Vis transient absorption spectra it was concluded that the use of phenyl Ru-Fc spacer resulted in formation of ³C₆₀ excited state in toluene, but the use of a more polar THF solvent and connected with this a lower reorganisation energy generated the CS state. When ethynyl unit was used instead, the charge separation was observed in both toluene and THF. Later, diphenylphosphine linkage was reported [62] but unfortunately no photophysical properties were described.

1.5. Light induced processes in ferrocene - porphyrin derivatives

The simplest, from the synthesis point of view, ferrocene-porphyrin architecture is achieved by direct link of Fc unit at the porphyrin four *meso* positions. Such a close proximity of the two units (top left picture of Figure 1.17) resulted in a very efficient quenching of the porphyrin luminescence [63] by injection of an electron from Fc, which occurs within 208 ± 10 fs [64], with a lifetime of the $\text{Fc}^+ \text{P}^-$ CS state being 17 ± 4 ps. The first report by Bruce group, on the ferrocene-porphyrin system excited state properties, describes a metal-free and Zn meso-tetrakis(4-ferrocenylphenyl)porphyrin (top right picture of Figure 1.17) [65]. The fluorescence of its oxidised tetraferrocenium form was expected to be smaller compared to unoxidised tetraferrocene porphyrin as result of electron transfer to the ferrocenium ion from the porphyrin excited state, but an opposite result was obtained. The energetic explanation and the slower electron transfer to metal centres were suggested, but the authors did not consider the electron transfer from ferrocene to porphyrin that forms the $\text{Fc}^+ \text{P}^-$ CS state, and as result fluorescence quenching. The Fc deactivation seems to be more effective than the ferrocenium mediated pathway, an expected result taking into account the lower oxidation potential of ferrocene compared to porphyrin, and redox fluorescence switches based on ferrocene-porphyrin molecules were reported by different groups [66].

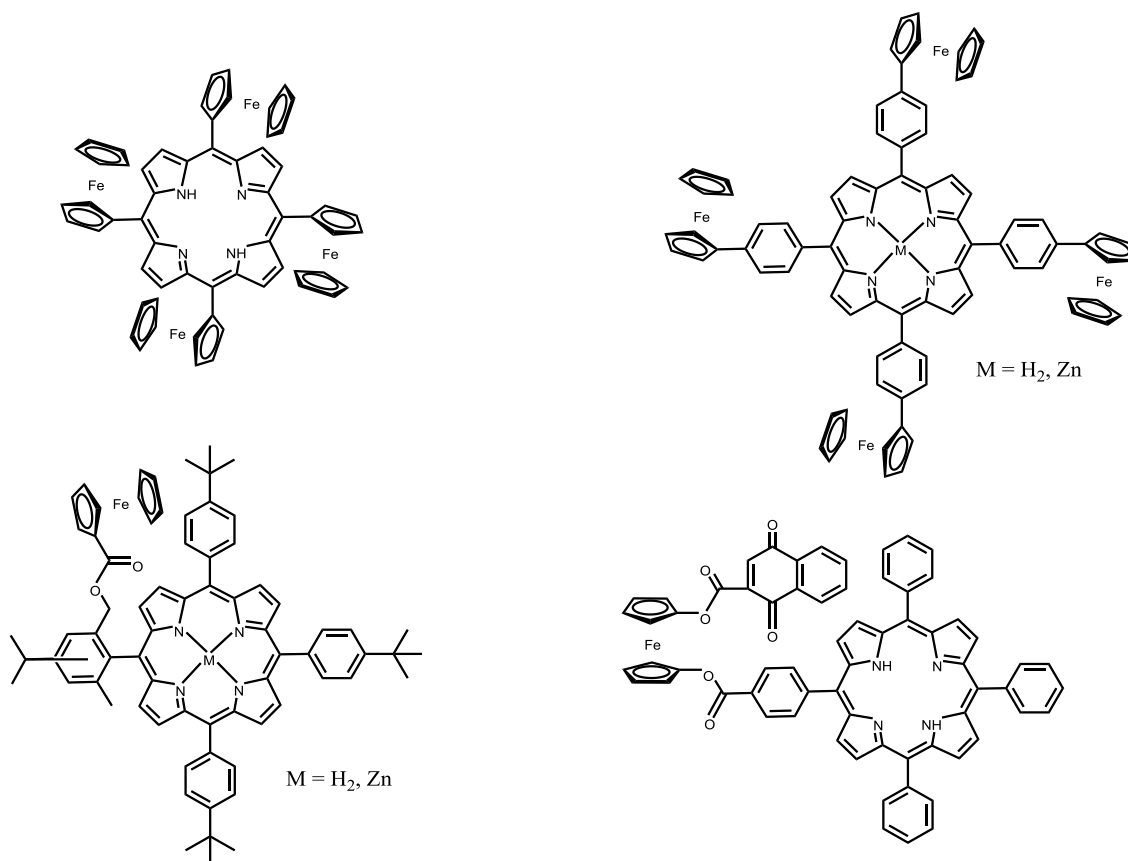


Figure 1.17. Examples of ferrocene - porphyrin design.

Shortly afterwards Beer group described a porphyrin-ferrocene-quinone molecule (bottom right picture of Figure 1.17) [67] whose luminescence was quenched by 90 % (versus tetraphenyl porphyrin reference), and the authors ascribed this to a rapid electron transfer from the singlet excited state of the porphyrin to the quinone acceptor, but the formation of porphyrin anion by Fc electron injection should be considered as well. A chemically alike system but lacking the quinone unit (bottom left picture of Figure 1.17), showed similar quenching of the porphyrin fluorescence and increasing the number of ferrocene units resulted in a more efficient quenching [68].

The use of an ethene linker to connect ferrocene to porphyrin *meso*-phenyl showed strong fluorescence quenching, while the saturated ethane linker slowed weaker excited state interaction and resulted in fluorescence restore from 0.38 to 0.84 (compared to phenyl analogue), as reported by Wrighton group [69]. The weaker electronic communication for the saturated linker resulted in a twice slower quenching process compared to unsaturated linker. At the same time it should be noted that the molecule geometry greatly alters system photodynamics so that the *cis* isomer showed an order of magnitude faster quenching compared to *trans* form. The use of ethyne linker showed fluorescence quench to 0.35 compared to phenyl analogue [70]. The intramolecular fluorescence quenching in monoferrocenyl-porphyrin with ethoxy spacer was studied in DNA scaffolding perspective [71]. The rate of photoinduced electron transfer was not much affected and changed only from $9 \times 10^9 \text{ s}^{-1}$ in N00 buffer ($1 \times 10^{10} \text{ s}^{-1}$ in MeOH) to $7 \times 10^9 \text{ s}^{-1}$ by intercalation into DNA, suggesting an insignificant influence on the electronic coupling between the donor and acceptor.

One to four porphyrin units connected by ethyne linker were used as “molecular wires” between Fc and C_{60} units to form $\text{Fc-P}_n\text{-C}_{60}$ ($n = 1, 2$ and 4) triads in a work by Winters et al [72]. Compared to $\text{P}_n\text{-C}_{60}$ dyad, the Fc induced lower quantum yields of initial charge separation. The authors ascribed this to competing quenching of ferrocene by Energy Transfer (EN) onto the low lying Fc excited states followed by rapid deactivation. However, when the CS state is formed subsequent charge shift occurs to form $\text{Fc}^+\text{-P}_n\text{-C}_{60}^-$ state, with a decay time rate of 0.64, 7.1 and 7.8 ns depending on linker. As expected, going from the porphyrin monomer to dimer a more than tenfold increase of lifetime was found, but insertion of two more porphyrin units gave much smaller changes. A tentative to explain long-range charge recombination process consists of the electron tunnelling through the conjugated porphyrin oligomer. An interesting study of Fc-ZnP dimer, formed by Zn complementary coordination to the *meso*-imidazolyl unit from the second porphyrin, was reported by Kobuke group [73]. A strong excitonic coupling between the porphyrin units of cofacial slipped ZnP dimers was suggested by the splitting of the Soret

absorption band. The degree of conjugation between ferrocene and porphyrin units strongly influenced the porphyrin fluorescence which was highly quenched by direct linkage, moderately for the phenylene-ethenylenes and marginally for the phenylene-ethyl linkers. This work was further continued and the monoacetylene-linked bis-ZnP dimer analogue axially linked with Fc/Fc, Fc/C₆₀, C₆₀/C₆₀ showed a fluorescence quenching efficiency of 44, 63 and 85 % [74]. Enhanced two-photon absorption was described, compared with above described ZnP dimer and the best results were obtained for asymmetrical Fc/C₆₀ system.

The study of β,β' -pyrrolic fused ferrocene–(zinc porphyrin)–fullerene is a good example which shows the influence of the connection site on the porphyrin ring on the system excited state dynamics [75]. Though the distance between Fc and fullerene units is shorter compared with its meso-porphyrin connected triad analogue, the ³CS state lifetime is almost 10² times longer.

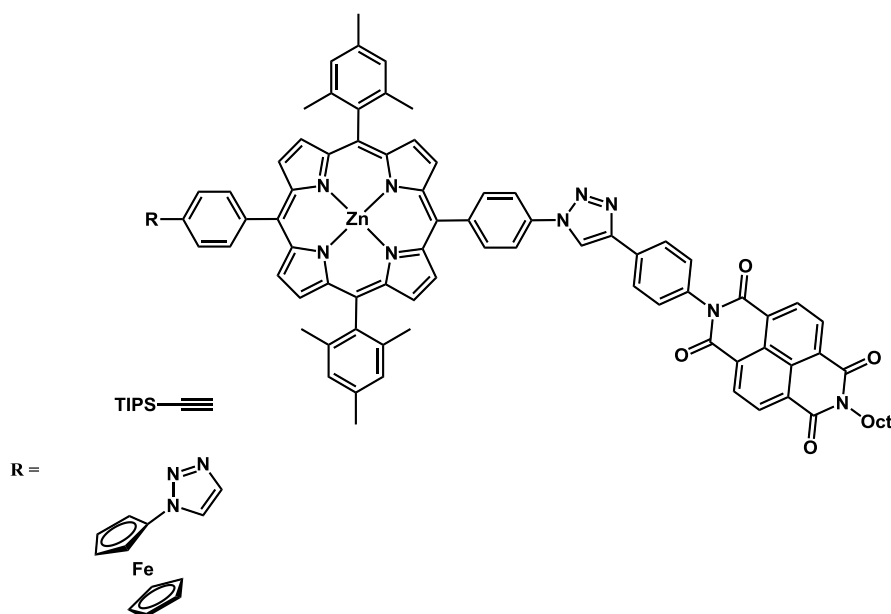


Fig. 1.18. Example of ferrocene - porphyrin - naphthalenediimide design.

The Odobel group constructed a Fc–(ZnP)–NDI (NDI - naphthalenediimide) triad (Figure 1.18) which shows very interesting excited state properties. Both excitation of ZnP or NDI resulted in formation of CS state, but the NDI excited state pathway was much more efficient for the triad and the reference “ferrocene-free” dyad. This could be explained by a greater driving force of both NDI singlet and triplet states, but the triazole bridged electron transfer could play a key role as well, as it was concluded from DFT calculations. Still, much more important is the influence of Fc unit on the further processes, as after initial ZnP⁺-NDI^{•-} charge separation the ferrocene-porphyrin charge shift takes place to form the Fc⁺-ZnP-NDI^{•-} CS

state with a remarkable lifetime of 1.9 μ s, much larger compared to reference dyad (subnanosecond for 1 CS state and 90 ns for 3 CS state).

A different design approach was used by Yuliang and Osamu groups for construction of a triad where both porphyrin and fullerene are linked by ester bonding to Fc-dicarboxylic acid [76]. The fluorescence lifetime measurements indicated two components for the triad and none of them corresponded to that determined in the porphyrin-ferrocene dyads. Their nature was not fully understood, requiring a more detailed study, but simultaneous intersystem crossing and electron transfer processes in fluorescence quenching mechanism were suggested. Later, they reported [77] the photophysical properties of a triad constructed by crown ether-alkylammonium cation complexation for binding of Fc-P conjugates with C_{60} . CS states of up to 7 μ s were reported and a lifetime decrease depending on the porphyrin central metal in order $Mg(II)P > Zn(II)P > H_2P$. These values are about 2 orders of magnitude lower compared to P- C_{60} dyads as the distance between ionic pair increases from about 17 to 27 Å.

Rotaxane systems consisting of ZnP crown ether necklace and C_{60} -Fc axle were studied for photophysical processes after excitation on ZnP unit [78]. It was found that in nonpolar solvents energy transfer to C_{60} is predominant, while in polar solvents $(ZnP^+; C_{60}^- - Fc)_{rotax}$ charge separation takes place. The further positive charge shift to Fc unit seems to be quite slow, because of a long-distance through-space process and only the slight difference in ZnP^+ and C_{60}^- decay rates in DMF indicated such a process. The lifetimes of the C_{60}^- moiety were evaluated to be 290 and 370 ns in benzonitrile and DMF, respectively. Later, excited state of a $C_{60}^{necklace-}Fc^{axle+}$ rotaxane, without porphyrin unit, was evaluated showing formation of CS species [79]. The lifetime of $(C_{60}^-; Fc^+)_{rot}$ state showed to be dependent of solvent polarity (20 and 33 ns in DMF and PhCN at RT), suggesting CS state stabilization in polar solvents. The increase of lifetimes at lower temperatures (up to 263 ns in DMF at 210 K) was ascribed by authors to stabilization of a larger distance between the C_{60} and Fc units. Shortening the C_{60} - crown ether spacer afforded expected shorter lifetimes of 10, 13 ns in DMF and PhCN respectively. Interesting systems were constructed by Schmitt et al. [80] comprising an additional redox-active $Cu(phen)_2$ spacer between Fc and P units, to form tetrads. Though it would potentially show complex excited state dynamics which could generate successive charge transfer and shift processes to finally generate $Fc^+ - Cu(phen)_2 - ZnP - C_{60}^-$ CS state, unfortunately no photophysical study was performed.

The ferrocene proved to efficiently transfer electron inter [81] and intramolecularly to the excited state of phthalocyanines too, and fluorescence quenching was monitored for dyads with ethoxy, ethynyl, peptide and oxycoumarin spacers [82,83]. The boron subphthalocyanine SubPc

emission intensities were reduced by several orders of magnitude, compared to chlorine analogue, when ferrocene-ethanol or ferrocene-carboxylic acid were axially bound to boron atom (Figure 1.19), with a decay rate of 5 and 21 ps respectively, as reported by Nemykin et al [84]. Later a more detailed study was reported [85], showing the Fc-to-SubPc electron transfer mechanism to be involved in SubPc^{*} excited state quenching. The charge separation process for ferrocene-ethanol and ferrocene-carboxylate substituted SubPc were found to occur in 5.1 and 1.5 ps, while lifetime of ion pairs were determined as 350 and 224 ps, respectively. The use of an ethynyl spacer resulted in a somehow slower CS rate, compared to carboxylate derivative, but the CR was found to be about three times faster ($\tau = 80$ ps). An explanation of this is the higher conformational flexibility provided by the ester and ether linkage compared to ethynyl, allowing larger changes in the relative orientations of the Fc and SubPc following forward charge transfer. The directly linked Fc – SubPc, as expected, showed an order of magnitude faster CS and a shorter lifetime of 41 ps.

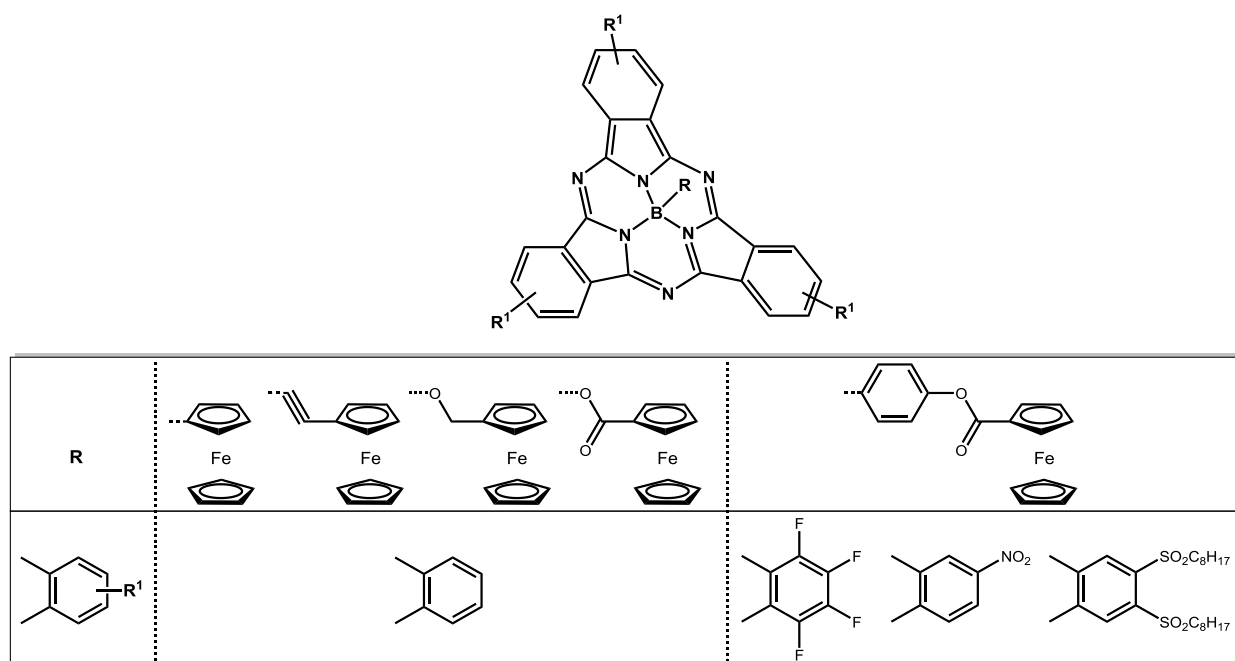


Fig. 1.19. Examples of ferrocene - boron subphthalocyanine design.

Introducing the Fc into SubPcs (Figure 1.19) with phenolate elongated spacer resulted in longer fluorescence lifetime of about 100 ps and two orders of magnitude reduction of emission intensity, suggesting a slower CS process compared to Fc-carboxylate decorated SubPc [86]. The transient absorption studies indicated remarkably long CS state lifetimes of 43 - 231 μ s in PhCN, increasing with changing electron withdrawing SubPc substituents in the order 5F, NO₂, SO₂C₈H₁₇, making these dyads attractive for artificial photosynthesis systems. The observed stabilization of ionic pair was suggested to be partially a result of specific axial polar B–X bond,

whose length and ionic character increases when SubPc is reduced resulting in poor overlap of SubPc⁻ LUMO and Fc⁺ HOMO. The same group reported later a fullerene modified Fc-SubPc triad and its photophysical properties [87]. A Fc⁺-SubPc-C₆₀⁻ CS state with a 94 μs lifetime was found to be generated as result of electron transfer from SubPc excited state to C₆₀ and subsequent hole shift to Fc⁺, as concluded from UV-Vis transient absorption spectra. It was shown that the degree of electronic coupling between SubPc and fullerene strongly affects the excited state behaviour. Hence, the introduction of an additional oxygen atom in the spacer resulted in generation of Fc⁺-SubPc⁻ species, which was not followed by charge shift to generate long lived state but a SubPc triplet excited state pattern was found in transient spectroscopy on the nanosecond time scale. Structurally related boron-dipyrromethene BODIPY molecules linked with Fc and C₆₀ were employed in design of dyads and triads [88]. These systems were used for light induced CS state generation, though relatively short subnanosecond lifetimes were noticed. Osuka group [89] found a quite strong Fc-subporphyrin electron interaction in *meso*-tris(4-ferrocenyl)subporphyrin in both ground and excited states as it can be seen from electrochemical data, red-shift in absorption spectra and very strong luminescence quenching. The ground state interaction is less pronounced in *meso*-tris(4-ferrocenylphenyl)subporphyrin, still the fluorescence is fully quenched as well, indicating an efficient intramolecular electron transfer into the excited state of subporphyrins.

1.6. Light induced processes in other ferrocene containing systems

Many other Fc containing systems were constructed and studied for CS state generation. Ferrocene / fullerene based dyads and triads are the most widely used for this purpose. Intermolecular charge transfer was shown to occur in 1,2,5-triphenylpyrrolidinofullerene cluster aggregates with several donor molecules, inclusive ferrocene, but the use of this cluster assembly as thin films on an OTE / SnO₂ electrode showed limited performance with IPCE of up to 0.2 % [90]. Araki et al. showed [91] that the intermolecular quenching of the ³C₆₀ excited state by Fc occurs via two mechanisms Fc-to-³C₆₀^{*} electron transfer ($\Phi_{ET} = 0.1$ in PhCN) and ³C₆₀^{*}-to-Fc energy transfer. As result of electron donating substituents, decamethylferrocene showed more pronounced charge transfer component ($\Phi_{et} = 0.46$ in PhCN and 0.58 in PhCN:DMF 1:2) as energy levels were tuned to give more driving force for CS and probably less driving force for EN onto Fc triplet state.

Guldi et al. worked out the mechanisms governing the excited-state dynamics for Fc-fulleropyrrolidine dyads with various spacers (Figure 1.20) [92]. Though all compounds showed

fluorescence quenching, the use of rigid alkenic linker showed kinetics slowdown by nearly one order of magnitude per introduction of two σ -bonds into the hydrocarbon bridge. In contrast, the use of a flexible alkanic ester linker revealed only 4.6 and 8.8 fold acceleration of the quenching rate upon extending the spacer length from two σ -bonds to seven and ten σ -bonds, respectively.

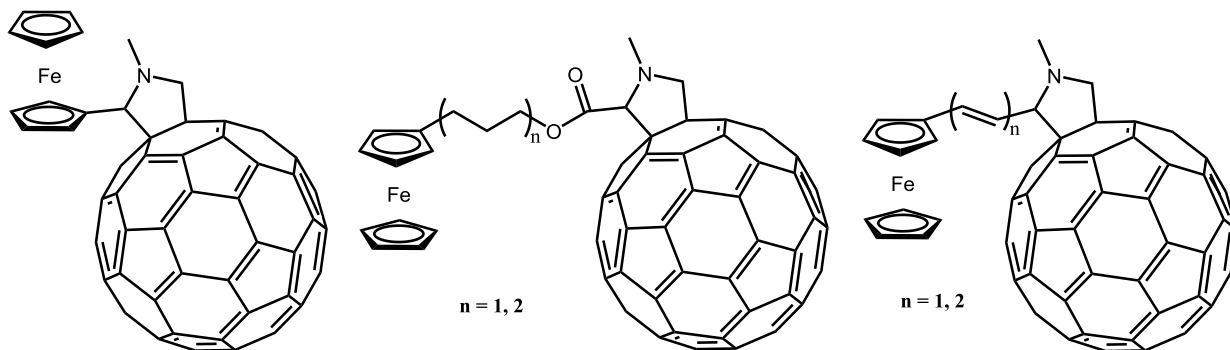


Fig. 1.20. Examples of ferrocene – C₆₀ design.

The transient absorption measurements showed formation of the $\text{Fc}^+ \text{-C}_{60}^-$ ion pair, as evidenced by fullerene anion absorption pattern resulted from electron transfer from Fc to the excited triplet state of the fullerene unit. The presence of a bent conformer was suggested for the flexible attached Fc, which permits intramolecular quenching mechanism with formation of long lived CS state ($\tau_{1/2}$ up to 2.5 μs in degassed benzonitrile). The alkene spacer showed fast quenching process after photoexcitation, but no transient intramolecular exciplex was observed, probably due to fast CR over the conjugated chain. The time-resolved EPR for a Fc-C₆₀ dyad based on 2,2,6,6-tetramethylpiperidine-1-oxyl radical labelled fulleropyrrolidines, showed the spacer dependence of the electron transfer so that a longer chain resulted in a faster process [93]. This is suggesting again the bending of molecule and "through space" CS mechanism. As expected, the direct link of Fc and azafullerene C₅₉N gave a very fast and almost quantitative quenching of the photoinduced excited state via charge-transfer pathway with 0.4 ns time constant for the recombination of the C₅₉N⁻-Fc⁺ ion pair [94]. The direct connection of ferrocene to pyrrolidine-fullerene showed fast kinetics of electron transfer, but the use of a more rigid connection via both cyclopentadienyl rings resulted in a longer lifetime of 23 ns [95]. It was proposed that contrary to the CS the CR in these systems occurs in the Marcus inverted region so that lowering the nuclear reorganization energy promotes rapid CS in the normal region, but leads to decreased rates for CR. Lower reorganization energy for another rigid bilinked ferrocene system was later proposed by other group as well [96]. Langa et al. showed [97] that for isoxazolo[60]fullerene-donor dyads, the Fc unit has much stronger quenching effect compared to various organic donors (e.g. PhNMe₂). Afterwards, they designed Fc-C₆₀-PhNMe₂ triad that

showed CS state with a lifetime of up to 50 ns [98]. It was not determined which donor is predominant in ET / CR processes, but the disappearance of CS pattern in transient spectra upon protonation of PhNMe₂ would indicate its importance in CS. Still the protonation of pyrazoline ring seems to occur as well so that other mechanisms could be employed. Later they showed [99] that compared to 4-phenyl dibuthylamino / dodecylether (PhNBu₂ and PhOC₁₂H₂₅), the Fc derivatives showed higher yields for light induced charge separation (up to 50 % increase) for (Donor)₂-C₆₀ systems. The comparison of isoxazoline and 4-nitrophenyl-pyrazoline rings as linkers to C₆₀ unit showed that the latter is a better choice in sense of somehow improved charge separation efficiency and a much slower charge recombination CR. The authors ascribed the stabilization of ion pair to the stronger electron-donation of the nitrogen atom of the pyrazoline ring compared with the oxygen atom of the isoxazoline ring. For isoxazoline derivative the PhNBu₂ substituent showed longest CS lifetime (25 ns compared to less than 2 ns for others in PhCN), while opposite results were obtained for 4-nitrophenyl-pyrazoline analogue where Fc units showed best results (110 ns for Fc, 90 ns - PhNBu₂, <7 ns - PhOC₁₂H₂₅ in PhCN). The lifetime was further increased to 160 ns by using toluene as solvent. The same group showed afterwards [100] that by using C₇₀ fullerene instead of C₆₀ a comparable CS rate and yield is obtained, but a prolonged lifetime of ion pair was found. Fc and PhNMe₂ linked to pyrazolino-C₇₀ form the Fc-C₇₀-PhNMe₂ triad and transient absorption experiments showed C₇₀⁻ pattern that decays with 38-100 ns time constant, with a tendency to increase with decreasing solvent polarity. Fc was ascribed by the authors to be predominantly responsible for CS and a triplet spin character of the radical ion pair was suggested as the decay rates of CS state and ³C₇₀^{*} were found to be almost equal. By varying the Fc / C₆₀ ratio several molecular systems Fc_n-Ph₃N-(C₆₀)_m (n, m = 1, 2) consisting of central triphenylamine (Ph₃N) and peripheral Fc, C₆₀ were obtained [101]. Faster CS was observed with increasing Fc / C₆₀ ratio, but at the same time the longest lifetime of 48 ns in toluene was obtained for Fc_n⁺-Ph₃N-(C₆₀)_m⁻ ion pair when n = 1 and m = 2. CR in non-polar solvents was suggested to take place via ³C₆₀ excited state as concluded from transient absorption spectroscopy in o-dichlorobenzene, while in polar solvents the CR process could take place via lower lying ³Fc^{*}. Another example of Fc-(C₆₀)₂ system connected by amide linkages was later published [102] showing fullerene fluorescence quenching, probably by Fc based EN or ET mechanism, but further studies are required to clarify this.

Two different donor substituents were connected to C₆₀ unit, by the Nazario group, in order to monitor competitive ET excited state quenching [103]. Tetrathiafulvalene (TTF) and quinonoid π -extended-TTF proved to transfer electron more efficiently onto the C₆₀ excited state and no subsequent charge shift was noticed. The anthraquinone and

tetracyanoanthraquinodimethane substituents did not induce any major changes in the C_{60} excited state quenching compared to Fc-only dyad. The insertion of various nitrophenylic acceptor units to 2-(ferrocenyl)fulleropyrrolidine showed to faster both charge separation and recombination processes, more pronounced for stronger acceptors [104]. The latter could suggest spatial back electron transfer from the nitrobenzene unit to the Fc^+ and ab initio-calculated distribution of LUMO orbital coefficients supports this, but no direct evidences for nitrobenzene based charge shift were found. Oligophenylenevinylene unit was studied as bridge for Fc- C_{60} dyad, but no evidences were found for ET after photoexcitation of fullerene [105]. The fulleropyrrolidine triplet state lifetime reduced from 15.7 μs (for reference non-Fc molecule) to 0.23 - 0.62 μs , depending on the bridge length. No CS species pattern was found using transient absorption spectroscopy, an explanation of this being a competing $^3C_{60}$ quenching via EN to Fc.

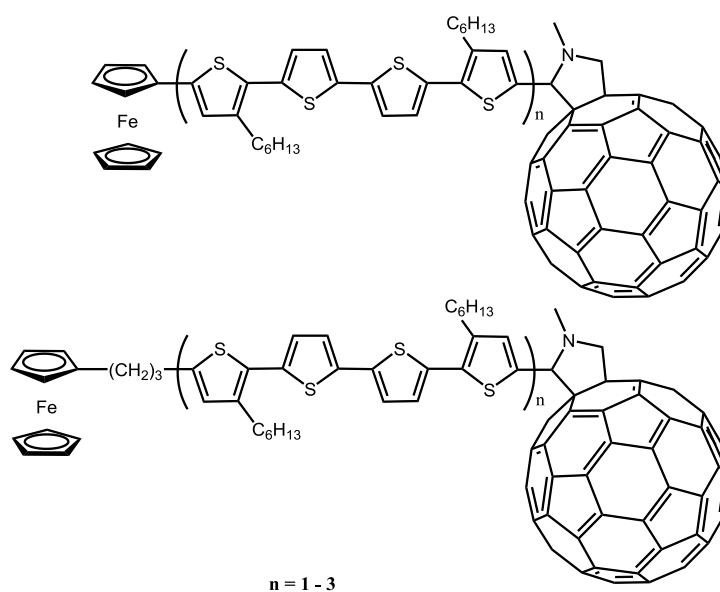


Fig. 1.21. Examples of ferrocene – C_{60} design.

The use of oligothiophene (nT) spacer in Fc-nT- C_{60} triads (Figure 1.21) results in competition of ET and EN, as concluded from steady-state fluorescence [106]. When Fc is directly linked to nT ET governs the excited state dynamics, while linking through $(CH_2)_3$ spacer results in loss of conjugation and EN becomes predominant. The transient absorption [107] showed that in fully conjugated Fc-nT- C_{60} in polar solvents the excitation of nT or C_{60} generates $(Fc-nT)^+-C_{60}^-$ CS state in which the positive charge is delocalized on both Fc and nT. It decays back with 0.1-50 ns time constant depending on the nT length (from 4 to 12 thiophene rings). In contrast, the Fc- $(CH_2)_3$ -nT- C_{60} triad excitation in polar solvents generates $Fc-(CH_2)_3-nT^+-C_{60}^-$ which by positive charge shift to Fc transforms into final $Fc^+-(CH_2)_3-nT-C_{60}^-$ CS state. The

obtained lifetimes are longer as result of conjugation break and by increasing the thiophene chain length values of 22-330 ns were obtained. In nonpolar solvents only EN processes were detected.

The use of perylenetetracarboxylic diimide chromophore (PBI) as bridge between the two units in Fc-PBI-C₆₀ triad (Figure 1.22), gave another type of ET cascade [108]. If in previous example the initially formed CS state suffers further positive charge shift (p-type cascade ET), in this case the excitation of PBI results in formation of Fc⁺-PBI-C₆₀ ion pair ($\tau_{CR} = 67$ ps) followed by negative charge shift (n-type) to form Fc⁺-PBI-C₆₀⁻ CS state ($\tau_{CR} = 1.18$ ns), still with a somehow low quantum efficiency of 0.24. The much longer lifetime of the latter is indicative of a good architecture for light harvesting. Later, naphthalenediimide chromophore based analogue showed alike results with 10 ps decay rate of initial Fc⁺-NDI-C₆₀ CS state and 0.94 ns for the final Fc⁺-NDI-C₆₀⁻ state [109].

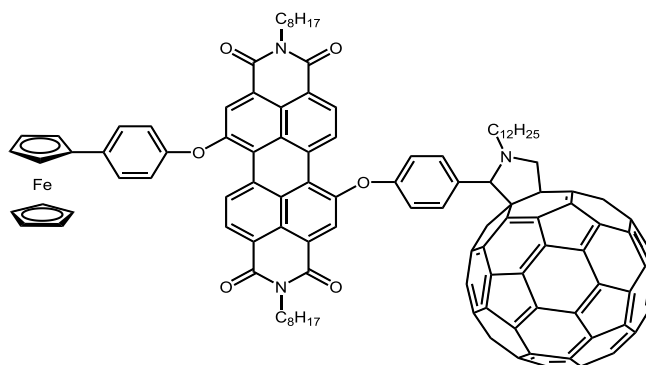


Fig. 1.22. Example of ferrocene – C₆₀ design.

A liquid-crystalline C₆₀-Fc was synthesized and its photophysical properties were studied by Campidelli et al [110]. It showed a quite stable CS state with a lifetime of 560, 490 ns in THF and PhCN respectively. The nonamethyl-Fc analogue showed faster excited state quenching [111], probably probably due to a higher driving force resulting from electron donating substituents, but the eventual C₆₀⁻-(CH₃)₉Fc⁺ lifetime was unfortunately not reported. The self-assembled Fc-crown and fulleropyrrolidine alkyl ammonium ions proved to be a good alternative for generation of dyads [112]. The transient absorption studies showed formation of C₆₀⁻-Fc⁺ ion pair with a lifetime of up to 243 ns, depending on the alkyl chain length. Rotaxane Fc / C₆₀ structures were reported as well [113], their photophysics being described in previous section compared to porphyrin containing analogues. Fc-C₆₀ excited state interaction was proved to be possible through hydrogen bonding as well [114]. In 2-Ureido-4(1H)-Pyrimidinone (UP) bridged quadruply hydrogen-bonded assembly Fc-UP...UP-C₆₀ quenching of ³C₆₀^{*} by EN to ³Fc^{*} ($\Phi = 0.73$) was found in DCM.

1.7. Photodriven H₂ evolution using ferrocene containing systems

It is clear that the energy accumulated by the long lived CS state can be potentially applied for performing useful redox reactions using either the electron (e.g. H₂ production, CO₂ reduction) or hole (e.g. O₂ production) from radical ion pair, and sacrificial reagent on the opposite side, or ideally using both negative and positive charges for useful reactions. It was shown before that combining a catalyst for proton reduction, photosensitizer (PS) and an electron donor, effective hydrogen generation systems can be obtained as result of photoinduced intermolecular electron transfer from PS to catalytic centre [115]. Another approach consists of linking all parts in triad molecules so that intramolecular charge and energy transfer would generate the CS state long enough to be employed in hydrogen generating reaction. For this purpose, ferrocene – zinc porphyrin – diiron hydrogenase model triads Fc-ZnTPP-[NMI-Fe^I-Fe^I-S₂(CO)₆] and Fc-Ph-ZnTPP-[NMI-Fe^I-Fe^I-S₂(CO)₆] (NMI - naphthalene monoimide) were designed (Figure 1.23) and fully studied by Wasielewski et al [116].

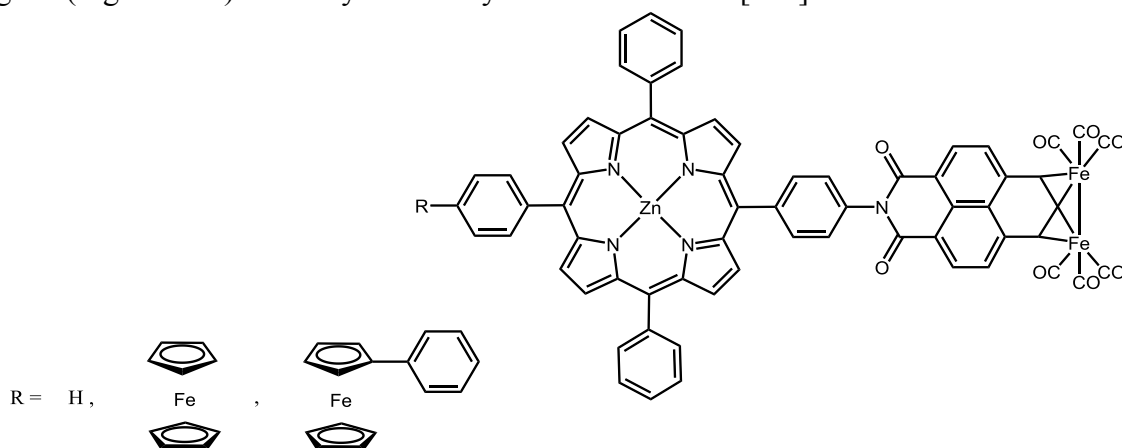


Fig. 1.23. Examples of ferrocene - porphyrin - naphthalene monoimide diiron hydrogenase design for photodriven H₂ evolution.

It was found that the simple introduction of the second phenyl spacer between porphyrin and ferrocene makes the diiron hydrogenase electron transfer more kinetically competitive compared to ferrocene mediated deactivation of porphyrin excited state, and the lifetime of Fc⁺-PS-[NMI-Fe⁰-Fe^I-S₂(CO)₆] CS state is extended from 9 ns to 67 ns. These values are well correlated with photoinduced hydrogen generation results. The irradiation of triads in 2 mmol solution of trifluoroacetic acid in DCM resulted in H₂ evolution only for Fc-Ph-ZnTPP-[NMI-Fe^I-Fe^I-S₂(CO)₆] triad with a 0.56 TON (without any sacrificial donor in the presence of TFA as acid source) showing that CS state lifetime is crucial for photodriven H₂ generation. The reference “ferrocene-free” dyad ZnTPP-[NMI-Fe^I-Fe^I-S₂(CO)₆] showed no hydrogen evolution

under the same conditions and the lifetime of the reduced diironhydrogenase model is shorter by more than 450 times.

Wu et al. constructed hydrogenase models linked with Re chromophores (Figure 1.24) [117]. While the bimolecular Fc-Re^{I} and $[\text{Fe}^{\text{I}}\text{Fe}^{\text{I}}]\text{-H}_2\text{ase}$ system showed very low photocatalytic activity, the triad $\text{Fc-Re}^{\text{I}}\text{-}[\text{Fe}^{\text{I}}\text{Fe}^{\text{I}}]\text{-H}_2\text{ase}$ showed almost ten-fold increase of TON. It clearly shows the advantage of intramolecular CS compared with intermolecular processes. It is worth mentioning that the lifetime reported for $[\text{Fe}^{\text{I}}\text{Fe}^{\text{0}}]\text{-H}_2\text{ase}$ in triad is extremely long (>2 ms at room temperature, compared to $708\ \mu\text{s}$ for bimolecular system) proving the efficiency of such a design. Later the same group showed the importance of the ferrocene unit by replacing it with a redox inactive *p*-toluene moiety [118]. It resulted in decrease of TON from 47 to 34 in the presence of Hantzsch 1,4-dihydropyridine both as sacrificial electron donor and proton source.

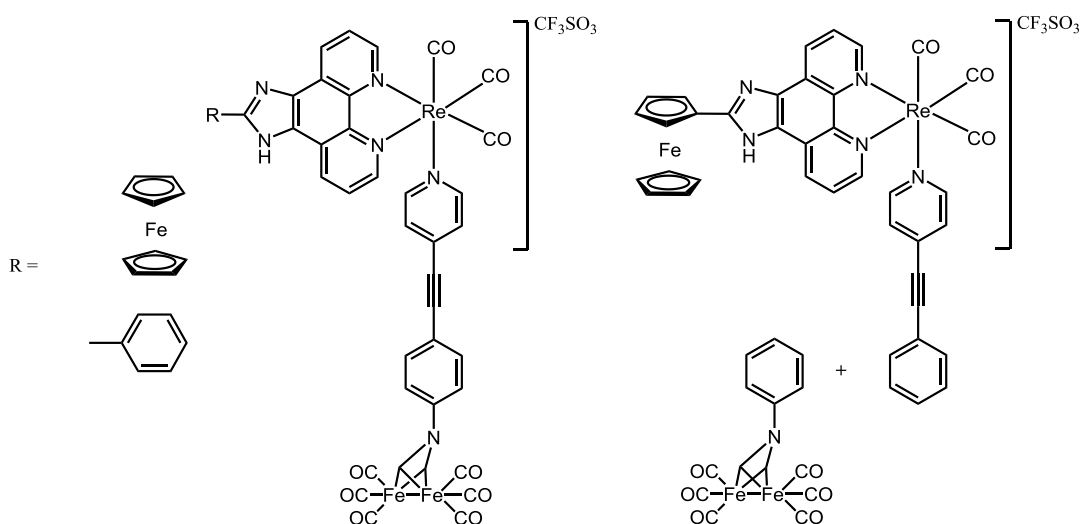


Fig. 1.24. Examples of ferrocene – Re^{I} polypyridyl - $[\text{Fe}^{\text{I}}\text{Fe}^{\text{I}}]\text{-H}_2\text{ase}$ design for photodriven H_2 evolution.

1.8. Ferrocene in Dye Sensitised Solar Cells

Very simple Fc derivatives bearing formyl, carboxylic acid and hydroxy anchoring groups were used as sensitizers for the TiO_2 surface [119]. By using propylene-carbonate-based electrolyte and I^-/I_3^- couple, efficiency of about half of the ruthenium dye N719 were obtained under the same conditions, but the low cost of Fc makes this research still a promising area. Ni, Cu, Cd, Hg, Pd, Pt, Pb, Co and UO_2 complexes of a dithiocarbamate derivative of Fc were obtained and tested as TiO_2 sensitizers by the same group [120]. The Ni, Co and Pd complexes showed the highest efficiencies of more than half (0.63 for $[\text{Ni}(\text{FcCH}_2\text{Bzdtc})_2]$) of the N719 dye, suggesting the square-planar geometry to be more efficient for this class of compounds. Later

they have reported the use in TiO₂ based DSSC of Ni, Pd and Pt heteroleptic complexes with 1,1'-bis(diphenylphosphino)ferrocene and *p*-substituted sulfonyl dithiocarbamate or 1-ethoxycarbonyl-1-cyanoethylene-2,2-dithiolate [121]. Once again nickel complexes showed best efficiencies of 3.48 %, compared to 5.58 % for N719 under identical conditions.

The zinc(II) porphyrin derivative containing three Fc groups appended at the meso positions and a benzoic acid anchoring moiety at the final *meso* site (ZnFcP1 from Figure 1.25) was obtained in our group [122]. The ultrafast UV-Vis transient absorption in THF showed efficient formation of Fc⁺-Porphyrin⁻ CS state with a lifetime of 24 ps. Adsorption on TiO₂ didn't afford any major difference and only a minor long lived component was noticed. These results suggest that only porphyrin excited state is employed in electron injection, while the porphyrin anion is not able to transfer electron into the conduction band of the TiO₂. One explanation for this is the very strong coupling between electron and hole as result of the short distance, so that the electron density redistribution is more feasible rather than a “real” radical ion pair. This is likely to be the main reason of its limited performance in DSSC (FF = 0.42, η = 0.0081%).

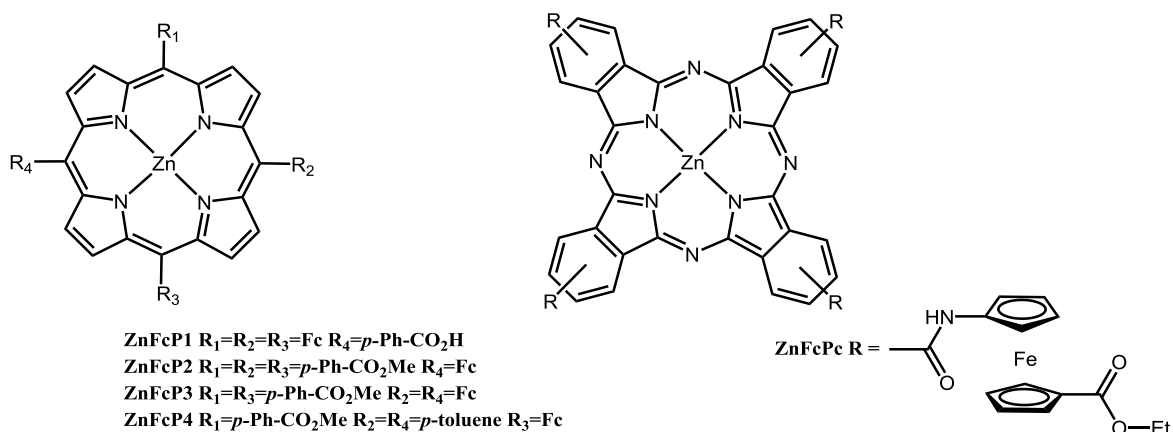


Fig. 1.25. Examples of ferrocene - porphyrin / phthalocyanine design for DSSC.

Analogous meso-ferrocenyl porphyrins were prepared by Rochford et al., namely Zn(II)-5-ferrocenyl-10,20-bistolyl-15-(4-methylbenzoate)porphyrin, Zn(II)-5-ferrocenyl-10,15,20-tris(4-methylbenzoate) porphyrin, Zn(II)-5,15-bisferrocenyl-10,20-bis(4-benzoate) porphyrin (ZnFcP2-4 from Figure 1.25) [123]. Although no solar cell measurements were done, our studies suggest that their performance would be poor. Very similar results were obtained for tetraferrocene Zn phthalocyanine (Figure 1.25) [124]. Though the Fc is connected through a peptide link to phthalocyanine ring the lifetime of CS state is still short (170 ps) and a poor efficiency was obtained in a TiO₂ DSSC. The use of an anchoring group which is separated from

the donor moiety and removing the ferrocene from the titania surface could improve the photocurrent response.

1.9. Ferrocene in other solar cell technologies

Gold electrodes modified with self-assembled monolayers (SAMs) of light harvesting molecules were reported as potential systems for artificial photosynthesis mimics. The Uosaki group [125] synthesized a porphyrin PS connected to Fc and an anchoring thiolic group, where all units are separated by alkane chains (left picture of Figure 1.26). Its attachment on the gold surface formed a well packed layer which upon irradiation injected a hole onto the gold after ferrocene-to-porphyrin electron transfer. The use of methyl-viologen dication MV^{2+} as electron acceptor resulted in an uphill transport of electrons of more than 1.2 eV. Applying an -0.2 V potential to the electrode and illumination at 430 nm showed quantum efficiency of 11 % and photoenergy conversion efficiency 1.8 %. These values were slightly improved by varying the alkyl chain length and surface roughness [126].

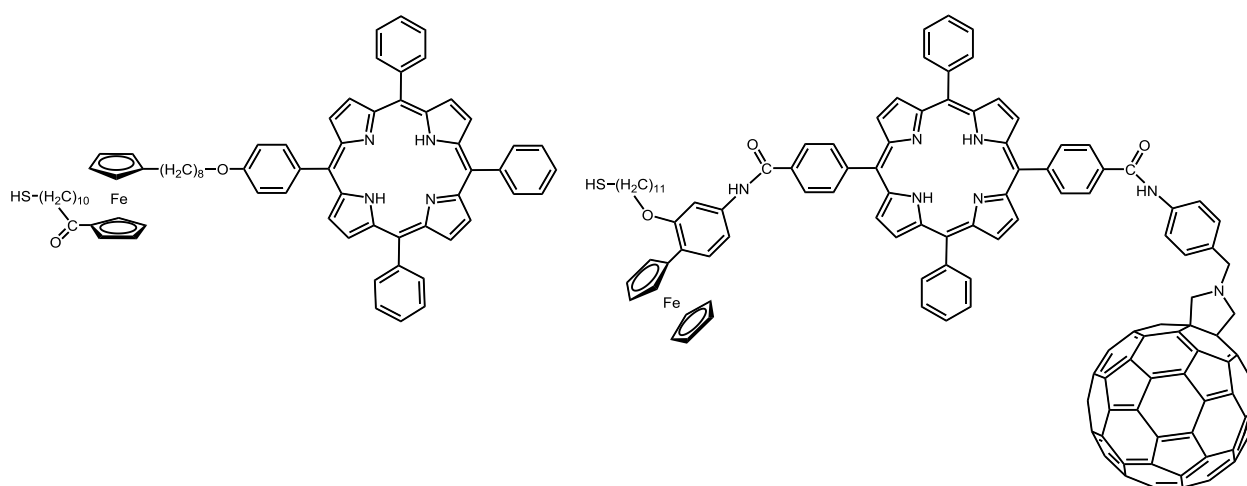


Fig. 1.26. Examples of ferrocene - porphyrin / phthalocyanine design for DSSC.

Imahori et al. reported [127] a substantial improvement of quantum yield by introducing the fullerene unit into ferrocene-porphyrin dyad (right picture of Figure 1.26). Vectorial porphyrin-to-fullerene electron or partial charge transfer is more probable rather than ferrocene mediated pathway. A subsequent porphyrin to ferrocene, and then to gold electrode charge shift occurs via alkanethiol linker, while the fullerene anion C_{60}^- transfer an electron to the counter electrode *via* methyl viologen based electrolyte. A very long lifetime of up to 15.6 μs was obtained for the reference triad $Fc^+-P-C_{60}^-$ CS state, without alkanethiol unit [128]. Interestingly, cosensitization with a boron-dipyrrin based dye showed not only charge transfer to gold surface,

but also energy transfer from BODIPY to porphyrin based dye too [129]. It resulted in quantum yields of up to 50 %, but the conversion efficiency is still lower than 2 %. Poorer results were obtained when using indium tin oxide (ITO) based systems. Once again the ferrocene containing triad showed better results compared to porphyrin-fullerene dyad [130] or slipped-cofacial porphyrin dimer [131]. The use of triosmium cluster to connect fullerene with porphyrin and ITO anchoring linker did not improve the quantum yield, still showing good electrochemistry and stability as result of robust C_{60} -Os₃ bonding [132]. The introduction of ferrocene was reported to increase the lifetime of photoinduced long lived CS species up to μ s order in ferrocene-porphyrin-fullerene photosynthetic models [133]. Though high efficiency of energy conversion was theoretically predicted for ferrocene-porphyrin-fullerene SAMs on conducting leads (IPCEs higher than 40%) [134], however the efficiencies of constructed devices are still low both for gold and ITO electrodes systems.

However, the introduction of Fc donor for charge separation is not always beneficial as it was shown for Al^{III}P based systems [135]. Thus the Fc-Al^{III}P-C₆₀ triad showed shorter CS lifetimes compared to Al^{III}P-C₆₀ dyad (17 and 38 ns respectively) resulting in a lower photovoltaic performance on the SnO₂ electrode (IPCE up to 24 % for Al^{III}P-C₆₀ dyad). A faster recombination pathway is suggested for Fc triad, showing that a fine tuning of both donor and acceptor is crucial for generation of long lived light induced species.

The “porphyrin-free” system comprising a deca(organo)fullerene, bearing five ferrocenyl groups proved to be able of generating photocurrent after deposition on ITO electrode. It showed an improved performance (quantum yield of 12%) compared with “ferrocene-free” analogue, which was ascribed to a longer-lived CS state. The one-electron Fc / Fc⁺ couple showed good performance when used as an alternative redox mediator instead of classical two-electron I^- / I_3^- in TiO₂ DSSC [136]. Using an organic dye Carbz-PAHTDIT, an increase of about 100 mV for the V_{OC} when using Fc based electrolyte was noticed. This is a result of a better redox potential match. The easiness of redox tuning by introducing substituents on the two Cp rings makes the Fc even more attractive, as it offers the possibility to optimize the dye reduction driving force and potentially give more V_{OC} profit. The use of a series of alkylated and halogenated Fcs with redox potential range of 0.09 to 0.94 V vs. NHE gave possibility to select the redox shuttle with a driving force “just enough” to regenerate the dye, which gave an increase of open circuit potential [137]. However this system showed some instability in the presence of O₂, probably as result of oxidation processes. Another potential application of Fc consists of replacement of Pt-based counter electrodes in TiO₂ DSSC. Ferrocene-derivatized large pore sized mesocellular carbon foam showed an improved performance (12 % enhanced η) compared to Fc free analogue [138].

1.10. Conclusions to Chapter 1

Porphyrins and comparable derivatives are ubiquitous in nature and constitute the molecular cornerstone of several light-driven processes which help maintain life on Earth. The good cross-section capture of visible photons for the chromophores, coupled to their excellent redox excited-state behaviour are but two reasons for the continued interest in porphyrin derivatives. Mimicry systems for artificial photosynthesis applications is certainly one major research area in which porphyrin derivatives have a special place. The manufacture of molecular dyads, triads and tetrads for propagating efficient, directional and long-lived charge separation continues to be of intense interest. Coupled to such fundamental studies is the application of porphyrin derivatives in areas such as sensors, photodynamic therapy sensitisers and dye sensitised solar cells (DSSC). In regard to the latter case the direct conversion of sunlight to electricity is of major relevance because of its potential application to lowpower technologies and the large-scale manufacture of devices by simple wet chemistry processing.

Transition metal porphyrins are well known for their applications in electrocatalysis including many industrially imperative reactions [139]. Particular attention has been paid to electrocatalytic reduction of carbon dioxide by metal (e.g., Ag, Pd, Co, Fe) porphyrin derivatives [140]. Examples of electrochemical proton reduction catalyzed by metal (e.g., Co, Fe) porphyrin derivatives are also well known [141], however no such examples for palladium(II) and copper(II) porphyrin complexes were found using available search engines (SciFinder, Reaxys, Web of Science). In fact, to the best of our knowledge the only, and very recently reported, use of Pd complex catalysed hydrogen evolution was based mostly on cyclic voltammetry experiments and no detection of the electrolysis products was performed [142].

As we have shown in this chapter, various light harvesting systems were constructed and studied in the past decades, including porphyrin and ferrocene containing architectures. Still, many challenges have to be faced in order to reach Nature photosynthetic machinery efficiency and construct economically sustainable artificial analogues. The highlight of the structure-property relationships, governing the photophysical and electrochemical properties of the constructed systems, is primordial in terms of application performance optimisation.

Keeping this in mind we followed the goal to design and study some ferrocene and porphyrin based molecules, described in the following chapters, in order to enrich the knowledge on the main topics addressed within this doctoral thesis.

2. DERIVATIVES OF 1,1'-DISUBSTITUTED FERROCENE

2.1. New pathway to asymmetrical ferrocenes via oxidation of 1,1'-ferrocene dicarboxaldehyde [143, 144]

The Cp rings of ferrocene are aromatic and hence it is possible to perform typical electrophilic substitution reactions on one or both of the rings. 1,1'- and 1,2-unsymmetrical ferrocene ligands are widely studied as catalysts for organometallic cross-coupling, hydrogenation, allylic substitution, hydroformylation, Au-, Ag-catalysed aldol reaction etc [145]. Selective reactions on a single Cp ring to introduce two disparate functional groups (e.g., PPh₂, dihydrooxazole) are also possible [146]. For this latter case the ferrocene subunit is used as a planar chiral ligand for asymmetric catalysis applications [147]. For each ring to incorporate a different functional group can be more difficult, often requiring selective BuLi reactions at low temperatures [148]. A long reaction time and a convoluted purification method is required starting from 1,1'-ferrocenedicarboxaldehyde **II.1** [149]. In the preparation of neutral receptor systems based on ferrocene, the selective hydrolysis of dimethyl 1,1'-ferrocenedicarboxylate was shown to produce the monoester [150].

A very mild and fast method to achieve a similar outcome would appear to be appealing, provided the two functional groups are useful for further reactions. It turned out that, as part of our research effort into producing ferrocene-based porphyrin and BODIPY compounds, we discovered such a simple procedure. A simple chromatography-free method for desymmetrizing ferrocene is described in this chapter starting from the readily available dialdehyde.

2.1.1. Oxidation of 1,1'-ferrocenedicarboxaldehyde

The oxidation of ferrocenecarboxaldehyde using aqueous KMnO₄ in acetone is well documented to produce the corresponding carboxylic acid [151]. By following the literature protocol ferrocenecarboxylic acid was obtained in reasonable yield. However, we found that the same procedure applied to **II.1** in acetone or acetonitrile did not produce the corresponding dicarboxylic acid (Figure 2.1). The ¹H NMR spectrum (left top picture of Figure 2.2) for the major product isolated from the acetonitrile reaction showed different resonances for the two Cp rings, confirming the product to be unsymmetrical. Furthermore, two downfield resonances at δ 193.21 and 170.77 ppm for the ¹³C{¹H} NMR spectrum (right top picture of Figure 2.2) were consistent with the presence of aldehyde and carboxylic acid groups. The mass spectrum showed a peak at m/z 259, while the strong stretches at 1717 cm⁻¹ (C=O), 1262 cm⁻¹ (C-O), and the

broad peak at ca. 2939 cm^{-1} (O–H) in the FT-IR spectrum confirmed production of a carboxylic acid group. The combined evidence verified the product to be 1'-formyl-ferrocenecarboxylic acid **II.2**, in which one aldehyde was oxidized but the other remained intact. Hence, under these conditions the ferrocene is desymmetrized since it contains two different functional groups. The overall yield for **II.2** is 49% after a fast and chromatography-free work up, providing material pure enough for further chemical transformations.

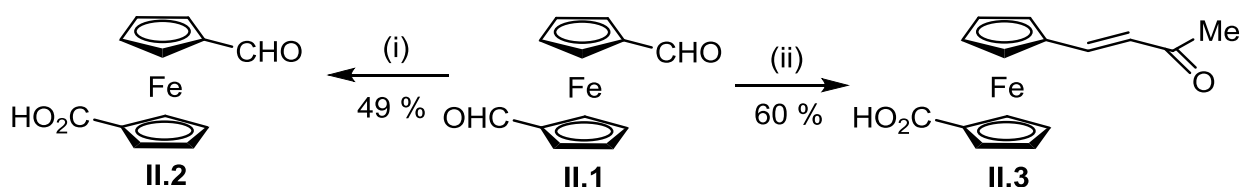


Fig. 2.1. Reagents and conditions: (i) KMnO_4 , $\text{CH}_3\text{CN} / \text{H}_2\text{O}$, $0\text{ }^\circ\text{C}$;
(ii) KMnO_4 , acetone / H_2O , $0\text{ }^\circ\text{C}$.

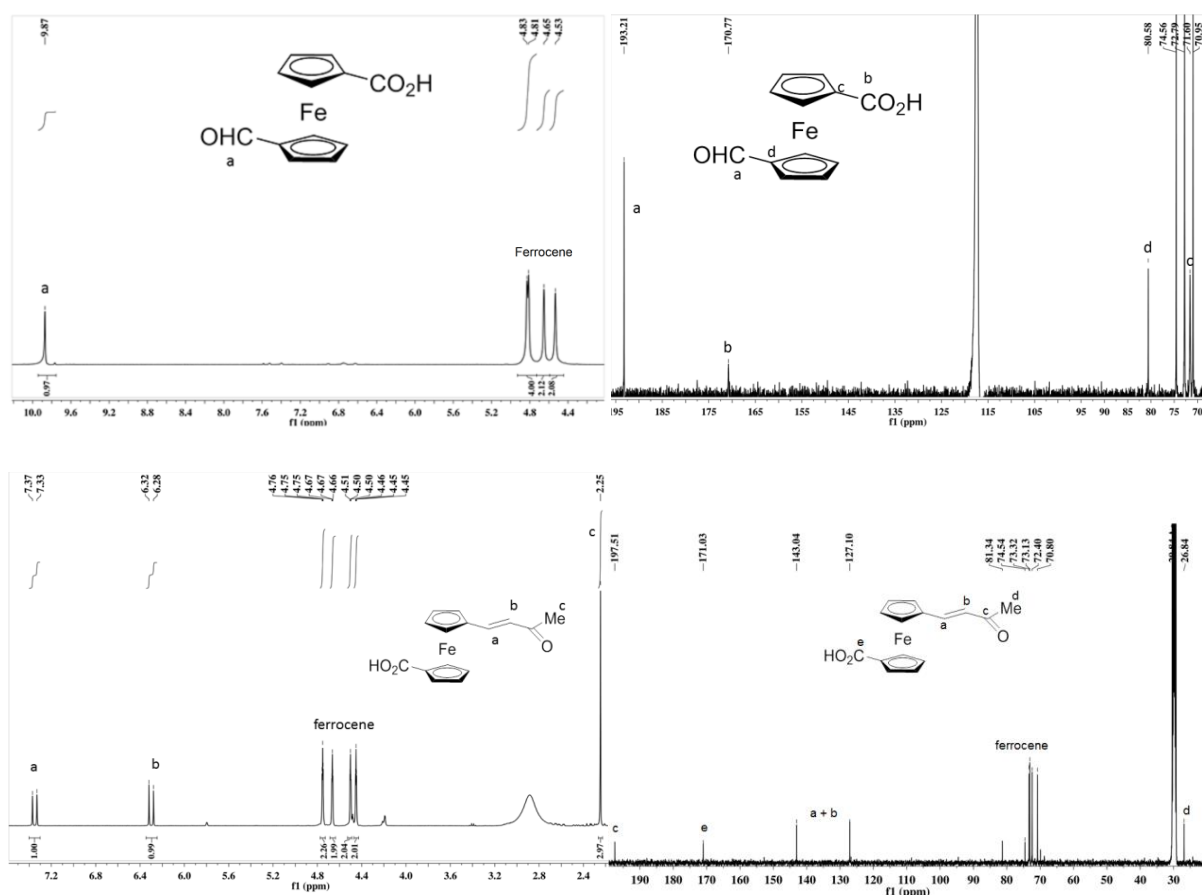


Fig. 2.2. ^1H & $^{13}\text{C}\{^1\text{H}\}$ spectra and assignment for **II.2** (top) and **II.3** (bottom).

A similar reaction performed in acetone / H₂O mixture (ca. 1:1) did not afford a product with a ¹H NMR spectrum (left bottom picture of Figure 2.2) consistent with compound **II.2**. Instead, additional resonances were observed in the olefinic region ($\delta = 7.35$ and 6.30 , $J = 16.2$ Hz) consistent with a *trans* double bond, together with a methyl resonance ($\delta = 2.25$ ppm) and a downfield resonance ($\delta = 197.51$ ppm) in the ¹³C{¹H} NMR spectrum (right bottom picture of Figure 2.2), which is consistent with the existence of a CH₃CO group [152]. The mass spectrum showed a peak at m/z 299, and once again the FT-IR spectrum corroborated the presence of a carboxylic acid (strong peaks at 1705 and 1264 cm⁻¹ for C=O and C–O stretching vibrations and the broad peak at 2934 cm⁻¹ for O–H stretching) [153]. The spectroscopic data are fully consistent with 1'-((E)-3-oxo-but-1-enyl)-ferrocenecarboxylic acid **II.3**.

We speculate that oxidation of one aldehyde to the carboxylic acid activates the other carbonyl in **II.2** to a condensation reaction with the acetone present in solution. Presumably for ferrocenecarboxaldehyde the reaction of the aldehyde with acetone is too slow to compete with oxidation. Rather surprisingly, compounds **II.2** and **II.3** could not be found in the literature using popular search tools (i.e., SciFinder, Reaxys). The closest analogue to **II.3** is the structural isomer (C₁₅H₁₄FeO₃) in which one ring has a formyl and the other (E)- β -(methoxycarbonyl)ethenyl subunit [149]. This material was produced by a controlled Wittig reaction with 1,1'-ferrocenedicarboxaldehyde, yielding a mixture of compounds which had to be separated by chromatography. Again for compound **II.2** the structural analogue (C₁₂H₁₀FeO₃) has both the formyl and carboxylic acid substituted on the same Cp ring [154].

2.1.2. Ferrocene – terpyridine complexes

Having established the simple procedure for desymmetrizing the ferrocene core, we were interested to see if useful chemical transformations could be carried out on compounds **II.2** and **II.3**. Noting that the carboxylic acid in **II.2** may act as an anchoring group to a semiconductor (e.g., TiO₂, NiO), the construction of a ligand from the aldehyde was attempted (Figure 2.3).

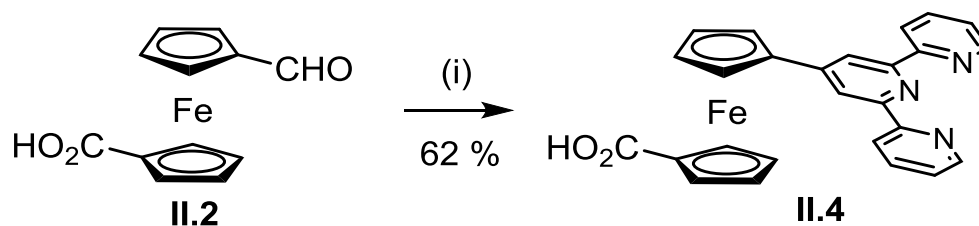


Fig. 2.3. Reagents and conditions: (i) 2-acetylpyridine, aq. NaOH / NH₄OH, dark.

In particular, the established Kröhnke method [155] for synthesizing 2,2':6',2''-terpyridine (terpy) attracted our attention. Reaction of **II.2** with 2-acetylpyridine in aqueous NaOH/NH₄OH, in a two-step one-pot reaction, gave after an easy column-free purification the terpy-type ligand **II.4** in 62 % yield. The material is stable in the solid state, but when in a solution of MeOH, DMSO or water, air-equilibrated or N₂-purged, the compound **II.4** is extremely light-sensitive. Exposure of solution to ambient light for several minutes produced a dark purple coloration. When kept in the dark no alteration in colour was observed. Interestingly, there is a report that the analogue of **II.4** without the carboxylic acid very slowly changes its colour under light illumination [156]. No further details were given, but it was assumed that oxidation of the ferrocenyl group gave the blue colour. Here we report a more thorough study into the instability of the Fc-tpy group in solution. ¹H NMR spectra for **II.4** as the light-driven reaction proceeded are shown in Figure 2.4. Resonances for the starting material decreased and new peaks appeared with a pattern very similar to authentic [Fe(Fc-tpy)₂]²⁺. The conversion yield, estimated from ferrocene integral values, is ca. 62%. The reaction could also be followed by UV–vis spectroscopy in MeOH, and as the reaction proceeded, a new band at λ_{max} = 580 nm appeared (right picture from Figure 2.5). The new absorption (left picture from Figure 2.5) is remarkably similar to the metal-to-ligand charge transfer band observed for [Fe(Fc-tpy)₂]²⁺ [157]. In addition, the mass spectrum of **II.4** in methanol exposed to the light showed peaks at m/z 977 and 489 that correspond to the ions [Fe(**II.4**)₂-H]⁺ and [Fe(**II.4**)₂]²⁺ = **FTF**²⁺.

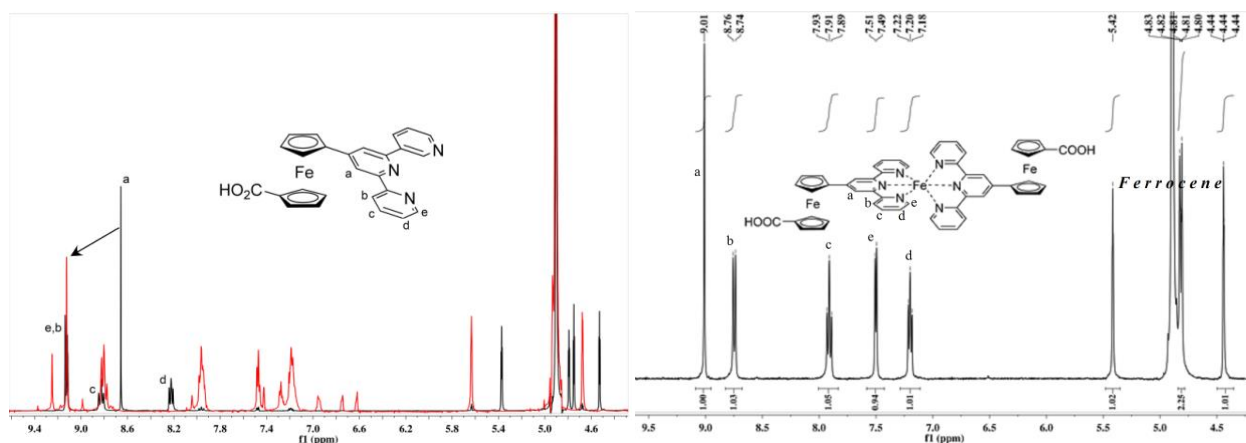


Fig. 2.4. Left: Selected partial 400 MHz ¹H NMR spectra for **II.4** (black) and light-driven degradation products (red). Assignments of proton resonances for the terpy ligand in **II.4** are shown. Right: Selected partial 400 MHz ¹H NMR spectra for **FTF**²⁺. Assignments of proton resonances for the terpy ligand in **FTF**²⁺ are shown.

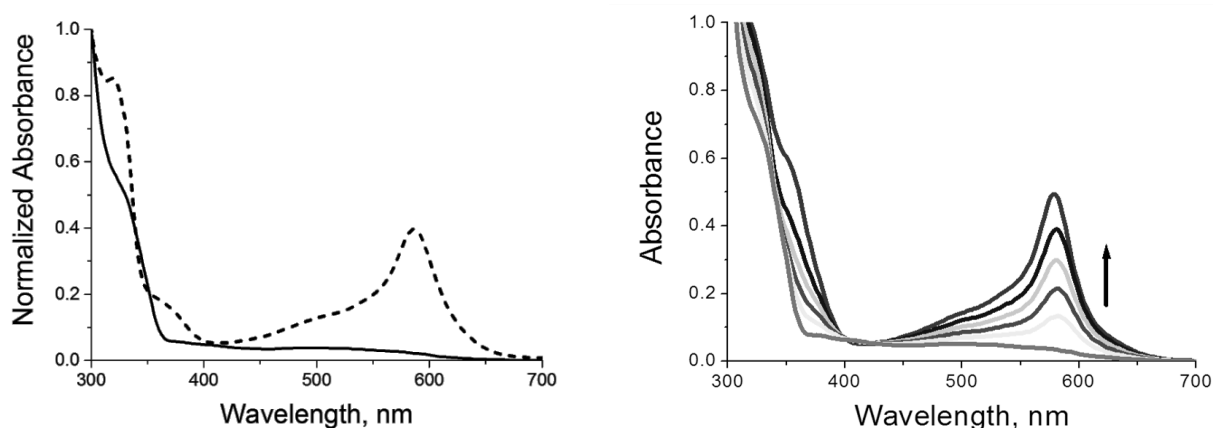


Fig. 2.5. Left: Normalized room temperature UV-Vis spectra for **II.4** (solid line) and **FTF**²⁺ (dashed line) in MeOH; Right: Room temperature UV-Vis spectra for **II.4** in MeOH as the light-driven reaction proceeds.

Hence, the source of the iron(II) must be ferrocene for the light-activated reaction to produce **FTF**²⁺. The reaction time is very dependent on the concentration of the starting material and is consistent with a bimolecular mechanism. It is speculated that a terpy ligand from one molecule of ground-state **II.4** bites onto the ferrocene iron(II) centre of another ‘activated’ molecule, leading to degradation of the compound. The identity of the activated ferrocene is not clear. However, the triplet quantum yield for ferrocene is very reasonable ($\Phi_T = 0.66$), although the lifetime (albeit in DMSO solution) is only 0.6 ns. The triplet energy is around 40 kcal mol⁻¹ (14,000 cm⁻¹) and the structure for the triplet state is known to be distorted [158]. The reaction must proceed via the triplet state and the presence of the carboxylic acid appears to promote compound degradation. This idea was tested by reacting under the same conditions a 1:1 mixture of 1,1'-ferrocenedicarboxylic acid and terpyridine in MeOH. When exposed to ambient light the solution became dark purple, with a very distinct absorption pattern suggesting a similar degradation of the ferrocene unit and formation of the [Fe(tpy)₂]²⁺ complex. Non-substituted ferrocene was indefinitely stable in methanol solution in the presence of terpyridine.

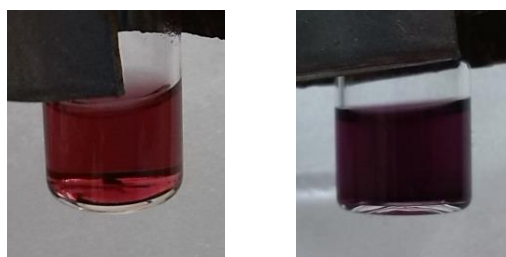


Fig. 2.6. The MeOH solution of **II.4**: initial color – left, after 5 min of illumination under laboratory room light - right.

Performing all steps, starting from 1,1'-ferrocenedicarboxaldehyde, under ambient light illumination gave after purification by column chromatography (silica gel, MeOH) a deep purple product in 11% yield. Suitable crystals for X-ray crystallographic analysis of the iron complex were obtained by slow diffusion precipitation with KPF₆, and the refined structure confirms its identity, although it is of relatively low precision, the marginal-quality crystals giving only weak diffraction. A reason for this are the solvent molecules included in the crystal network. The elemental analysis suggests half a water molecule and half a MeOH per one molecule of complex. The structure of the cation is illustrated in Figure 2.7, highlighting the six-coordinate iron(II) center and the two Fe-tpy ligands of compound **II.4**. The Fe1 – N1 (1.876 Å) and Fe1 – N4 (1.875 Å) bond lengths are typically shorter than the remaining Fe – N bond lengths (Fe1 – N2 1.974, Fe1 – N3 1.968, Fe1 – N5 1.972, Fe1 – N6 1.971 Å). As observed in previous [Fe(tpy)₂]²⁺ complexes [159] the bite angle of the ligand is not perfectly *trans*, as reflected in the N2 – Fe1 – N3 and N5 – Fe1 – N6 bond angles of 161.66° and 162.33°, respectively. A point to note is that each ferrocene group is in its carboxylic acid form and so hexafluorophosphates (not shown in Figure 2.7) are present as counter-ions. Additional crystallographic data for **FTF**(PF₆)₂ are given in Table 4.2.

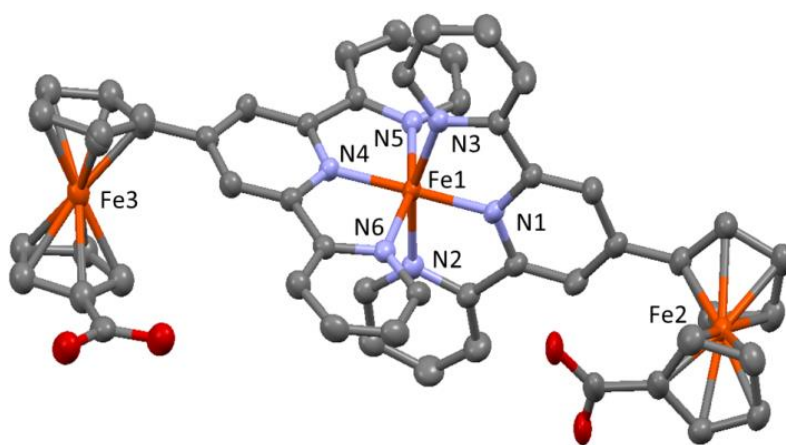


Fig. 2.7. X-ray determined structure of the dication **FTF**²⁺. Counter-ions, solvent molecules, and hydrogen atoms are omitted for clarity.

The tpy unit in **II.4** can be easily coordinated to metal ions in order to obtain new useful materials. Using Ru(tpy)Cl₃ as intermediate, the heteroleptic complex [(**II.4**)Ru(tpy)](PF₆)₂ = **RTF**(PF₆)₂ was easily obtained, as depicted in Figure 2.8. The ¹H and ¹³C{¹H} NMR spectra clearly showed that the two terpyridine ligands are different, and the asymmetrically substituted ferrocene was easily identified as well. The mass spectrum showed peaks at *m/z* 398,

795 and 941 corresponding to the ions \mathbf{RTF}^{2+} , $[\mathbf{RTF} - \text{H}]^+$ and $[\mathbf{RTF} + \text{PF}_6]^+$, while the IR spectrum corroborated the presence of carboxylic acid unit (peaks at 1612 and 1248 cm^{-1} for C=O and C–O stretching vibrations and the broad peak at 2924 cm^{-1} for O–H group stretching).

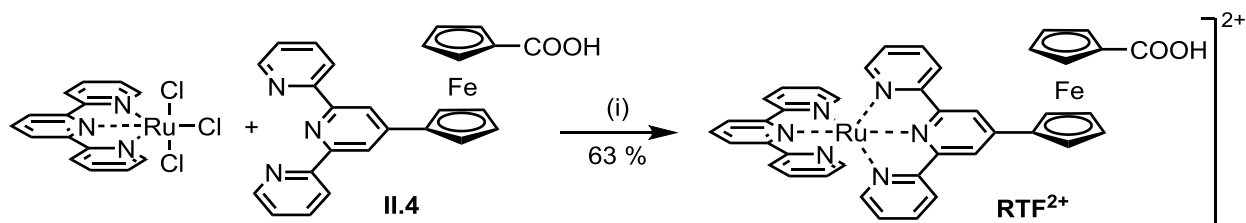


Fig. 2.8. Reagents and conditions: (i) N-ethylmorpholine, MeOH.

The compound described above can be outlined as Photosensitizer – Donor – Linker structure, suitable for photosensitization of p-type semiconductors. Hence, a NiO based DSSC was assembled having the semiconductor surface modified with the dye $\mathbf{RTF}(\text{PF}_6)_2$ and using solution of LiI (1.0 M) and I_2 (0.1 M) in acetonitrile as electrolyte, following a previously described methodology [160]. The plot of photocurrent density versus voltage (under standard AM 1.5 global sunlight at 1000 W m^{-2} and a temperature of 298 K) for $\mathbf{RTF}(\text{PF}_6)_2$ is shown in Figure 2.9. The experiment was repeated in darkness to prove the photovoltaic nature of the effect.

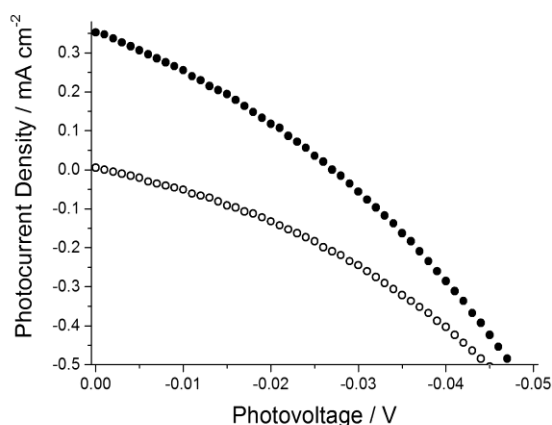


Fig. 2.9. Example of plot of photocurrent density versus voltage (\circ = dark, \bullet = light) for a $\mathbf{RTF}(\text{PF}_6)_2$ based NiO solar cell. $V_{\text{OC}} = -27 \text{ mV}$ and $J_{\text{SC}} = 0.352 \text{ mA cm}^{-2}$.

The short circuit current density was found to be $J_{\text{SC}} = 0.352 \text{ mA cm}^{-2}$, and the open circuit voltage $V_{\text{OC}} = -27 \text{ mV}$. While the current density is similar to a non-sensitized solar cell, showing the inactivity of the dye $\mathbf{RTF}(\text{PF}_6)_2$ in holes injection onto the semiconductor surface, the somehow improved open circuit voltage (-10.1 mV for a dye-free cell) could be explained as the semiconductor surface block. The limited sensitizing performance could be explained by

either low absorption coefficient of the $\text{Ru}(\text{tpy})_2$ derivative or poor adsorption on the NiO surface. Both these factors could be responsible for the weak absorption of $\text{RTF}(\text{PF}_6)_2$ modified NiO films (Figure 2.10) and no major change in the photocurrent action spectrum was found compared with dye free solar cell (Annexe 1).

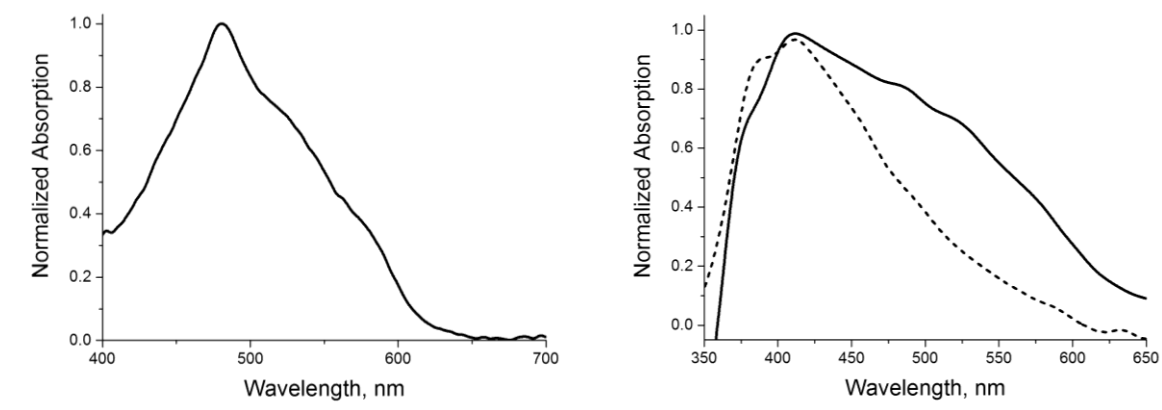


Fig. 2.10. Room temperature UV-Vis absorption spectrum for $\text{RTF}(\text{PF}_6)_2$ in MeOH (left) and NiO films on FTO coated glass (right): dashed line – unmodified film, solid line - $\text{RTF}(\text{PF}_6)_2$ modified film.

2.1.3. Michael addition products

The double bond activated by the ketone group in the condensation product **II.3** is ideally suited for a Michael addition reaction. Thus, reaction of **II.3** with diethylmalonate in ethanol, catalysed by sodium ethoxide (Figure 2.11), gave after quenching with water, acidification, and purification by column chromatography (silica gel, CH_2Cl_2 / MeOH 9:1) a yellow product in 35% yield.

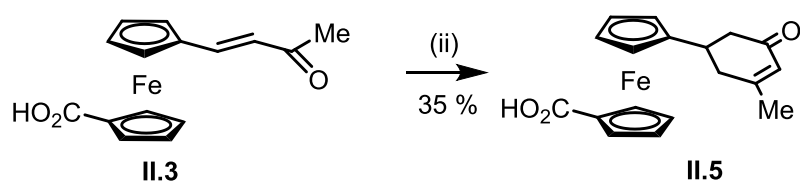


Fig. 2.11. Reagents and conditions: (ii) a. diethyl malonate, NaOEt , EtOH; b. H_2O , H^+ .

The ^1H , $^{13}\text{C}\{^1\text{H}\}$ and DEPT-135° NMR spectra (Figure 2.12) showed resonances typical for a cyclohexenone group [161]. The 2D ^1H - ^1H COSY-45° and heteronuclear ($^1\text{H}/^{13}\text{C}$ HMQC and HMBC) correlation spectra, are consistent with 1'-(5-methylcyclohex-4-en-3-

one)ferrocenecarboxylic acid (**II.5**). The mass spectrum showed peaks at m/z 321, 339, and 677 that match for the $[M - OH]^+$, $[M + H]^+$, and $[2M + H]^+$ ions (Figure 2.12).

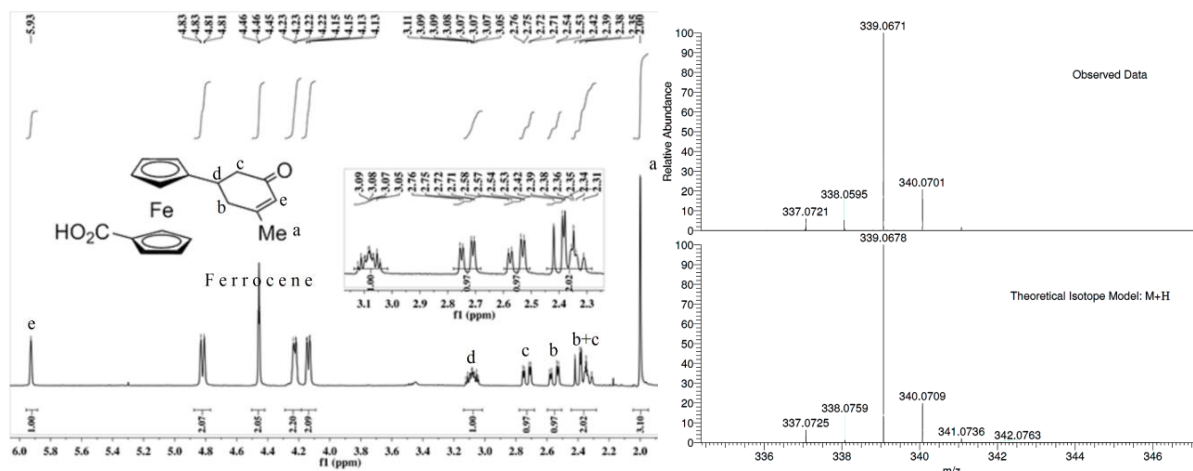


Fig. 2.12. Selected partial 400 MHz ^1H NMR spectrum with partial assignment (left) and APCI/ASAP Accurate Mass spectrum showing the observed and theoretical $[M+H]^+$ pattern (right) for **II.5**.

After several attempts, crystals of the compound suitable for synchrotron X-ray analysis were obtained. The molecular structure is shown in Figure 2.13, and confirms unequivocally the identity of product **II.5**.

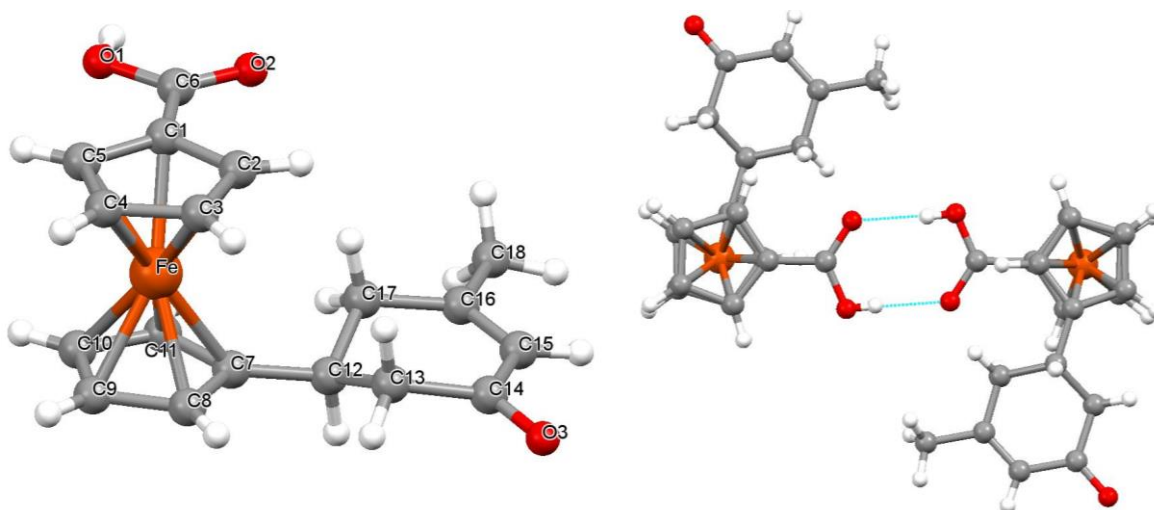


Fig. 2.13. X-ray diffraction molecular structure for racemic compound **II.5** showing here the S form (left) and the centrosymmetric dimer (right).

The C15 – C16 bond length of 1.354 Å is consistent with the expected double bond, and other C – C bond lengths in the cyclohexenone ring are typical for C – C single bonds. C12 is a

chiral centre and both the R and S enantiomers of **II.5** are present in the crystal. The cyclopentadiene planes form an angle of 3.8° and are almost eclipsed. A centrosymmetric dimer is generated in the crystal structure containing both enantiomers (Figure 2.13), as a result of typical hydrogen bonding at the carboxylic acid site (O – O distance 2.664 Å and O – H – O angle 175.8°). Additional crystallographic data for **II.5** are given in Table 4.2.

The intriguing conundrum is the mechanism by which compound **II.3** is converted into **II.5**, since there is no immediately obvious route. The purity of the diethyl malonate was checked to eliminate any suggestion that the starting material was incorrect. A tentative mechanism is suggested from the initially produced Michael addition product, followed by aldol addition of the second diethyl malonate molecule and cyclohexanone ring closure through a Dieckmann condensation reaction (Figure 2.14) [162]. Hydrolysis of the esters and acidification is followed by dehydration of the aldol intermediate and a series of decarboxylations to end up eventually with the racemate of the identified product **II.5**.

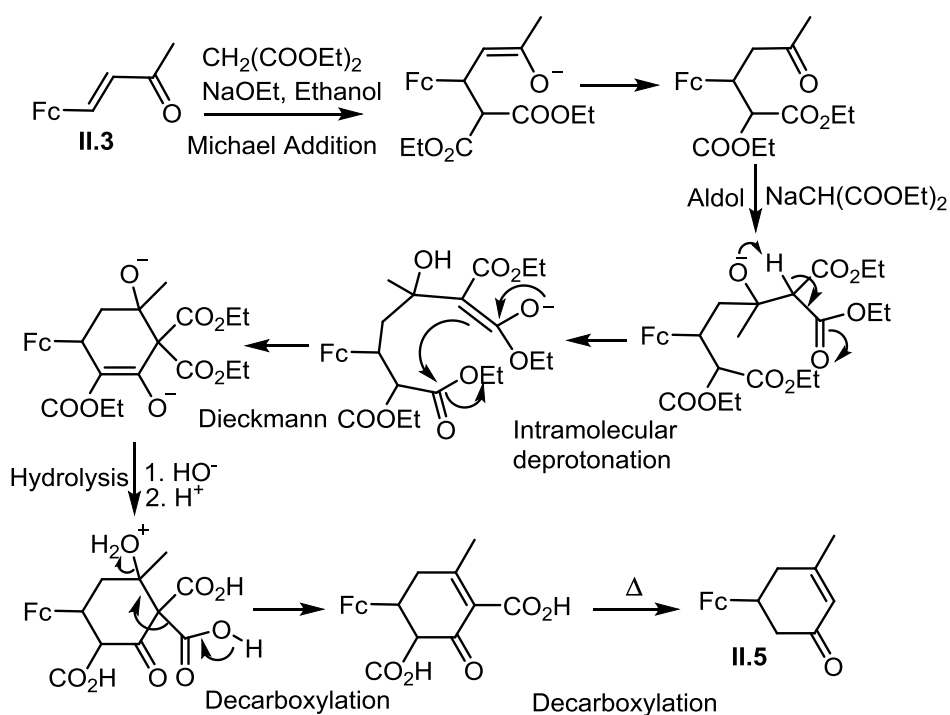


Fig. 2.14. Proposed mechanism to explain the formation of compound **II.5**. Fc = ferrocenecarboxylic acid.

*The alternative ring closure product is from a lactonization of the ketodiester intermediate. There is no obvious mechanism to convert this derivative into the final product.

The Kröhnke method for terpyridine synthesis consists of three steps: aldol condensation, Michael addition and pyridine ring closure. A pentanedione intermediate product can be isolated if no ammonia or ammonium salt is added, preventing pyridine ring formation [163]. An

unexpected product was obtained in the attempt to isolate the intermediate to **II.4**. Using the identical conditions used to access **II.4**, but lacking ammonia source resulted in formation of a product containing three pyridine rings as suggested by elemental analysis. The NMR spectroscopy (Annexe 2) suggested a domino reaction [164] consisting of initial Claisen-Schmidt condensation and Michael addition to form the intermediate diketone, followed by double aldole reaction with the third 2-acetyl pyridine (Figure 2.15). It results in stereo- and regioselective formation of a six-membered carbocycle with four chiral centres - sodium 1'-[3,5-dihydroxy-2-picolinoyl-3,5-di(pyridin-2-yl)cyclohexyl] ferrocenecarboxylate Na**II.6**, with a moderate yield 38 %. Twelve protons found in the aromatic region of ^1H NMR spectrum correspond to three pyridine rings while a complicated pattern found in the aliphatic region is consistent with 1,2,3,5-substituted cyclohexane unit. The ASAP/APCI-FTMS accurate mass spectrum showed a strong expected molecular ion peak pattern $[\text{M}-\text{H}]^-$ at m/z 602, together with weaker peaks due to the dimer $[2\text{M} - \text{H}]^-$ at m/z 1205 and the sodium adduct $[2\text{M} - 2\text{H} + \text{Na}]^-$ at m/z 1227.

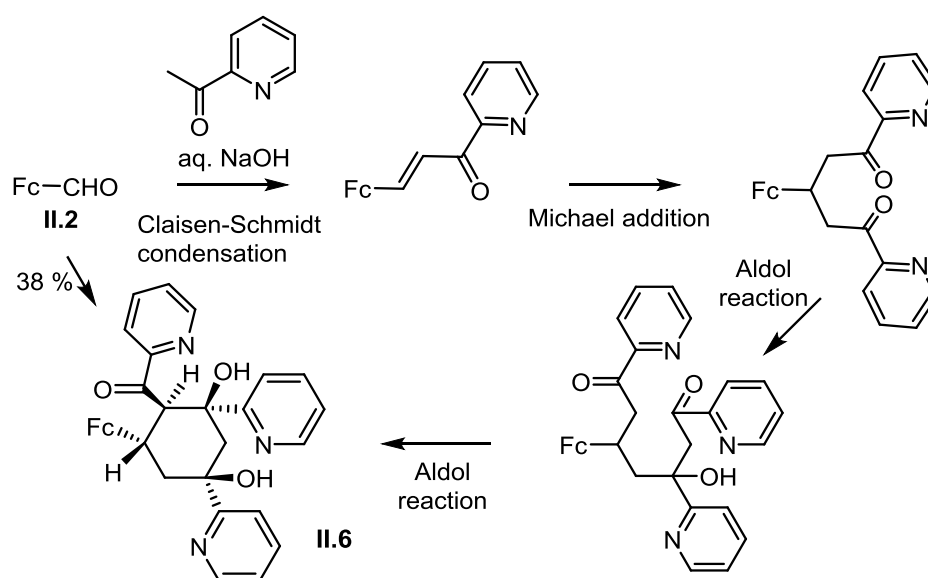


Fig. 2.15. The domino condensation mechanism of cyclohexyl ring formation in compound **II.6** showing the relative conformation of substituents. Fc = ferrocenecarboxylic acid or its Na salt.

Single crystal X-ray crystallographic analysis for **II.6** showed the compound to be a racemic mixture crystallised in the triclinic centrosymmetric space group P-1. All aromatic substituents are arranged in the optimal equatorial positions, so that the four chiral atoms C12, C13, C14, C16 are arranged in 12RS, 13SR, 14RS, 16RS configuration (S – counter clockwise rotation, R - clockwise rotation). The enantiomers of **II.6** are connected in a centrosymmetric dimer generated from typical hydrogen bonding at the carboxylic acid site (O – O distance 2.638 Å, O – H – O angle 176.2°) (Figure 2.16).

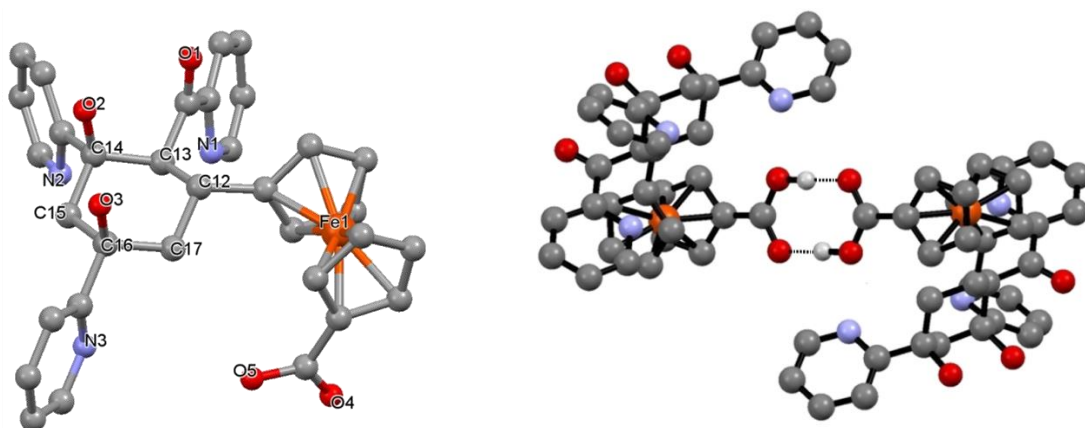


Fig. 2.16. The crystal structure of **II.6** showing here the RSRR form (left) and the special arrangement of the carboxylic bonding dimer (right). Hydrogens are omitted for clarity.

The two hydroxyl groups have different arrangement for RSRR and SRSS configurations, due to four types of hydrogen bonding present in the crystal structure (Figure 2.17). Two intramolecular O – H \cdots O hydrogen bonds are generated by both hydroxyl (O2 and O3) and ketone (O1) groups in one case, with the O – O distances of 2.904 Å (O1 – H_{O2} – O2 angle 150.3°) and 2.759 Å (O2 – H_{O3} – O3 angle 154.4°). The other arrangement involves an intramolecular and one intermolecular O – H \cdots O hydrogen bonds with the O – O distances of 2.759 Å (O2 – H_{O2} – O3 angle 146.3°) and 2.904 Å (O3 – H_{O3} – O3' angle 170.5°), respectively. In this case the ketone oxygen is not involved in hydrogen bond formation. The intermolecular bond is generating a dimer by connecting the two enantiomers. The cyclopentadienyl rings are non-coplanar by 5.2° and are almost fully eclipsed.

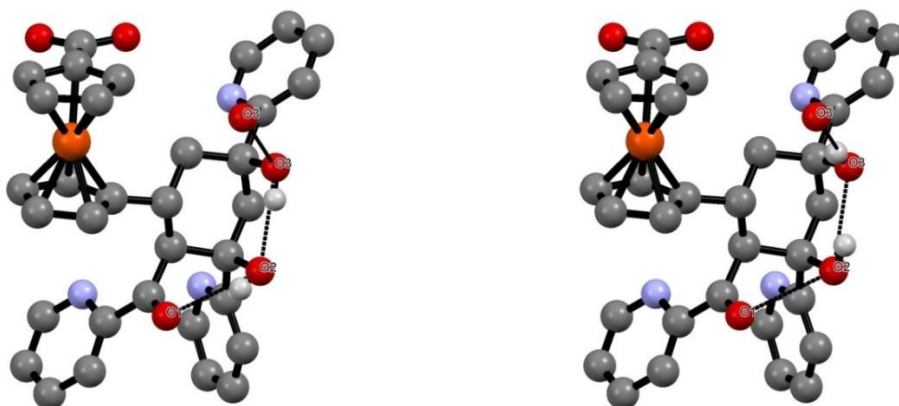


Fig. 2.17. The crystal structure of **II.6** showing the special arrangement of hydroxyl units and resulting hydrogen bonds. Hydrogens are omitted for clarity.

It should be noted that the three pyridine rings and ferrocene carboxylic acid form a “pocket” (Figure 2.18), suitable for hosting small molecules with groups able to interact through hydrogen or ionic bonding with pyridine-N atoms and carboxylic acid-O atoms. While other

pyridine bearing molecules were used as hosts for molecular recognition purposes [165], none of the few previously reported systems similar [164] to the one presented herein were used for practical applications. Keeping this in mind we studied the host-guest interactions of **II.6** with a series of α -amino acids.

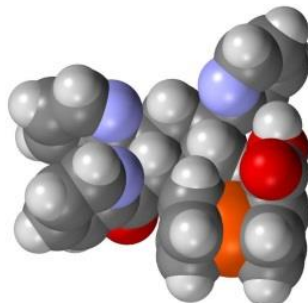


Fig. 2.18. The space fill of compound **II.6** showing the internal “pocket” with N_3O_2 bonding sites.

Attempts to see UV-Vis changes after addition of a series of aminoacids to solutions of **II.6** in MeOH and DMSO failed. Due to the carboxylic unit, the compound **II.6** is slightly soluble in water at pH 7, but addition of aminoacids generated no detectable changes, probably due to the competing strong hydrogen bonding interactions with solvent molecules. In order to make the intermolecular interactions more pronounced, a lower pH was used instead, so that the pyridine groups would be protonated to form the tricharged cation $H_3II.6^{3+}$. Titration of aq. solution of **II.6** with HCl showed an increase of the electronic absorption over the whole visible spectrum, which became less pronounced at further acidulation (Figure 2.19). The additional absorption could be rationalized as charge transfer from ferrocene to the pyridinium units.

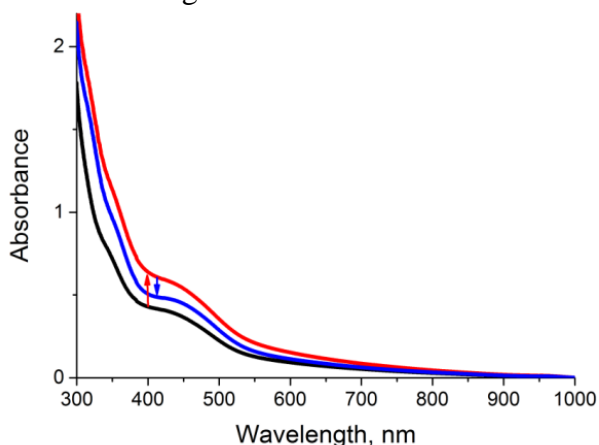


Fig. 2.19. Selected room temperature UV-Vis spectra for **II.6** in water as the hydrochloric acid is added. Black line is showing the initial absorption. Arrows are showing the changes sequence.

Further addition of aminoacids resulted in a general decrease of the absorption profile as a result of the precipitation process (Figure 2.20). We speculate that the less soluble host-guest complex of the general formula $HAA^+ \cdots H_3II.6^{3+}$ (where HAA^+ is the protonated aminoacid

molecule) formed in solution would precipitate as the concentration of aminoacid is increased. Identical results were obtained for glycine, alanine and valine.



Fig. 2.20. Pictures of acidulated aqueous solution of **II.6** before (left) and after (right) addition of glycine.

2.1.4. Temperature dependence of ^{57}Fe -Mössbauer spectra for ferrocene-terpyridine systems

Mössbauer spectrometry is a powerful tool for the study of various elements, especially for ^{57}Fe [166]. Its main hyperfine interaction parameters are the Isomer Shift (IS), Quadrupole Splitting (QS) and magnetic hyperfine interaction. While the first one depends on the total electron density on the examined nucleus (mainly s orbitals), the second is a measure of the electric field gradient. Using these parameters, a comprehensive description of the studied atom can be made (e.g. the oxidation state, spin state, changes in symmetry). The temperature dependence of the Debye-Waller factor of the Mössbauer Spectra gives information on the vibration of atom in the molecule and of molecule in the crystal. The Debye temperature (θ_D) can be determined and used for comparison of forces that bind an atom in the molecule and crystal lattice [167]. The Mössbauer Spectra of **II.4** and **FTFCl₂** are shown in Figure 2.21 with relevant parameters presented in Table 2.1. The room temperature spectrum of **II.4** is typical for a ferrocene derivative and consists of a large and clear doublet. The IS value of 0.43 mm/s is similar (within the error limits) to the parent ferrocene, while the QS decreased by 0.22 mm/s. This is a result of the electron withdrawing effect of the carboxylic substituent which increases the symmetry of the electron environment on the iron nucleus, by removing electron density from the cyclopentadiene ring and consequently from Fe d_{z^2} , d_{xz} , d_{yz} orbitals. The QS is even lower than for ferrocene-carboxylic acid [168], which suggests an additional effect of the terpyridine group. A similar effect was reported for the ferrocene diketones [169] and confirmed by DFT calculations.

The spectrum of **FTFCl₂** comprises two partially overlapped doublets attributed to the two carboxy-ferrocenes and $[\text{Fe}(\text{tpy})_2]^{2+}$ components, with parameters consistent with the literature data [170]. All iron nuclei are low-spin ($S=0$) iron (d^6), but a more symmetrical pseudo-octahedral N_6 coordination results in a lower QS for $[\text{Fe}(\text{tpy})_2]^{2+}$ compared to ferrocene. Decrease of the QS could be expected for ferrocene in **FTFCl₂** compared to **II.4** as result of terpyridine-to-Fe(II) electron pair donation but experimentally a slightly higher (+0.04 mm/s) QS is observed. An explanation is the metal-to-ligand back donation, well-known for $[\text{Fe}(\text{tpy})_2]^{2+}$ [171], which is partially compensating the electron density on terpyridines and consequently on cyclopentadienyl rings. However, the “bowing” of the terpyridine ring upon complexation should be taken into account too.

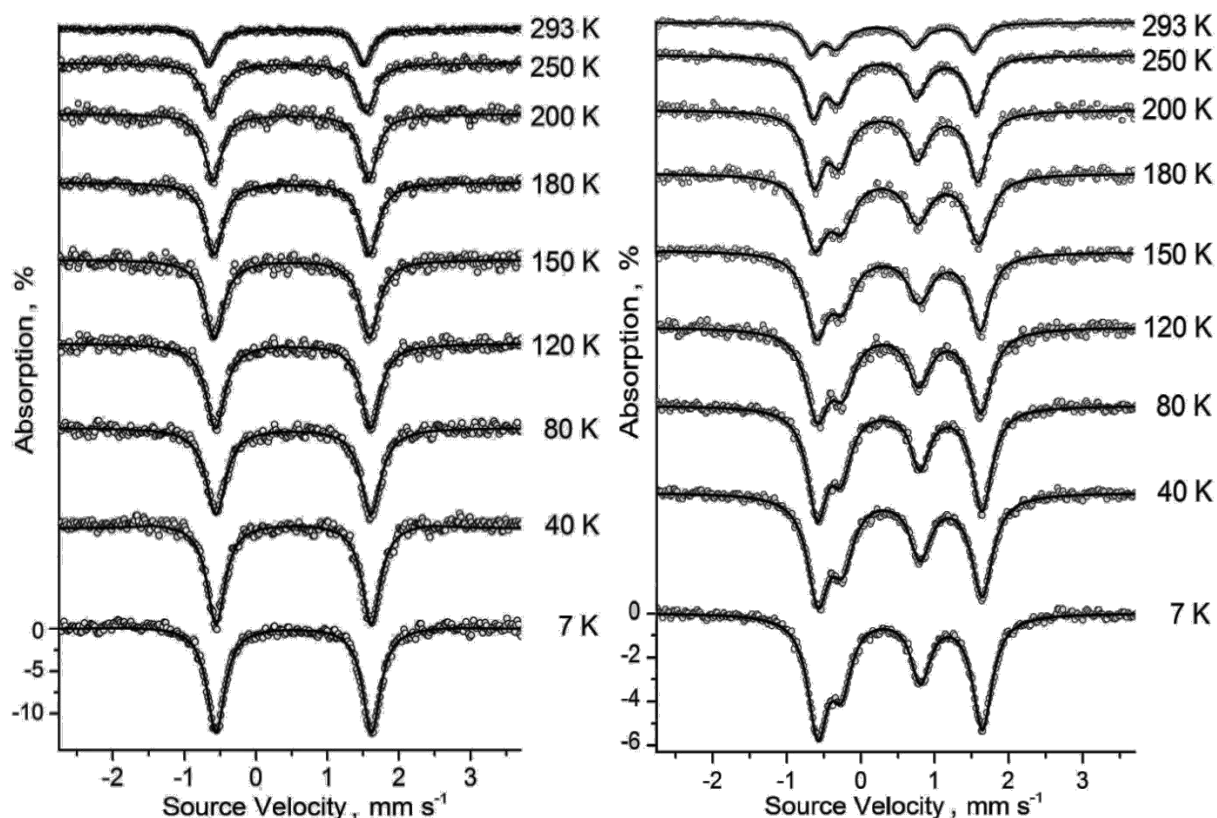


Fig. 2.21. The Mössbauer spectra for **II.4** (left) and **FTFCl₂** (right) over 7 – 293 K temperature range.

Table 2.1. Experimental Mössbauer parameters for **II.4**, **FTFCl₂** and reference compounds.

Compound	Temperature, K	Isomer Shift ^{*,**} , δ , mm/s	Quadr. Splitting ^{**} , ΔE_Q , mm/s	Relative Absorption f'_T/f'_{7K}
II.4	7	0.53	2.18	1.00
	40	0.53	2.18	0.97
	80	0.53	2.17	0.90
	120	0.52	2.18	0.83
	150	0.50	2.18	0.76
	180	0.50	2.17	0.63
	200	0.49	2.18	0.59
	250	0.46	2.17	0.46
	297	0.43	2.17	0.30
Fc in FTFCl₂	7	0.55	2.22	1.00
	40	0.54	2.22	0.94
	80	0.53	2.23	0.82
	120	0.52	2.22	0.73
	150	0.51	2.22	0.64
	180	0.50	2.23	0.58
	200	0.49	2.22	0.50
	250	0.46	2.22	0.36
	293	0.44	2.21	0.20
[Fe^{II}(tpy)₂]²⁺ in FTFCl₂	7	0.27	1.10	1.00
	40	0.27	1.08	0.99
	80	0.27	1.07	0.97
	120	0.27	1.06	0.98
	150	0.27	1.05	0.91
	180	0.26	1.05	0.85
	200	0.25	1.06	0.76
	250	0.23	1.05	0.66
	293	0.21	1.05	0.38
Fc	7	0.54	2.40	1.00
	80	0.53	2.39	0.93
	120	0.52	2.40	0.79
	160	0.51	2.41	0.66
	200	0.50	2.40	0.54
	293	0.45	2.39	0.31
[Fe(tpy)₂]²⁺ ^a	80	0.28	1.05	n/a
Fc-COOH ^b	293	0.53	2.21	n/a

* - IS and QS values are given relative to α -Fe at RT. ** - the standard deviation for values of IS and QS is ± 0.02 mm/s. ^{a, b} Data taken from references [170] and [168], respectively.

The temperature dependence of Mössbauer parameters is expressed in a number of observed changes in the spectra. With decreasing the temperature, a strong increase of the absorption for the Fc was observed, less pronounced for the $[\text{Fe}(\text{tpy})_2]^{2+}$ nucleus. The effect of the increase of recoil free fraction with decreasing the temperature was previously explained as the result of vibration diminution for the examined atom in the crystal lattice. The logarithmic form of the relation between recoil free absorption f' of the γ rays and temperature T for a “thin” absorber is given by equation (1) [172].

$$\ln f' = -\frac{6E_r}{k\theta_D^2} T, \text{ at } T > \frac{\theta_D}{2} \quad (1)$$

where E_r is the recoil energy and k is Boltzmann's constant.

Plots of $\ln f'$ versus T allow us to calculate the Debye temperature from the slope of the line $\Delta(\ln f')/\Delta T$. The $f'_T/f'_{7K} = k_{eff} \times A_T / k_{eff} \times A_{7K} = A_T/A_{7K}$ can be used instead of f' , where A is the experimentally determined area of peak and k_{eff} is an effective constant which takes into consideration the experimental conditions (sample and equipment).

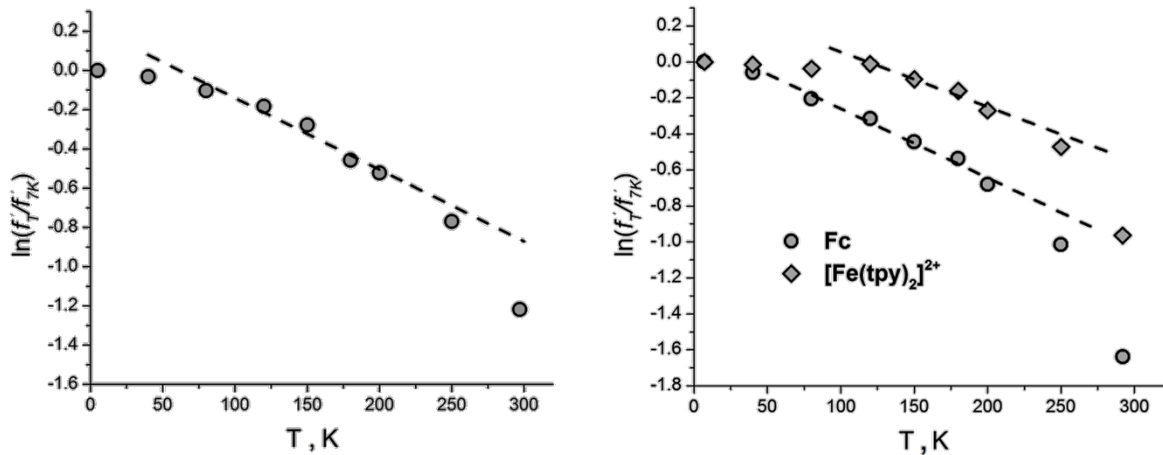


Fig. 2.22. Plots of $\ln f'_T/f'_{7K}$ versus T for **II.4** (left) and **FTFCl₂** (right). Points between 80-200 K for Fc in **II.4** and **FTFCl₂**, but 120-200 K for $[\text{Fe}(\text{tpy})_2]^{2+}$ component were least-squares linearly fitted ($R^2 > 0.99$).

The plot of $\ln f'_T/f'_{7K}$ versus T (Figure 2.22) for **II.4** is linear over the temperature range 80 K to 200 K and has a slope $\frac{6E_r}{k\theta_D^2} = (4.0 \pm 0.3) \times 10^{-3}$ which corresponds to $\theta_D = (184 \pm 14)$ K. This value is somehow higher compared to that of parent ferrocene

$\theta_D = (173 \pm 10)$ K. For the **FTFCl₂** two linear regressions with the slopes of $(4.2 \pm 0.4) \times 10^{-3}$ and $(2.9 \pm 0.2) \times 10^{-3}$ were obtained for Fc and $[\text{Fe}(\text{tpy})_2]^{2+}$ nuclei, which give $\theta_D = (180 \pm 17)$ K and $\theta_D = (218 \pm 15)$ K. The higher Debye temperature for the latter is suggesting a more rigid N₆ bonding of Fe atom by the two terpyridine molecules compared to the ferrocene "sandwich" structure. This is a reasonable result taking in account the well-known stability of the $[\text{Fe}(\text{tpy})_2]^{2+}$ complexes [173] and is in perfect accordance with the light induced instability of ferrocene derivatives in the presence of terpyridine ligand and in **II.4**.

The difference in Debye temperature for the two types of Fe nuclei in **FTFCl₂** results in a different ratio of Fc/ $[\text{Fe}(\text{tpy})_2]^{2+}$ peaks area at temperature variation (Figure 2.23). The plot of area ratio versus temperature can be seen in the bottom picture of Figure 2.23, showing the transition from Fc/ $[\text{Fe}(\text{tpy})_2]^{2+} = 1$ at RT to the stoichiometrically expected Fc/ $[\text{Fe}(\text{tpy})_2]^{2+} = 2$ at 7 K.

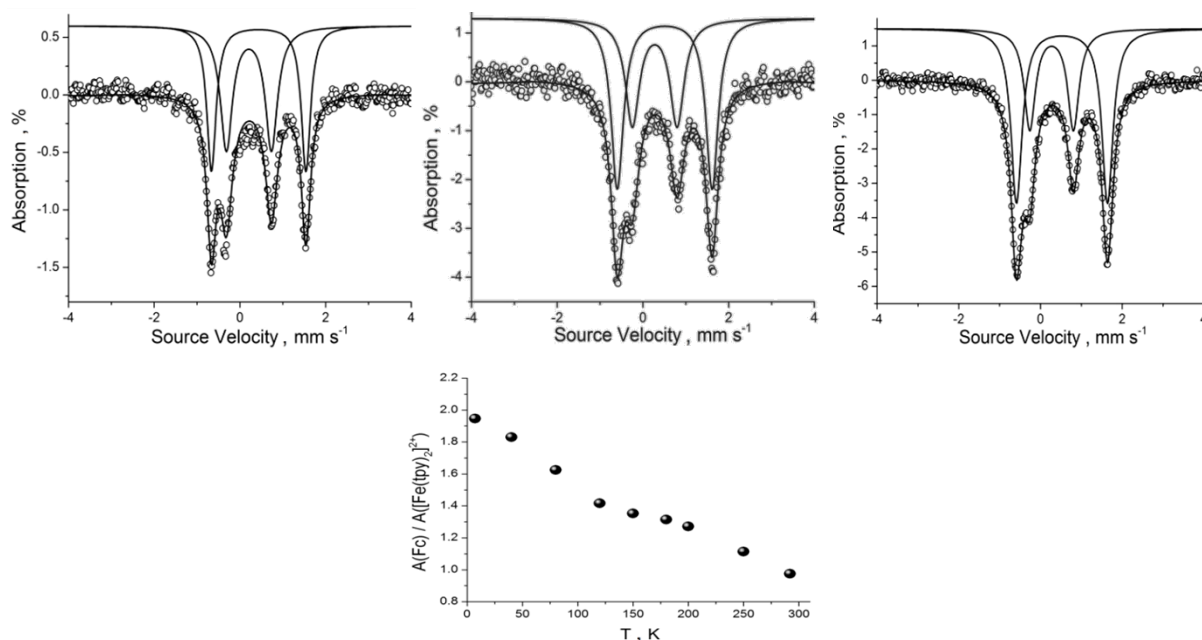


Fig. 2.23. Top: The experimental and fitted Mossbauer spectra for **FTFCl₂** at 293 K (left), 150 K (centre) and 7K (right). Bottom: Plot of $A(\text{Fc}) / A([\text{Fe}(\text{tpy})_2]^{2+})$ ratio versus T .

Another observed change in the spectra with the decrease of temperature is the increment of the IS (Figure 2.24). This is a result of the temperature dependent second-order Doppler shift contribution to the IS [174]. This effect was observed for all studied nuclei but while for the Fc the IS was increasing over the whole range of temperature, the $[\text{Fe}(\text{tpy})_2]^{2+}$ IS almost stopped to increase at 150 K. The IS increased with 0.1 mm/s for Fc from both **II.4** and **FTFCl₂**, but with only 0.07 mm/s for the $[\text{Fe}(\text{tpy})_2]^{2+}$ component.

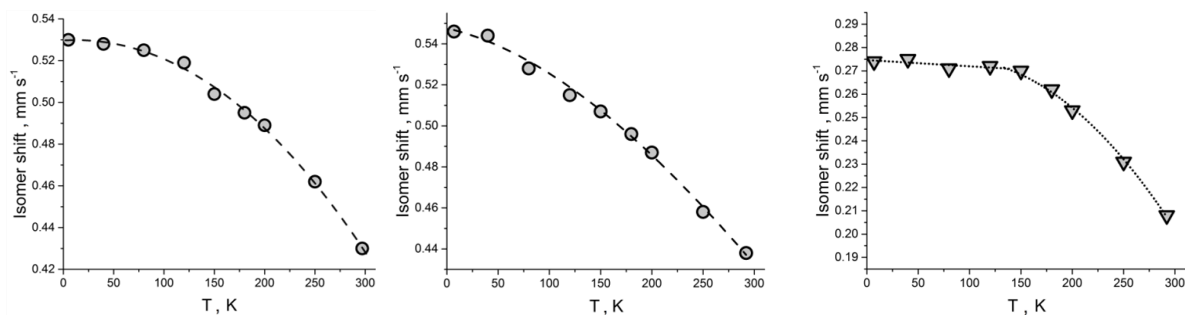


Fig. 2.24. Plot of IS vs T for Fc from **II.4** (left), **FTFCl₂** (middle) and for $[\text{Fe}(\text{tpy})_2]^{2+}$ from **FTFCl₂** (right).

The QS is more “inert” to the temperature variation (Figure 2.25) so that only a minor increment of 0.01 mm/s was observed for Fc but a more pronounced effect of 0.04 mm/s was noticed for $[\text{Fe}(\text{tpy})_2]^{2+}$. As result of these changes the two doublets are less overlapped at higher temperatures.

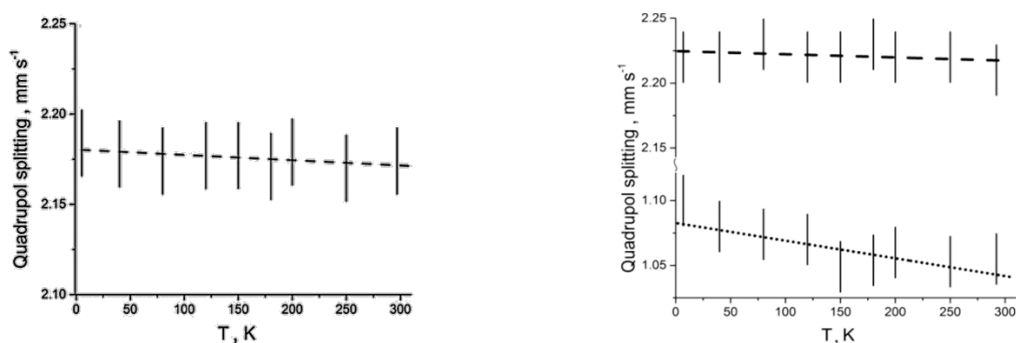


Fig. 2.25. Plots of QS vs T for **II.4** (left) and **FTFCl₂** (right). Dashed lines (---) show the trend for Fc components, while dotted line (···) - for $[\text{Fe}(\text{tpy})_2]^{2+}$ from **FTFCl₂**.

2.2. Synthesis, molecular structure and properties of a ferrocene-based difluoropyrrolo-oxaborole derivative [175]

The incorporation of the chelating boron difluoride (BF_2) group into bidentate sites of flexible molecular species is a simple method to rigidify their structures. The structural modification can have a major effect, particularly on the excited state, and this is particularly true for dipyrromethene derivatives [176]. The basic unit is flexible and excited-state emission is not noticeably strong, which can be attributed to efficient internal conversion promoted by facile molecular distortion. In comparison, the BF_2 version BODIPY fluoresces strongly and quantum yields can easily reach unity in fluid solution [177]. It is not surprising that, over the past few years, attention has turned to other potential organic groups into which the BF_2 group could be introduced [178]. It is noticeable that for the preparation of BODIPY derivatives, the half-way

product is the 2-ketopyrrole, which is rarely isolated since it reacts further to form the dipyrromethane. Considering the N (pyrrole) and O (ketone) atoms are arranged to facilitate formation of a five-membered ring chelate with BF₂, it is surprising that only two examples have been discussed in the literature [179,180]. In attempts to prepare a bis(BODIPY)ferrocene derivative we found that the bis(ketopyrrole) derivative **FKP** was produced instead and could be converted readily into the BF₂ complex, **FBF**.

Reaction of 1,1'-ferrocenedicarbonyl chloride with 3-ethyl-2,4-dimethylpyrrole in DCM produced the half-way product, namely, the ferrocene bis(2-ketopyrrole) derivative **FKP** and not the expected bis(dipyrromethene) compound. The 2-ketopyrrole compound readily reacted with BF₃·Et₂O to produce the bis(difluoropyrrolo-oxaborole) compound, **FBF**, as a red/brown solid which was characterised by X-ray crystallography. ⁵⁷Fe Mössbauer spectra for **FKP** and **FBF** were consistent with low-spin iron(II) (d⁶) ferrocene derivatives. A cyclic voltammogram for **FKP** in acetonitrile revealed a reversible wave at +0.31 V vs. Fc⁺/Fc (ferrocene-based) and an irreversible wave at -2.38 V vs. Fc⁺/Fc (ketopyrrole-based). The electrochemical behaviour is severely perturbed by the chelation of the BF₂ groups. Alterations to the electronic properties of **FKP** by formation of **FBF** are also evident in the absorption profiles. DFT calculations [B3PW91, 6-31G(3df)] support the observed changes in the electrochemistry findings and the Mössbauer spectroscopic data. Unlike some previous examples, the compound **FBF** is nonfluorescent. Excited state quenching is highly probable because of the close proximity of the redox-active ferrocene to the difluoropyrrolo-oxaborole.

2.2.1. Synthesis of 1,1'-ferrocene bis(2-(4-ethyl-3,5-dimethylpyrro)methanone borondifluoride)

It has been established that, starting from ferrocenecarbaldehyde and pyrrole, the corresponding nonalkylated Fc-BODIPY derivative can be prepared in reasonable yield [181]. At first our interest was to see if the same reaction could be carried out by using 1,1'-ferrocenedicarbonyl chloride instead. Several attempts to directly prepare the BODIPY derivative **FBD1** failed (Figure 2.26). The dipyrromethane derivative **II.9** is known [182] and was prepared straightforwardly in 70 % yield. All attempts in our hands to oxidise **II.9** and chelate two BF₂ groups to the dipyrromethene groups failed to yield any product which could be identified as the desired derivative.

Unsubstituted pyrroles are prone to oxidation and so a change in the reagent to 3-ethyl-2,4-dimethylpyrrole and reaction with 1,1'-ferrocenedicarbonyl chloride was attempted. Once

again the desired product **FBD2** was not isolated. Instead of producing the dipyrromethene the reaction actually stopped at the diketone **FKP**, and all our attempts to encourage this to react further with the pyrrole derivative and using Lewis acids were unsuccessful. However, compound **FKP** readily reacted with $\text{BF}_3 \cdot \text{Et}_2\text{O}$ to afford **FBF** as a red-brown solid.

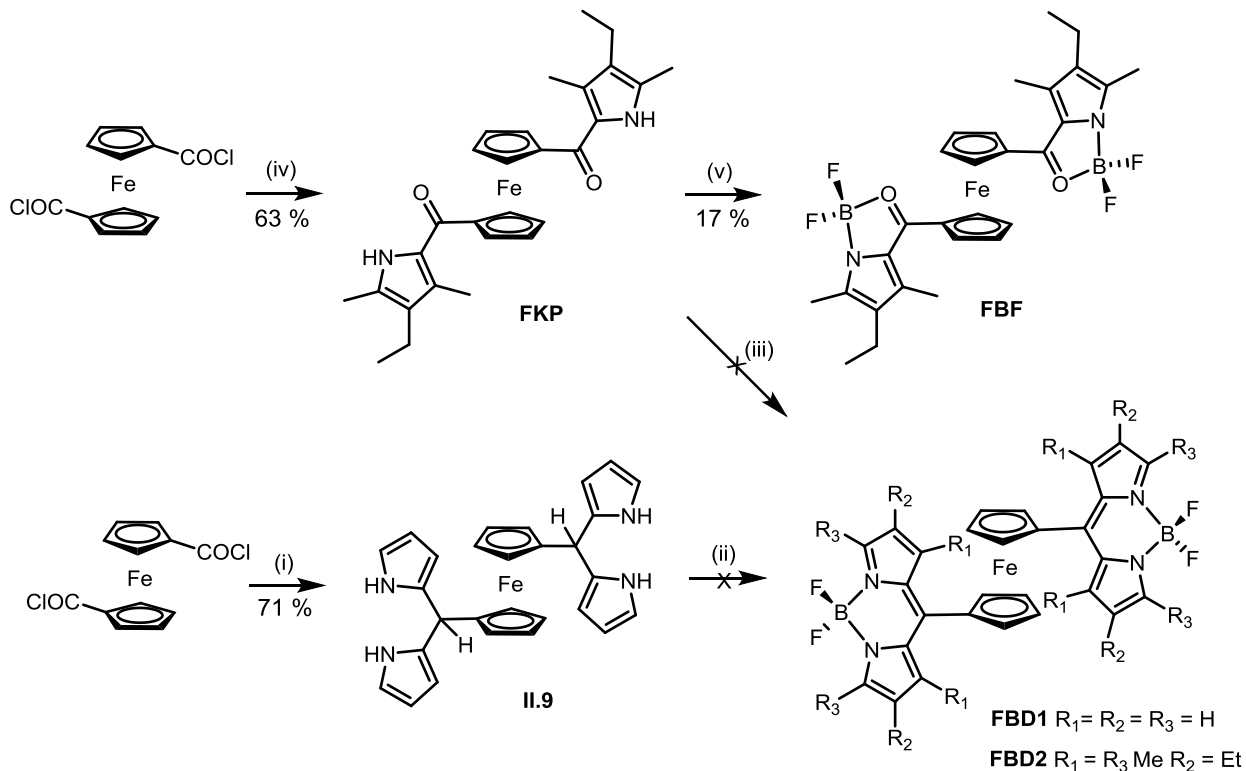


Fig. 2.26. Reagents and conditions: (i) pyrrole, TFA (ii) DDQ or p-chloranil or activated MnO_2 (iii) 3-ethyl-2,4-dimethylpyrrole, Et_3N , $\text{BF}_3 \cdot \text{OEt}_2$; POCl_3 , 3-ethyl-2,4-dimethylpyrrole, Et_3N , $\text{BF}_3 \cdot \text{OEt}_2$ (iv) 3-ethyl-2,4-dimethylpyrrole (v) Et_3N , $\text{BF}_3 \cdot \text{OEt}_2$.

The compound **FBF** was characterised by NMR spectroscopy including ^1H , $^{13}\text{C}\{^1\text{H}\}$, ^{11}B and ^{19}F nuclei (left picture of Figure 2.27). From inspection of **FBF** we might expect, because of restricted rotation, that the two fluorine nuclei for each ketopyrrole are inequivalent, resulting in F–F coupling. Typical J values are around 100 Hz for vicinal fluorines and 20 Hz for intramolecular through-space interactions [183]. The actual spectrum consists of two signals at $\delta = -149.9$ (broad) and -158.0 ppm (doublet, $J = 26$ Hz). In contrast, only a single broad peak at $\delta = 2.16$ ppm was observed in the ^{11}B NMR spectrum. The ESI-MS spectrum showed a peak at $m/z = 485$ corresponding to loss of BF_2 groups, while an ASAP/APCI-FTMS experiment resulted in molecular ion peaks $[\text{M}]^+$ and $[\text{M} + \text{NH}_4]^+$ at m/z 580 and m/z 598 together with fragmentation patterns for sequential loss of BF_2 groups: m/z 561 $[\text{M} - \text{F}]^+$, m/z 533 $[\text{M} - \text{BF}_2 + 2\text{H}]^+$, m/z 513 $[\text{M} - \text{BF}_3 + \text{H}]^+$, m/z 485 $[\text{M} - 2\text{BF}_2 + 3\text{H}]^+$ (right picture of Figure 2.27).

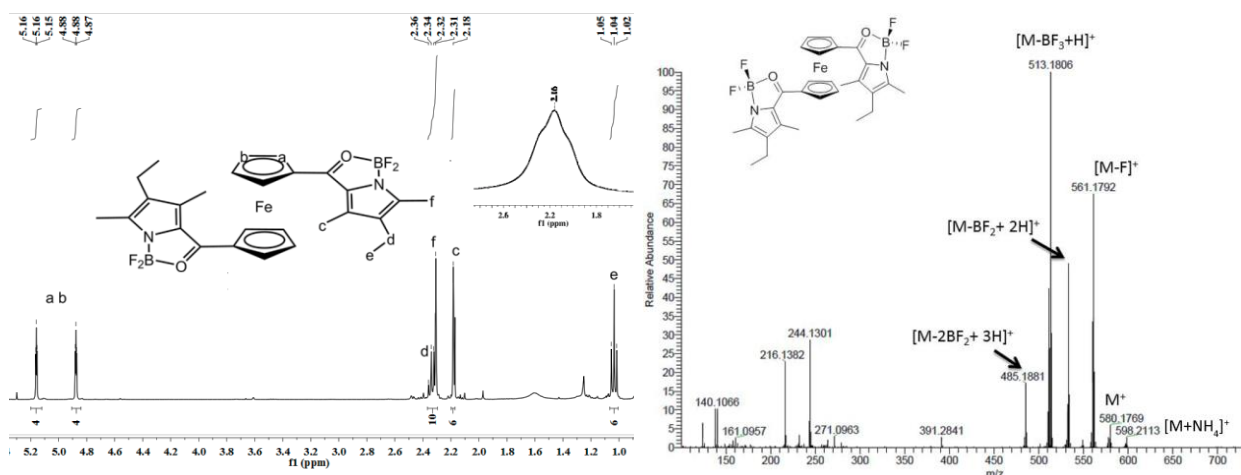


Fig. 2.27. Left: Selected partial 400 MHz ¹H NMR spectrum with partial assignment of signals for **FBF**. Insert is showing the ¹¹B NMR spectrum. Right: APCI/ASAP Mass spectrum and peaks assignment for **FBF**.

2.2.2. X-ray crystallography

As part of characterisation of the final compound and precursors, single crystals were grown for compounds **II.9**, **FKP** and **FBF**, and were subjected to X-ray diffraction analysis. The structures of **II.9** and **FKP** (Figure 2.28) confirmed their identity.

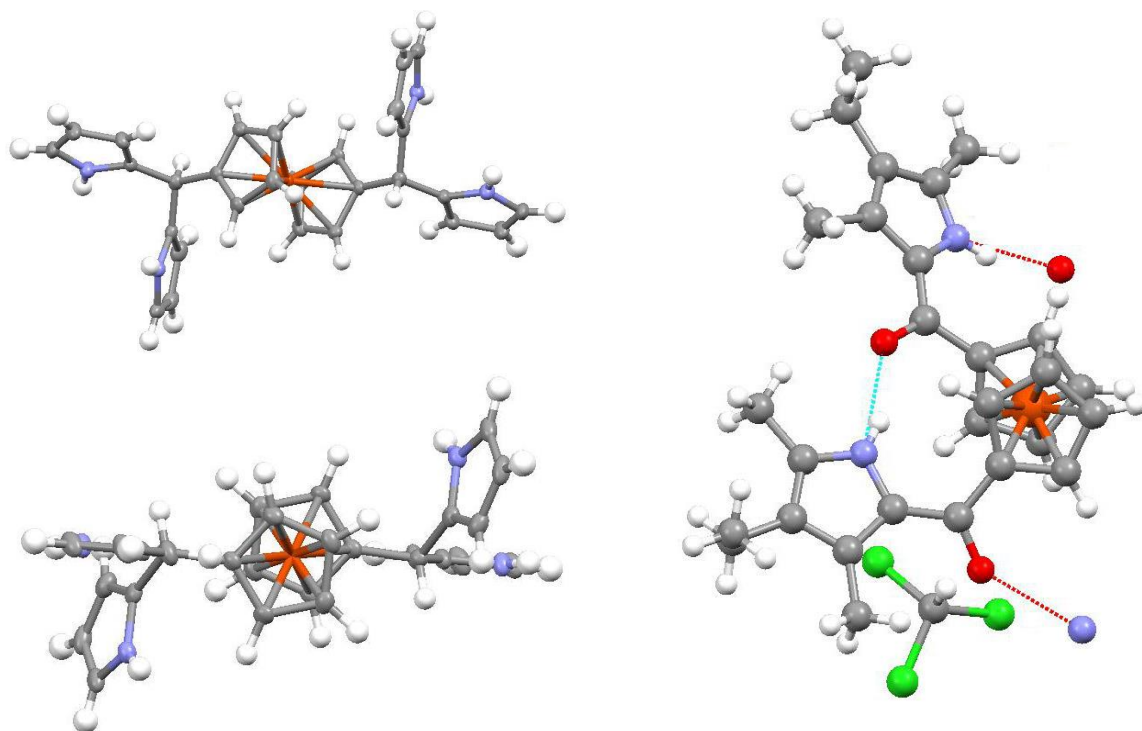


Fig. 2.28. Crystallographically determined molecular structures for **II.9** (left) and **FKP** with incorporated CHCl₃ molecule (right).

Two points are worth noting about the structure of **FKP**. The first is the N – H \cdots O intramolecular hydrogen bond between a pyrrole and ketone on the two cyclopentadienyl (Cp) rings (N – O distance 2.783 Å, N – H – O angle 160.3 °). The effect is to twist the pyrromethanone groups out of conjugation with their Cp rings by different amounts (dihedral angles 48.5° and 30.3°). The other N – H \cdots O hydrogen bond is intermolecular (N – O distance 2.851 Å, N – H – O angle 160.1 °), linking the molecules in chains. The second point is the incorporation of a chloroform solvent molecule.

The compound **FBF** crystallises in the orthorhombic space group Pbcn. The asymmetric unit comprises half the molecular structure, the iron lying on a crystallographic twofold rotation axis. The structure for **FBF** is illustrated in Figure 2.29 and selected bond lengths and angles are collected in Table 2.2. The geometry at the boron centre is close to tetrahedral. The F – B – N bond angles are noticeably greater than the ideal 109.5° and the smallest angle is formed by the endocyclic N – B – O atoms. The bond lengths are quite similar to those found for the two other known literature structures containing the basic pyrroloxaborole ring [179, 180]. The C6 – O bond length is certainly longer than expected for a formal double bond and is consistent with a shift in electron density towards the boron centre. The two difluoropyrrolo-oxaborole groups are arranged tail-to-tail and are partially eclipsed which is more clearly seen in the right picture of Figure 2.29. The angle between planes created using the two equivalent sets of Fe – C5 – C6 atoms is 62.3°. The two cyclopentadienyl rings for the ferrocene are almost eclipsed (7.9°) and practically coplanar (Cp-Cp' angle 1.96°). The torsion angle C1 – C5 – C6 – O is only 8.0° meaning the Cp ring and the pyrroloxaborole group are almost coplanar.

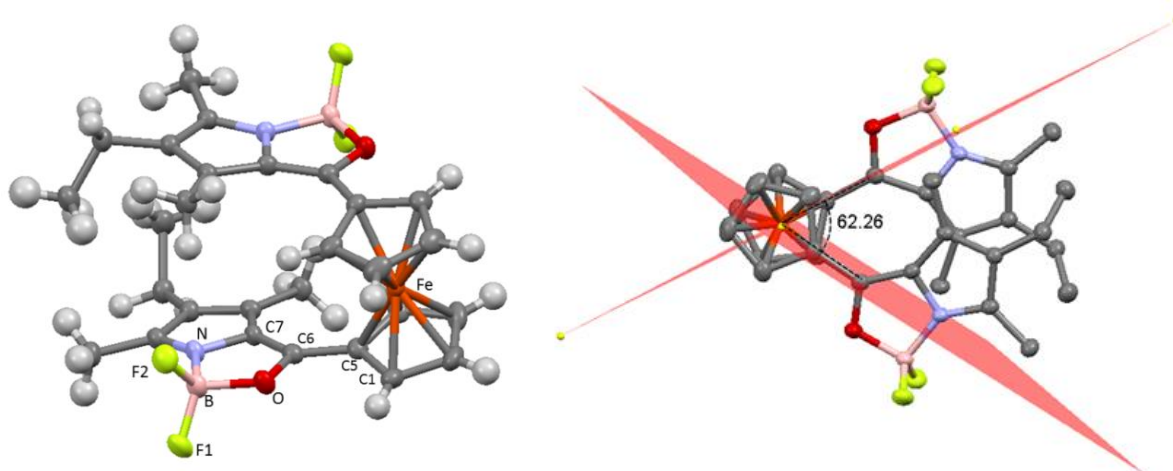


Fig. 2.29. Crystallographically determined molecular structure for **FBF** showing selected atom labelling (left) and a view showing the angle between the planes created to show the eclipsed arrangement (right).

Table 2.2. Selected bond lengths and angles for **FBF**.

Atoms	Bond Length / Å	Atoms	Bond Angle / °
C6-C7	1.396 (1.400) ^[b]	N-C7-C6	107.44 (107.52) ^[b]
C7-N	1.391 (1.385) ^[b]	C7-C6-O	112.40 (113.16) ^[b]
N-B	1.538 (1.560) ^[b]	C6-O-B	110.90 (111.19) ^[b]
O-B	1.509 (1.535) ^[b]	O-B-N	99.26 (97.92) ^[b]
O-C6	1.328 (1.304) ^[b]	F1-B-F2	110.60 (112.95) ^[b]
B-F2	1.373 (1.375) ^[b]	F2-B-N	114.20 (112.48) ^[b]
B-F1	1.383 (1.363) ^[b]	F2-B-O	110.40 (108.69) ^[b]
Fe-C5	2.036 (2.035) ^[b]	F1-B-N	112.00 (113.22) ^[b]
Fe-C (av) ^[a]	2.045 (2.041) ^[b]	F1-B-O	109.90 (110.50) ^[b]

[a] Average bond length calculated from the other four Fe–C bonds.

[b] The first value in each case was crystallographically determined and the second (in parentheses) was calculated by using DFT (B3PW91) and the 6-31G(3df) basis set.

2.2.3. Temperature dependence of ⁵⁷Fe-Mössbauer spectra

The Mössbauer spectra at 7 K for **FKP** and **FBF** are shown in Figure 2.30 with relevant parameters presented in Table 2.3. For comparison purposes, Fc, 1,1'-diacetylferrocene (DAF) and 1,1'-dibenzoylferrocene (DBF) were used as reference compounds.

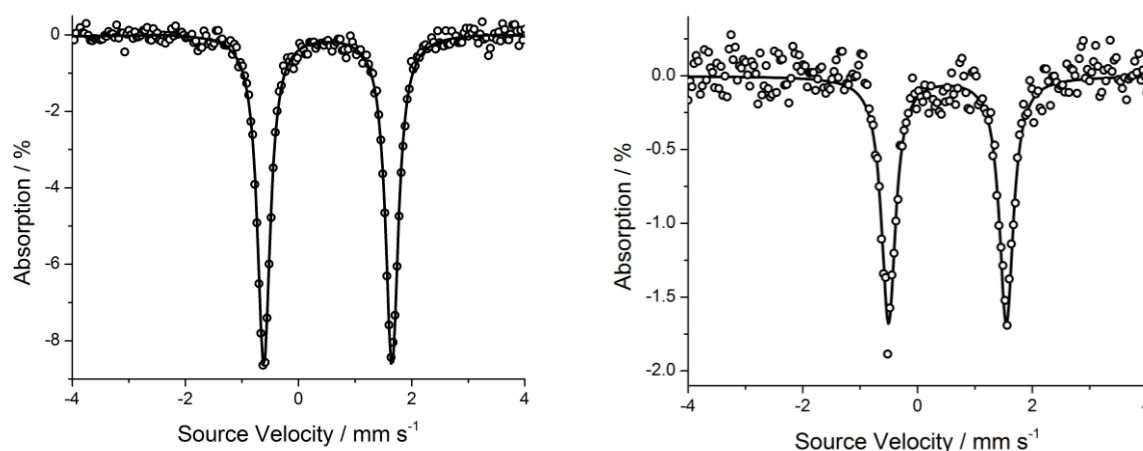


Fig. 2.30. ⁵⁷Fe Mössbauer spectra for **FKP** (left) and **FBF** (right) measured at 7 K.

Table 2.3. Experimental Mössbauer parameters for **FKP**, **FBF** and reference compounds.

Compound	Temp, K	Isomer Shift δ , mm/s	Quadrupole Splitting ΔEQ , mm/s	Relative Absorption f/f_{7K}
FKP	7 K	0.54	2.28	-
	293 K	0.44	2.26	0.095
FBF	7 K	0.52	2.06	-
	300 K	0.44	2.03	0.27
DAF ^{a,b}	77 K	0.53	2.15	na
	300 K	0.43	2.20	na
DBF ^b	80 K	0.53	2.17	na
Fc	7 K	0.54	2.40	-
	293 K	0.45	2.39	0.31

* - IS and QS values are given relative to α -Fe at RT. ** - the standard deviation for values of IS and QS is ± 0.02 mm/s. ^a Data taken from ref. [184]; ^b Data taken from ref. [185]; n.a.: not available.

The isomer shift and large quadrupole splitting for the clear doublet are typical for low-spin iron (d^6) ferrocene derivatives. The isomer shift for both **FKP** and **FBF** are similar to those found for the reference compounds. Its value increase with lowering the temperature is again associated with second-order Doppler shift [174]. The relatively low quadrupole splitting for the diketones compared with that of Fc are typical for conjugated electron-withdrawing substituents which increase the symmetry of the electron environment on the iron nucleus by removing electron density from the cyclopentadienyl rings [169]. The lower quadrupole splitting for **FBF** compared with that of **FKP** can be explained by the higher coplanarity of the electron-withdrawing substituents with the cyclopentadienyl rings, which ensures better overlap of π orbitals and an additional withdrawing effect of the BF_2 group. The corollary is a reduction in electron density on the cyclopentadienyl rings, as supported by the DFT calculations, which results in a lower electric field gradient at the iron nucleus. The recoil-free fractions for **FKP** and **FBF** are highly temperature-dependent as seen from their relative absorption ratios f'_T/f'_{7K} . The logarithmic form of the relation between recoil-free absorption f' of the γ rays and temperature T for a “thin” absorber was given before in Equation (1). Plots of $\ln(f'_T/f'_{7K})$ vs. T (Figure 2.31) are linear over the temperature range 80 K to 200 K and from the slopes the corresponding θ_D values were calculated.

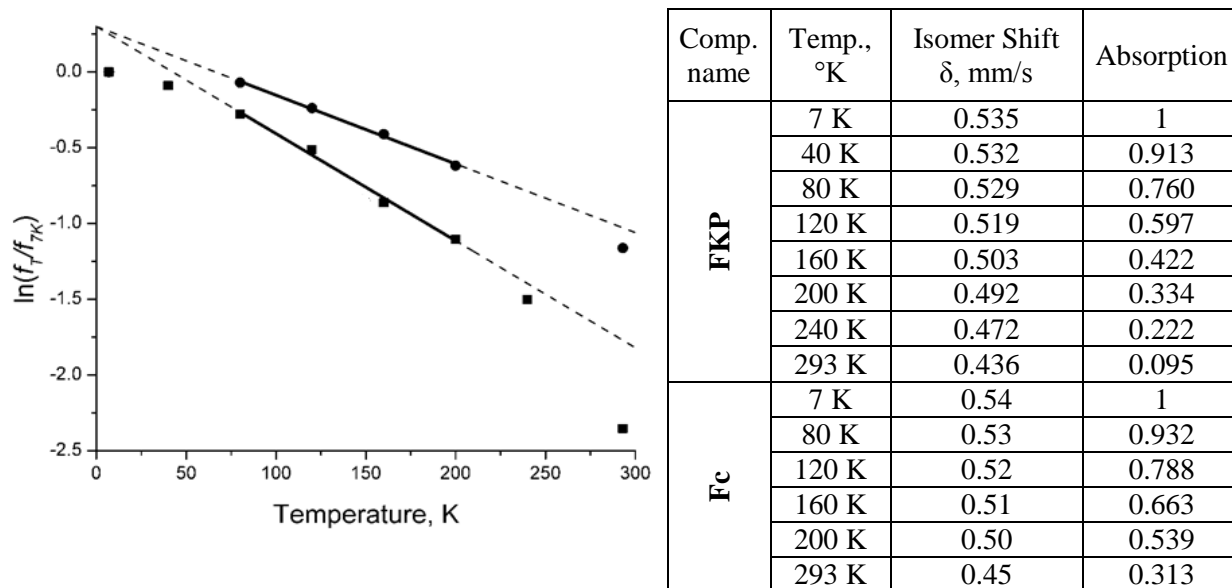


Fig. 2.31. Left: Plot of $\ln(f_T/f_{7K})$ vs T for Fc (●) and **FKP** (■). Points between 80-200 K were least-squares linearly fitted ($R^2 > 0.99$). Dashed lines are shown as a continuation of the fitted lines. Right: Experimental Mössbauer parameters at various temperatures used for plotting graphs.

The θ_D value for ferrocene was estimated at 173 K. As the relative absorption of **FBF** at room temperature has only a minor decrease compared with the parent ferrocene, it was taken as being a very close value. As can be seen from Figure 2.31, the slope for the relative absorption of **FKP** is greater than that of the parent ferrocene. The calculated θ_D value is about 139 K. The lower Debye temperature for **FKP** compared with ferrocene and **FBF** suggests there are weaker intermolecular interactions or weaker Fe-Cp bonding.

2.2.4. DFT molecular modelling

A preliminary inspection of the molecular structure for **FBF** would suggest that the eclipsed conformer does not represent the energy minimum. Despite this, our first goal was to establish the electron density on the Cp rings of the ferrocene and compare this with the uncomplexed derivative **FKP**. The main driver for finding such information was to explain the Mössbauer results. Since the latter relied on collecting data on solid crystalline samples, DFT calculations to elucidate Mulliken charges on selected atoms were performed directly on models generated from the X-ray structures for **FBF** and compound **FKP**. In order to determine firstly the best basis set, molecular models for **FBF** were constructed from different starting geometries and the energy minimised (Annexe 3). Bond lengths and angles were compared with those in the X-ray determined molecular structure. We found that DFT calculations using B3PW91 and the 6-31G (3df) basis set afforded structures for which Fe-C bond lengths for the ferrocene group

were close to those found by X-ray analysis (Table 2.2). Other bond lengths were in reasonable agreement with the X-ray determined structures. Hence, Mulliken charges were calculated for the X-ray structures of **FBF** and **FKP** using DFT (B3PW91) and the 6-31G (3df) basis set (Figure 2.32). The first point to note is the increase in positive charge at the iron centre for **FBF** (+0.677) compared with that in **FKP** (+0.647). Because **FBF** is C_2 symmetric, the summation of Mulliken charges for carbon atoms at each Cp ring is identical (−0.739) and less than values for the Cp rings in compound **FKP** (−0.850, −0.874). There appears to be a slight extra build-up of negative charge (−0.024) on the one Cp ring for compound **FKP**. It is clear from the structure that this Cp ring and the difluoropyrrolo-oxaborole are more conjugated since the dihedral angle is only 11.9° compared with 40.9° at the other Cp site. The corresponding dihedral angle for **FBF** is only 8° meaning any conjugation is maximised for this system but it also contains the electron-withdrawing BF_2 unit.

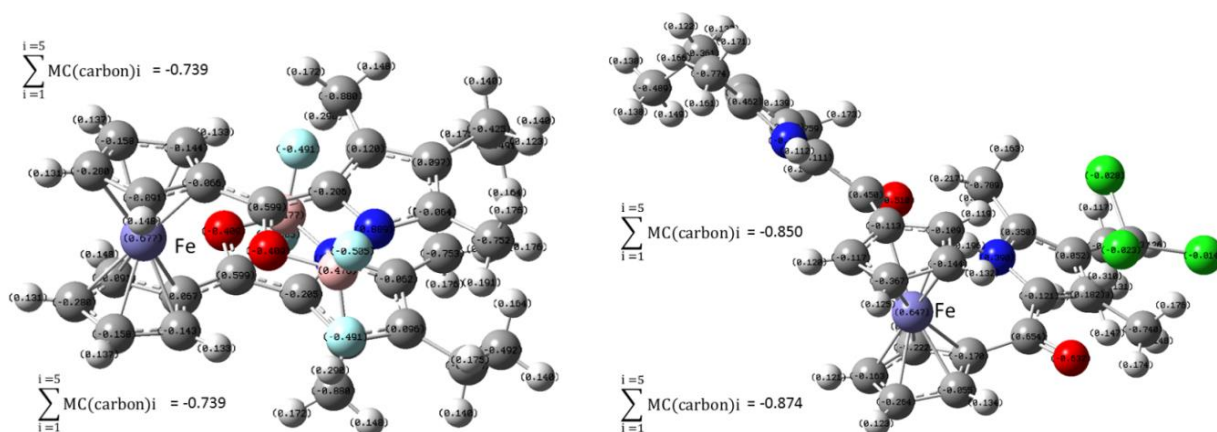


Fig. 2.32. Mulliken charges on the atoms calculated by using DFT (B3PW91) and the 6-31G(3df) basis set for X-ray determined structures of **FBF** (left) and **FKP·CHCl₃** (right). The summation of the Mulliken charges (MC) for carbons only in each Cp ring of the ferrocene is also shown.

To delve more into the effect of conjugation on the Mulliken charge at the ferrocene centre, the starting structure for **FBF** was again minimised by using DFT (B3PW91) and the 6-31G (3df) basis set. The results from these calculations are deemed to better represent a solution phase structure. The refined structure is some 216 kcal mol^{−1} lower in energy and the dihedral angle is increased to 20.8°. As a result of the decrease in conjugation, the Mulliken charge at the iron is reduced to +0.548 and the charge on each Cp ring is increased to −0.936. The same calculation performed on **FKP** is rather similar in that there is a build-up of negative charge at the Cp rings and a reduction of charge at the iron centre. A summary of the results is collected in

Table 2.4. From inspection of the data it is possible to predict that the iron(II) centre in the ferrocene for **FBF** will be harder to oxidise than the uncomplexed version. In addition, we can also speculate that the electric field across the iron nucleus will decrease slightly for **FBF** compared with the one in compound **FKP**.

Table 2.4. Collection of Mulliken charges (MC) for selected atoms and groups.

Compound	FKP	FBF	
MC (Fe)			$\Delta MC^{[a]}$
Opt structure	+0.530 (-0.117) ^[b]	+0.548 (-0.129) ^[b]	+0.018
Unopt structure	+0.647	+0.677	+0.03
MC (CP)			$\Delta MC^{[a]}$
Opt structure	-1.103/-1.107	-0.936 (-0.197) ^[b]	+0.167/+0.171
Unopt structure	-0.850/-0.874	-0.739	+0.111/+0.135

[a] $\Delta MC = MC_{\text{FBF}} - MC_{\text{FKP}}$. [b] $\Delta MC = MC_{\text{opt}} - MC_{\text{unopt}}$.

2.2.5. Electrochemistry and absorption spectroscopy

The redox behaviour of **FKP** and **FBF** was studied by using cyclic voltammetry in dry acetonitrile with 0.2 M TBABF₄ as the background electrolyte. The cyclic voltammogram of **FKP** (left picture Figure 2.33) revealed a reversible wave at +0.31 V vs. Fc⁺/Fc associated with the ferrocene redox site, and an irreversible wave at -2.38 V vs. Fc⁺/Fc. The reduction wave must be associated with the pyrrolo-ketone group. There is also evidence of an additional irreversible process present at potentials greater than +1 V – cycling to such a potential also removes the reversibility of the ferrocene couple. Complexation of **FKP** with BF₂ causes a series of changes to the redox behaviour of **FBF** (Annexe 4). The redox potential for the ferrocene is anodically shifted to +0.66 V vs. Fc⁺/Fc and two quasi-reversible waves can be observed at -1.54 and -1.84 V vs. Fc⁺/Fc. The shift to a more positive potential for the ferrocene unit is consistent with the electron-withdrawing effect of the pyrrolo-oxaborole substituents and fully supported by the DFT calculations. It was noted that the ferrocene redox behaviour is irreversible in **FBF**, implying that a decomposition pathway is introduced for the ferrocenium ion. Considering that an electrophilic centre is created in close proximity to a polarised B – F bond, nucleophilic attack of a fluorine atom at the ferrocenium is one possible breakdown mechanism. To support this idea, NaBr was added to a solution of **FKP** in MeCN, which resulted in complete loss of reversibility of the ferrocene couple (right picture of Figure 2.33). Additionally, the

irreversible anodic wave shifts to a lower potential, affording a very similar voltammogram to that of **FBF** alone.

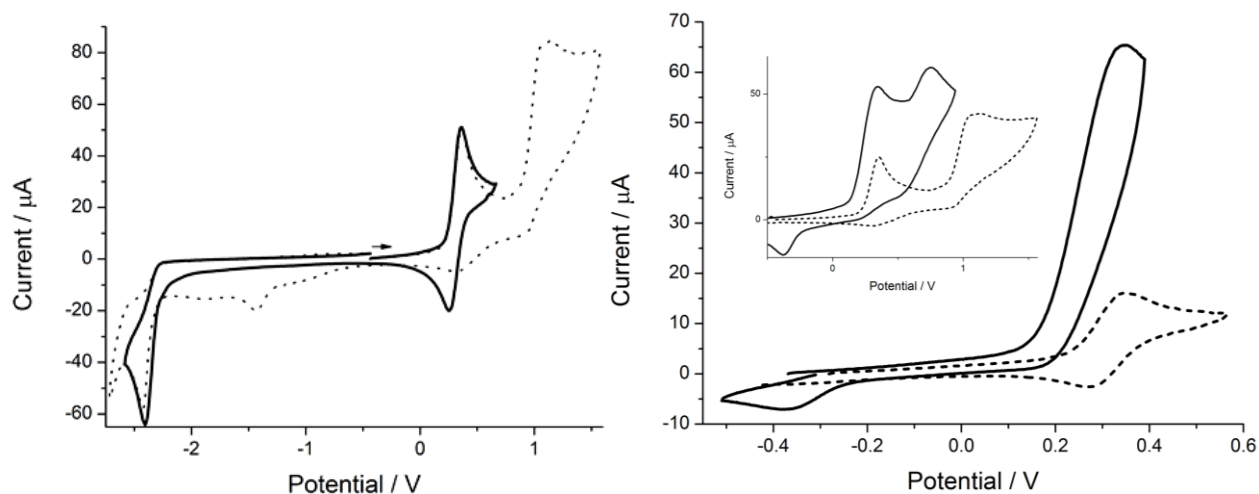


Fig. 2.33. Left: Cyclic voltammogram recorded for **FKP** in acetonitrile containing 0.2 M TBABF₄ vs. Fc⁺/Fc. The dashed line shows the additional irreversible oxidation peak when the potential window is increased. Right: Cyclic voltammograms recorded for **FKP** before (dashed line) and after addition of NaBr (solid line). The insert shows the voltammograms where the potential is increased to > 1 V.

The room-temperature electronic absorption spectra for **FKP** and **FBF** are shown in Figure 2.34. The spectrum of **FKP** consists of a band in the near-UV region at $\lambda_{\text{max}} = 271$ nm ($\epsilon_{\text{max}} = 1.7 \times 10^4$ M⁻¹ cm⁻¹) and a moderately strong narrow band at $\lambda_{\text{max}} = 337$ nm ($\epsilon_{\text{max}} = 3.4 \times 10^4$ M⁻¹ cm⁻¹). According to DFT calculations (Annexe 5) this band is likely associated with the HOMO–LUMO transition localised on the ketopyrrole unit and the calculated energy gap is 3.69 eV (336 nm). A much less intense broad band can also be observed in the visible region at $\lambda_{\text{max}} = 462$ nm ($\epsilon_{\text{max}} = 1.3 \times 10^3$ M⁻¹ cm⁻¹). This latter band was assigned to electronic transitions for the ferrocene group.

Chelation with BF₂ changes the absorption profile entirely, resulting in a considerably broader but weaker band in the visible region at $\lambda_{\text{max}} = 407$ nm ($\epsilon_{\text{max}} = 1.4 \times 10^4$ M⁻¹ cm⁻¹) with a shoulder at 339 nm. The intensity of the band at $\lambda_{\text{max}} = 272$ nm ($\epsilon_{\text{max}} = 7.5 \times 10^3$ M⁻¹ cm⁻¹) is considerably less. Both these absorption bands are consistent with the spectra of previous difluoropyrrolo-oxaborole derivatives [179, 180]. Also prominent in the spectrum is a broad featureless band in the region 500–650 nm, which must arise from the perturbed ferrocene group. No room-temperature fluorescence is observable from **FBF** in fluid solution, in the solid state or when oxidised.

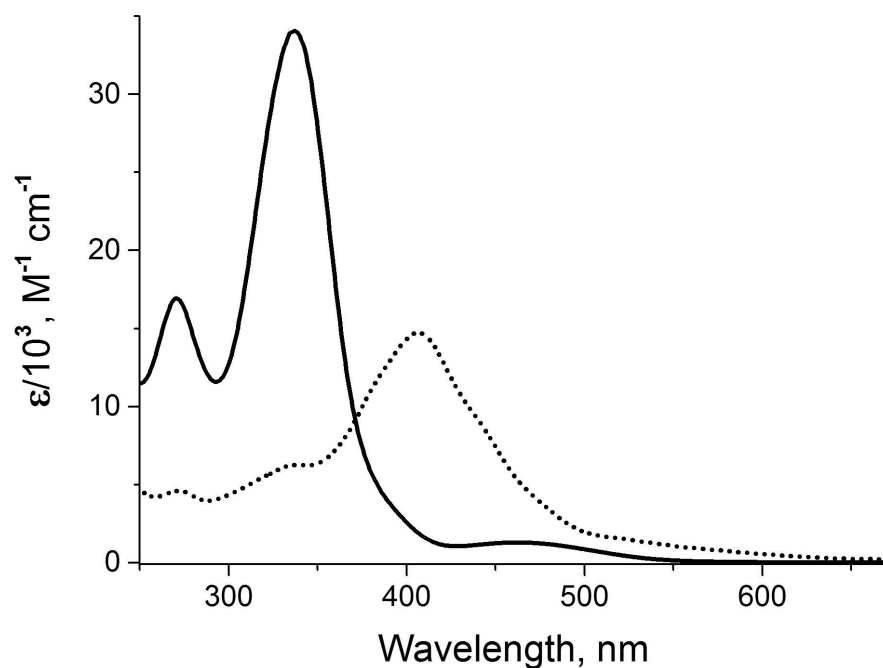


Fig. 2.34. Room-temperature UV-Vis absorption spectra for **FKP** (solid line) and **FBF** (dotted line) in acetonitrile.

2.2.6. UV-Vis spectroelectrochemistry

Perturbation of the UV-Vis spectra for **FKP** and **FBF** was monitored by using an OTTLE and the spectroelectrochemistry method by application of negative and positive potentials. Application of a negative potential of -1.8 V to the working electrode for a solution of **FKP** in acetonitrile produced a small increase in the ferrocene-based region around 460 nm, coupled with a slight change in the band shape and a tail stretching to around 800 nm (Figure 2.35). There was a concomitant decrease in the high-energy side of the spectrum which is consistent with ketopyrrole reduction. The tail is likely from a weak charge-transfer transition. The original spectrum could not be reproduced by application of an oxidising potential.

Oxidation of the ferrocene unit at $+0.7$ V for **FKP** resulted in an expected red-shift for the visible absorption band because of ferrocenium ion formation. The most notable effect is the change to the high-energy absorption band which is actually replaced by a broader feature located around 400 nm (Figure 2.35 insert). Again we might expect to observe some charge-transfer character because of electron donation from the ketopyrrole to the ferrocenium ion. The original spectrum was restored by application of a reducing potential.

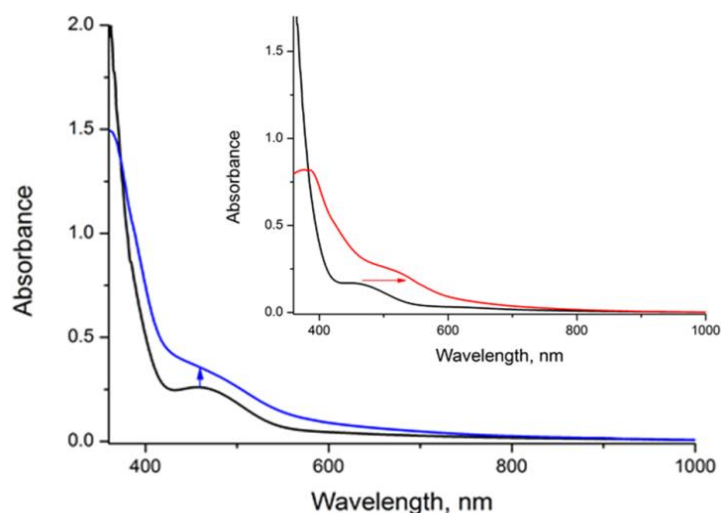


Fig. 2.35. Main: Electronic absorption spectra for **FKP** in acetonitrile showing starting spectrum (black) and after reduction (blue). Insert: Absorption spectra before (black) and after oxidation (red).

Similar spectroelectrochemistry experiments performed using **FBF** in acetonitrile are shown in Figure 2.36. Application of a reduction potential at -1.2 V resulted in a very noticeable band-narrowing and a blue shift by 5 nm together with an increase in peak intensity. Further reduction at -1.6 V followed the same trend and can be explained by electron addition to the second difluoropyrrolo-oxaborole group. The alteration in the absorption profile was reversible. Applying a positive potential of $+0.7$ V and then $+1.2$ V resulted only in a decrease in the absorption profile at 400 nm (Figure 2.36 insert). Considering that the oxidation wave for **FBF** is irreversible, the effect is likely due to compound degradation.

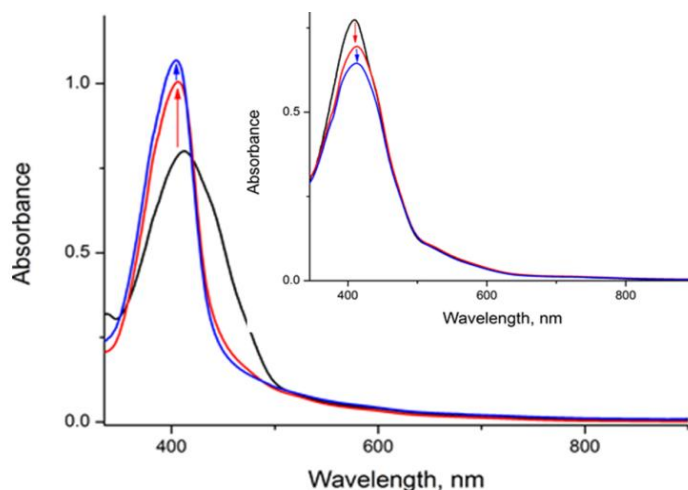


Fig. 2.36. Main: Electronic absorption spectra for **FBF** in acetonitrile at the start (black) and after reduction at -1.2 V (red) and -1.6 V (blue). Insert: Absorption spectra before (black) and after oxidation at $+0.7$ V (red) and blue $+1.2$ V (blue).

2.3. Conclusions to Chapter 2

Chapter 2.1: A new method for desymmetrization of ferrocene molecule was elaborated consisting of simple oxidation with potassium permanganate of 1,1'-ferrocenedicarboxaldehyde, to give the desymmetrized compounds 1'-formyl-ferrocenecarboxylic acid and 1'-((E)-3-oxo-but-1-enyl)-ferrocenecarboxylic acid. These proved to be useful starting materials employed in various reactions like Michael addition and Kröhnke reactions, and as result five new products were obtained.

The study into the light driven instability of **II.4** in solution disclosed some additional details on the mechanism of ferrocene derivatives instability. The temperature dependence of the ^{57}Fe Mössbauer spectra for **II.4** and **FTFCl₂** was fully described. The Debye temperature was found to be (184 ± 14) and (180 ± 17) K for ferrocene components of **II.4** and **FTFCl₂** and $\theta_D = (218\pm 15)$ K for $[(\text{Fe}(\text{tpy})_2)]^{2+}$ unit, which supports the stronger metal-ligand binding and higher stability of the latter. Altogether, this example shows how the difference of Debye temperatures in polynuclear systems strongly affects the Mössbauer spectrum and should be taken in account when interpreting the experimental results. In the attempt to perform a classical Michael addition reaction on compound **II.3** an unexpected product was obtained **II.5**. A reliable mechanism was proposed consisting of initial Michael addition followed by aldol addition of the second diethyl malonate molecule and cyclohexanone ring closure through a Dieckmann condensation reaction. The preliminary study of the host guest interactions of **II.6** with amino acids showed the potential of this class of compounds in visual recognition application.

Chapter 2.2: Although mono-BODIPY ferrocene derivatives are known, it would appear that the bis derivative may be more difficult to achieve, especially using the conventional approaches toward BODIPY synthesis. The failure to obtain the compound is surprising considering that the dipyrromethane precursor **II.9** was used by Butenschön et al. to prepare a bis(porphyrin) derivative. A steric argument for failure does not therefore seem to be valid. The deactivation of the dipyrromethane towards oxidation by the presence of a second group on the other Cp ring seems to be the only feasible explanation. Certainly we have seen that oxidation of one aldehyde group in 1,1'-ferrocenedicarbaldehyde deactivates reaction at the other site. The electrochemistry of **FKP** and **FBF** showed the ferrocene centred redox processes to be sensitive to nucleophiles by inter- or intramolecular attack on electrochemically generated ferrocenium cation. The chelation with BF_2 showed to strongly influence both redox and absorption behaviour of ferrocene derivatives.

3. FERROCENE-PORPHYRIN CONJUGATES

3.1. Synthesis, properties of a *meso*-tris-ferrocene appended zinc(II) porphyrin and evaluation of its dye sensitised solar cell performance [122]

The basic working of DSSC relies on the injection of an excited state electron into the conduction band of an appropriate n-type semiconductor. The classic material used is TiO_2 . The hole left behind on the sensitizer dye is plugged by a redox shuttle and the circuit is completed by the electron from the conduction band reducing via a secondary electrode the oxidised redox relay [186]. Numerous reports are available discussing the different processes in DSSC and trying to identify the “bottle-neck” which is limiting the efficiency of manufactured devices [187]. There is one argument that charge must be shifted away from the semiconductor surface rapidly to generate long-lived charge-separated species [188] and avoid the charge recombination which was estimated to occur in the range of $100\ \mu\text{s} - 1\ \text{ms}$ [189]. The analogy with natural photosynthetic reaction centre complexes is clear, but like in Nature the required assemblies to perform such task become more intricate. One challenge is to identify rudimentary molecular systems that may perform secondary charge shift.

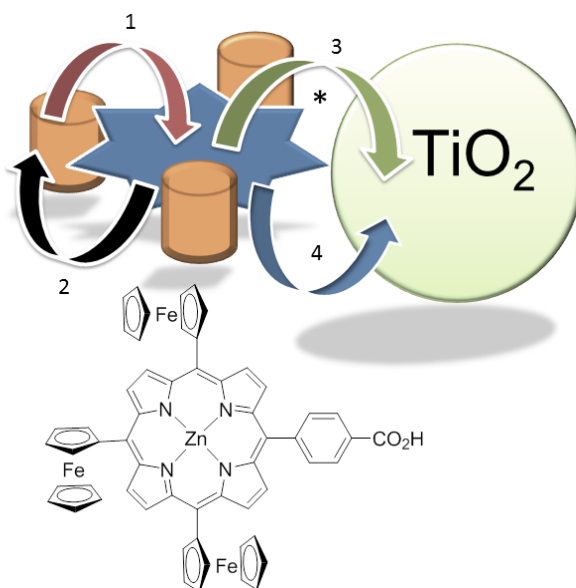


Fig. 3.1. Top: Simple cartoon showing potential electron transfer pathways following excitation of the zinc(II) porphyrin. Brown cylinders represent Fc units, blue star represents porphyrin macrocycle, arrows represent electron transfer pathways: 1. charge separation involving oxidation of a ferrocene; 2. charge recombination; 3. electron injection into conduction band of TiO_2 from zinc-porphyrin excited state; 4. electron injection into conduction band of TiO_2 from porphyrin radical anion. Bottom: Tris-ferrocene zinc(II) porphyrin **F3P** containing the carboxylic acid anchoring unit.

The most basic porphyrin based molecular system incorporating *meso*-ferrocene units is exemplified in Figure 3.1. The cartoon represents the basic working of the system following excitation of the porphyrin moiety, where process 1 is oxidation of a ferrocene by the excited state and process 2 is the charge recombination. It could be argued that if charge injection from the porphyrin excited state (process 3) competed with process 1, then the system would operate. Alternatively, if electron injection from the porphyrin anion (process 4) was fast and efficient, then the energy wasting recombination process 2 would become less significant. We are, of course, not considering the recombination process involving back electron transfer from the conduction band of the TiO₂.

Evidently, knowledge of the intramolecular chromophore electron transfer events is critical. Prior work by Nadtchenko and co-workers suggested for the free-base tetraferrocenyl porphyrin that processes 1 and 2 occurred in around 200 fs and 17 ps, respectively [64]. There are no reports on the zinc(II) analogue. In this work we consider the zinc(II) tris-ferrocenyl porphyrin **F3P** and elucidation of its properties especially probing the rates for processes 1 to 4. The dye attaches to TiO₂ but performance in a DSSC is limited.

3.1.1. Synthesis of Zn(II) 5,10,15-trisferrocenyl-20-(4-carboxyphenyl) porphyrin

Preparation of symmetrical porphyrin derivatives is relatively undemanding, requiring only a suitable aldehyde to couple with pyrrole in the presence of an acid [26]. Complexity is introduced when the requirement is to have non-identical *meso* groups, and have them proximal or distal to each other in the case of bis-aryl derivatives. Various methods to control the spatial location of the *meso*-aryl groups were introduced by Lindsey and co-workers [27]. Since we only required the presence of a single aryl carboxylate group, the simplest approach was to incorporate three ferrocene units. Two strategies were attempted for the preparation of **F3P** via the free-base porphyrin. The synthesis scheme is illustrated in Figure 3.2.

Certainly, the most uncomplicated method is the condensation of methyl 4-formylbenzoate and three equivalents of ferrocenecarboxaldehyde with pyrrole in the presence of trace acid. The drawback with this approach is the number of side-products formed by competing aldehyde-pyrrole coupling reactions. However, following very careful column chromatography on silica gel, **III.4** was isolated in 14% yield as a purple solid. The alternative strategy involved the use of the preformed 5-ferrocenyldipyrromethane **III.3** [190] and its condensation with **III.2** and ferrocenecarboxaldehyde. Although at the first glance this may appear to be a better method, the final yield was only slightly improved to 18%, probably because of the scrambling reactions.

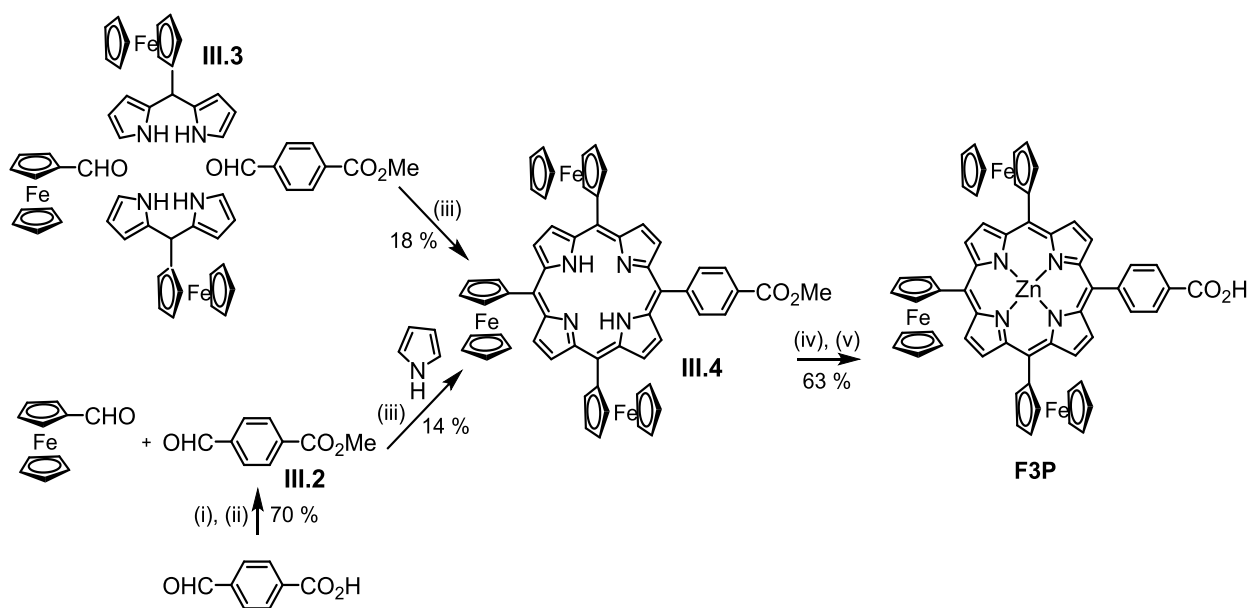


Fig. 3.2. Reagents and conditions: (i) H_2SO_4 , MeOH / CHCl_3 ; (ii) TsOH, Acetone; (iii) TFA, DDQ, DCM, RT; (iv) $\text{Zn}(\text{OAc})_2 \cdot 2\text{H}_2\text{O}$, MeOH; (v) NaOH, MeOH / H_2O / THF, reflux.

^1H NMR spectra recorded for samples of **III.4** prepared by both methods were identical. A *cis* isomer of bisferrocenyl porphyrin was isolated as well, namely 5,10-bisferrocenyl-15,20-bis(4-methyl benzoate)porphyrin **III.5** according to ^1H NMR spectrum (Annexe 6). The final two reactions of incorporation of zinc(II) into the porphyrin ring to obtain intermediate **III.6** and ester group hydrolysis worked in high yields to afford the desired compound Zn(II) 5,10,15-trisferrocenyl-20-(4-carboxyphenyl) porphyrin **F3P**. The recently reported meso-ferrocenyl porphyrin analogues of **F3P**, were prepared by Rochford et al. [123] for evaluation as sensitizers in DSSC. The group used a somehow different approach in order to obtain Zn(II) 5-ferrocenyl-10,20-bistolyl-15-(4-methyl benzoate)porphyrin, Zn(II) 5-ferrocenyl-10,15,20-tris(4-methyl benzoate)porphyrin and Zn(II) 5,15-bisferrocenyl-10,20-bis(4-methyl benzoate)porphyrin.

Full characterisation of **F3P** by ^1H , $^{13}\text{C}\{^1\text{H}\}$ and DEPT-135° NMR spectra, as well as two-dimensional homo- ($^1\text{H}/^1\text{H}$ COSY-45°) and heteronuclear ($^1\text{H}/^{13}\text{C}$ HSQC and HMBC) correlation spectra (Annexe 7) corroborated the A_3B structure of porphyrin ring (δ : 9.86 ppm - 4H, β -pyrrole-Fc-Fc; 9.77 ppm - 2H, β -pyrrole-Ph-Fc; 8.52 ppm - 2H, β -pyrrole-Ph-Fc), the presence of three ferrocene units of two slightly different form (example δ : 4.13 - 5H, CpH'; 4.11 - 10H, CpH'') and 4-carboxyphenyl moiety (δ : 8.36 - 2H, *m*-Ph; 8.22 - 2H, *o*-Ph; 167.75 - $\text{C}_{\text{carboxylic acid}}$) (Figure 3.3). The IR spectrum for **F3P** displayed a strong stretching absorption at 1690 cm^{-1} (C=O) and a broad peak at 3090 cm^{-1} (O-H) in agreement with the presence of the carboxylic acid group. The MALDI mass spectrum in positive ion mode (Figure 3.3) for **F3P** contained a cluster of peaks at $m/z = 1044$ assigned to the molecular ion and a theoretical isotopic

pattern which agreed well with the observed data. There were additional peaks at $m/z = 923$ for the degradation product resulted from benzoic acid unit loss and $m/z = 1061$ which can be assigned to a deprotonated water adduct.

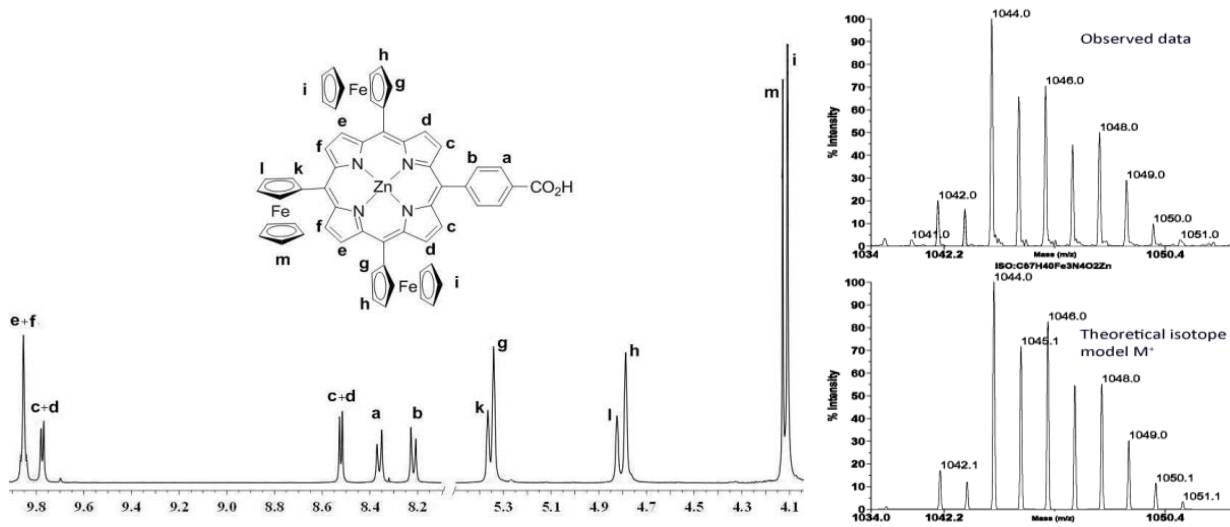


Fig. 3.3. Selected partial 400 MHz ¹H NMR spectrum in DMSO-d₆ with peaks assignment (left) and MALDI-TOF Mass spectrum showing the observed and theoretical [M]⁺ pattern (right) for Zn(II) 5,10,15-trisferrocenyl-20-(4-carboxyphenyl) porphyrin **F3P**

3.1.2. DFT molecular orbital calculations

Previous work by Nemykin and co-workers [191] determined the frontier molecular orbital picture for free-base tetraferrocenyl porphyrin derivatives. Part of this study was to rationalize the observation that as the number of ferrocene groups in meso(ferrocenyl) containing porphyrins increased there are subtle shifts in both the Q- and B-bands in their absorption spectra. Part of the reason is introduction of HOMOs associated with the ferrocene units into the overall MO picture and potential charge transfer contributions to the absorption envelope. Considering these previous findings we considered it was prudent to map out a clear MO picture for **F3P**. For a typical calculation the ground-state structure of **F3P** was modelled using a semi-empirical (AM1) method. The obtained structure was then refined further using DFT (B3LYP) and the 3-21G* and 6-31G(d) basis sets. Prior work by Slota et al. [192] suggested that B3LYP with the LanL2DZ basis set is more conducive to collecting accurate structures for large metalloporphyrin molecules. The alternative approach employed by Nemykin et al. [193] was the Perdew nonlocal correlation function (B3PW91). Hence, calculations were re-run under more complex basis sets for comparison purposes (Table 3.1).

Table 3.1. Comparison of selected bond lengths calculated by DFT for **F3P**.^a

Method	Average Zn–N bond Length / Å	Average Fe–C bond length / Å
B3LYP 3-21G*	1.98	2.05 (free); 2.04 (meso)
B3LYP 6-31G(d)	2.03	2.06 (free); 2.06 (meso)
B3LYP LanL2DZ	2.06	2.13 (free); 2.13 (meso)
B3PW91 6-31G(d)	2.02	2.03 (free); 2.04 (meso)

^a Calculated using the programme Gaussian 03.

There is a definite increase in the Zn–N bond lengths (ca. 2–4%) by changing the basis set from 3-21G* to 6-31G(d) to LanL2DZ and to B3PW91 6-31G(d); values for the latter three methods are more consistent with crystallographically determined bond lengths (Zn–N 2.04 Å). It should be noted that the average Fe–C (ferrocene) bond lengths calculated using B3LYP (LanL2DZ) are longer than corresponding values returned from the other methods. The average crystallographically determined Fe–C bond length for ferrocene is 2.05 Å. The molecular picture for **F3P** is only slightly modified depending on the method. A representative structure is shown in Figure 3.4. Consistent with previous calculations is the observed “bowing” of the porphyrin ring (Annexe 8). In addition, the ferrocene units are twisted relative to the plane of the porphyrin ring because of the unfavourable steric interactions. The barrier to rotation of the ferrocene group around the connector meso axis has been previously estimated to be in the order of 10.4 kcal mol⁻¹, and so in solution ferrocene internal rotation is very likely [194].

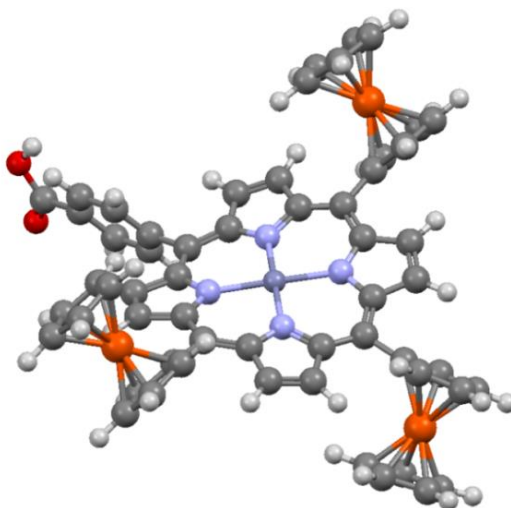


Fig. 3.4. Energy-minimised computer calculated structure for **F3P** using DFT (B3PW91) and a 6-31G(d) basis set.

From the four calculations the three most consistent molecular orbital diagrams were obtained using B3PW91 6-31G(d), B3LYP 6-31G(d) and B3LYP LanL2DZ; in the latter the

basis set core electron are frozen (48 for **F3P**). The frontier molecular orbital picture calculated by B3LYP 3-21G* was slightly different to the other three cases. We have taken the MO picture from the B3PW91 6-31G(d) calculation (Figure 3.5) to be more comprehensive, and collected in Annexe 9 are MO pictures from the other three calculations. The HOMO is predominantly localised on the three ferrocene moieties, whereas the HOMO-1 is exclusively porphyrin based. The MOs HOMO-2 to HOMO-6 are entirely ferrocene centred. It turns out that the LUMO and LUMO+1 are degenerate and porphyrin-based π^* orbitals in agreement with Gouterman's four orbital model [195]. Both orbitals are well separated in energy from the LUMO+2 which resides on the *meso* benzoic acid group. Very crudely the HOMO-LUMO gap represents ferrocene-to-porphyrin charge transfer, the energy difference being 2.59 eV (479 nm).

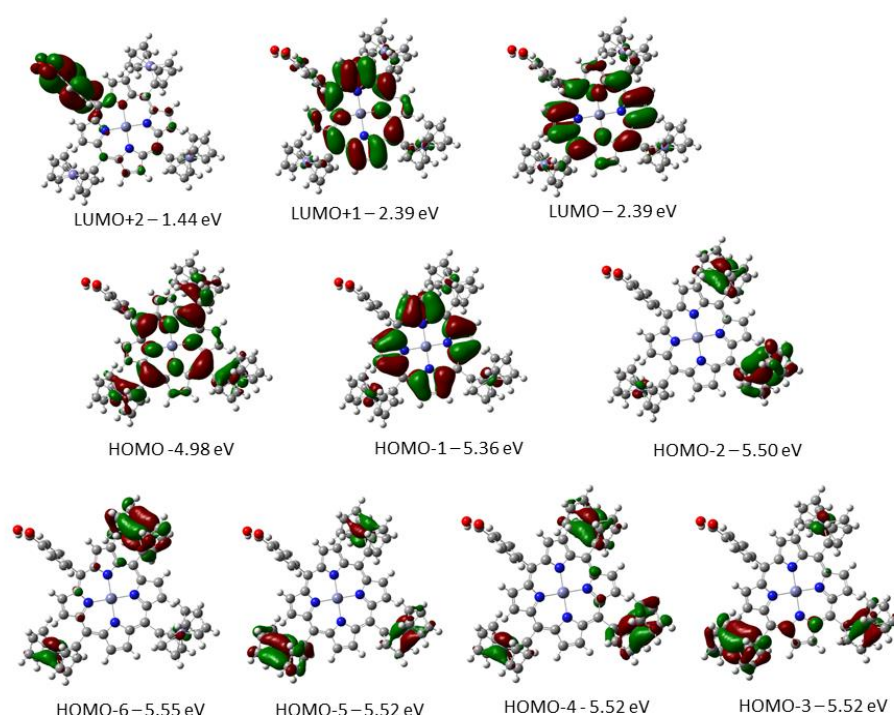


Fig. 3.5. Selected molecular orbitals pictures and their corresponding energy for **F3P**, calculated by DFT (B3PW91) and using a 6-31G(d) basis set.

3.1.3. Electrochemistry and absorption spectroscopy

The redox behaviour of **F3P** was measured by cyclic voltammetry in dry THF using 0.2 M TBABF₄ as background electrolyte. DCM afforded rather poor results probably because of solubility problems. The cyclic voltammogram (Figure 3.6) reveals redox processes associated with both the porphyrin and ferrocene groups. On the oxidation side of the CV a clear quasireversible wave is observed at +0.04 V vs. Fc⁺/Fc, which is associated with redox at the ferrocene sites. No splitting of the wave is seen but the peak's separation difference of 180 mV

would suggest that there are a series of overlapping waves. At a more positive potential an irreversible wave is observed at +1.1 V vs. Fc^+/Fc which is porphyrin-based oxidation. Upon scanning to negative potentials two quasi-reversible one-electron waves are seen at -1.87 V and -2.20 V vs. Fc^+/Fc and are again associated with redox at the porphyrin site. The overall redox behaviour for **F3P** is consistent with previous work carried out on ferrocenyl–porphyrin derivatives [196]. It is worth noting that the computer calculated difference in energy between oxidation of a ferrocene (HOMO) and porphyrin (HOMO-1) is only 380 mV (Figure 3.5). The much larger value found electrochemically (ca. 1 V) is rationalised, in part, by the large electrostatic repulsion created by a tri-positive charge so close to the porphyrin core.

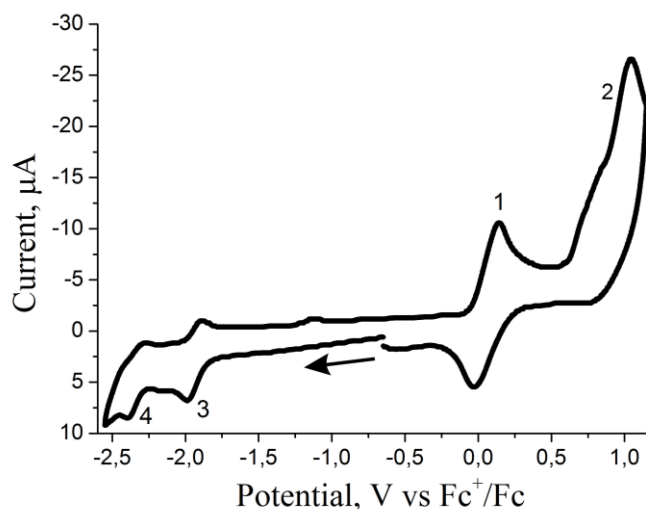


Fig. 3.6. Cyclic voltammogram for **F3P** in THF (0.2 M TBABF_4) at a glassy carbon working electrode . Scan rate = 50 mV s^{-1} .

The room temperature UV-Vis absorption spectra for metal-free tris-Fc-porphyrin **III.4** and *cis*-bis-Fc porphyrin **III.5** in CHCl_3 are given in Figure 3.7 with relevant parameters in Table 3.2. Interestingly, the absorption profile of porphyrins is severely perturbed by changing the *meso*-substituents. A general red-shift of absorption bands (from 3 to 21 nm) for **III.5** compared to **III.4** was observed. This effect was previously described by Nemykin et al. [191] for phenyl substituted (C_6H_5) analogues, resulting from increased non-planarity of porphyrin core when ferrocenyl substituents were added. At the same time the higher coplanarity was found to slightly increase the absorption intensity of Soret band. However, in our case a much stronger absorption was observed for *cis*-bisferrocenyl-bis(4-methylbenzoate) porphyrin **III.5** compared to **III.4** (~1.6 times higher extinction coefficient), while the C_6H_5 analogues showed almost identical absorption intensity. The planarity argument is no longer valid as Nemykin showed a strong dependence of NH proton chemical shift on the porphyrin ring non-planarity, and the ^1H NMR spectra for **III.4** and **III.5** showed NH shifts similar with C_6H_5 analogues. It could be argued that

the push-pull framework, created by Fc donor and benzoate acceptor, results in a strong hyperchromic effect when a symmetrical *cis* configuration is adopted, so that the two Fc donor units are on the one side of molecule and the electron withdrawing benzoate units on the other. At the same time, the intensity of both Q bands only slightly increased.

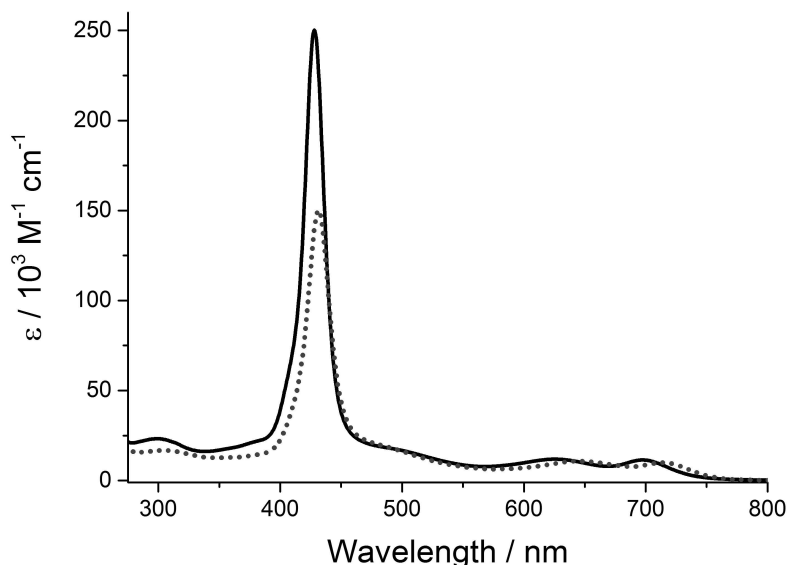


Fig. 3.7. Room temperature UV-Vis absorption spectrum for **III.4** (dotted line) and **III.5** (solid line) in CHCl_3 .

Table 3.2. UV-Vis absorption parameters for **III.4** and **III.5** in CHCl_3 .

Compound name	N-band, nm (ϵ , $10^3 \text{ M}^{-1} \text{ cm}^{-1}$)	Soret band, nm (ϵ , $10^3 \text{ M}^{-1} \text{ cm}^{-1}$)	Q-band, nm (ϵ , $10^3 \text{ M}^{-1} \text{ cm}^{-1}$)
III.4	304 (17)	431 (151), 500 (sh)	646 (11), 714 (10)
III.5	298 (22)	428 (235), 500 (sh)	625 (11), 697 (11)

The room temperature electronic absorption spectrum for **F3P** in chloroform is shown in Figure 3.8. The spectrum comprises a strong Soret B-band at 431 nm ($1.6 \times 10^5 \text{ M}^{-1} \text{ cm}^{-1}$) and a much weaker Q-band at 661 nm ($1.7 \times 10^4 \text{ M}^{-1} \text{ cm}^{-1}$), typical of a divalent metalloporphyrin. The weak band at 310 nm ($2.1 \times 10^4 \text{ M}^{-1} \text{ cm}^{-1}$) may be assigned to the lesser discussed porphyrin N-band. The Soret band also contains a shoulder in the region of ~ 490 nm which is ascribed by Nemykin et al. to predominantly ferrocene-to-porphyrin charge transfer. Certainly this interpretation is consistent with the computer calculated energy-gap discussed previously in this work. Note that the absorption in the visible spectrum of the porphyrin **F3P** is improved in the region between Soret and Q-bands compared to the tetra-phenyl porphyrin analogue, due to additional absorption in the Soret band shoulder.

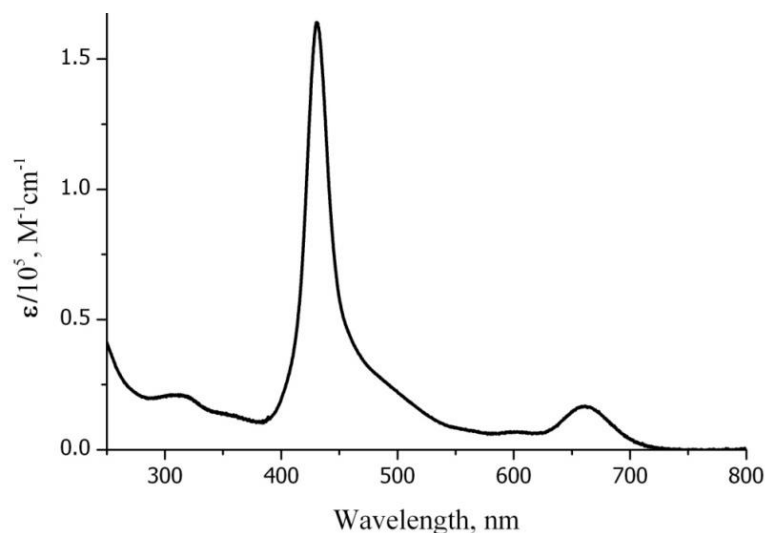
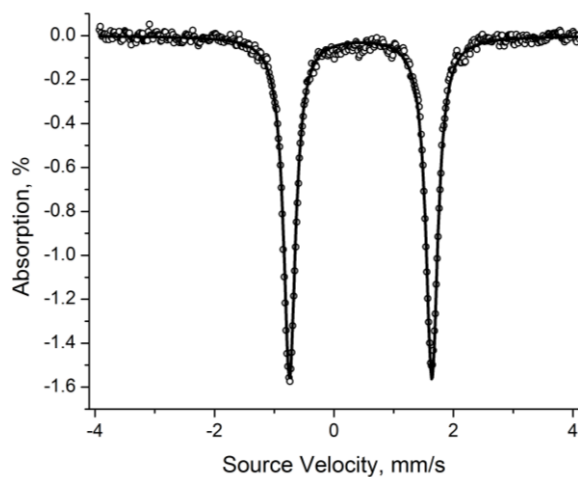


Fig. 3.8. Room temperature UV-Vis absorption spectrum for **F3P** in chloroform.

3.1.4. ^{57}Fe Mössbauer spectroscopy

The room temperature Mössbauer spectrum for **F3P** with pertinent parameters is shown in Figure 3.9, along with the data for the reference compound zinc(II) tetraferrocenylporphyrin (**ZnTFP**) [197].



Comp.	$\delta^{*,**}$, mm/s	ΔE_Q^{**} , mm/s	Γ , mm/s
ZnTFP^a	0.45	2.35	na
F3P	0.44	2.35	0.27
Fc	0.45	2.39	0.29

Fig. 3.9. Left: Room temperature ^{57}Fe -Mössbauer spectrum for **F3P** showing the characteristic doublet pattern. Right: Experimental Mössbauer parameters for **F3P** and reference compounds at room temperature. * - IS and QS values are given relative to $\alpha\text{-Fe}$ at RT. ** - the standard deviation for values of IS and QS is ± 0.02 mm/s.

^a Reference compound as discussed in the text taken from reference [197].

The isomer shift δ and large quadrupole splitting ΔE_Q for the clear doublet are typical for low-spin iron (d^6) ferrocene derivatives. The comparison of **F3P** and parent ferrocene data shows

that the porphyrin core has no major influence on the electron density at the iron nucleus, despite the close proximity of the ferrocene and porphyrin groups. The presence of only one doublet and the narrow line width (Γ), indicates that the three ferrocene moieties are essentially identical. It is worth noting that no ferrocenium assignable signals were observed, excluding partial oxidation of ferrocene. Altogether, Mössbauer data suggest that at least in the ground state and solid state the compound **F3P** behaves as if it comprises isolated ferrocene and porphyrin subunits.

3.1.5. Dye Sensitised Solar Cell performance

Since the Γ/I_3^- electrolyte couple does not have enough driving force to reduce the ferrocenium, photovoltaic experiments were conducted in a cell using $\text{Co}^{(\text{II/III})}\text{tris}(4,4'\text{-dimethoxy-bipyridine})\text{perchlorate}$ ($E^0 = -0.26 \text{ V vs. Fc}^+/\text{Fc}$). The electrolyte consisted of 0.1 M $\text{Co}^{(\text{II/III})}$ complex, 0.1 M 4-tert-butylpyridine, 0.2 M, tert-butyl ammonium perchlorate and 0.015 M NOPF_6 in propylene carbonate as solvent. The plot of photocurrent density versus voltage (under standard AM 1.5 global sunlight at 1000 W m^{-2} and a temperature of 298 K) for **F3P** is shown in Figure 3.10.

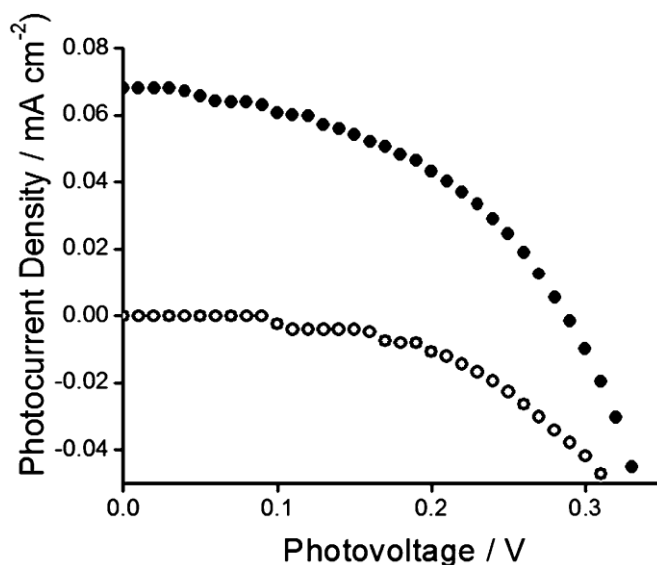


Fig. 3.10. Example of an I–V curve (\circ = dark, \bullet = light) for a **F3P** based dye sensitised solar cell using $[\text{Co}(\text{II}) (4,4'\text{-dimethoxy-2,2'-bipyridine})_3] (\text{ClO}_4)_2$ 0.1 M, 4-tert-butylpyridine 0.2 M, tert-butyl ammonium perchlorate 0.1 M and NOPF_6 0.015 M in propylene carbonate. $V_{\text{OC}} = 0.28 \text{ V}$ and $J_{\text{SC}} = 0.068 \text{ mA cm}^{-2}$.

The experiment was repeated in darkness and proved the photovoltaic nature of the effect. The short circuit current density (J_{SC}) was found to be 0.068 mA cm^{-2} , the open circuit voltage (V_{OC}) was 283 mV, the fill factor (FF) was 0.42 and the power conversion efficiency

was evaluated to be 0.0081%. Each of these values is extremely low and **F3P** can be considered a poor sensitizer for a DSSC.

3.1.6. Pump-probe spectroscopy

The excited-state property for **F3P** was elucidated using femtosecond pump-probe spectroscopy in MeCN and THF. The latter solvent was found to be much better and avoided unnecessary precipitation of the material during data collection. The compound was excited with a 70 fs laser pulse at 480 nm which almost exclusively populates the S_2 (Soret) state for the porphyrin. Time resolved transient absorption spectra with compensated group velocity dispersion are presented in Figure 3.11, along with decay profiles at a few selected wavelengths. The measurements were also fitted globally to three and four exponential models. Although a four exponential fit gave roughly a 15% improvement of the sigma value it mainly resulted in a very short-lived component (80 fs) which arises most probably from “non-exponential” fast thermal relaxation and will not be discussed further.

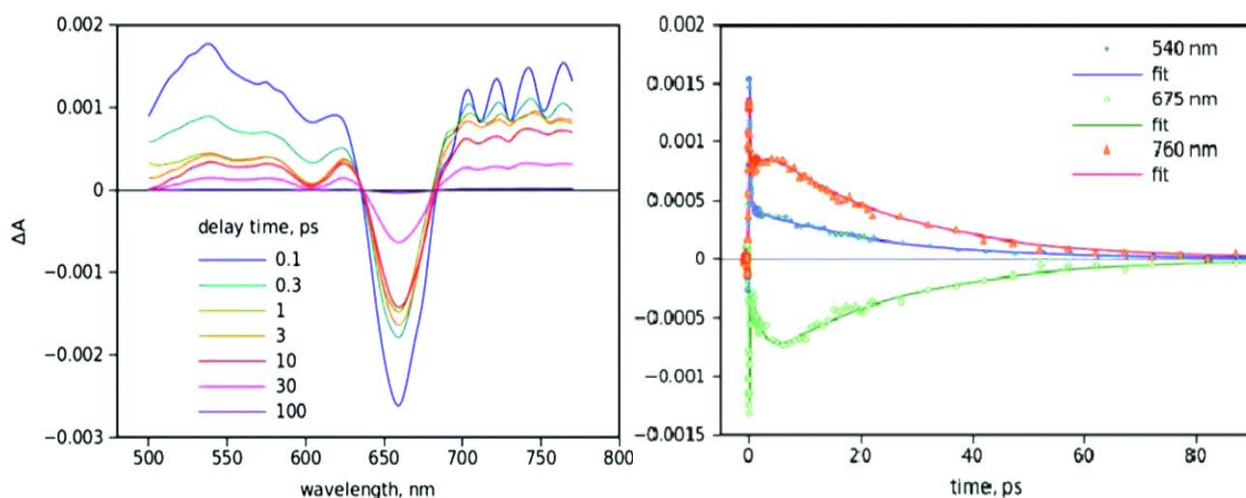


Fig. 3.11. Selected transient absorption spectra recorded after excitation of **F3P** in THF with a 70 fs laser pulse delivered at 480 nm (left). Transient absorption decay profiles of **F3P** in THF at selected wavelengths (right). Symbols are measured data and lines are fit curves.

There is an almost instantaneous bleach in the region around 660 nm corresponding to the Q-bands of the porphyrin. To the low energy side of this bleach is a broad profile which is assigned to the zinc-porphyrin radical anion [198]. It is not possible to identify the ferrocenium ion because of its low molar absorption coefficient, but it must be produced as part of the charge transfer process to account for the anion. The results from a global fit of the spectroscopic data

are presented in Figure 3.12, and shows the decay component spectra (curves with symbols) and time-resolved transient spectra right after the excitation (at 0 ps) and after fast relaxation with 0.19 ps time constant (at 1 ps). An interesting feature is that initial bleaching of the Q-band at 670 nm recovers by roughly half with a time constant of 0.19 ps, but then the bleaching increases by one third with a time constant 2.5 ps before complete recovery with a time constant of 24 ps. The interpretation of the results is not straightforward, though it is noticeable that the 2.5 ps component does not affect the spectrum much outside the Q-band region. Tentatively this component can be attributed to conformation changes associated with the charge separated state. The fast time constant is presumably formation of the CS state. The S₂ to S₁ conversion in zinc tetraphenylporphine is, depending on the solvent, on the order of 1–3.5 ps. There are reports of energy and electron transfer from the S₂ state of zinc porphyrin adducts [199]. Considering the rate for charge separation we cannot discount that the process is competing with internal conversion. The charge recombination process, though slower by comparison, is still extremely rapid and reforms the ground state in $\tau = 24$ ps. This measured value is very similar to that reported by Nadochenko and co-workers for a free-base porphyrin analogue [64]. The presence of the zinc(II) ion appears to have no real effect on the charge recombination process.

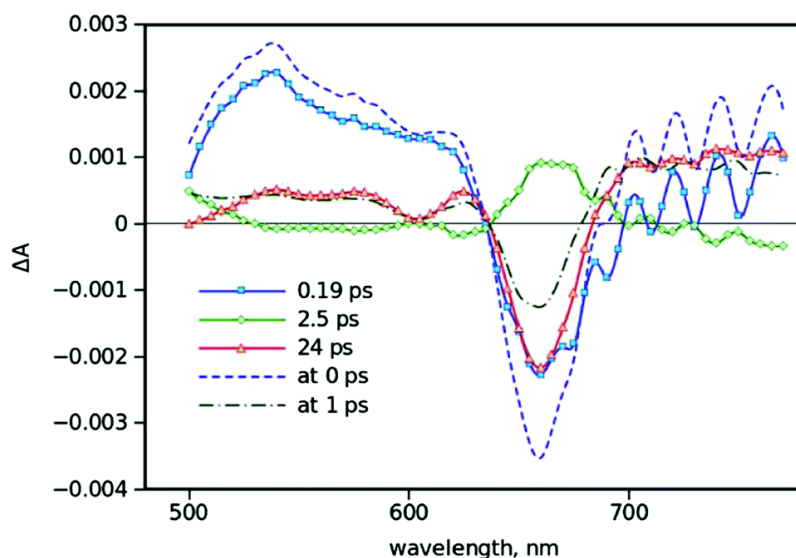


Fig. 3.12. Decay component spectra (lines with symbols) and time-resolved spectra at 0 and 1 ps delay time for **F3P** in THF.

The behaviour for **F3P** attached to TiO₂ was also measured and compared to a control compound containing phenyl groups instead of the ferrocene moieties (**ZnTTP**). Time-resolved transient absorption spectra are presented in Annexe 10, and except for a relatively weak long-lived component the results are similar to those obtained in THF solution. The rather good

agreement between the transient absorption responses for **F3P** in solution and attached to TiO_2 indicates that charge separation in the molecule is not affected by the presence of TiO_2 surface. Another significant finding is electron injection from the porphyrin anion to the TiO_2 does not take place in the lifetime of the CS state (29 ps). It is very noticeable (Figure 3.13) that the minor long-lived component has clear bleaching of the porphyrin Q-band and probably comes from direct injection of electron from the photo-excited porphyrin into the TiO_2 . This is the only indication of possible electron injection and its low intensity is in good agreement with the low efficiency of the DSSC.

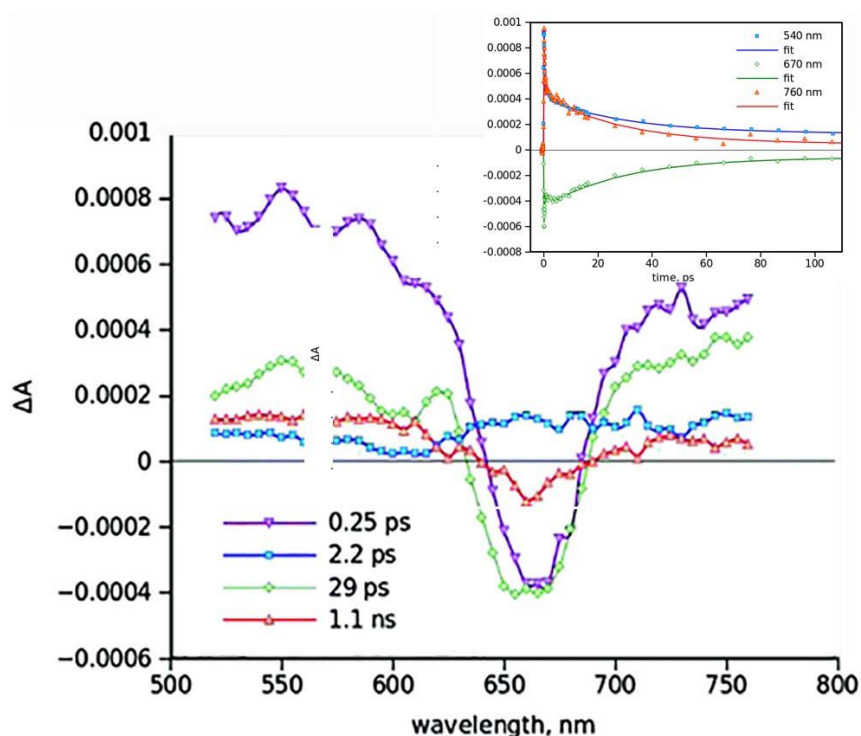


Fig. 3.13. Decay component spectra obtained from global fit of transient absorption data for **F3P** on TiO_2 . Insert shows transient absorption decay profiles at three selected wavelengths. Symbols are experimental data and curves are the data fits.

The decay component spectra for **ZnTPP** attached to TiO_2 are very different to those shown in Figure 3.13 (see Annexe 11). The fast component, 0.13 ps, can be attributed to electron injection into the TiO_2 because of the broad negative band around 670 nm, which is assigned to the porphyrin cation. Further reshaping of the cation band takes place with a time constant of 3.1 ps and is in qualitative agreement with other similar systems. Recombination is also a “multi-exponential” process with lifetimes in the range from few tens of picoseconds to nanoseconds.

3.1.7. Evaluation of excited state deactivation for DSSC application

The excited state spectroscopic data for **F3P** attached to TiO₂ shows unequivocally that the dye is rather poor at injecting electrons into the conduction band of the semiconductor TiO₂. Generally electron injection into TiO₂ is extremely fast and in the order of 300 fs [200]. For the control compound the excited state porphyrin injects electrons in around 130 fs. Assuming this latter value is the same for **F3P**, the maximum yield of electrons into the TiO₂ conduction band is only 60%.

It is clear that injection of an electron from the photo-generated porphyrin anion (Figure 3.1) into the TiO₂ conduction does not take place. One possible reason for this is the rather strong coupling between the electron and hole due to the short distance between the donor and acceptor. The strong electronic coupling is also in fitting with the strong ground state charge transfer character which results in the charge transfer absorption band. This interpretation would mean that the CS state is not a “real” radical ion pair, but rather an electron density redistribution. It is noted that the driving force is very favourable for anion injection and estimated from electrochemistry data ($E_{\text{red}} = -1.5$ V vs. NHE) and the conduction band energy for TiO₂ (-0.5 V vs. NHE) to be around 1.0 eV. There is the possibility that the reduction potential for the porphyrin is altered by its attachment to the TiO₂ and the driving force is much smaller.

Considering that direct electron injection from the porphyrin excited state (process 3, Figure 3.1) occurs, it is very probable that hole transfer to the appended ferrocene (process 1, Figure 3.1) also takes place to generate the ferrocenium ion. Given that the Co²⁺/Co³⁺ couple for the cobalt bipyridyl- and terpyridyl-based electrolytes have redox potentials of -0.21 V and -0.32 V vs. Fc⁺/Fc, [201] then again it is feasible that the redox shuttle process should proceed in a DSSC incorporating **F3P**.

Other contributing factors to the very low photocurrent are twofold. One evident problem is the close proximity of the ferrocene groups to the semi-conductor surface which will facilitate charge recombination. Even the presence of a blocking layer on the TiO₂ surface may not be sufficient to prevent back electron transfer. There is the additional argument that ferrocenium / ferrocene may not be conducive for coupling to the Co^(II/III) electrolyte redox relay because of slow electron exchange kinetics [202].

3.2. Electrocatalytic hydrogen production using Palladium(II) and Copper(II) *meso*-tetraferrocenyl porphyrin complexes

As it was previously shown [203], ferrocene can operate as three electron donor for the four-electron reduction of O_2 by using an iron^(III)(tetraferrocenyl)porphyrin; a triazole moiety acts as a bridge between the porphyrin and ferrocene groups and by hydrogen bonding has a role in proton transfer pathway into the active site of catalyst. Keeping this in mind we synthesized the palladium(II) (**PdTFP**) and copper(II) (**CuTFP**) tetraferrocenylporphyrin complexes (Figure 3.14) for the intention of focussing on electrocatalytic CO_2 reduction.

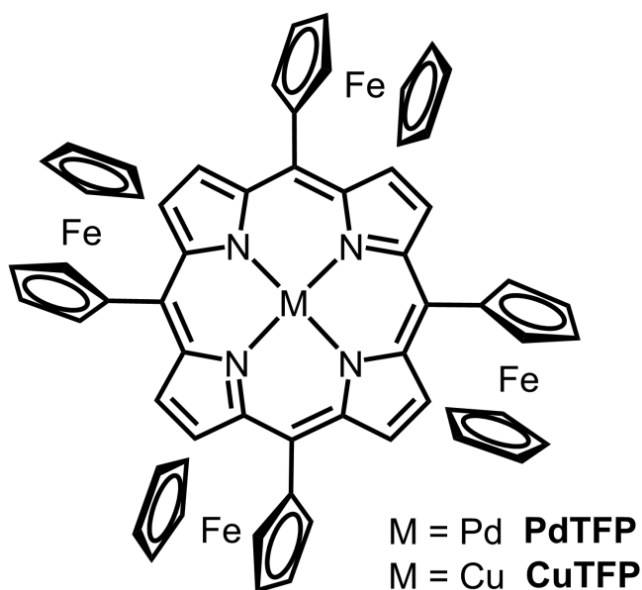


Fig. 3.14. Illustration of porphyrin compounds discussed in the text.

Even though the compounds were found not to be active for this reaction, they proved to be a reasonable electrocatalyst for proton reduction into molecular hydrogen when using trifluoroacetic acid (TFA) and triethylamine hydrochloride (TEAHCl) as proton source. The main point to note is that the copper complex of tetraphenylporphyrin (**TPP**) was reported to be a non-active hydrogen evolving catalyst (with TEAHCl or CHF_2COOH), and we found that both **CuTPP** and **PdTPP** are less active than their ferrocene analogue when using TFA as acid source, and inactive in the presence of TEAHCl. The appended ferrocene groups appear to be extremely important in the catalytic process. The enhancement in electrocatalytic reactivity is assigned to increase of the electron density on the periphery of the porphyrin ring, while the central metal has shown to play a role in the stabilization of negative charge on the pyrrole unit, which jointly contribute to second proton addition to the *meso*-tetraferrocenyl porphyrin anion **TFPH⁻**.

3.2.1. Synthesis of Palladium(II) and Copper(II) *meso*-tetraferrocenyl porphyrin

The free-base *meso*-tetraferrocenylporphyrin **H₂TFP** was prepared by the standard literature procedure [204]. The palladium(II) tetraferrocenylporphyrin and copper(II) derivative [197] were obtained by complexation of **H₂TFP** with palladium(II) acetate or copper(II) acetate in moderate yields. The careful chromatography purification procedure is one reason for the low yield. The ¹H NMR spectrum for **PdTFP** (Figure 3.15) showed a clear singlet for the β-protons for a symmetrical porphyrin at 9.67 ppm (8H) and two apparent triplets at 5.27 (8H) and 4.74 ppm (8H) together with a singlet at 3.98 ppm (20 H) typical for a mono-substituted ferrocene. Integration of proton signals is consistent with a ferrocene / porphyrin four to one ratio. The lack of NH signal (-0.5 ppm) associated with the free-base tetraferrocenyl porphyrin together with presence of only one Q band proved the insertion of Pd into the porphyrin ring.

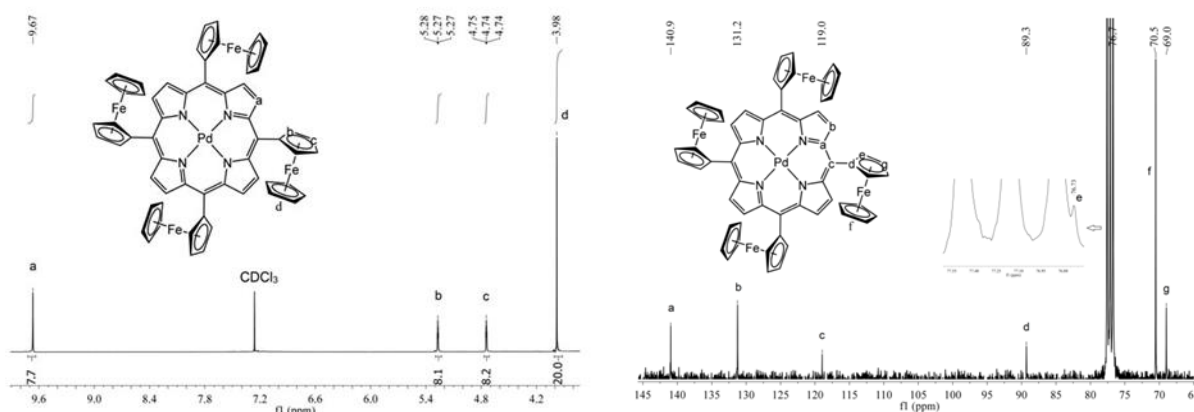


Fig. 3.15. Selected 400 MHz ¹H NMR and ¹³C{¹H}-NMR spectra and peaks assignment for **PdTFP**.

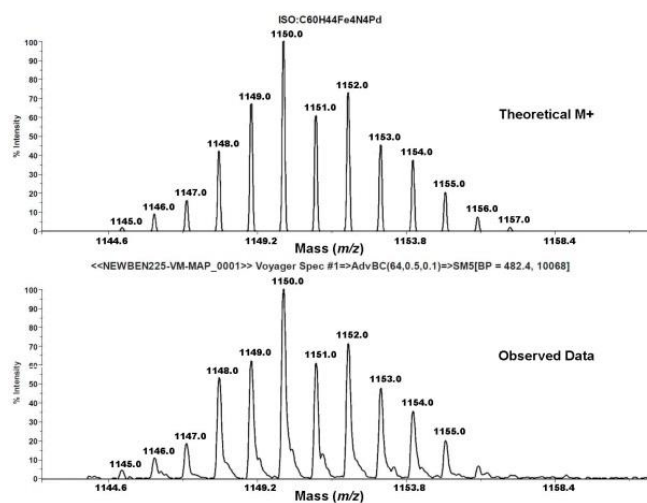


Fig. 3.16. MALDI-TOF Mass spectrum showing the observed data and theoretical [M]⁺ pattern for **PdTFP**.

The cluster of peaks at m/z 1150 in the MALDI-TOF mass spectrum corresponding to the theoretical pattern corroborated the expected structure (Figure 3.16). Similarly, the expected molecular ion pattern was found for Cu, Co and Ni analogues at m/z 1107, 1103 and 1102, respectively.

All our attempts to obtain crystals of **Pd** and **CuTFP** suitable for X-ray analysis failed [197], so that the metal-free analogue was chosen as the closest comparative model. The structure of **H₂TFP** repeatedly [191] obtained in this work (Figure 3.17) confirmed its identity. The compound crystallized in tetragonal space group P-42₁/c. The porphyrin macrocycle is strongly “bowed” while the ferrocene moieties are twisted relative to the porphyrin ring plane by 35.22°. The ferrocene cyclopentadiene planes form an angle of 5.15° and are almost eclipsed. The two NH protons have 2 possible locations with 50 % probability.

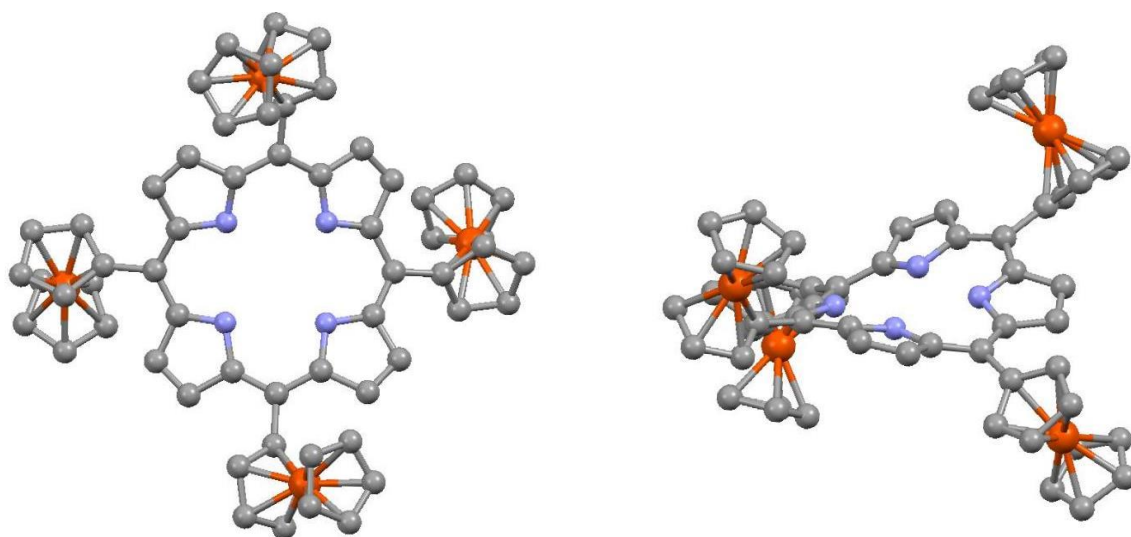


Fig. 3.17. Crystallographically determined molecular structure for **H₂TFP**: left – plane view, right – side view.

3.2.2. ⁵⁷Fe Mössbauer spectroscopy

The room temperature Mössbauer spectrum for **PdTFP** is shown in Figure 3.18 with relevant parameters collected in Table 3.3. Data pertaining to **PdTFP**, **CuTFP** and reference compounds **H₂TFP**, **ZnTFP**, **F3P** and ferrocene are also included for comparison purposes. The isomer shift values are very close for all the compounds; any influence from the porphyrin ring, metal ion or other meso-substituent on the ferrocene electronic configuration is negligible. The quadrupole splitting for **Cu** and **PdTFP** is mostly similar, in the error limit, compared with parent Fc. Still a permanent tendency of a reduced quadrupole splitting for a large series of ferrocene-porphyrins (both from this paper and literature data) may suggest that there is some electron donation onto the porphyrin ring, which would result in increased symmetry of the

electron environment at the iron nucleus. The presence of only one clear large doublet proves no ferrocenium is present in the complex which might arise from oxidation of the sample.

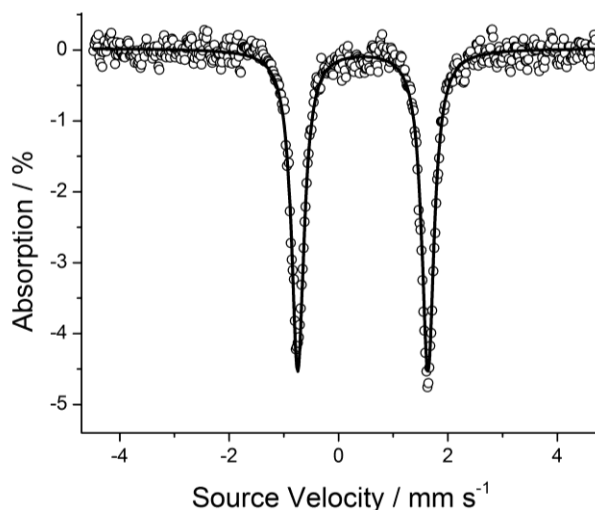


Fig. 3.18. Room temperature ^{57}Fe Mössbauer spectrum for **PdTFP**.

Table 3.3. Experimental Mössbauer parameters for **PdTFP** and reference compounds.

Compound	Temp, K	Isomer Shift $\delta^{*,**}$, mm/s	Quadrupole Splitting ΔE_Q^{**} , mm/s
PdTFP	7 K	0.55	2.39
	293 K	0.44	2.34
CuTFP	293 K	0.45	2.35
ZnTFP ^a	293 K	0.45	2.38
F3P	293 K	0.44	2.35
H₂TFP ^a	293 K	0.45	2.35
Fc	293 K	0.45	2.39

* - Values are given relative to α -Fe at RT.

** - the error limit for values of IS and QS is ± 0.02 mm/s.

^a Data taken from reference [197]

3.2.3. Electrochemistry and absorption spectroscopy

The redox behaviour for **PdTFP** was measured by cyclic voltammetry in dry DMF and DCM using 0.2 M TBABF₄ as background electrolyte. The cyclic voltammogram in DMF consists of redox patterns for a porphyrin and ferrocene moieties (left picture of Figure 3.19). Upon scanning to positive potentials a quasi-reversible wave at +0.08 V vs. Fc⁺/Fc is seen,

which is associated with redox at the ferrocene sites. No splitting of the wave is evident but the peak's separation difference of 150 mV would suggest that there are series of overlapping waves. At a more positive potential an irreversible wave is observed at +0.93 V vs. Fc^+/Fc and is a porphyrin-based oxidation. The shift to more positive potential compared to other porphyrins is explained by the presence of a four-positive charge which makes the porphyrin more difficult to oxidize. Scanning to such a potential does not remove the reversibility of the ferrocene couple but give rise to a new wave at -0.38 V vs. Fc^+/Fc which probably results from the chemical modification of the five-charged specie. The reduction side of the voltammogram shows two quasi-reversible one-electron waves at -1.72 V and -2.21 V vs. Fc^+/Fc and are again associated with redox at the porphyrin site. The use of DCM as solvent results in several changes to the redox processes (Annexe 12). The reversibility of the first reduction wave is removed and shifted to a much more negative potential at -2.06 V vs. Fc^+/Fc . The second reduction wave cannot be seen as it is beyond the solvent potential window. The ferrocene is slightly easier to oxidize in DCM, half-wave potential being shifted to -0.05 V vs. Fc^+/Fc , while the oxidation potential for the porphyrin is shifted to +1.05 V vs. Fc^+/Fc and the redox couple is no longer reversible. Presumably the low solubility of multicharged species in DCM could cause adsorption / desorption processes generating non-faradaic currents. The overall redox behaviour for **PdTFP** is consistent with previous work carried out on ferrocenyl-porphyrin derivatives. The electrochemistry of **CuTFP** in DCM was described before [205] showing a similar to **PdTFP** behaviour. The use of DMF as solvent gives a picture similar to Pd analogue with four processes at -2.23, -1.70, +0.08 and +0.75 V vs. Fc^+/Fc (right picture of Figure 3.19).

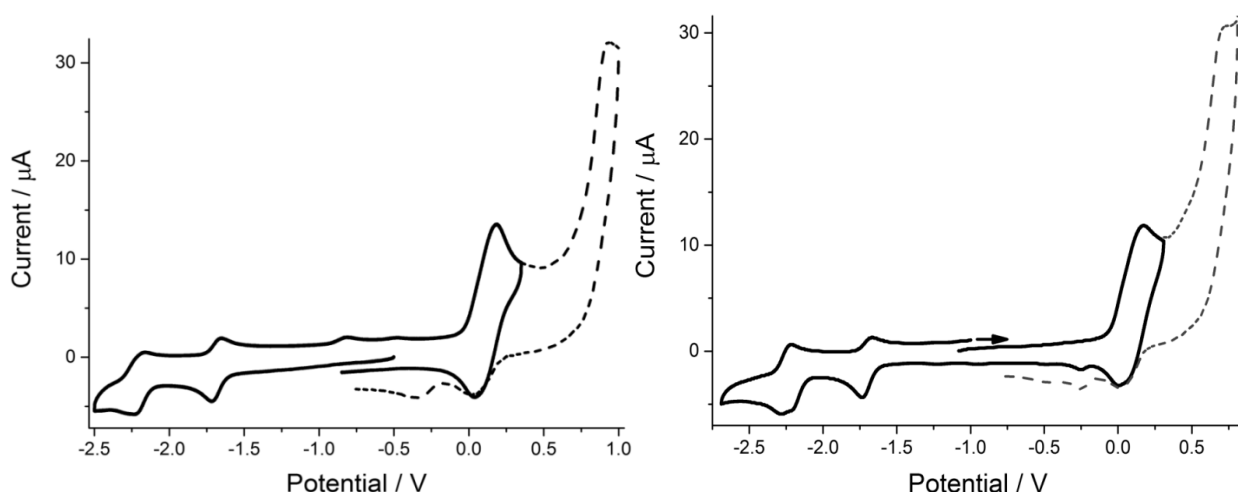


Fig. 3.19. Cyclic voltammograms recorded for **PdTFP** (left) and **CuTFP** (right) in DMF containing 0.2 M TBABF_4 vs Fc^+/Fc . The dashed line shows the additional irreversible oxidation peak when the potential window was increased.

The room temperature electronic absorption spectra for **H₂TFP**, **CuTFP** and **PdTFP** in THF are shown in Figure 3.20 with the relevant parameters in Table 3.4. Absorption parameters for metal-free porphyrin **H₂TFP** and its Co(II), Ni(II), Cu(II) and Zn(II) complexes **MTFP** in CHCl₃, taken from ref. [197], are given as well. The spectra comprise a strong Soret B-band and one weaker Q-band for metalated porphyrins, while two Q-band were found for **H₂TFP**. The weak band at the high energy side of spectrum may be assigned to the porphyrin N-band. The Soret band also contains a shoulder in the region of ~500 nm which is ascribed by Nemykin et al. to predominantly ferrocene-to-porphyrin charge transfer.

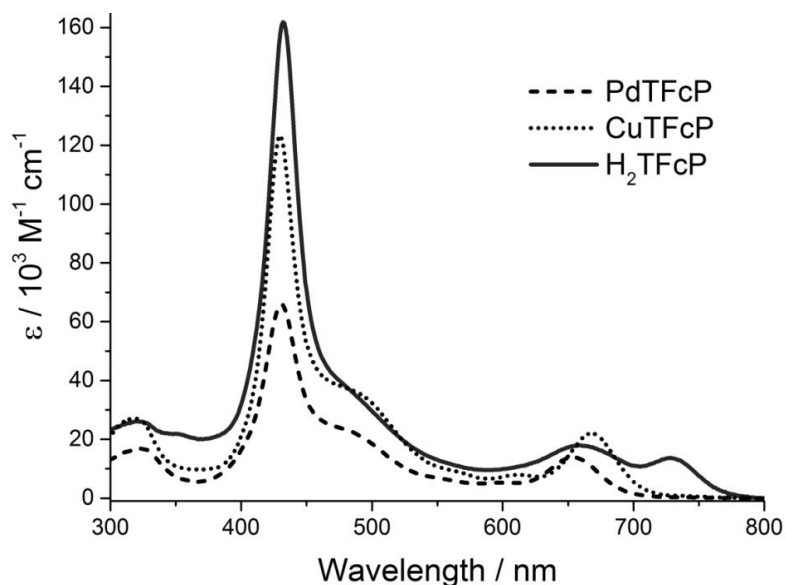


Fig. 3.20. Room temperature UV-Vis absorption spectra for **H₂TFP**, **CuTFP** and **PdTFP** in THF.

Table 3.4. UV-Vis absorption parameters for **H₂TFP**, **CuTFP** and **PdTFP** in THF and of reference compounds in CHCl₃.

Compound name	Solvent	N-band, nm (ϵ , $10^3 \text{ M}^{-1} \text{ cm}^{-1}$)	Soret band, nm (ϵ , $10^3 \text{ M}^{-1} \text{ cm}^{-1}$)	Q-band, nm (ϵ , $10^3 \text{ M}^{-1} \text{ cm}^{-1}$)
H₂TFP	THF	321 (26)	432 (162)	660 (18), 728 (14)
CuTFP	THF	319 (27)	430 (123)	668 (22)
PdTFP	THF	324 (17)	431 (66)	654 (14)
H₂TFP^a	CHCl ₃	na	434 (121)	661 (17), 726 (15)
CuTFP^a	CHCl ₃	314 (52)	430 (202)	669 (29)
ZnTFP^a	CHCl ₃	320 (34)	435 (143)	681 (32)
CoTFP^a	CHCl ₃	320 (67)	420 (134)	660 (30)
NiTFP^a	CHCl ₃	329 (51)	430 (150)	681 (39)

^a Reference compound as discussed in the text taken from reference [197].

The overall absorption of **PdTFP** is weaker than its free metal and Cu(II) analogues, especially the Soret band is more than twice reduced in intensity, while the Q-band is blue shifted compared to **CuTFP**. There is clearly a dependence on the solvent nature of the **TFPs** absorbance (CHCl_3 and THF), but no further studies were performed. Still, dipole-dipole and π - π interactions are suggested to be responsible for the observed changes [206].

3.2.4. UV-Vis spectroelectrochemistry

Perturbation of the UV-Visible spectrum of **PdTFP** was monitored using an optically transparent thin-layer electrode (OTTLE) and the spectroelectrochemistry method by application of negative and positive potentials to the platinum working electrode in THF solutions of **MTFPs**. Application of a negative potential of -1.3 V to the working electrode produced a drastic decrease in the Soret band and the appearance of a red-shifted broad band. The Q-band almost fully disappeared and three new weak and broad bands appeared at 750, 875 and 1035 nm (Figure 3.21). The N-band is blue-shifted by 35 nm and there is a concomitant three-fold increase in its intensity. The spectrum is typical for a porphyrin mono-anion **MTFP**⁻ [198] so the first reduction process is porphyrin centered.

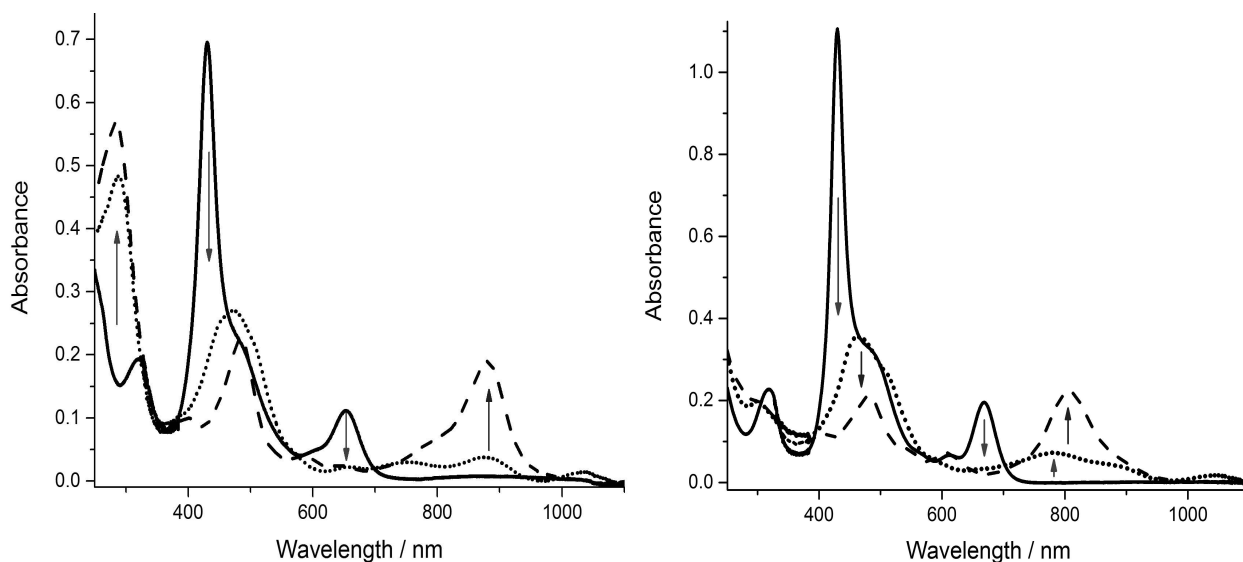


Fig. 3.21. Electronic absorption spectra for **PdTFP** (left) and **CuTFP** (right) in THF: at the start (solid line) and after reduction at -1.3 V (dotted line) and -1.7 V (dashed line).

Further reduction at -1.7 V resulted in a narrowing and slight decrease in the Soret band. In the low-energy side of the spectrum is witnessed a substantial increase in the absorption at

880 nm. There is also a slight increase in intensity of the N-band. The formation of the porphyrin dianion **MTFP**²⁻ would result in disappearance of the near-IR bands, but a similar strong band at 825 nm was reported to correspond to the Zn(II) tetraphenylphlorin monoanion obtained both by chemical [198] and electrochemical reduction [207] of Zn(II) tetraphenylporphyrin, and 830 nm for a metal free tetraphenylphlorin [208]. It means that the second reduction results in formation of **MTFP**²⁻ followed by protonation to give the phlorin anion **MTFPH**⁻. Very similar results were obtained for the reduction of **CuTFP** (Figure 3.21), the main difference being the higher energy (807 nm) of the near-IR band and the lack of N-band.

The oxidation of **PdTFP** was performed in DMF / THF mixture to avoid unwanted precipitation of the tetra-positive cation (Figure 3.22). Application of a potential at +0.9 V resulted in a decrease in intensity for the entire absorption profile. It should be noted that the Soret band is slightly red-shifted and the low-energy shoulder completely disappeared. No IVCT band was observed which confirm that all four ferrocenes were oxidized. The results are consistent with the work carried out by Nemykin and co-workers on metal-free and some transition metal ferrocene-porphyrins [191]. The alteration of absorption profile was fully reversible both in the reduction and oxidation experiments.

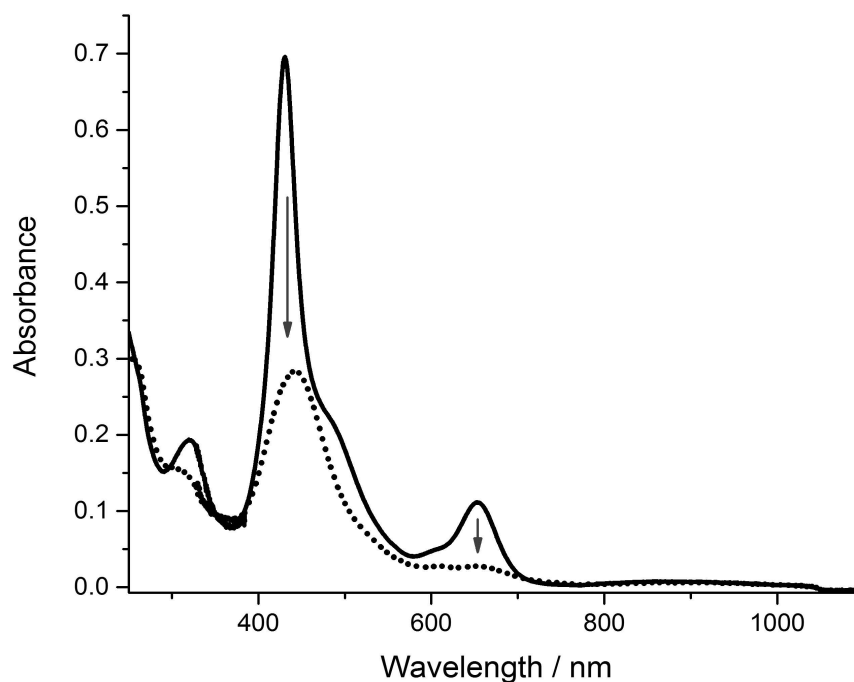


Fig. 3.22. Electronic absorption spectra for **PdTFP** in THF/DMF at the start (solid line) and after oxidation (dotted line).

3.2.5. Electrocatalytic proton reduction

Cyclic voltammetry study of catalytic process

The addition of trifluoroacetic acid as a proton source to **PdTFP** or **CuTFP** gave rise to a new catalytic wave (left picture of Figure 3.23 and Figure 3.24) in cyclic voltammetry experiment at -2.0 V vs Fc⁺/Fc (the half height of the wave [209]). The current response increased with further addition of acid with gradual shift of the peak maximum from -2.0 to -2.4 V. The form of the wave is representative for a diffusion limited process and its amplitude constantly increases with addition of acid up to 200 eq of TFA for **PdTFP** and 500 eq of TFA for **CuTFP**. The higher i_c/i_p ratio (where i_c - current response of the catalytic wave and i_p - current response of the sample in the absence of acid) for **CuTFP** suggests a higher turnover frequency (TOF).

The metal-free, Zn(II) and Co(II) **TFP** showed no catalytic activity in identical conditions, while Ni(II) **TFP** showed weak current response at a more negative potential. The use of a weaker acid TEAHCl as the proton source resulted in no catalytic activity for **PdTFP**, while **CuTFP** showed similar behaviour as for TFA. No change in the CV curve was observed when substituting the Ar atmosphere with CO₂, with or without TFA.

An overpotential of -1.0 V was estimated as described by Artero and coworkers [209] (Equation 2).

$$E_{1/2} = E_{H^+/H_2}^o - \frac{2.303 \times RT}{F} pK_a + \varepsilon_D - \frac{RT}{2F} \ln \frac{C_0}{C_{H_2}^o} \quad (2)$$

were $E_{H^+/H_2}^o = -0.62$ V is the standard potential for the reduction of protons in DMF,

$R = 8.617 \times 10^{-5}$ V C / mol K is the Boltzmann constant,

T – absolute temperature,

$F = 96485$ C mol⁻¹ is the Faraday constant,

$pK_a = 6 \pm 0.3$ is the dissociation constant of TFA in DMF,

$\varepsilon_D = 40$ mV is the correction factor which reflects the difference in diffusion coefficients of the acid and H₂,

C_0 - the total concentration of acid,

$C_{H_2}^o = 1.9$ mmol L⁻¹ the saturating concentration of dissolved H₂ under 1 bar H₂.

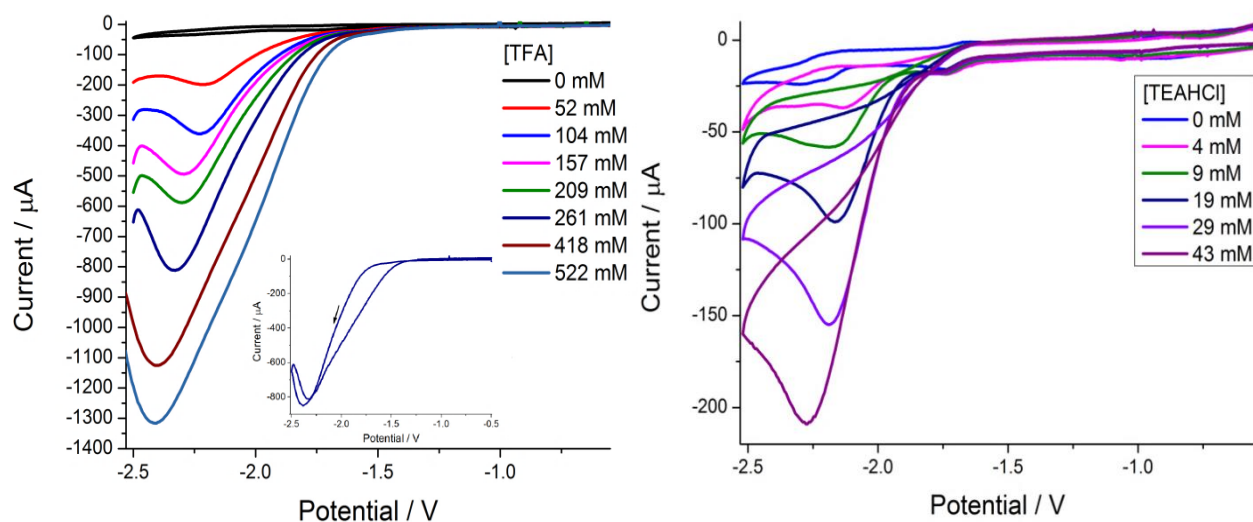


Fig. 3.23. Selected cyclic voltammograms of 1 mM of **CuTFP** at a glassy carbon electrode in DMF in the presence of increasing quantities of TFA (left) and TEAHCl (right).

Voltammograms show that the addition of acid leads to the appearance of an irreversible wave of increasing amplitude corresponding to the reduction of protons catalysed by **CuTFP**.

Conditions: $T = 298\text{ K}$, scan rate 100 mV/s . Supporting electrolyte: 0.2 M TBABF_4 .

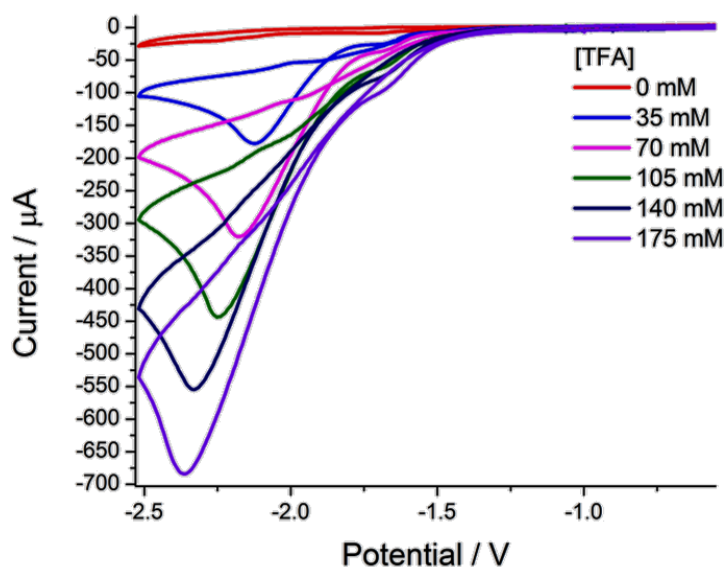


Fig. 3.24. Selected cyclic voltammograms of 1 mM of **PdTFP** at a glassy carbon electrode in DMF in the presence of increasing quantities of TFA. Voltammograms show that the addition of hydrochloride leads to the appearance of an irreversible wave of increasing amplitude corresponding to the reduction of protons catalysed by **PdTFP**.

Conditions: $T=298\text{ K}$, scan rate 100 mV/s . Supporting electrolyte: 0.2 M TBABF_4 .

In order to elucidate the importance of the ferrocenyl units for the proton reduction, Pd(II) tetraphenylporphyrin **PdTFP** was tested in similar conditions. Addition of TFA to the sample gave rise to a catalytic wave which is shifted to a more negative potential by ~200 mV as compared to **PdTFP** (Annexe 13). A lower i_c/i_p ratio suggest a lower TOF compared to the ferrocenyl analogue. The Cu(II) tetraphenyl porphyrin **CuTFP** was reported by Saveant group as being inactive for the catalysis of proton reduction in either TEAHCl or CHF₂COOH [141]. We have repeated this experiment using TEAHCl and proved the lack of electrocatalytic response. The higher catalytic activity of ferrocene substituted porphyrins could be attributed to stabilization of protonated intermediates by increasing electron density on the porphyrin periphery, which is suggested from Mössbauer spectroscopy data. Formation of *meso*-protonated porphyrin intermediate was seen in spectroelectrochemical experiments so a catalysis mechanism based on initial phlorin formation is highly probable. It was previously shown that phlorins can undergo dehydrogenation in the presence of a proton source (HCl, MeOH) so that the parent porphyrin is generated [210]. Another explanation of ferrocene role is the stabilization of phlorins by steric hindrance of parent porphyrin, previously proposed for other porphyrin systems [211]. Still, the steric concept was later criticized by other groups [212].

GC analysis of the electrolysis products

Continuous flow rig with in-line GC analysis was used to detect the molecular hydrogen produced during electrocatalytic proton reduction in DMF in the presence of TFA or TEAHCl. It was found that applying a potential of -1.5 V vs Saturated Calomel Electrode at Glassy Carbon working electrode results in formation of molecular hydrogen. The quantity of produced H₂ was determined by calibration with a known amount of a prepared H₂/Ar mixture by checking the proportionality between the peak surface area and the injected hydrogen quantity. Comparing this value with the charge consumed during the electrolysis, converted to the theoretical amount of hydrogen, the Faradaic yield of the process was calculated.

Undoubtedly the presence of 0.1 mM of the catalyst greatly increased the amount of electroreduced protons, as indicated by the GC analysis. Concomitantly increase of the current response at the identical potential was noticed. Using 0.1 mM of **CuTFP** in DMF solution of 50 mM TFA with 0.1 M TBABF₄ as supporting electrolyte resulted in electrocatalytic production of 5.47×10^{-6} mols of H₂ by consuming 1.55 Coulombs, corresponding to 68 % Faradaic yield (Figure 3.25).

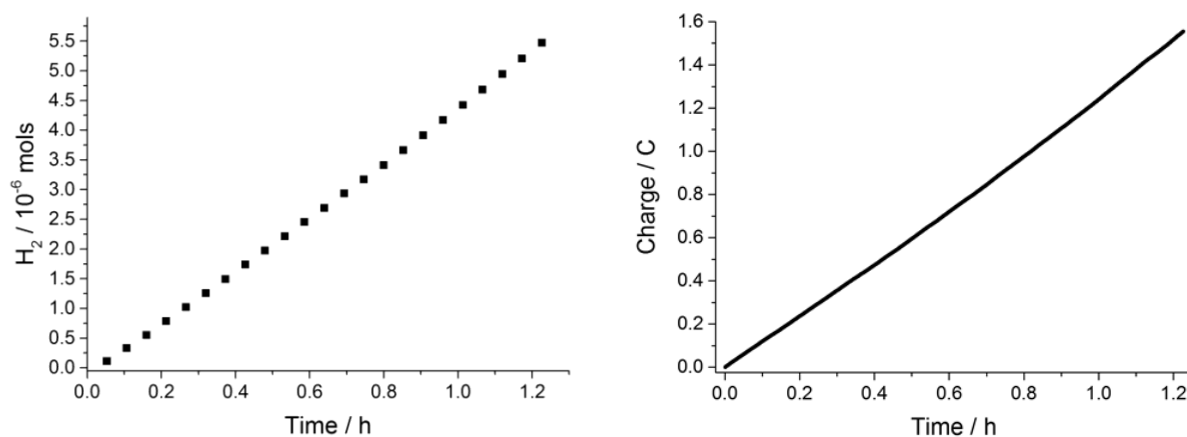


Fig. 3.25. Electrocatalytic hydrogen production vs time (left) and charge vs time (right) by applying -1.5 V vs SCE to a glassy carbon electrode in 0.1 M TBABF₄ sol. of DMF containing 50 mM TFA and 0.1 mM **CuTFP**.

A Faradaic efficiency of 70 % was obtained by the use of (Annexe 14), but smaller amount of protons were reduced in the same period of time consistent with lower catalytic current response in cyclic voltammetry experiments. For both compounds current response during bulk electrolysis was constant for a period of at least one turn over cycle. On a prolonged timescale other Faradaic processes were noticed and as result modification of the glassy carbon electrode surface resulting in increase of current response. This could be attributed to processes associated with ferrocene oxidation and sample decomposition, with further material adsorption on the electrode. Certainly the **H₂TFP** was shown to be oxidized by TFA to the **H₂TFPⁿ⁺** cations [196], which could be unstable in solution.

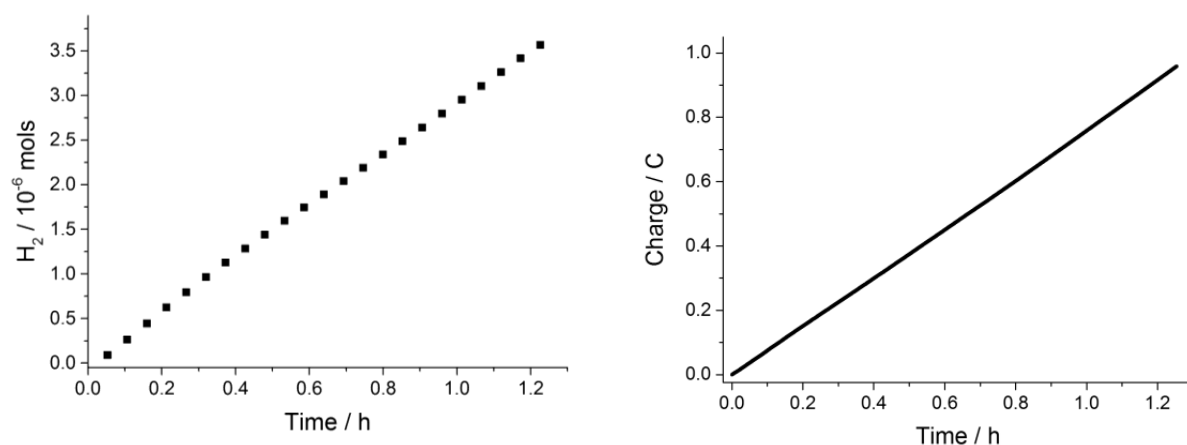


Fig. 3.26. Electrocatalytic hydrogen production vs time (left) and charge vs time (right) by applying -1.5 V vs SCE to a glassy carbon electrode in 0.1 M TBABF₄ sol. of DMF containing 50 mM TEAHCl and 0.1 mM **CuTFP**.

As only **CuTFP** showed electrocatalytic behaviour in CV experiments when TEAHCl was employed as proton source, it was used to generate H₂ from this weaker acid (Figure 3.26). As expected, the catalysis process is slower for this acid at the same concentration C_M = 50 mM and identical applied potential, as result of higher pK_a = 9.2 (pK_a = 6 for TFA) [209, 213]. 3.57 × 10⁻⁶ mols of H₂ were produced by consuming 0.94 Coulombs, corresponding to 73 % Faradaic yield.

In order to elucidate the importance of the ferrocenyl units in the catalysis mechanism, the reference *meso*-tetraphenyl analogues **CuTPP** and **PdTPP** were obtained. The addition of the TFA acid generated catalytic wave, still with a lower current response and a higher overpotential. Using the weaker TEAHCl proton source did not show any catalytical current response for tetraphenyl analogues, showing the importance of the ferrocenyl units. Still the central metal atom influence should be taken in account as well, as in the CV conditions Cu(II) and Pd(II) complexes showed much more pronounced electrocatalytical behaviour. A dependence on the redox potential can be marked as it decreases in the series Pd > Cu > Ni > Co > Zn and the catalytic effectiveness is decreasing likewise. The electronegativity of the copper(II) and palladium(II) ions appear to be conducive to stabilise the negative charge at the pyrrole for the phlorin anion and thus disfavour resonance forms which would generate the chlorin. Certainly it was shown before that Ni(II) and especially Cu(II) **TPP** can be used to obtain 2-formyl-**TPP** by selective electrophilic attack to a β-pyrrolic position [214], so increase of electron density on the pyrrole β-position is suggested.

3.3. Conclusions to Chapter 3

Chapter 3.1: A zinc(II) porphyrin derivative, **F3P**, was prepared containing a single ferrocene group appended at three of the meso positions. The final meso position contains a benzoic acid unit, and was designed to be an anchoring moiety to a semiconductor surface. The cyclic voltammogram for the porphyrin derivative revealed that the three ferrocene units are oxidised and reduced at E_{1/2} = +0.04 V vs Fc⁺/Fc. Other redox responses are porphyrin based at +1.1 V vs Fc⁺/Fc (irreversible) and -1.87 V and -2.20 V vs Fc⁺/Fc (both quasi-reversible). The room temperature Mössbauer spectrum for **F3P** comprises a doublet (δ_{Fe} 0.44 mm/s; ΔE_Q 2.35; mm/s; peak width 0.27 mm/s). The data are consistent with the ferrocene groups non-interacting with the porphyrin moiety in the ground state. Excitation of the compound with an ultra-short laser pulse produces in less than 1 ps the charge separated state which comprises Fc⁺-porp⁻ and decays back to the ground state in 20 ps. The performance of the dye attached to TiO₂ as a DSSC

device is limited ($FF = 0.42$, $\eta = 0.0081\%$). These results suggest that direct coupling of donors and porphyrin should be avoided in the design of DSSC sensitizers as the injection from the rapidly generated porphyrin anion onto the TiO_2 surface does not occur.

Although the Rochford group published no measurements, our studies would suggest that performance will be poor especially for derivatives where ferrocenes are close to the anchoring carboxylic acid group. However, it will be interesting to see if an improved response is observed for compounds where the ferrocene is *trans* to the carboxylic acid anchoring unit. The ferrocenium produced would be away from the semiconductor surface and we could expect charge recombination to be much slower.

Chapter 3.2: Cu(II) and Pd(II) *meso*-tetraferrocenylporphyrins were employed as catalysts for electrochemical proton reduction. Cyclic voltammetry and gas chromatography were aimed at the investigation of key parameters of catalytic process and identifying the generated gases. In order to reveal the structure – properties relationship UV-Vis spectroelectrochemistry and Mössbauer spectroscopy were used. A tentative mechanism based on phlorin anion generation was proposed.

The spectroelectrochemistry measurements showed that the reduction processes are porphyrin centred and the porphyrin dianion **MTFP²⁻** is protonated in the *meso* position to form the phlorin anion **MTFPH⁻**. This latter is stable in THF under spectroelectrochemical conditions but addition of a proton source would result in second protonation, followed by H_2 evolution and regeneration of catalyst. Electrochemical reduction of Cu(II) and Pd(II) **TFP** solutions in THF, containing proton source (TFA or TEAHCl), resulted in enhanced generation of molecular hydrogen as compared to *meso*-tetraphenyl analogues. An explanation of this would be the change of electron density on the porphyrin ring, as result of introduction of ferrocenyl substituents, which influences the stability constant of the intermediate hydrogenated products. The protonation is favoured by the high electron density on the porphyrin ring which could explain why porphyrins with electron-donating ferrocene units are better catalyst than their phenyl analogues. Still, the steric factor introduced by bulky ferrocene units should be taken in account as well. At the same time the central metal role consists of localizing the negative charge in the β -pyrrolic position close to the *meso*-H of the phlorin molecule.

4. EXPERIMENTAL SECTION

In the first half of this chapter a detailed information on the instruments used to study the materials obtained within this work is given, together with the software used to run the apparatus, process data and perform quantum-chemical calculations. The second part is providing the reader with details on the reaction conditions employed to obtain the compounds discussed in Chapters 2 and 3, and X-ray crystallographic data.

4.1. Physical methods of investigation

Physical methods of investigation – structural characterisation

^1H , $^{13}\text{C}\{^1\text{H}\}$ and DEPT-135° NMR spectra, as well as two-dimensional homo- ($^1\text{H}/^1\text{H}$ COSY-45°) and heteronuclear ($^1\text{H}/^{13}\text{C}$ HSQC and HMBC) correlation spectra were acquired with Bruker – Avance-III 400 MHz and Jeol ECS-400 MHz, using TopSpin or Delta Data processing software respectively. Chemical shifts for ^1H and $^{13}\text{C}\{^1\text{H}\}$ NMR spectra are referenced relative to TMS or the residual protiated solvent. ^{11}B NMR spectrum is referenced relative to $\text{BF}_3\cdot\text{OEt}_2$ ($\delta = 0.0$ ppm) as external reference. ^{19}F NMR spectrum is referenced relative to CF_3COOH ($\delta = -76.55$ ppm vs. CFCl_3) as external reference.

Waters LCT Premier TOF and Thermofisher LTQ Orbitrap XL (Mass Accuracy: <3 ppm RMS) with nanospray were used for accurate mass ESI and ASAP / APCI measurements. Ammonium acetate was used in the ion source, to assist ionisation. MALDI-TOF experiments were conducted using Voyager DE-STR instrument with Linear and Reflectron analysers and a Nd:YAG laser ($\lambda = 355\text{nm}$) by Elforlight. The typical preparation procedure of sample consisted of co-crystallization from DCM solutions of porphyrin and trans-2-[3-(4-tert-butylphenyl)-2-methylprop-2-enylidene]malononitrile matrix. Accurate mass Electron Ionisation (HREI) spectra in positive ionisation mode were obtained on the high resolution double focussing mass spectrometer Finnigan MAT 95 XP by "peak matching", using perfluorotributylamine as reference compound.

FTIR spectra were recorded by using Varian 800 FTIR and Perkin Elmer 100 FT-IR spectrometers controlled with Resolutions and Spectrum software respectively.

Atomic absorption spectra were measured using AAS-3 Carl Zeiss Jena spectrometer equipped with a hollow-cathode lamp FeHK at a wavelength of 248.3 nm.

Elemental analysis was tested on a Carlo Erba 1108 Elemental Analyser controlled with CE Eager 200 software, ran in accordance with the manufacturer's instructions, weighed using a

certified Mettler MX5 Microbalance and calibrated with Acetanilide Organic Analytical Standard. Alternatively, Elemental Vario EL3 machine was used as well.

Single crystal X-ray diffraction data were collected using Xcalibur Eos, Xcalibur Atlas Gemini ultra and Rigaku Saturn 724+ diffractometers. Using Olex2 [215], the structure was solved with the ShelXS [216] structure solution program with Direct Methods and refined with the ShelXL refinement package using Least Squares minimisation.

Physical methods of investigation – properties characterisation

Electronic absorption spectra were recorded by using a Hitachi U3310 and Perkin Elmer's LAMBDA 25 UV/Vis systems instruments, controlled with UV Solutions or UV WinLab utilities respectively.

The ^{57}Fe -Mössbauer spectra were acquired with a conventional spectrometer in the constant-acceleration mode (SEE Co MS4, Edina, USA) equipped with a ^{57}Co source in a rhodium matrix and controlled with W302 software. Variable temperature Mössbauer experiments were done using closed cycle He gas refrigerator cryostat and a dual channel temperature controller SeeCo Model 106. Isomer shifts are given relative to α -Fe at RT. The spectrum was fitted using the freely available Mössbauer Spectral Analysis Software WMOSS4 Version F[217]. The error limit for the each experimental point in the MS is ± 0.02 mm/s for source velocity and less than 0.5 % for absorption axis. All spectra were fitted for a lowest χ_R^2 value, $\chi_R^2 < 0.60$ for **II.4** and $\chi_R^2 < 0.75$ for **FTFCl₂**. The linearity of plots was checked by the use of R^2 factor and respective error limits were determined.

The cyclic voltammetry experiments were conducted in a three-electrode set-up consisting of a glassy carbon working electrode, a platinum wire counter electrode and an Ag/AgCl [NaCl (3M)] reference electrode by using a Princeton Applied Research Potentiostat model 263a controlled with Power Suite utility or fully automated HCH Instruments Electrochemical Analyzer model 600a controlled with CHI software. Ferrocene was used as an internal standard. For spectroelectrochemical experiments, platinum was used as the working and counter electrodes and silver wire was used as a pseudoreference electrode in an OTTLE by LabOmak. All studies were performed in dry, deoxygenated solvents containing TBABF₄ (0.2 M) as background electrolyte. Redox potentials were reproducible to within ± 15 mV.

Femto- to pico-second time-resolved absorption spectra were collected using a pump-probe apparatus consisting of a Libra F-1K (Coherent Inc.) generator producing 100 fs pulses with 1 mJ energy at 800 nm with a repetition rate of 1 kHz, and a Topas-C (Light Conversion

Ltd.) OPA providing pump pulses in a wide spectrum range (UV-Visible - near IR). The measurements part for the pump-probe method was a ExciPro (CDP Inc., Russia) equipped with two array detectors coupled to a spectrometer (CDP2022i) for probe detection in the visible (300–1000 nm) and near IR (900–1700 nm) ranges. A white light continuum was used as the probe and was generated in a sapphire plate, and the overall time resolution of the instrument was 100–200 fs depending on the sample type and wavelength range. The samples were placed in 1 mm rotating cuvettes, and averaging of 100 pulses at a 10 Hz repetition rate was used to improve the signal-to-noise ratio. Absorption spectra were recorded prior to and after all experiments to check for compound degradation.

Time-resolved transient absorption data were manipulated using the freely available software package - Decfit. In a typical analysis the whole collection of differential absorption spectra was inspected over the full timescale, and decay kinetics were obtained in the whole measured wavelength range with 5 nm step by averaging spectra in 5 nm intervals at each delay time. Lifetimes were obtained by global fit of the whole data set. Best fits were judged by the usual methods of remaining residuals and sigma value.

Current-Voltage characteristics of the DSSCs were measured under 1000 Wm^{-2} and 100 Wm^{-2} AM 1.5 G illumination using a Newport solar simulator (model 91160) and a Keithley 2400 source per meter.

Computer assisted molecular modelling

Computational calculations were performed using a 32-bit version of Gaussian 03[218] on a quadruple-core Intel Xeon system with 4 GB RAM. The calculations were run in parallel, fully utilising the multi-core processor. Energy minimisation calculations were monitored using Molden and run in parallel with frequency calculations to ensure optimised geometries represented local minima.

4.2. Solar cell preparation

Fluorine-doped tin oxide glass substrates (Pilkington, TEC15, sheet resistance 15Ω per square) were cleaned in an ultrasonic bath overnight using (in order) ethanol, water and ethanol. The conducting glass substrates were pretreated by immersion in a 40 mM aqueous TiCl_4 solution at 70°C for 25 minutes and then washed with water. Mesoporous TiO_2 films were prepared with an area of 0.25 cm^2 by screen printing two layers of transparent colloidal TiO_2 paste (Solaronix, Ti-Nanoxide T/SP) followed by one layer of a light-scattering TiO_2 paste

(Solaronix, Ti-Nanoxide R/SP) and heated at 450 °C in an air atmosphere in an oven (Nabertherm LE 14/11/B150) for 30 minutes between deposition steps. The conducting glass substrates were post-treated by immersion in a 40 mM aqueous TiCl_4 solution at 70 °C for 25 minutes and then washed with water. The electrodes were gradually heated in an oven (Nabertherm LE 14/11/B150) at 450 °C in an air atmosphere. TiO_2 films were immersed in a dye bath containing 0.28 mM **F3P** and 0.60 mM chenodeoxycholic acid in DCM and left at RT for 18 h. The films were then rinsed in ethanol to remove excess dye and dried at RT. Solar cells were assembled with a thermally platinized counter electrode (Pilkington TEC8, sheet resistance 8 Ω per square) using a 30 mm thick thermoplastic frame (Dyesol, Surlyn 1702). The electrolyte solution, containing either 1-propyl-3-methylimidazolium iodide 0.8 M, tert-butyl pyridine 0.3 M, iodine 0.1 M, and guanidinium thiocyanate 0.05 M in methoxypropionitrile (data not shown), or $\text{Co}(4,4'\text{-dimethoxy-2,2'-bipyridine})_3 (\text{ClO}_4)_2$ 0.1 M, 4-tert-butylpyridine 0.2 M, tertbutyl ammonium perchlorate 0.1 M, NOPF_6 0.015 M, in propylene carbonate, was introduced through the pre-drilled hole in the counter electrode, which was sealed afterwards with Surlyn and a glass cover slide.

4.3. Electrocatalysis cell and GC analysis

A three electrode electrocatalysis cell with 20 mL volume was used for proton reduction. A glassy carbon electrode was used as working electrode, platinum mesh as counter electrode and SCE reference electrode. The solution was deaerated and the working electrode polished every time prior to experiments. Argon of a high purity was used as carrier gas. The continuous flow rig with in-line GC consisted of EL-FLOW® Select – GAS Mass Flow Controller, a six-port sampling and switching valve and Shimadzu GC-2014 gas chromatographer with a capillary column.

The chromatography peak area was calibrated using a prepared H_2 / Ar mixture. A negative potential was applied to the working electrode in a chronoamperometry mode and the produced gas was carried with Ar bubbled through the solution. Injecting a sample every three minutes into the gas chromatograph and integrating the area of peak allowed calculating the amount of produced hydrogen.

4.4. Synthetic procedures for compounds discussed in Chapters 2 and 3

All chemicals were purchased from commercial sources and used as received unless otherwise stated. Basic solvents for synthesis were dried using literature methods. Solvents for spectroscopic investigations were of the highest purity available. Starting materials (**II.1**) [219], (**II.7**) [220], (**II.8**) [221], **III.1** [222], **III.2** [223] and the 1,1'-ferrocene bis(2,2'-dipyrromethane) (**II.9**) [182] were obtained using adapted literature procedures. Metal-free **H₂TFP** and Cu(II), Co(II), Ni(II), Zn(II) tetraferrocenylporphyrin complexes **MTFP** were obtained as described by Nemykin et al [197].

Preparation of 1'-Formyl-ferrocenecarboxylic acid (II.2)

To a solution of **II.1** (400 mg, 1.65 mmol) in acetonitrile (20 mL) at 0 °C was slowly added a solution of KMnO₄ (800 mg, 5.06 mmol) in water (13 mL). After stirring for 15 min a solution of aq. NaOH (2 mL, 20% w/v) was added and stirred for a further 5 minutes. The reaction mixture was filtered through Celite and washed with aq. NaOH (3 mL, 10% w/v). The filtrate was washed with Et₂O (3 × 30 mL) to remove the unreacted starting material and slowly acidified to pH = 3 with a solution of aq. HCl (10 %). Extraction with chloroform (3 × 40 mL) with further drying over Na₂SO₄ and evaporation of the solvent gave the desired compound **II.2** as an orange solid (210 mg, 49 % yield).

¹H NMR (400 MHz, acetonitrile-d₃, δ): 9.87 (s, 1 H), 4.83 (s, 2 H), 4.81 (s, 2 H), 4.65 (s, 2 H), 4.53 (s, 2 H). ¹³C{¹H} NMR (101 MHz, acetonitrile-d₃, δ): 193.21, 170.77, 80.58, 74.56, 72.79, 71.60, 70.95. FTIR (cm⁻¹): 624 (w), 718 (m), 747 (vs), 785 (vw), 816 (m), 834 (s), 836 (s), 879 (vw), 912 (vw), 1032 (s), 1051 (vw sh), 1151 (s), 1212 (vw), 1244 (s), 1262 (vs), 1295 (vw), 1332 (vw), 1372 (m), 1396 (m), 1455 (w), 1472 (m), 1529 (vw), 1630 (s, sh), 1640 (vs), 1673 (m), 1690 (m), 1717 (s), 2533 (vw, br), 2615 (w, br) 2865 (w, br), 2939 (m, br), 3111 (w, br). HRMS (ASAP/APCI-FTMS, *m/z*): found [M + H]⁺ 259.0047, [M - OH]⁺ 240.9942, calcd for C₁₂H₁₁FeO₃ 259.0052. Anal. (%) Calcd for C₁₂H₁₀FeO₃: C, 55.85; H, 3.91; N, 0.00, found: C, 56.10; H, 3.89; N, 0.00.

Preparation of 1'-((E)-3-oxo-but-1-enyl)-ferrocenecarboxylic acid (II.3)

To a solution of **II.1** (500 mg, 2.07 mmol) in acetone (20 mL) at 0 °C was slowly added (1h) a solution of KMnO₄ (1.30 g, 8.23 mmol) in water (21 mL). After stirring for 15 min aq.

NaOH (3 mL, 20%) was added and the solution was stirred for a further 5 minutes. The reaction mixture was filtered through Celite and washed with aq. NaOH (6 mL, 10%). The filtrate was washed with Et₂O (3×40 mL) to remove the unreacted starting material and slowly acidified to pH = 2 with a solution of aq. HCl (10 %). The precipitate formed was collected by filtration, washed with distilled water and dried to give the desired compound **II.3** as an orange solid (370mg, 60 % yield). Some more impure compound (ca. 50 mg) could be obtained by extracting the filtrate with ethylacetate.

¹H NMR (400 MHz, acetone-d₆, δ): 7.35 (d, *J* = 16.2 Hz, 1 H), 6.30 (d, *J* = 16.2 Hz, 1 H), 4.75 (ap t, *J* = 1.9 Hz, 2 H), 4.67 (ap t, *J* = 1.7 Hz, 2 H), 4.50 (ap t, *J* = 1.7 Hz, 2 H), 4.45 (ap t, *J* = 1.9 Hz, 2 H), 2.25 (s, 3 H). ¹³C{¹H} NMR (101 MHz, acetone-d₆, δ): 197.51, 171.03, 143.04, 127.10, 81.34, 74.54, 73.32, 73.13, 72.40, 70.80, 26.84. FTIR (cm⁻¹): 717 (m), 739 (vw), 783 (w), 821 (m), 869 (vw, sh), 910 (vw, sh), 931 (vw, sh), 966 (m), 1030 (m), 1049 (w), 1145 (s), 1185 (vw), 1264 (vs), 1281(w, sh), 1361 (m), 1398 (w, sh), 1471 (s), 1524 (w), 1626 (vs), 1667 (s), 1705 (s), 1750 (vw), 2633 (w, br), 2934 (m, v br), 3440 (w, br). HRMS (ESI, *m/z*): found [M + H]⁺ 299.0367, [M + Na]⁺ 321.0182, [2M + Na]⁺ 619.0499, calcd for C₁₅H₁₅FeO₃ 299.0371. Anal. (%) Calcd for C₁₅H₁₄FeO₃: C, 60.43; H, 4.73; N, 0.00, found: C, 60.50; H, 4.92; N, 0.00.

Preparation of 1'-Terpyridine ferrocenecarboxylic acid (II.4)

To a solution of 1'-formyl ferrocenecarboxylic acid **II.2** (100 mg, 0.39 mmol) in aq. NaOH (2 mL, 10 %) were added 2.3 equivalents of 2-acetylpyridine (0.1 mL, 0.89 mmol). Over about 5 minutes the solution became purple coloured and NH₄OH (1 mL, 28 - 30 %) was added and the reaction mixture was stirred overnight at RT under N₂ in the dark. The dark yellow solution formed was acidified with aq. HCl (10 %) to pH = 2-3. The precipitate formed was filtered, washed with aq. HCl (2 mL, 3 %) and dried overnight under reduced pressure to give the desired compound **II.4** as a dark red solid (110 mg, 62 % yield).

¹H NMR (400 MHz, CD₃OD, δ): 9.15 – 9.17 (m, 4 H), 8.88 (ap td, *J*_t = 7.9 Hz, *J*_d = 1.6 Hz, 2 H), 8.67 (s, 2 H), 8.27 (ddd, 2 H, *J*₁ = 7.6 Hz, *J*₂ = 6.0 Hz, *J*₃ = 0.9 Hz), 5.38 (ap t, *J* = 1.9 Hz, 2 H) 4.79 (ap t, *J* = 1.9 Hz, 2 H), 4.75 (ap t, *J* = 1.9 Hz, 2 H), 4.53 (ap t, *J* = 1.9 Hz, 2 H). ¹³C{¹H} NMR (101 MHz, CD₃OD, δ): 176.36, 160.79, 159.97, 154.71, 152.23, 139.35, 128.41, 124.80, 121.39, 84.34, 82.19, 73.63, 73.52, 72.13, 70.16. FTIR (cm⁻¹): 623 (vw), 648 (vw), 667 (vw), 676 (vw), 720 (vw), 738 (w), 764 (vw, sh), 781 (m), 810 (vw), 861 (vw), 891 (w), 915 (vw), 951 (w), 992 (w), 1008 (vw), 1029 (w), 1067 (vw), 1100 (w), 1118 (vw), 1159 (m), 1239

(m), 1268 (m), 1293 (m, sh), 1332 (vw), 1351 (w), 1365 (w), 1397 (w), 1432 (m), 1470 (m), 1500 (vw), 1531 (s), 1598 (vs), 1619 (vw), 1648 (vw), 1687 (m), 2870 (m, v br), 3058 (m, br), 3362 (m, br). HRMS (ASAP/APCI-FTMS, m/z): found $[M + H]^+$ 462.0894, calcd for $C_{26}H_{20}FeN_3O_2$: 462.0899. Anal. (%) Calcd for $C_{26}H_{19}FeN_3O_2$: C, 67.70; H, 4.15; N, 9.11, found: C, 65.62; H, 4.27; N, 8.41. Calcd for $C_{26}H_{19}FeN_3O_2 + 1/2H_2O$: C, 66.40; H, 4.28; N, 8.93. Calcd for $C_{26}H_{19}FeN_3O_2 + H_2O$: C, 65.15; H, 4.42; N, 8.77.

*Preparation of [Bis(1'-terpyridine ferrocenecarboxylic acid) Fe(II)]Cl₂ **FTFCl₂***

To a solution of **II.1** (400 mg, 1.65 mmol) in acetonitrile (20 mL) at 0 °C was slowly added a solution of $KMnO_4$ (800 mg, 5.06 mmol) in water (13 mL). After stirring for 15 min aq. NaOH (2 mL, 20 %) was added and stirred for further 5 min. The reaction mixture was filtered through Celite and washed with aq. NaOH (3 mL, 10 %). The filtrate was washed with Et_2O (3×30 mL) to remove the unreacted material. 2.3 Eq of 2-acetylpyridine (0.43 mL, 3.84 mmol) and NH_4OH (8 mL, 28-30 %) were added and solution stirred at RT, in darkness, under N_2 for overnight. A dark red solution formed by next day. Acidification with aq. HCl (10 %) to pH = 4 gave a deep purple precipitate (ca. 400 mg). The crude material was purified by column chromatography on silica gel using MeOH as eluent. Collection of the purple fraction, reduction of solvent under reduced pressure and further wash with aq. HCl (2 %) gave final product **FTFCl₂** as purple microcrystalline solid (100 mg, 11 % yield). X-ray suitable crystals were obtained by slow diffusion precipitation of **FTFCl₂** from methanol solution with aq. sat. KPF_6 .

1H NMR (400 MHz, CD_3OD , δ): 9.01 (s, 2H), 8.75 (d, $J = 8.0$ Hz, 2H), 7.91 (ap t, $J = 7.7$ Hz, 2H), 7.50 (d, $J = 5.5$ Hz, 2H), 7.20 (ap t, $J = 6.5$ Hz, 2H), 5.42 (ap t, $J = 1.6$ Hz, 2H), 4.83 (ap t, $J = 1.6$ Hz, 2H), 4.81 (ap t, $J = 1.7$ Hz, 2H), 4.44 (ap t, $J = 1.7$ Hz, 2H). $^{13}C\{^1H\}$ NMR (101 MHz, CD_3OD , δ): 176.36, 160.79, 159.97, 154.71, 152.23, 139.35, 128.41, 124.80, 121.39, 84.34, 82.19, 73.63, 73.52, 72.13, 70.16. FTIR (cm^{-1}): 623 (vw), 655 (w), 669 (w), 732 (w), 756 (m), 788 (s), 879 (w), 910 (w), 1026 (m), 1058 (w), 1108 (m), 1163 (w), 1183 (w), 1250 (m), 1267 (vw), 1288 (vw), 1343 (s), 1383 (s), 1403 (w), 1435 (s), 1461 (m), 1498 (m), 1558 (vs), 1615 (s), 1651 (w), 3079 (m, br), 3300 (s, v br). HRMS (ESI, m/z): found $[M]^{2+}$ 489.0483, $[M - H]^+$ 977.0933, calcd for $C_{52}H_{37}FeN_6O_4$: 977.0924. Anal. (%) Calcd for $C_{52}H_{38}Cl_2Fe_3N_6O_4$: C, 59.52; H, 3.65; N, 8.01. $C_{52}H_{38}Cl_2Fe_3N_6O_4 + 1/2H_2O + 1/2CH_3OH$: C, 58.69; H, 3.85; N, 7.82, found: C, 58.60; H, 3.89; N, 7.74.

Preparation of [1'-terpyridineferrocenecarboxylic acid Ru(II) terpyridine](PF₆)₂
RTF(PF₆)₂

Ru(tpy)Cl₃ (44 mg, 0.1 mM) and ligand **II.4** (46.2 mg, 0.1 mM) were dissolved in 12 mL MeOH and 10 drops of N-ethylmorpholine were added. Refluxing in darkness under Ar for 5 h resulted in a deep red solution. Addition of sat. aq. KPF₆ resulted in precipitation of final product **RTF(PF₆)₂** as a red solid (50 mg, 63 %).

¹H NMR (400 MHz, CD₃OD, δ): δ 8.92 (d, J = 8 Hz, 2H, tpy-H^{3',5'}), 8.90 (s, 2H, tpy'-H^{3',5'}), 8.82 (d, J = 8 Hz, 2H, tpy-H^{3,3''} or tpy'-H^{3,3''}), 8.66 (d, J = 8 Hz, 2H, tpy-H^{3,3''} or tpy'-H^{3,3''}), 8.44 (t, J = 8 Hz, 1H, tpy-H^{4'}), 7.97 (m, 4H, tpy-H^{4,4''} and tpy'-H^{4,4''}), 7.82 – 7.76 (dd, J = 5.5, 0.6 Hz, 2H, tpy-H^{6,6''} or tpy'-H^{6,6''}), 7.42 – 7.37 (dd, J = 5.5, 0.6 Hz, 2H, tpy-H^{6,6''} or tpy'-H^{6,6''}), 7.31 (ddd, J = 7.2, 5.5, 1.2 Hz, 2H, tpy-H^{5,5''} or tpy'-H^{5,5''}), 7.21 (ddd, J = 7.2, 5.5, 1.2 Hz, 2H, tpy-H^{5,5''} or tpy'-H^{5,5''}), 5.41 (ap t, J = 1.7 Hz, 2H, Cp), 4.94 (s, 5H, CpH), 4.50 (ap t, J = 1.7 Hz, 2H, Cp). FTIR (cm⁻¹): 766 (vs), 786 (vs), 834 (vs), 1029 (m), 1055 (w), 1111 (w), 1164 (w), 1184 (w), 1248 (m), 1284 (w), 1350 (w), 1387 (s), 1434 (m), 1449 (m), 1464 (w), 1497 (w), 1538 (w), 1561 (w), 1612 (s), 1695 (m br), 2924 (m, br), 3087 (w, br), 3395 (w, br), 3648 (w, br). HRMS (ASAP/APCI-FTMS, *m/z*): found [M]²⁺ 398.0410, [M - H]⁺ 795.0744, [M + PF₆]⁺ 941.0468, calcd for C₄₁H₃₀FeN₆O₂Ru: 398.0413. Anal. (%) Calcd for C₂₆H₂₀FeN₃O₂P₂F₁₂: C, 45.36; H, 2.79; N, 7.74, found: C, 44.84; H, 3.01; N, 7.51.

Preparation of 1'-(3-Methyl-5-oxocyclohex-3-enyl)ferrocenecarboxylic acid (II.5)

1'-((E)-3-oxo-but-1-enyl) ferrocenecarboxylic acid **II.3** (250 mg, 0.84 mmol) and diethylmalonate (0.4 mL, 2.6 mmol) were dissolved in ethanol (5 mL). A solution of sodium ethoxide, prepared *in situ* by stirring a piece of Na (100 mg) in ethanol (10 mL), was added and the obtained solution was stirred under a N₂ atmosphere overnight. The reaction mixture was quenched with water (5 mL) and acidified to pH = 4 with aq. HCl (10 %). Extraction with EtOAc (3 × 30mL) and further washing with distilled water, drying on Na₂SO₄ and evaporation of solvent under reduced pressure gave a brown precipitate. The crude material was purified by column chromatography on SiO₂ using DCM / MeOH (99:1) as eluent. Collecting the first big orange spot and the subsequent removal of solvent under reduced pressure afforded the final compound **II.5** as a yellow solid (100 mg, 35 %).

¹H NMR (400 MHz, CDCl₃, δ): 5.93 (s, 1H), 4.82 (d, J = 9 Hz, 2H), 4.46 (ap t, J = 1.8 Hz, 2H), 4.23 (dd, J = 6, 1.6 Hz, 2H), 4.14 (dd, J = 7, 1.2 Hz, 2H), 3.08 (dd ap t, J = 9.9, 9.2, 4.4 Hz, 1H), 2.73 (dd, J = 16.3, 4.1 Hz, 1H), 2.55 (dd, J = 18.0, 4.6 Hz, 1H), 2.44 – 2.28 (m, 2H),

2.00 (s, 3H). $^{13}\text{C}\{^1\text{H}\}$ NMR (101 MHz, CD_3OD , δ): 199.29, 176.59, 161.96, 126.68, 93.61, 72.55, 72.45, 71.42, 71.16, 70.48, 69.81, 69.71, 68.49, 67.93, 43.88, 38.84, 34.02, 24.58. FTIR (cm^{-1}): 656 (vw), 745 (w), 781 (vw), 810 (w), 820 (m), 839 (vw), 848 (vw), 884 (vw), 917 (w), 1007 (vw), 1027 (w), 1053 (vw), 1107 (vw), 1140 (vw), 1167 (m), 1223 (vw), 1254 (w), 1266 (w), 1297 (s), 1347 (vw), 1366 (w), 1383 (w), 1408 (vw), 1432 (vw), 1481 (m), 1656 (vs), 1671 (vs), 1719 (vw), 2588 (w, br), 2647 (w, br), 2683 (vw, br), 2771 (vw, br), 2888 (w, br), 2905 (w, br), 2956 (w, br), 2972 (w, br), 2076 (w, br), 3120 (w, br). HRMS (ASAP/APCI-FTMS, m/z): found $[\text{M} - \text{OH}]^+$ 321.0568, $[\text{M} + \text{H}]^+$ 339.0671, $[2\text{M} + \text{H}]^+$ 677.1267, calcd for $\text{C}_{18}\text{H}_{19}\text{O}_3\text{Fe}$: 339.0678. Anal. (%) Calcd for $\text{C}_{18}\text{H}_{18}\text{FeO}_3$: C, 63.93.85; H, 5.37; N, 0.00, found: C, 63.02; H, 5.37; N, 0.00.

Preparation of Sodium 1'-[3,5-dihydroxy-2-picolinoyl-3,5-di(pyridin-2-yl)cyclohexyl]ferrocenecarboxylate (NaII.6)

To a solution of 1'-formyl ferrocenecarboxylic acid **II.2** (50 mg, 0.19 mmol) in aq. NaOH (2 mL, 10 %) were added 2.3 equivalents of 2-acetylpyridine (0.1 mL, 0.89 mmol) and the reaction mixture was stirred at RT under N_2 in the darkness for 1 h. An amorphous pale precipitate formed and solution got a red brownish colour. The mixture was filtered, washed with 10 % NaOH and distilled water. Purification by preparative TLC on SiO_2 using MeOH / DCM 10% mixture, extraction with DMF, further removed under reduced pressure gave product NaII.6 as a yellow amorphous solid (45 mg, 38 %).

^1H NMR (400 MHz, D_2O , δ): 8.53 (d, $J = 5.0$ Hz, 1H), 8.19 (d, $J = 4.5$ Hz, 1H), 8.04 (d, $J = 4.7$ Hz, 1H), 7.93 (td, $J = 7.8, 1.7$ Hz, 1H), 7.82 (d, $J = 8.1$ Hz, 1H), 7.63 (td, $J = 7.8, 1.5$ Hz, 1H), 7.51 (td, $J = 7.8, 1.5$ Hz, 1H), 7.45 – 7.34 (m, 3H), 7.29 (dd, $J = 7.8, 5.0$ Hz, 1H), 6.93 (dd, $J = 7.6, 5.0$ Hz, 1H), 4.53 (ap t, $J = 1.8$ Hz, 2H), 4.45 (d, $J = 11.5$ Hz, 1H), 4.35 – 4.26 (m, 3H), 3.93 (s, 1H), 3.81 (s, 1H), 3.79 (s, 1H) 3.67 (ap td, $J = 11.5, 4.3$ Hz, 1H), 2.79 (d, $J = 14.7$ Hz, 2H), 2.73 – 2.58 (m, 2H), 2.05 (dd, $J = 14.7, 1.2$ Hz, 1H). FTIR (cm^{-1}): 623 (w), 648(vw), 667 (vw), 676 (vw), 721 (w), 738 (m), 781 (s), 810 (vw), 861 (vw), 892 (w), 915 (vw), 951 (w), 992 (m), 1008 (vw), 1029 (w), 1100 (w), 1159 (m), 1239 (m), 1268 (s), 1294 (s), 1351 (w), 1365 (w), 1397 (vw), 1432 (m), 1470 (m), 1531 (s), 1598 (vs), 1619 (w), 1649 (w), 1687 (m), 2549 (vw, br), 2610 (w, br), 2870 (m, br), 2923 (w, br), 3050 (m, br), 3362 (m, br). HRMS (ASAP/APCI-FTMS, m/z): found $[\text{M} - \text{H}]^-$ 602.1356, $[2\text{M} - \text{H}]^-$ 1205.2698, $[2\text{M} - 2\text{H} + \text{Na}]^-$ 1227.2511, calcd for $\text{C}_{33}\text{H}_{28}\text{FeN}_3\text{O}_5$: 602.1384. Anal. (%) Calcd for $\text{C}_{33}\text{H}_{28}\text{FeN}_3\text{O}_5\text{Na}$: C, 63.37; H, 4.51; N, 6.72, found: C, 63.59; H, 4.56; N, 6.69.

Preparation of 1,1'-Ferrocene dicarboxylic acid (II.7)

To the suspension of ferrocene (1.0 g, 5.4 mmol) and tetramethylethylenediamine (2.5 mL, 16.7 mmol) in dry diethyl ether (13 mL), was added 2.5 M n-BuLi (6 mL, 15 mmol) in hexane and the resulting solution was stirred under N₂ at RT for 20 h. The mixture containing lithiated intermediate was cooled to -78 °C and dry ice was added every 10 minutes during 2h. The reaction mixture was acidified to pH 2 with a solution of aqueous HCl (9%). The resulting precipitate was collected and washed with water and diethyl ether in order to obtain 1.24 g (yield 84%) of **II.7** as a yellow solid.

¹H NMR (400 MHz, CDCl₃): δ 4.68 (s, H-Cp, 4H), 4.44 (s, H-Cp, 4H). FTIR (cm⁻¹): 751 (m), 781 (w), 818 (w), 844 (w), 918 (m), 987 (w), 1032 (m), 1053 (w), 1068 (s), 1298 (s), 1371 (w), 1405 (w), 1489 (s), 1669 (vs), 2560 (w), 2634 (w), 3117 (w), 3402 (m, br).

Preparation of 1,1'-Ferrocene bis(2,2'-dipyrromethane) (II.9)

A solution of **II.1** (0.5 g, 2.1 mmol) dissolved in 10 mL (144 mmol, 70 eq) of pyrrole was bubbled with Ar for 15 mins. TFA (0.04 mL, 0.52 mmol, 0.25 eq) was added and the solution was stirred at RT under an Ar atmosphere. After 30 mins aqueous NaOH (0.1 M, 6 mL) was added to stop the reaction. The mixture was poured into water (30 mL) and extracted with ethyl acetate (3 × 10 mL). The collected organic layer was washed with distilled water (3 × 20 mL), separated and dried over anhydrous Na₂SO₄, filtered and solvent removed *in vacuo*. The obtained crude product was purified by chromatography on silica-gel using a petroleum ether (40 – 60 °C): ethyl acetate (6:1) mixture as eluent, collecting the first brown coloured band. The solvent was removed *in vacuo* to give 0.7 g (yield 71%) of the product **II.9** as a yellow crystalline solid.

¹H NMR (400 MHz, CDCl₃): δ 7.85 (br s, 4H, NH), 6.64 (d, *J* = 1.5 Hz, 4H, H²+H^{2'}-pyrrole), 6.13 (dd, *J* = 5.7, 2.8 Hz, 4H, H³+H^{3'}-pyrrole), 5.94 (s, 4H, H⁴+H^{4'}-pyrrole), 5.00 (s, 2H, H-methane), 4.04 (s, 2H, α-Cp), 3.95 (s, 2H, β-Cp). ¹³C{¹H} NMR (101 MHz, CDCl₃): δ 133.5 (C⁵+C^{5'}-pyrrole), 116.7 (C²+C^{2'}-pyrrole), 108.2 (C³+C^{3'}-pyrrole), 106.4 (C⁴+C^{4'}-pyrrole), 90.0 (*ipso*-Cp), 69.1 (β-Cp), 68.5 (α-Cp), 38.0 (methane-C).

Preparation of 1,1'-Ferrocene bis(2-(4-ethyl-3,5-dimethylpyrro)methanone) (FKP)

II.8 (310 mg, 1 mmol) was dissolved in dry DCM (12 mL) under a N₂ atmosphere and 3-ethyl-2,4-dimethylpyrrole (0.4 mL, 3 mmol) was added. The solution was stirred under N₂ at RT

in the dark for 15 h after which time TLC analysis indicated no starting material was left. Solvents were reduced *in vacuo* and the resulting solid was redissolved in DCM and chromatographed on SiO₂ using a DCM / MeOH (1%) mixture as eluent, in order to obtain 305 mg (yield 63 %) of product **FKP** as a yellow microcrystalline solid.

¹H NMR (400 MHz, CDCl₃): δ 10.20 (s, NH, 2H), 4.72 (ap t, H-Cp, *J* = 1.9 Hz, 4H), 4.51 (ap t, H-Cp, *J* = 1.9 Hz, 4H), 2.43 (q, CH₂-ethyl, *J* = 7.5 Hz, 4H), 2.37 (s, CH₃-5-methyl, 6H), 2.27 (s, CH₃-3-methyl, 6H), 1.09 (t, CH₃-ethyl, *J* = 7.5 Hz, 6H). ¹³C{¹H} NMR (101 MHz, CDCl₃): δ 185.28 (C=O), 132.25 (C⁵-pyrrol), 129.31 (C³-pyrrol), 127.18 (C²-pyrrol), 125.35 (C⁴-pyrrol), 84.55 (ipso-Cp), 72.72 + 71.34 (α+β-Cp), 17.26 (CH₂-ethyl), 15.34 (CH₃-ethyl), 11.66 (CH₃-3,5-methyl). FTIR (cm⁻¹): 650 (w), 733 (w), 769 (m), 786 (m), 825 (w), 859 (m), 973 (m), 1027 (w), 1043 (w), 1106 (m), 1141 (w), 1206 (w), 1235 (w), 1284 (s), 1328 (m), 1377 (s), 1423 (s), 1450 (s), 1486 (vs), 1568 (s), 2867 (w), 2926 (w), 2960 (w), 3203 (w, br). HRMS (ESI, m/z): found [M+H]⁺ 485.1875, calcd for C₂₈H₃₃FeN₂O₂: 485.1891. Anal. (%) Calcd for C₂₈H₃₂FeN₂O₂: C 69.42, H 6.66, N 5.78, found: C 69.15, H 6.83, N 5.61.

Preparation of 1,1'-Ferrocene bis(2-(4-ethyl-3,5-dimethylpyrro)methanone borondifluoride) (FBF)

II.8 (200 mg, 0.65 mmol) was dissolved in dry DCM (10 mL) under a N₂ atmosphere and 3-ethyl-2,4-dimethylpyrrole (0.27 mL, 2.0 mmol) was added. The solution was stirred under N₂ at RT in the dark for 15 h after which time TLC analysis indicated no starting material was left. Et₃N (1.5 mL) and BF₃·OEt₂ (2 mL) were added and the reaction mixture was stirred for a further 3 h until TLC analysis showed no intermediate product remained. The solvents were reduced *in vacuo* and the resulting solid redissolved in DCM and chromatographed in darkness on SiO₂ using a DCM / petroleum ether (1:1) mixture as eluent, in order to obtain 40 mg (yield 11 %) of the product **FBF** as a red-brown solid.

¹H NMR (400 MHz, CDCl₃): δ 5.16 (ap t, H-Cp, *J* = 1.9 Hz, 4H), 4.88 (ap t, H-Cp, *J* = 1.9 Hz, 4H), 2.34 (q, CH₂-ethyl, *J* = 7.6 Hz, 4H), 2.31 (s, CH₃-5-methyl, 6H), 2.18 (s, CH₃-3-methyl, 6H), 1.04 (t, *J* = 7.6 Hz, 2H). ¹³C{¹H} NMR (101 MHz, CDCl₃): δ 175.84 (C=O), 151.21 (C⁵-pyrrol), 136.01 (C⁴-pyrrol), 132.38 (C³-pyrrol), 131.98 (C²-pyrrol), 76.47 + 74.37 (α+β-Cp), 73.37 (ipso-Cp), 17.66 (CH₂-ethyl), 14.70 (CH₃-ethyl), 12.62 (CH₃-(3-methyl)), 12.54 (CH₃-(5-methyl)). FTIR (cm⁻¹): 663 (w), 748 (w), 801 (w), 829 (w), 886 (w), 973 (m), 996 (m), 1025 (s), 1054 (s), 1097 (s), 1134 (m), 1166 (s), 1261 (w), 1307 (m), 1362 (m), 1383 (w), 1401 (w), 1451 (w), 1490 (w), 1589 (s), 1682 (w), 2874 (w), 2930 (w), 2967 (w). Anal. (%) Calcd for

C₂₈H₃₀B₂F₄FeN₂O₂: C 57.98, H 5.21, N 4.83, found: C 57.70, H 5.45, N 4.62. HRMS (ASAP/APCI-FTMS, m/z): found [M+NH₄]⁺ 598.2113, [M]⁺ 580.1769, [M-F]⁺ 561.1792, [M-BF₂+2H]⁺ 533.1862 [M-BF₃+H]⁺ 513.1807 [M-2BF₂+3H]⁺ 485.1881, calcd for C₂₈H₃₀B₂F₄FeN₂O₂: 580.1784. HRMS (ESI, m/z): found [M-2BF₂+3H]⁺ 485.1887, calcd for C₂₈H₃₃FeN₂O₂: 485.1891.

Preparation of Methyl 4-formylbenzoate dimethyl acetal (III.1)

Concentrated H₂SO₄ (3.2 mL, 60 mmol, 1.5 eq) was slowly added to a solution of 4-formylbenzoic acid (6 g, 40 mmol) in MeOH / CHCl₃ (130 mL / 30 mL), and the resulting mixture was refluxed for 4 h. During the reaction water was removed by azeotropic distillation. The resulting reaction mixture was left to cooling to room temperature, poured into water (100 mL) and extracted with CHCl₃ (100 mL). The separated organic layer was washed with aqueous NaHCO₃ (10%, 2 × 50 mL) and distilled water (2 × 50 mL). The separated organic layer was dried over anhydrous Na₂SO₄, filtered and the solvent removed *in vacuo* to give **III.1** (6 g, 29 mmol, 71% yield).

¹H NMR (400 MHz, CDCl₃, TMS, δ): 8.04 (d, *J* = 8.2 Hz, 2H, *o*-Ph), 7.53 (d, *J* = 8.2 Hz, 2H, *m*-Ph), 5.44 (s, 1H, acetal), 3.91 (s, 3 H, methyl ester), 3.32 (s, 6H, dimethyl acetal).

Preparation of Methyl 4-formylbenzoate (III.2)

A mixture of **III.1** (6 g, 28.6 mmol) and *p*-toluenesulfonic acid monohydrate (5.4 g, 28.4 mmol, 1 eq) in acetone (150 mL) was stirred at RT. When TLC analysis indicated that all the starting material was consumed (ca. 20 h) the reaction mixture was poured into CHCl₃ (200 mL). The solution was washed with aqueous NaOH (10 %, 3 × 100 mL) and distilled water (100 mL). The organic layer was separated, dried over anhydrous Na₂SO₄, filtered and the solvent removed *in vacuo* to give **III.2** (4.6 g, 28.0 mmol, 98%).

¹H NMR (400 MHz, CDCl₃, TMS, δ): 10.10 (s, 1H, formyl), 8.20 (d, *J* = 8.1 Hz, 2H, *o*-Ph), 7.95 (d, *J* = 8.1 Hz, 2H, *m*-Ph), 3.96 (s, 3H, methyl ester).

Preparation of 5-Ferrocenyldipyrromethane (III.3)

A solution of ferrocenecarboxaldehyde (4 g, 18.7 mmol) dissolved in pyrrole (50 mL, 0.75 mol, 40 eq) was bubbled with Ar for 15 mins. TFA (0.14 mL, 1.82 mmol, 0.1 eq) was added

and the solution was stirred at RT in an Ar atmosphere. After 15 mins aqueous NaOH (0.1 M, 23 mL) was added to stop the reaction. The mixture was poured into water (40 mL) and extracted with ethyl acetate (60 mL). The collected organic layer was washed with distilled water (2 × 60 mL), separated and dried over anhydrous Na₂SO₄, filtered and solvent removed *in vacuo*. The obtained crude product was purified by chromatography on silica-gel using a petroleum ether (40 – 60 °C): ethyl acetate (9:1) mixture as eluent, collecting the first brown coloured band. The solvent was removed *in vacuo* to give **III.3** (4.9 g, 14.8 mmol, 79%).

¹H NMR (400 MHz, CDCl₃, TMS, δ): 7.87 (br s, 2H, NH), 6.64 (ddd, *J* = 2.6, 2.6, 1.6 Hz, 2H, H²+H^{2'}-pyrrole), 6.16 (dd, *J* = 5.9, 2.7 Hz, 2H, H³+H^{3'}-pyrrole), 6.02 (tdd, *J* = 2.3, 1.6, 0.7 Hz, 2H, H⁴+H^{4'}-pyrrole), 5.20 (s, 1H, methane), 4.16 (ap t, 2H, α-Cp), 4.09 (s, 5H, CpH), 4.08 (ap t, 2H, β-Cp). ¹³C{¹H} NMR (101 MHz, CDCl₃, δ): 133.29 (C⁵+C^{5'}-pyrrole), 116.94 (C²+C^{2'}-pyrrole), 108.12 (C³+C^{3'}-pyrrole), 106.67 (C⁴+C^{4'}-pyrrole), 90.33 (*ipso*-Cp), 69.03 (CpH), 68.16 (β-Cp), 67.69 (α-Cp), 38.26 (methane).

Preparation of 5,10,15-Trisferrocenyl-20-(methyl 4-benzoate) porphyrin (III.4)

a) Synthesis from 5-Ferrocenyldipyrromethane

A mixture of **III.2** (0.25 g, 1.5 mmol), ferrocenecarboxaldehyde (0.32 g, 1.5 mmol, 1 eq), **III.3** (1.0 g, 3.0 mmol, 2 eq) and TFA (0.09 mL, 1.2 mmol, 0.8 eq) in DCM (320 mL) was stirred at RT under an Ar atmosphere. When TLC analysis indicated that all ferrocenecarboxaldehyde was consumed (~ 2 h), DDQ (0.34 g, 1.5 mmol, 1 eq) was added and the mixture was refluxed for another 1.5 h. After this period the reaction mixture was deposited on silica-gel and chromatographed using DCM / MeOH (100 : 3) mixture as eluent. The obtained crude product was purified by column chromatography on silica-gel using toluene: petroleum ether (40 – 60 °C): (Et)₃N (15 : 10 : 1) mixture as eluent. The major green-brown fraction was collected, solvent reduced *in vacuo* and precipitate recrystallized from toluene / hexane mixture to give **III.4** (0.27 g, 0.27 mmol 18%) as a purple microcrystalline powder.

b) Direct condensation of aldehydes

A mixture of **III.2** (0.49 g, 3 mmol), ferrocenecarboxaldehyde (2.12 g, 9.9 mmol, 3.3 eq), pyrrole (1 mL, 14.4 mmol, 4.8 eq) and TFA (0.2 mL, 2.6 mmol, 0.87 eq) in DCM (250 mL) was stirred at RT in Ar atmosphere. When TLC analysis indicated that all ferrocenecarboxaldehyde was consumed (1.5 h) DDQ (0.68 g, 3.0 mmol, 1 eq) was added and the mixture refluxed for another 1.5 h. After this period the reaction mixture was deposited on

silica-gel and chromatographed using DCM / MeOH / (Et)₃N (100 : 4 : 1) mixture as eluent. The obtained crude product was purified by two consecutive column chromatography on silica-gel using toluene : (Et)₃N (50 : 1) and toluene : petroleum ether (40 – 60 °C) : (Et)₃N (15 : 10 : 1) mixtures as eluent. The major green-brown fraction was collected, solvent reduced *in vacuo* and precipitate recrystallized from toluene / hexane mixture to give **III.4** (0.41 g, 0.41 mmol, 14% with respect to **III.2**) as a purple microcrystalline powder.

¹H NMR (400 MHz, CDCl₃, TMS, δ): 9.76 (ap q, *J* = 4.8 Hz, 4H, β-pyrrole-Fc-Fc), 9.66 (d, *J* = 4.8 Hz, 2H, β-pyrrole- Ph-Fc), 8.53 (d, *J* = 4.8 Hz, 2H, β-pyrrole-Ph-Fc), 8.43 (d, *J* = 8.1 Hz, 2H, *m*-Ph), 8.23 (d, *J* = 8.1 Hz, 2H, *o*-Ph), 5.40 (ap t, *J* = 1.7 Hz, 6H, α-Cp_{1,2,3}), 4.80 (ap t, *J* = 1.7 Hz, 2H, β-Cp₂), 4.77(ap t, *J* = 1.7 Hz, 4H, β-Cp_{1,3}), 4.12 (s, 3H, methyl ester), 4.02 (s, 15H, CpH_{1,2,3}), -1.12 (s, 2H, NH). ¹³C{¹H} NMR (101 MHz, CDCl₃, δ): 167.51 (C-carboxylic), 147.15 (*i*-Ph), 146.0 – 147.0 (α-pyrrole-Ph-Fc, vbr), 145 – 147 (α-pyrrole-Fc-Fc, vbr), 143.5 – 144.5 (α-pyrrole-Ph-Fc, vbr), 134.48 (*o*-Ph), 131.47 (β-pyrrole-Ph-Fc), 131.18 (β-pyrrole-Fc-Fc), 130.55 (β-pyrrole-Fc-Fc), 129.76 (β-pyrrole-Ph-Fc), 129.57 (*p*-Ph), 128.15 (*m*-Ph), 118.53 (meso-C-Fc₂), 118.23 (meso-C-Ph), 118.00 (meso-C-Fc_{1,3}), 89.80 (C_i-Cp₂), 89.16 (C_i-Cp_{1,3}), 77.60 (α-Cp₂), 77.11 (α-Cp_{1,3}), 70.60 (CpH), 69.29 (β-Cp_{1,3}), 69.22 (β-Cp₂), 52.54 (C-methyl ester). UV-Vis (CHCl₃): λ_{max}, nm (ε, 10³ mol⁻¹ cm⁻¹): 304 (17), 431 (151), 500 (sh), 646 (11), 714 (10).

Small amount of *cis*-5,10-Bisferrocenyl-15,20-bis(4-methylbenzoate) porphyrin (**III.5**) was isolated as well.

¹H NMR (400 MHz, CDCl₃, δ): 9.95 (s br, 2H, β-pyrrole-Fc-Ph), 9.81 (s br, 2H, β-pyrrole- Fc-Fc), 8.66 (d, *J* = 4.4 Hz, 2H, β-pyrrole-Ph-Fc), 8.61 (s, 2H, β-pyrrole-Ph-Ph), 8.43 (d, *J* = 7.8 Hz, 4H, *m*-Ph), 8.26 (d, *J* = 7.8 Hz, 4H, *o*-Ph), 5.51 (s, 4H, α-Cp), 4.84 (s, 4H, β-Cp), 4.13 (s, 10H, CpH), 4.11 (s, 6H, methyl ester), -1.83 (s, 2H, NH). UV-Vis (CHCl₃): λ_{max}, nm (ε, 10³ mol⁻¹ cm⁻¹): 298 (22), 428 (235), 500 (sh), 625 (11), 697 (11).

Preparation of Zn(II) 5,10,15-trisferrocenyl-20-(methyl 4-benzoate) porphyrin (III.6)

A solution of Zn(OAc)₂·2H₂O (220 mg, 1.0 mmol, 10 eq) in MeOH (8 mL) was added to a solution of free base **III.4** (100 mg, 0.1 mmol) in benzene (50 mL) with stirring at RT. When TLC analysis indicated that all starting material was consumed (2 h) the reaction mixture was washed with distilled water (3x50 mL), the solution dried over anhydrous Na₂SO₄, filtered and solvent removed *in vacuo* to give **III.6** (90 mg, 85 μmol, 85%) as a purple microcrystalline powder.

^1H NMR (400 MHz, CDCl_3 , TMS, δ): 10.01 (ap q, $J = 4.8$ Hz, 4H, β -pyrrole-Fc-Fc), 9.92 (d, $J = 4.7$ Hz, 2H, β -pyrrole-Ph-Fc), 8.65 (d, $J = 4.7$ Hz, 2H, β -pyrrole-Ph-Fc), 8.41 (d, $J = 8.4$ Hz, 2H, m -Ph), 8.24 (d, $J = 8.4$ Hz, 2H, o -Ph), 5.45 (ap t, $J = 1.8$ Hz, 2H, α -Cp₂), 5.43 (ap t, $J = 1.9$ Hz, 4H, α -Cp_{1,3}), 4.81 (ap t, $J = 1.8$ Hz, 2H, β -Cp₂), 4.78 (ap t, $J = 1.8$ Hz, 4H, β -Cp_{1,3}), 4.10 (s, 3H, methyl ester), 4.091 (s, 10H, CpH_{1,3}), 4.090 (s, 5H, CpH₂). $^{13}\text{C}\{^1\text{H}\}$ NMR (101 MHz, CDCl_3 , δ): 167.58 (C-carboxylic), 150.68 (α -pyrrole-Ph-Fc), 150.13 (α -pyrrole-Fc-Fc), 149.76 (α -pyrrole-Fc-Fc), 148.31 (α -pyrrole-Ph-Fc), 147.98 (i -Ph), 134.45 (o -Ph), 132.70 (β -pyrrole-Ph-Fc), 131.92 (β -pyrrole-Fc-Fc), 131.77 (β -pyrrole-Fc-Fc), 130.34 (β -pyrrole-Ph-Fc), 129.44 (p -Ph), 128.01 (m -Ph), 119.46 (meso-C-Fc₂), 119.28 (meso-C-Ph), 118.81 (meso-C-Fc_{1,3}), 90.70 (C_i-Cp₂), 90.51 (C_i-Cp_{1,3}), 77.72 (α -Cp₂), 77.36 (α -Cp_{1,3}), 70.65 (CpH), 68.90 (β -Cp_{1,2,3}), 52.47 (C-methyl ester). Anal. (%) Calcd for $\text{C}_{58}\text{H}_{42}\text{Fe}_3\text{N}_4\text{O}_2\text{Zn}$: C 65.72, H 3.99, N 5.29, found: C 66.60, H 4.25, N 5.15.

Preparation of Zn(II) 5,10,15-trisferrocenyl-20-(4-carboxyphenyl) porphyrin (F3P)

NaOH (53 mg, 1.33 mmol, 20 eq) in MeOH (8 mL) and H₂O (2 mL) was added to a solution of ester **III.5** (70 mg, 66 μmol) in THF (8 mL). The mixture was refluxed for 12 h under Ar atmosphere, then left for cooling over night at RT. CHCl_3 (70 mL) and water (70 mL) were added and mixture acidulated to pH = 6 with 2.0 M HCl. The resulting green-brownish coloured organic layer was separated, washed with water (3×50 mL), dried over anhydrous Na_2SO_4 , filtered, solvent removed *in vacuo* and precipitate recrystallized from toluene / hexane mixture to give **F3P** (51 mg, 49 μmol , 74%) as a purple microcrystalline powder.

^1H NMR (400 MHz, DMSO- d_6 , δ): 9.86 (ap t, $J = 5.3$ Hz, 4H, β -pyrrole-Fc-Fc), 9.77 (d, $J = 4.7$ Hz, 2H, β -pyrrole-Ph-Fc), 8.52 (d, $J = 4.7$ Hz, 2H, β -pyrrole-Ph-Fc), 8.36 (d, $J = 8.0$ Hz, 2H, m -Ph), 8.22 (d, $J = 8.0$ Hz, 2H, o -Ph), 5.37 (s, 2H, α -Cp₂), 5.34 (s, 4H, α -Cp_{1,3}), 4.82 (s, 2H, β -Cp₂), 4.79 (s, 4H, β -Cp_{1,3}), 4.13 (s, 5H, CpH₂), 4.11 (s, 10H, CpH_{1,3}). $^{13}\text{C}\{^1\text{H}\}$ NMR (101 MHz, DMSO- d_6 , δ): 167.75 (C-carboxylic acid), 149.70 (α -pyrrole-Ph-Fc), 149.23 (α -pyrrole-Fc-Fc), 148.94 (α -pyrrole-Fc-Fc), 147.46 (i -Ph), 147.33 (α -pyrrole-Ph-Fc), 134.20 (o -Ph), 132.11 (β -pyrrole-Ph-Fc), 131.30 (β -pyrrole-Fc-Fc), 131.22 (β -pyrrole-Fc-Fc), 129.82 (β -pyrrole-Ph-Fc), 127.65 (m -Ph), 118.79 (meso-C-Ph), 118.04 (meso-C-Fc₂), 117.53 (meso-C-Fc_{1,3}), 90.50 (C_i-Cp₂), 90.21 (C_i-Cp_{1,3}), 77.19 (α -Cp₂), 76.97 (α -Cp_{1,3}), 70.35 (CpH), 68.58 (β -Cp_{1,3}), 68.52 (β -Cp₂). MS (MALDI-TOF, DCTB matrix, m/z): $[\text{M}-\text{C}_7\text{H}_5\text{O}_2]^+$ 923.0, $[\text{M}]^+$ 1044.0, $[\text{M}+\text{O}+\text{H}]^+$ 1061.0. HREI-MS (m/z): $[\text{M}]^+$ 1044.0495, calcd for $\text{C}_{57}\text{H}_{40}\text{Fe}_3\text{N}_4\text{O}_2\text{Zn}$: 1044.0486. Anal. (%) Calcd for $\text{C}_{57}\text{H}_{40}\text{Fe}_3\text{N}_4\text{O}_2\text{Zn}$: C 65.46, H 3.85, N 5.36, found: C 66.54, H 4.21, N 5.19.

Atomic absorption calcd for $C_{57}H_{40}Fe_3N_4O_2Zn$: Fe 16.0, found: Fe 15.5. FTIR (cm^{-1}) 622 (m), 646 (w), 720 (s), 767 (sh), 794 (vs), 810 (sh), 821 (sh), 874(w), 923 (m), 999 (s), 1030 (w), 1058 (m), 1079 (w), 1107 (m), 1176 (sh), 1191 (w), 1216 (w), 1236 (w), 1264 (w), 1291 (sh), 1312 (w), 1337 (w), 1353 (w), 1389 (w), 1410 (w), 1484 (m), 1565 (w), 1605 (m), 1689 (s), 1730 (sh), 2929 (vw), 3090 (br).

*Preparation of 5,10,15,20-Tetraferrocenyl porphyrin (**H₂TFP**)*

Ferrocene carboxaldehyde (1 g, 4.67 mmol), pyrrole (0.37 mL) and $BF_3 \cdot OEt_2$ (80 μ L) in 120 mL DCM were stirred at RT, under N_2 in darkness till TLC analysis indicated that all starting material was consumed (20 h). DDQ (1.6 g) was then added and the reaction mixture refluxed for 1 h. The solvent was removed and the residue chromatographed on silica gel (DCM / MeOH 100:1) to give **H₂TFP** (230 mg, 19%) as a black microcrystalline powder.

1H NMR (400 MHz, $CDCl_3$, ppm): δ 9.60 (s, 8H, β -pyrrole), 5.31 (s, 8H, α -Cp), 4.74 (s, 8H, β -Cp), 3.95 (s, 20H, CpH), -0.5 (s, 2H, NH). $^{13}C\{^1H\}$ NMR (101 MHz, $CDCl_3$, ppm): δ 145.6 (α -pyrrole), 130.9 (β -pyrrole), 117.4 (*meso*-C), 89.4 (*ipso*-Cp), 77.0 (α -Cp, solvent overlap), 70.5 (CpH), 69.1 (β -Cp).

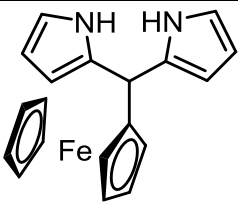
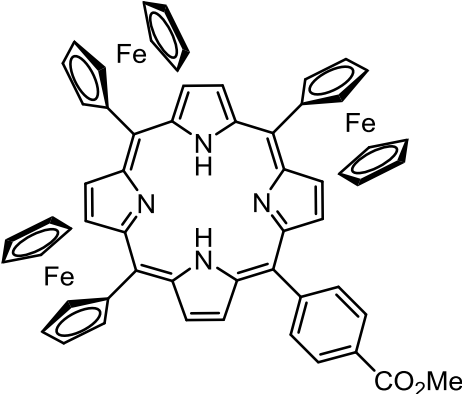
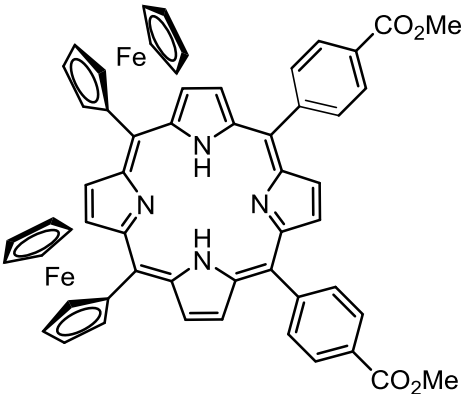
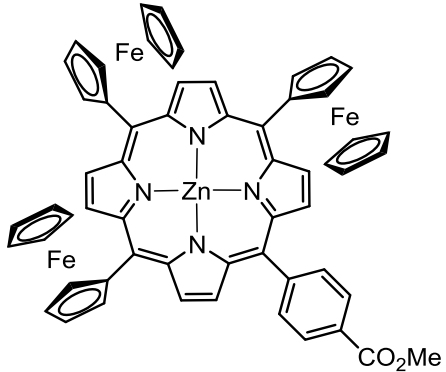
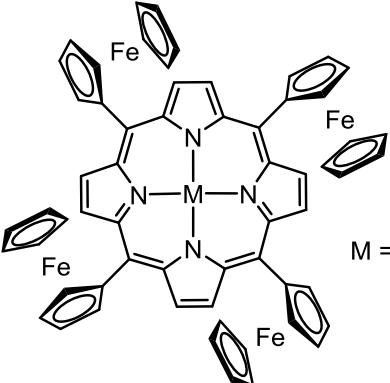
*Preparation of Pd(II) 5,10,15,20-tetraferrocenyl porphyrin (**PdTFP**)*

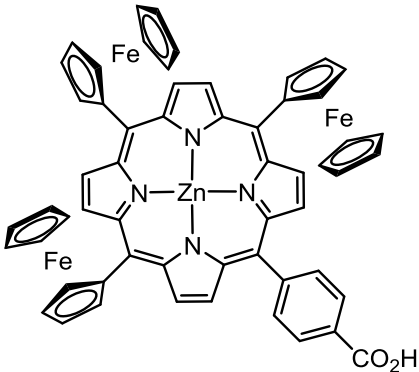
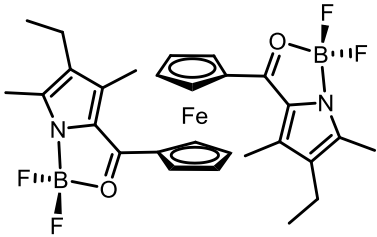
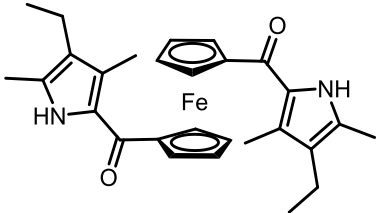
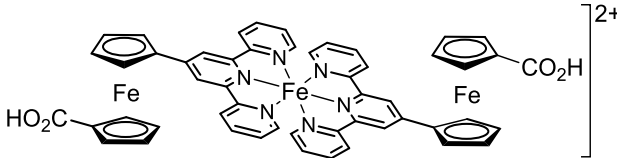
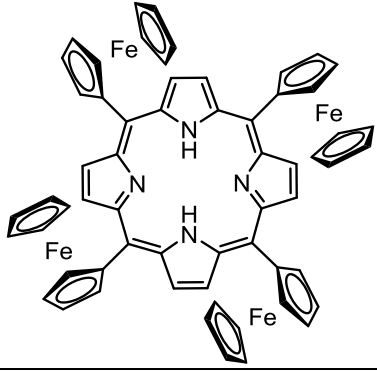
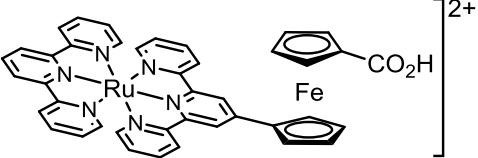
The solution of $Pd(OAc)_2$ (85 mg, 0.38 mmol, 2 eq) and **H₂TFP** (200 mg, 0.19 mmol) in toluene (25 mL) was refluxed under N_2 in darkness until the TLC analysis indicated that all starting material was consumed (20 h). The reaction mixture was washed with distilled water (3 \times 30 mL), the organic phase dried over anhydrous Na_2SO_4 , filtered, concentrated and the residue was eluted with toluene on a silica gel column to obtain **PdTFP** (43 mg, 20%) as a purple microcrystalline powder.

1H NMR (400 MHz, $CDCl_3$, ppm): δ 9.67 (s, 8H, β -pyrrole), 5.27 (ap t, $J = 1.8$ Hz, 8H, α -Cp), 4.74 (ap t, $J = 1.8$ Hz, 8H, β -Cp), 3.98 (s, 20H, CpH). $^{13}C\{^1H\}$ NMR (101 MHz, $CDCl_3$, ppm): δ 140.9 (α -pyrrole), 131.2 (β -pyrrole), 119.0 (*meso*-C), 89.3 (*ipso*-Cp), 76.7 (α -Cp, solvent overlap), 70.5 (CpH), 69.0 (β -Cp). UV-Vis (THF): λ_{max} , nm (ϵ , 10^3 mol $^{-1}$ cm $^{-1}$): 324 (17), 431 (66), 490 (sh), 654 (14). MS (MALDI-TOF, DCTB matrix, m/z): found $[M]^+$ 1150.0, calcd for $C_{60}H_{44}Fe_4N_4Pd$: 1150.0. Anal. (%) Calcd for $C_{60}H_{44}Fe_4N_4Pd$: C 62.62, H 3.85, N 4.87, found: C 63.84, H 4.04, N 4.76. (Note: a small trace of toluene is evident in the 1H NMR spectrum, thus accounting for the high carbon content) Anal. (%) Calcd for $C_{60}H_{44}Fe_4N_4Pd \cdot 1/3C_6H_5CH_3$: C 63.37, H 3.98, N 4.74.

Table 4.1. The list of compounds obtained within this work,
including the shortcuts and their structure

Shortcut	Full name	Structure
II.1	<i>1,1'-Ferrocene dicarboxaldehyde</i>	
II.2	<i>1'-Formyl-ferrocenecarboxylic acid</i>	
II.3	<i>1'-((E)-3-oxo-but-1-enyl)-ferrocenecarboxylic acid</i>	
II.4	<i>1'-Terpyridine ferrocenecarboxylic acid</i>	
II.5	<i>1'-(3-Methyl-5-oxocyclohex-3-enyl)ferrocenecarboxylic acid</i>	
II.6	<i>Sodium 1'-[3,5-dihydroxy-2-picolinoyl-3,5-di(pyridin-2-yl)cyclohexyl]ferrocenecarboxylate</i>	
II.7	<i>1,1'-Ferrocene dicarboxylic acid</i>	
II.8	<i>1,1'-Ferrocene dicarbonyl dichloride</i>	
II.9	<i>1,1'-Ferrocene bis(2,2'-dipyrromethane)</i>	
III.1	<i>Methyl 4-formylbenzoate dimethyl acetal</i>	
III.2	<i>Methyl 4-formylbenzoate</i>	

Shortcut	Full name	Structure
III.3	5-Ferrocenyldipyrromethane	
III.4	5,10,15-Trisferrocenyl-20-(methyl 4-benzoate) porphyrin	
III.5	cis-5,10-Bisferrocenyl-15,20-bis(4-methylbenzoate) porphyrin	
III.6	Zn(II) 5,10,15-trisferrocenyl-20-(methyl 4-benzoate) porphyrin	
CoTFP	Co(II) 5,10,15,20-tetraferrocenyl porphyrin	 <p>M = Co, Cu, Ni, Pd, Zn</p>
CuTFP	Cu(II) 5,10,15,20-tetraferrocenyl porphyrin	
NiTFP	Ni(II) 5,10,15,20-tetraferrocenyl porphyrin	
PdTFP	Pd(II) 5,10,15,20-tetraferrocenyl porphyrin	
ZnTFP	Zn(II) 5,10,15,20-tetraferrocenyl porphyrin	

Shortcut	Full name	Structure
F3P	<i>Zn(II) 5,10,15-trisferrocenyl-20-(4-carboxyphenyl) porphyrin</i>	
FBF	<i>1,1'-Ferrocene bis(2-(4-ethyl-3,5-dimethylpyrro)methanone borondifluoride)</i>	
FKP	<i>1,1'-Ferrocene bis(2-(4-ethyl-3,5-dimethylpyrro)methanone)</i>	
FTF²⁺	<i>[Bis(1'-terpyridine ferrocenecarboxylic acid) Fe(II)]²⁺</i>	
H₂TFP	<i>5,10,15,20-Tetraferrocenyl porphyrin</i>	
RTF²⁺	<i>[1'-Terpyridine ferrocenecarboxylic acid Ru(II) terpyridine]²⁺</i>	

4.5. Crystallographic data

Table 4.2. Crystallographic data for compounds **FTF(PF₆)₂**, **II.5**, and **II.6**.

Compound	FTF(PF₆)₂	II.5	II.6
Formula	C ₅₄ H ₄₇ F ₁₂ Fe ₃ N ₆ O _{6.5} P ₂	C ₁₈ H ₁₈ FeO ₃	C ₃₃ H ₂₉ FeN ₃ O ₅
<i>M_r</i>	1341.5	603.8	603.4
Crystal system	triclinic	triclinic	triclinic
Space group	<i>P</i> -1	<i>P</i> -1	<i>P</i> -1
<i>a</i> (Å)	9.4839(4)	7.511(2)	11.3754(6)
<i>b</i> (Å)	15.8466(7)	9.708(3)	12.1118(8)
<i>c</i> (Å)	17.8117(8)	10.869(3)	12.5240(4)
β (°)	78.680(4)	86.089(3)	65.209(4)
<i>V</i> (Å ³)	2547.1(2)	751.39 (4)	1399.57(13)
Crystal size (mm ³), colour (if available)	0.45 × 0.21 × 0.07	0.20 × 0.10 × 0.05 yellow	0.8 × 0.4 × 0.15
<i>Z</i>	2	2	2
Unique data, parameters	8975, 762 restraints - 1702	4201, 205	5499, 385
<i>R</i> (<i>F</i> , <i>F</i> ² > 2σ)	0.0724	0.0473	0.0355
<i>R_w</i> (<i>F</i> ² , all data)	0.2281	0.1313	0.0857
Data collection method	Xcalibur, Atlas, Gemini ultra thick- slice ω scans	Rigaku Saturn 724+ on kappa diffractometer wide-frame ω scans	Xcalibur, Eos

Table 4.3. Crystallographic data for compounds **II.9**, **FKP**, and **FBF**.

Compound	II.9	FKP	FBF
Formula	C ₂₈ H ₂₆ FeN ₄	C ₂₈ H ₃₂ FeN ₂ O ₂ ·CHCl ₃	C ₂₈ H ₃₀ B ₂ F ₄ FeN ₂ O ₂
<i>M_r</i>	474.4	603.8	580.0
Crystal system	monoclinic	orthorhombic	orthorhombic
Space group	<i>P</i> 2 ₁ / <i>n</i>	<i>Pbca</i>	<i>Pbcn</i>
<i>a</i> (Å)	8.8878(4)	20.174(4)	14.561(6)

Compound	II.9	FKP	FBF
<i>b</i> (Å)	13.6514(5)	13.240(3)	11.950(5)
<i>c</i> (Å)	18.5142(7)	21.343(5)	14.581(6)
β (°)	97.310(4)		
<i>V</i> (Å ³)	2228.09(16)	5701(2)	2537.2(18)
Crystal size (mm ³), colour (if available)	0.34 × 0.04 × 0.04	0.06 × 0.04 × 0.03, red	0.010 × 0.005 × 0.005, red
<i>Z</i>	4	8	4
Unique data, parameters	4987, 317	8756, 349	3134, 181
<i>R</i> (<i>F</i> , <i>F</i> ² > 2σ)	0.0322	0.0393	0.0427
<i>R</i> _w (<i>F</i> ² , all data)	0.0817	0.0986	0.1097
Data collection method	Xcalibur, Atlas, Gemini ultra thick- slice ω scans	Rigaku Saturn 724+ on kappa diffractometer wide- frame ω scans	Rigaku Saturn 724+ on kappa diffractometer wide-frame ω scans

4.5. Conclusions to Chapter 4

Using the twenty seven synthesis procedures described in the above chapter, twenty six products were synthesized (Table 4.1), from which fourteen are new ferrocene and porphyrin based derivatives. Nine products are heteronuclear homo- and heteroleptic coordination compounds of ferrocene based ligands with boron(III), iron(II), cobalt(II), nickel(II), copper(II), zinc(II), ruthenium(II) and palladium(II) atoms. The composition and structure of compounds was confirmed by IR, NMR, atomic absorption, mass spectrometries, elemental analysis and X-ray crystallography. In order to study and explain the physico-chemical properties of products a number of modern methods were used, namely: Mössbauer, UV-Vis absorption spectrometries, cyclic voltammetry, UV-Vis spectroelectrochemistry, ultrafast transient absorption (pump-probe experiment) spectrometry and computer assisted DFT calculations. Application potential of the final products was studied in a number of systems including Dye Sensitised Solar Cells and electrocatalytic proton reduction cell.

OVERALL CONCLUSIONS AND RECOMMENDATIONS

1. A new method for desymmetrization of the ferrocene molecule was elaborated based on KMnO_4 oxidation of 1,1'-ferrocenedicarboxaldehyde. The two resulting products were employed in classical organic reactions (e.g. Aldol condensation, Michael addition, Kröhnke pyridine formation etc.) to form compounds **II.4** – **II.6**.

Interestingly, the compound **II.4** showed to be light sensitive and more detailed study showed a light induced degradation of ferrocene unit to form the $[\text{Fe}(\text{tpy})_2]^{2+}$ complexes. As result the complex **FTF**²⁺ was isolated and studied with various method, including Mössbauer spectrometry. It was found that the Debye temperature has the values: (184 ± 14) and (180 ± 17) K for ferrocene components of **II.4** and **FTFCl₂** and $\theta_D = (218 \pm 15)$ K for $[(\text{Fe}(\text{tpy})_2)]^{2+}$ unit.

The mechanism leading to formation of derivative **II.5** is a fascinating example of the organic / organometallic chemistry complexity. The cyclohexenone ring contains a chiral centre showing the potential of generating materials for applications in asymmetric catalysis. At the same time, compound **II.6** could find application in visual α -aminoacids recognition by precipitation of host-guest complexes in acidified aqueous solutions.

2. In the attempt to obtain 1,1'-ferrocene bis(BODIPY), the half way ketopyrrole product and its BF_2 complex were obtained. UV-Vis absorption, Mössbauer spectroscopies, cyclic voltammetry and spectroelectrochemistry, combined with DFT calculations, were used in order to characterize their properties. Unfortunately the poor irreversible electrochemistry witnessed for the pyrroloxaborole derivative **FBF** does preclude its use as a useful redox reporter. On the other hand, compound **FKP** may be more suitable by using the chelating properties of the ketopyrrole group, and the binding of groups with nucleophilic character. Noting that the absorption profile for **FBF** stretches well into the red region, the compound may have more application as a dark-state energy transfer quencher for fluorophores which emit between 500 and 600 nm.

3. In the preparation of the trisubstituted ferrocene-based porphyrin derivative it would appear that the “one-pot” stoichiometry-correct reaction works as well as the preorganised method starting from a ferrocene–dipyrrromethane precursor. The only advantage of the second method is the slightly easier purification of the final product.

Our results clearly show that only direct photoinjection from the porphyrin excited state is relevant for the outlined ferrocene–porphyrin derivatives. Hence in the design of porphyrin-based systems for DSSC applications strongly coupled donor–acceptor pairs should be avoided.

4. Cu(II) and Pd(II) tetraferrocenylporphyrins were synthesized and used as catalysts for electrochemical proton reduction. The cyclic voltammetry experiments showed that electrocatalysis occurs when proton source is added (TFA or TEAHCl) at a moderate potential. The formation of phlorin intermediate was proved by UV-Vis spectroelectrochemistry. Performing bulk electrolysis with concomitant continuous flow rig with in-line GC analysis was used to detect qualitatively and quantitatively the molecular hydrogen produced with up to 73 % Faradaic efficiency. Certainly the introduction of ferrocene enhanced the electrocatalytic activity of porphyrin molecules, compared with tetraphenyl analogues. A cooperative ferrocenyl and metal influence is suggested, resulting in increased electron density on the β -pyrrole site of phlorin anion.

Hence, while most of the literature examples are based on the metal redox chemistry, this is an example of carbon-centred electrocatalysis of proton reduction. Still, the use of a more stable donor species is recommended in further research.

REFERENCES:

1. Kealy T.J., Pauson P.L. A New Type of Organo-Iron Compound. In: *Nature*, 1951, nr.168, p. 1039-1040.
2. Miller S.A., Tebboth J.A., Tremaine J.F. Dicyclopentadienyliron. In: *J. Chem. Soc.*, 1952, p. 632-635.
3. Woodward R.B., Rosenblum M., Whiting M.C. A new aromatic system. In: *J. Am. Chem. Soc.*, 1952, nr. 74 (13), p. 3458-3459.
4. Fischer E.O. et al. Aromatic complexes of metals XCIV. Competitive friedel—crafts acetylations of π -cyclopentadienyl metal complexes. *Journal of Organometallic Chemistry*, 1967, 7 (1), p. 113-119.
5. Smart J. C., Pinsky B. L. The chemistry of bis(fulvalene)divanadium. In: *J. Am. Chem. Soc.*, 1980, nr. 102, 1009-1015.
6. Hendrickson D.N., Sohn Y.S., Gray H.B. Magnetic susceptibility study of various ferricenium and iron(III) dicarbollide compounds. In: *Inorg. Chem.* 1971, nr. 10, 1559-1563.
7. Farre C. et al. Synthesis and electropolymerization studies of water-soluble pyrrole-ferrocene derivatives towards biochip device application. In: *Synthetic Metals*, 2007, nr. 157, p. 125-133.
8. Štěpnička P. *Ferrocenes: Ligands, Materials and Biomolecules*. Chichester: John Wiley & Sons Ltd, 2008. 655 p.
9. Kadish K., Smith K., Guillard R. *The Porphyrin Handbook*, Volume 6. London: Academic Press, 2000. 131 p.
10. Kadish K., Smith K., Guillard R. *The Porphyrin Handbook*, Volume 4. London: Academic Press, 2000. 62 p.
11. Kadish K., Smith K., Guillard R. *Handbook of Porphyrin Science. With Applications to Chemistry, Physics, Materials Science, Engineering, Biology and Medicine*. Volume 10: *Catalysis and Bio-Inspired Systems*. London: World Scientific Publishing, 2010. 533 p.
12. Kadish K., Smith K., Guillard R. *Handbook of Porphyrin Science. With Applications to Chemistry, Physics, Materials Science, Engineering, Biology and Medicine*. Volume 33: *Applications — Part II*. London: World Scientific Publishing, 2014. 488 p.
13. Kadish K., Smith K., Guillard R. *Handbook of Porphyrin Science. With Applications to Chemistry, Physics, Materials Science, Engineering, Biology and Medicine*. Volume 34: *Harnessing Solar Energy*. London: World Scientific Publishing, 2014. 392 p.
14. Nazeeruddin K., Pechy P., Gratzel M. Efficient panchromatic sensitization of nanocrystalline TiO₂ films by a black dye based on a trithiocyanato-ruthenium complex. In: *Chem. Commun.*, 1997, p. 1705-1706.
15. Allen M.R. et al. Warming caused by cumulative carbon emissions towards the trillionth tonne. In: *Nature*, 2009, nr. 458, p. 1163-1166.

16. Blaser H.-U., Spindler F. Enantioselective Catalysis for Agrochemicals: The Case History of the DUAL MAGNUM® Herbicide. In: CHIMIA International Journal for Chemistry, 1997, nr. 51 (6), p. 297-299.
17. Crossley M.J. et al. Regiospecific introduction of four substituents to porphyrin systems at antipodal pyrrolic positions. In: J. Chem. Soc., Chem. Commun., 1991, p. 1564-1566.
18. Fischer H., Orth H. Die Chemie des Pyrrols, Vol. 1. Leipzig: Akad. Verlagsges. 1934. (Johnson Reprint, New York and London, 1968)
19. Martin Gouterman. Study of the Effects of Substitution on the Absorption Spectra of Porphin. In: J. Chem. Phys., 1959, nr. 30, p. 1139-1161.
20. Dolphin D., Wijesekera T. Synthetic Aspects of Porphyrin and Metalloporphyrin Chemistry. In: Metalloporphyrins in Catalytic Oxidations, 1994, nr. 7, p. 193-239.
21. Rothmund P. Formation of porphyrins from pyrrole and aldehydes. In: J. Am. Chem. Soc., 1935, nr. 57 (10), p. 2010-2011.
22. Rothmund P. A New Porphyrin Synthesis. The Synthesis of Porphin. In: J. Am. Chem. Soc., 1936, nr. 58 (4), p. 625-627.
23. Rothmund P., Menotti A.R. Porphyrin Studies. IV. The Synthesis of $\alpha,\beta,\gamma,\delta$ -Tetraphenylporphine. In: J. Am. Chem. Soc. 1941, nr. 63, p. 267-270.
24. Adler A. D. et al. A simplified synthesis for meso-tetraphenylporphine. In: J. Org. Chem. 1967, nr. 32 (2), p. 476.
25. Dolphin D. Porphyrinogens and porphodimethenes, intermediates in the synthesis of meso-tetraphenylporphins from pyrroles and benzaldehyde. In: J. Heterocycl. Chem. 1970, nr. 7 (2), p. 275-283.
26. Lindsey J.S. Rothmund and Adler-Longo Reactions Revisited: Synthesis of Tetraphenyl porphyrins under Equilibrium Conditions. In: J. Org. Chem. 1987, nr. 52, p. 827-836.
27. Geier G.R. III, Lindsey J.S. Investigation of porphyrin-forming reactions. Part 1. Pyrrole aldehyde oligomerization in two-step, one-flask syntheses of meso-substituted porphyrins. In: J. Chem. Soc., Perkin Trans. 2, 2001, p. 677-686.
28. Geier G.R. III, Lindsey J.S. Investigation of porphyrin-forming reactions. Part 2. Examination of the reaction course in two-step, one-flask syntheses of meso-substituted porphyrins. In: J. Chem. Soc., Perkin Trans. 2, 2001, p. 687-700.
29. Hideki K. et al. Synthesis of 2-(Substituted Methyl)-3,4-Disubstituted Pyrroles and Their Conversion into the Corresponding Porphyrins. In: Bull. Chem. Soc. Jpn., 1992, nr. 65 (10), p. 2660-2667.
30. Arsenault G.P., Bullock E., MacDonald S.F. Pyrromethanes and Porphyrins Therefrom. In: J. Am. Chem. Soc., 1960, nr. 82 (16), p. 4384-4389.
31. Markovac A., MacDonald S. F. Syntheses with 5-dibromomethyl- and 5-formylpyrromethenes. In: Can. J. Chem., 1965, nr. 43, p. 3364-3371.

32. Geier G.R. III, Littler B.J., Lindsey J.S. Investigation of porphyrin-forming reactions. Part 3. The origin of scrambling in dipyrromethane aldehyde condensations yielding trans-A₂B₂-tetraarylporphyrins. In: J. Chem. Soc., Perkin Trans. 2, 2001, p. 701–711.
33. Johnson A.W. Synthesis of Porphyrins from 1,19-Dideoxybiladienes-ac and 1,19-Dideoxybilenes-b. In: The Porphyrins, Vol. I: Structure and Synthesis, Part A. New York: Academic Press, 1978, p. 235-264.
34. Turta C., Duca G., Marin I., Sirbu D. Chapter 3: Electrochemical Solar Cells Based on Pigments. In: *Management of Water Quality in Moldova*, SPRINGER, Series: *Water Science and Technology Library*, 2014, Vol. 69, p. 48-59.
35. Kay A., Graetzel M. Artificial photosynthesis. 1. Photosensitization of titania solar cells with chlorophyll derivatives and related natural porphyrins. In: J. Phys. Chem., 1993, nr. 97 (23), p. 6272–6277.
36. Wang X.-F. et al. Dye-sensitized solar cells using a chlorophyll derivative as the sensitizer and carotenoids having different conjugation lengths as redox spacers. In: Chem. Phys. Lett., 2005, nr. 408, p. 409-414.
37. Wang X.-F. et al. Effects of plant carotenoid spacers on the performance of a dye-sensitized solar cell using a chlorophyll derivative: Enhancement of photocurrent determined by one electron-oxidation potential of each carotenoid. In: Chem. Phys. Lett., 2006, nr. 423, p. 470-475.
38. Wang X.-F. et al. A dye-sensitized solar cells using pheophytin-carotenoid adduct: Enhancement of photocurrent by electron and singlet-energy transfer and by suppression of singlet-triplet annihilation due to the presence of the carotenoid moiety. In: Chem. Phys. Lett., 2007, nr. 439, 115-120.
39. Wang X.-F. et al. Extension of p-conjugation length along the Q_y axis of a chlorophyll a derivative for efficient dye-sensitized solar cells. In: Chem. Commun., 2009, p. 1523-1525.
40. Wang X.-F. et al. Chlorophyll-a derivatives with various hydrocarbon ester groups for efficient dye-sensitized solar cells. In: Langmuir, 2010, nr. 26, p. 6320-6327.
41. Cherian S., Wamser C.C. Adsorption and Photoactivity of Tetra(4-carboxyphenyl)porphyrin (TCPP) on Nanoparticulate TiO₂. In: J. Phys. Chem. B, 2000, nr. 104 (15), p. 3624-3629.
42. Nazeeruddin M.K. et al. Application of Metalloporphyrins in Nanocrystalline Dye-Sensitized Solar Cells for Conversion of Sunlight into Electricity. In: Langmuir, 2004, nr. 20, p. 6514-6517.
43. Wang Q. et al. Efficient Light Harvesting by Using Green Zn-Porphyrin-Sensitized Nanocrystalline TiO₂ Films. In: J. Phys. Chem. B, 2005, nr. 109 (32), p. 15397-15409.
44. Campbell W.M. et al. Highly Efficient Porphyrin Sensitizers for Dye-Sensitized Solar Cells. In: J. Phys. Chem. C, 2007, nr. 111 (32), p. 11760-11762.
45. Tanaka M. et al. Novel unsymmetrically π -elongated porphyrin for dye-sensitized TiO₂ cells. In: Chem. Commun., 2007, p. 2069-2071.

46. Lee C.-W. et al. Novel Zinc Porphyrin Sensitizers for Dye-Sensitized Solar Cells: Synthesis and Spectral, Electrochemical, and Photovoltaic Properties. In: *Chem.-Eur. J.*, 2009, nr. 15, p. 1403-1412.
47. Yella A. et al. Porphyrin-Sensitized Solar Cells with Cobalt (II/III)–Based Redox Electrolyte Exceed 12 Percent Efficiency. In: *Science*, 2011, nr. 334, p. 629-634.
48. Chiba Y. et al. Dye-Sensitized Solar Cells with Conversion Efficiency of 11.1%. In: *Jpn. J. Appl. Phys.*, 2006, nr. 45 (25), p. L638-L640.
49. Atkinson R.C.J., Gibson V.C., Long N.J. The syntheses and catalytic applications of unsymmetrical ferrocene ligands. In: *Chem. Soc. Rev.*, 2004, nr. 33, p. 313-328.
50. Bayly S.R., Beer P.D. Metal-Based Anion Receptor Systems. In: *Struct. Bond.*, 2008, nr. 129, p. 45-94.
51. Lee E.J., Wrighton M.S. Competitive Energy and Electron-Transfer Quenching of Excited Ruthenium Polypyridyls by Ferrocene Derivatives. In: *J. Am. Chem. Soc.*, 1991, nr. 113, p. 8562-8564.
52. Benniston A.C. et al. Electron Delocalization in Polyene-Bridged Binuclear Complexes. In: *J. Phys. Chem.*, 1994, nr. 98, p. 7798-7804.
53. Delgadillo A., Leiva A.M., Loeb B. Intramolecular excited state quenching: 5-[(E)-2-ferrocenylvinyl]-1,10-phenanthroline, a new donor ligand. In: *Polyhedron*, 2005, nr. 24, p. 1749–1754.
54. Geißer B., Alsfasser R. A peptide approach to covalently linked $[\text{Ru}(\text{bipy})_3]^{2+}$ -ferrocene and $[\text{Ru}(\text{bipy})_3]^{2+}$ -tyrosine conjugates. In: *Inorganica Chimica Acta*, 2003, nr. 344, p. 102-108.
55. Choua S. et al. Excited state properties of bis-tetraazaphenanthrene-Ru (II) diad complexes with a ferrocenyl unit. In: *Journal of Photochemistry and Photobiology A: Chemistry*, 1996, nr. 99, p. 127-136.
56. Heinze K., Hempel K., Beckmann M. Multielectron Storage and Photo-Induced Electron Transfer in Oligonuclear Complexes Containing Ruthenium(II) Terpyridine and Ferrocene Building Blocks. In: *Eur. J. Inorg. Chem.*, 2006, p. 2040-2050.
57. Hutchison K. et al. Spectroscopic and Photophysical Properties of Complexes of 4'-Ferrocenyl-2,2':6',2''-terpyridine and Related Ligands. In: *Inorg. Chem.*, 1999, nr. 38, p. 2516-2523.
58. Dong T.-Y. et al. Micromodulating the Electronic Coupling Across Redox-Active Ferrocenyl Spacer in Binuclear Ruthenium(II) Terpyridine Complexes: Synthesis, Electrochemistry, and Photophysical Properties in progress. In: *Organometallics*, 2008, nr. 27, p. 555-562.
59. Siemeling U. et al. Ferrocenyl-Functionalised Terpyridines and Their Transition-Metal Complexes: Syntheses, Structures and Spectroscopic and Electrochemical Properties. In: *Chem. Eur. J.*, 2003, nr. 9, p. 2819-2833.

60. Benniston A.C. et al. Electron Delocalization in Ethynyl-Bridged Binuclear Ruthenium (II) Polypyridine Complexes. *Angew. In: Chem. Int. Ed., Angew. Chem. Int. Ed. Engl.*, 1994, nr. 33, p. 1884-1885.
61. Matsuo Y. et al. A Ruthenium Bridge in Fullerene–Ferrocene Arrays: Synthesis of $[\text{Ru}(\text{C}_{60}\text{Me}_5)\text{R}(\text{CO})_2]$ ($\text{R}=\text{C}_6\text{H}_4\text{Fc}$, $\text{C}\equiv\text{CFc}$) and Their Charge-Transfer Properties. In: *Chem. Asian J.*, 2008, nr. 3, p. 841-848.
62. Matsuo Y. et al. Synthesis of Ruthenium Pentamethyl[60]fullerene Complexes Bearing Monodentate Diphenylphosphino-methane, -ferrocene, and -butane Ligands. In: *Bull. Korean Chem. Soc.*, 2010, nr. 31 (3), p. 697-699.
63. Nadtochenko V.A. et al. Photochemical and photophysical properties of meso-tetraferrocenylporphyrin. Quenching of meso-tetraphenylporphyrin by ferrocene. In: *Russian Chemical Bulletin*, 1999, nr. 48 (10), p. 1900-1903.
64. Nadtochenko V.A. et al. Femtosecond dynamics of relaxation of photoexcited mesotetraferrocenylporphyrin in the nonprotonated and diprotonated forms (Fc_4PH_2 and $\text{Fc}_4\text{PH}_4^{2+}$). In: *Russian Chemical Bulletin, International Edition*, 2002, nr. 51 (6), p. 986-993.
65. Schmidt E.S., Calderwood T.S., Bruce T.C. Synthesis and Characterization of a *meso*-Tetrakis(4-ferrocenylphenyl)porphyrin and Examination of Its Ability To Undergo Intramolecular Photocatalyzed Electron Transfer. In: *Inorg. Chem.*, 1986, nr. 25 (20), p. 3718-3720.
66. Solntsev P.V. et al. Unexpected fluorescence properties in an axially π -bonded ferrocenyl-containing porphyrin. In: *Chem. Commun.*, 2010, nr. 46, p. 6581-6583.
67. Paul D.B., Stefan S.K. A novel porphyrin-ferrocene-quinone linked molecule. In: *Journal of Organometallic Chemistry*, 1989, nr. 366, p. C6-C8.
68. Mansour H. et al. Synthesis and photophysical studies of porphyrin-ferrocene conjugates. In: *J. Porphyrins Phthalocyanines* 2007, nr. 11, p. 719-728.
69. Giasson R. et al. Inter- and Intramolecular Quenching of the Singlet Excited State of Porphyrins by Ferrocene. In: *J. Phys. Chem.*, 1993, nr. 97, p. 2596-2601.
70. Pareek Y., Ravikanth M. Synthesis and properties of cyclophosphazenes appended with covalently linked porphyrineferrocene conjugates. In: *Journal of Organometallic Chemistry*, 2013, nr. 724, p. 67-74.
71. Thornton N.B. et al. Intramolecular Quenching of Porphyrin Fluorescence by a Covalently Linked Ferrocene in DNA Scaffolding. In: *J. Phys. Chem. B* 1998, nr. 102, p. 2101-2110.
72. Winters M.U. et al. Probing the Efficiency of Electron Transfer through Porphyrin-Based Molecular Wires. In: *J. Am. Chem. Soc.*, 2007, nr. 129, p. 4291-4297.
73. Kalita D., Morisue M., Kobuke Y. Synthesis and electrochemical properties of slipped-cofacial porphyrin dimers of ferrocene-functionalized Zn-imidazolyl-porphyrins as potential terminal electron donors in photosynthetic models. In: *New J. Chem.*, 2006, nr. 30, p. 77-92.

74. Tanihara J., Ogawa K., Kobuke Y. Two-photon absorption properties of conjugated supramolecular porphyrins with electron donor and acceptor. In: *Journal of Photochemistry and Photobiology A: Chemistry*, 2006, nr. 178, p. 140-149.
75. Lee S.-H. et al. Long-lived long-distance photochemically induced spin-polarized charge separation in β,β' -pyrrolic fused ferrocene-porphyrin-fullerene systems. In: *Chem. Sci.*, 2012, nr. 3, p. 257-269.
76. Li Y. et al. Synthesis and characterization of porphyrin-ferrocene-fullerene triads. In: *Tetrahedron*, 2006, nr. 62, p. 4285-4293.
77. D'Souza F. et al. Design and Studies on Supramolecular Ferrocene-Porphyrin-Fullerene Constructs for Generating Long-Lived Charge Separated States. In: *J. Phys. Chem. B*, 2006, nr. 110, 25240-25250.
78. Maes M. et al. Photoinduced electron and energy transfer processes in rotaxanes containing zinc porphyrin as pendant and [60]fullerene and ferrocene as axle ends. In: *J. Porphyrins Phthalocyanines*, 2005, nr. 9, p. 724-734.
79. Rajkumar G.A. et al. Prolongation of the Lifetime of the Charge-Separated State at Low Temperatures in a Photoinduced Electron-Transfer System of [60]Fullerene and Ferrocene Moieties Tethered by Rotaxane Structures. In: *J. Phys. Chem. B*, 2006, nr. 110, p. 6516-6525.
80. Schmitt M., Kishore R.S.K., Bats J.W. Synthesis of supramolecular fullerene-porphyrin-Cu(phen)₂-ferrocene architectures. A heteroleptic approach towards tetrads. In: *Org. Biomol. Chem.*, 2007, nr. 5, p. 78-86.
81. Delaire J.A., Delouis J.-F., Zakrzewski J. Formation and quenching of the photoexcited triplet state of tetrasulfonated zinc phthalocyanine, ZnPcS₄⁴⁻ by azaferrocene and ferrocene. In: *Journal of Photochemistry and Photobiology A: Chemistry*, 2001, nr. 141, p. 169-173.
82. Poon K.-W. et al. Synthesis and Electrochemistry of Ferrocenylphthalocyanines. In: *Organometallics*, 1999, nr. 18, p. 3528-3533.
83. Poon K.-W. et al. Tetrapyrrole Derivatives Substituted with Ferrocenylethynyl Moieties. Synthesis and Electrochemical Studies. In: *J. Org. Chem.*, 2001, nr. 66, p. 1553-1559.
84. Solntsev P.V. et al. Photoinduced Charge Transfer in Short-Distance Ferrocenylsubphthalocyanine Dyads. In: *Inorg. Chem.*, 2012, nr. 51, p. 6537-6547.
85. Maligaspe E. et al. Redox and Photoinduced Electron-Transfer Properties in Short Distance Organoboryl Ferrocene-Subphthalocyanine Dyads. In: *Inorg. Chem.*, 2014, nr. 53, p. 9336-9347.
86. González-Rodríguez D. et al. Photoinduced Charge-Transfer States in Subphthalocyanine-Ferrocene Dyads. In: *J. Am. Chem. Soc.*, 2006, nr. 128 (33), p. 10680-10681.
87. González-Rodríguez D. et al. Activating Multistep Charge-Transfer Processes in Fullerene-Subphthalocyanine-Ferrocene Molecular Hybrids as a Function of π - π Orbital Overlap. In: *J. Am. Chem. Soc.*, 2010, nr. 132 (46), p. 16488-16500.
88. Liu J.-Y. et al. Photoinduced Electron Transfer in a Ferrocene-Distyryl BODIPY Dyad and a Ferrocene-Distyryl BODIPY-C₆₀ Triad. In: *Chem. Phys. Chem*, 2012, nr. 13 (8), p. 2030-2036.

89. Sugimoto H., Tanaka T., Osuka A. Ferrocene-appended Subporphyrins. In: *Chem. Lett.*, 2011, nr. 40, p. 629-631.
90. Biju V. et al. Photoinduced Electron Transfer between 1,2,5-Triphenylpyrrolidinofullerene Cluster Aggregates and Electron Donors. In: *Langmuir*, 2001, nr. 17, p. 2930-2936.
91. Araki Y., Yasumura Y., Ito O. Photoinduced Electron Transfer Competitive with Energy Transfer of the Excited Triplet State of [60]Fullerene to Ferrocene Derivatives Revealed by Combination of Transient Absorption and Thermal Lens Measurements. In: *J. Phys. Chem. B*, 2005, nr. 109, p. 9843-9848.
92. Guldi D.M. et al. Intramolecular Electron Transfer in Fullerene/Ferrocene Based Donor-Bridge-Acceptor Dyads. In: *J. Am. Chem. Soc.*, 1997, nr. 119 (5), p. 974-980.
93. Conti F. et al. Time-resolved EPR investigation of intramolecular photoinduced electron transfer in spin-labeled fullerene/ferrocene dyads. In: *Phys. Chem. Chem. Phys.*, 2001, nr. 3, p. 3526-3531.
94. Hauke F. et al. Evidence of Pronounced Electronic Coupling in a Directly Bonded Fullerene - Ferrocene Dyad. In: *Chem. Phys. Chem.* 2002, nr. 3, p. 195-205.
95. Caporossi F. et al. Enhanced Electron Transfer Rate in a Rigid Ferrocene–Fulleropyrrolidine Dyad. In: *Eur. J. Org. Chem.*, 2006, p. 4362–4366.
96. Kumar A., Menon S.K. Fullerene-ferrocene dyad linked by rigid bilinkage: synthesis, photophysical properties and application as copper ion sensor. In: *Journal of Physical Organic Chemistry*, 2009, nr. 22 (7), p. 661-669.
97. Langa F. et al. Synthesis and Properties of Isoxazolo[60]fullerene-Donor Dyads. In: *J. Org. Chem.* 2000, nr. 65, p. 8675-8684.
98. Delgado J.L. et al. Synthesis and photophysical properties of a [60]fullerene compound with dimethylaniline and ferrocene connected through a pyrazolino group: a study by laser flash photolysis. In: *Phys. Chem. Chem. Phys.*, 2006, nr. 8, p. 4104-4111.
99. Perez L. et al. Comparison between the Photophysical Properties of Pyrazolo- and Isoxazolo[60]fullerenes with Dual Donors (Ferrocene, Aniline and Alkoxyphenyl). In: *Eur. J. Org. Chem.*, 2007, p. 2175-2185.
100. Oswald F. et al. Photophysical Properties of the Newly Synthesized Triad Based on [70]Fullerene Studies with Laser Flash Photolysis. In: *J. Phys. Chem. B*, 2007, nr. 111, p. 4335-4341.
101. Seok J.H. et al. Photoinduced processes of newly synthesized bisferrocene and bisfullerene-substituted tetrads with a triphenylamine central block. In: *J. Organomet. Chem.*, 2009, nr. 694, p. 1818-1825.
102. Andersson C.-H., Nyholm L., Grennberg H. Synthesis and characterization of a ferrocene-linked bis-fullerene[60] dumbbell. In: *Dalton Trans.*, 2012, nr. 41, p. 2374-2381.
103. Herranz M.A. et al. Donor/Acceptor Fulleropyrrolidine Triads. In: *J. Org. Chem.*, 2000, nr. 65, p. 5728-5738.

104. D'Souza F. et al. A Ferrocene-C₆₀-Dinitrobenzene Triad: Synthesis and Computational, Electrochemical, and Photochemical Studies. In: *J. Phys. Chem. A*, 2002, nr. 106, p. 649-656.
105. Figueira-Duarte T.M. et al. Synthesis and electronic properties of fullerene derivatives substituted with oligophenylenevinylene-ferrocene conjugates. In: *New J. Chem.*, 2008, nr. 32, p. 54-64.
106. Kanato H. et al. Synthesis and Photophysical Properties of Ferrocene-Oligothiophene-Fullerene Triads. In: *J. Org. Chem.*, 2004, nr. 69, p. 7183-7189.
107. Nakamura T. et al. Effects of Extension or Prevention of π -Conjugation on Photoinduced Electron Transfer Processes of Ferrocene-Oligothiophene-Fullerene Triads. In: *J. Phys. Chem. A*, 2006, nr. 110, p. 3471-3479.
108. Wu Y. et al. N-type cascade electron transfer along an oxidative gradient. In: *Chem. Commun.*, 2009, p. 6955-6957.
109. Supur M. et al. Elongation of Lifetime of the Charge-Separated State of FerroceneNaphthalenediimide[60]Fullerene Triad via Stepwise Electron Transfer. In: *J. Phys. Chem. A*, 2011, nr. 115, p. 14430-14437.
110. Campidelli S. et al. Liquid-crystalline fullerene-ferrocene dyads. In: *J. Mater. Chem.*, 2004, nr. 14, p. 1266-1272.
111. Campidelli S. et al. Photophysical, electrochemical, and mesomorphic properties of a liquid-crystalline [60]fullerene-peralkylated ferrocene dyad. In: *J. Mater. Chem.*, 2008, nr. 18, p. 1504-1509.
112. Araki Y. et al. Self-Assembled Supramolecular Ferrocene-Fullerene Dyads and Triad: Formation and Photoinduced Electron Transfer. In: *J. Phys. Chem. C*, 2008, nr. 112, p. 2222-2229.
113. Mateo-Alonso A., Prato M. Synthesis of Fullerene-Stoppered Rotaxanes Bearing Ferrocene Groups on the Macrocycle. In: *Eur. J. Org. Chem.* 2010, p. 1324-1332.
114. Feng K. et al. Photoinduced Triplet-Triplet Energy Transfer in a 2-Ureido-4(1H)-Pyrimidinone-Bridged, Quadruply Hydrogen-Bonded Ferrocene-Fullerene Assembly. In: *Chem. Phys. Chem.*, 2013, nr. 14, p. 198-203.
115. Na Y. et al. Visible Light-Driven Electron Transfer and Hydrogen Generation Catalyzed by Bioinspired [2Fe2S] Complexes. In: *Inorg. Chem.*, 2008, nr. 47, p. 2805-2810.
116. Poddutoori P. et al. Photoinitiated multistep charge separation in ferrocene-zinc porphyrin-diiron hydrogenase model complex triads. In: *Energy Environ. Sci.*, 2011, nr. 4, p. 2441-2450.
117. Wang F. et al. Artificial Photosynthetic Systems Based on [FeFe]-Hydrogenase Mimics: the Road to High Efficiency for Light-Driven Hydrogen Evolution. In: *ACS Catal.*, 2012, nr. 2, p. 407-416.
118. Wu L.-Z. et al. Enhancement of the Efficiency of Photocatalytic Reduction of Protons to Hydrogen via Molecular Assembly. In: *Acc. Chem. Res.*, 2014, nr. 47, p. 2177-2185.

119. Chauhan R. et al. Application of p-Extended Ferrocene with Varied Anchoring Groups as Photosensitizers in TiO₂-Based Dye-Sensitized Solar Cells (DSSCs). In: Chem. Asian J., 2011, nr. 6, p. 1525-1532.
120. Kumar A. et al. Synthesis, Structure and Light-Harvesting Properties of Some New Transition-Metal Dithiocarbamates Involving Ferrocene. In: Chem. Eur. J., 2010, nr. 16, p. 4307-4314.
121. Singh S.K. et al. Syntheses and structural characterization of new heteroleptic 1,10-bis(diphenyl phosphino)ferrocene-dithio complexes of Ni, Pd and Pt: Their uses as sensitizers in TiO₂ dye sensitized solar cells. In: Journal of Organometallic Chemistry, 2013, nr. 745-746, p. 190-200.
122. Sirbu D. et al. Synthesis and properties of a meso-tris-ferrocene appended zinc(II) porphyrin and a critical evaluation of its dye sensitised solar cell (DSSC) performance. In: RSC Adv., 2014, nr. 4, p. 22733-22742.
123. Harney J.P., Dransfield T., Rochford J. Convergent synthesis of meso-ferrocenyl porphyrins for TiO₂ sensitization. In: Tetrahedron Lett., 2013, nr. 53, p. 4700-4703.
124. Minshi A., Soonwha K., Jong-Dal H. Synthesis and Characterization of Peripherally Ferrocene-modified Zinc Phthalocyanine for Dye-sensitized Solar Cell. In: Bull. Korean Chem. Soc., 2010, nr. 31 (11), p. 3272-3278.
125. Uosaki K. et al. Very Efficient Visible-Light-Induced Uphill Electron Transfer at a Self-Assembled Monolayer with a Porphyrin-Ferrocene-Thiol Linked Molecule. In: J. Am. Chem. Soc., 1997, nr. 119, p. 8367-8368.
126. Kondo T. et al. Effect of Surface Morphology of a Gold Substrate on Photocurrent Efficiency at a Gold Electrode Modified with a Self-Assembled Monolayer of a Porphyrin-Ferrocene-Thiol Linked Molecule. In: Chemistry Letters, 2000, nr. 29 (8), p. 964-965.
127. Imahori H. et al. Vectorial Multistep Electron Transfer at the Gold Electrodes Modified with Self-Assembled Monolayers of Ferrocene-Porphyrin-Fullerene Triads. In: J. Phys. Chem. B, 2000, nr. 104 (9), p. 2099-2108.
128. Fujitsuka M. et al. Long-Lived Charge Separation with High Quantum Yield in a Ferrocene-Porphyrin-Fullerene Triad. In: Chemistry Letters, 1999, nr. 28 (8), p. 721-722.
129. Imahori H. et al. Light-Harvesting and Photocurrent Generation by Gold Electrodes Modified with Mixed Self-Assembled Monolayers of Boron-Dipyrrin and Ferrocene-Porphyrin-Fullerene Triad. In: J. Am. Chem. Soc., 2001, nr. 123, p. 100-110.
130. Imahori H. et al. Vectorial Electron Relay at ITO Electrodes Modified with Self-Assembled Monolayers of Ferrocene-Porphyrin-Fullerene Triads and Porphyrin-Fullerene Dyads for Molecular Photovoltaic Devices. In: Chem. Eur. J., 2004, nr. 10, p. 5111-5122.
131. Morisue M. et al. Fine-tuning of a ferrocene|porphyrin|ITO redox cascade for efficient sequential electron transfer commenced by an S₂ photoexcited special pair mimic. In: Chem. Commun., 2007, p. 2348-2350.

132. Lee M.H., Kim J.W., Lee C.Y. [60] Fullerene-porphyrine-ferrocene triad self-assembled monolayers (SAMs) for photovoltaic applications. In: J. Organomet. Chem., 2014, nr. 761, p. 20-27.
133. Wijesinghe C.A. et al. A Charge-Stabilizing, Multimodular, Ferrocene–Bis(triphenylamine)–Zincporphyrin–Fullerene Polyad. In: Chem. Eur. J., 2013, nr. 19, p. 9629-9638.
134. Smirnov A.Y. et al. High-Efficiency Energy Conversion in a Molecular Triad Connected to Conducting Leads. In: J. Phys. Chem. C, 2009, nr. 113, p. 21218-21224.
135. Prashanth K.P. et al. Photoinduced Charge Separation in a Ferrocene-Aluminum(III) Porphyrin-Fullerene Supramolecular Triad. In: J. Phys. Chem. B, 2010, nr. 114, p. 14348-14357.
136. Daeneke T. et al. High-efficiency dye-sensitized solar cells with ferrocene-based electrolytes. In: Nature Chemistry, 2011, nr. 3, p. 211-215.
137. Daeneke T. et al. Dye regeneration and charge recombination in dye-sensitized solar cells with ferrocene derivatives as redox mediators. In: Energy Environ. Sci., 2012, nr. 5, p. 7090-7099.
138. Ramasamy E., Lee J. Ferrocene-derivatized ordered mesoporous carbon as high performance counter electrodes for dye-sensitized solar cells. In: Carbon, 2010, nr. 48, p. 3715-3720.
139. Phougat N. et al. Metal porphyrins as electrocatalysts for commercially important reactions. In: Transition Metal Chemistry, 2003, nr. 28, p. 838-847.
140. Bhugun I., Lexa D., Saveant J.-F. Catalysis of the Electrochemical Reduction of Carbon Dioxide by Iron(0) Porphyrins. Synergistic Effect of Lewis Acid Cations. In: J. Phys. Chem., 1996, nr. 100, p. 19981-19985.
141. Bhugun I., Lexa D., Saveant J.-F. Homogeneous Catalysis of Electrochemical Hydrogen Evolution by Iron(0) Porphyrins. In: J. Am. Chem. Soc., 1996, nr. 118 (16), p. 3982-3983.
142. Jing Chu et al. Synthesis and electro-catalytic properties of a dinuclear palladium(I) 1,3-bis[(2-chloro)benzene]triazene complex. In: Inorganica Chimica Acta, 2014, nr. 410, p. 191–194.
143. Benniston A.C., Sirbu D. et al. A simple method for desymmetrizing 1,1'-ferrocenedicarboxaldehyde. In: Tetrahedron Letters, 2014, nr. 55 (28), p. 3777-3780.
144. Sirbu D. Temperature dependence of ^{57}Fe -mössbauer spectra for a $\text{Fe}_{\text{Fc}}^{\text{II}} - \text{Fe}_{\text{tpy}}^{\text{II}} - \text{Fe}_{\text{Fc}}^{\text{II}}$ trinuclear system. In: Chemistry Journal of Moldova. General, Industrial and Ecological Chemistry, 2015, nr. 10 (1), p. 84-88.
145. U. Nettekoven et al. Steric and Electronic Ligand Perturbations in Catalysis: Asymmetric Allylic Substitution Reactions Using C2-Symmetrical Phosphorus-Chiral (Bi)ferrocenyl Donors. In: J. Org. Chem., 2001, nr. 66, p. 759-770.
146. Dong T.-Y., Lai L.-L. A novel method to synthesize asymmetrical disubstituted ferrocenes. In: J. Organomet. Chem., 1996, nr. 509, p. 131-134.

147. L.-X. Dai et al. Asymmetric catalysis with chiral ferrocene ligands. In: *Acc. Chem. Res.*, 2003, nr. 36, p. 659-667.
148. Zhang W. et al. Novel chiral P,N-ferrocene ligands in palladium-catalyzed asymmetric allylic alkylations. In: *Tetrahedron: Asymmetry*, 1998, nr. 9, p. 3371-3380.
149. Argyropoulos N., Coutouli-Argyropoulos E. Synthesis of unsymmetrical 1,1'-disubstituted ferrocenes. Formation of ferrocenophanes via intramolecular cycloaddition. In: *J. Organomet. Chem.*, 2002, nr. 654, p. 117-122.
150. Li C. et al. Neutral Molecule Receptor Systems Using Ferrocene's "Atomic Ball Bearing" Character as the Flexible Element. In: *J. Am. Chem. Soc.*, 1997, nr. 119, p. 1609-1618.
151. Batsanov A.S. et al. Synthesis and Structure of Planar Chiral, Bifunctional Aminoboronic Acid Ferrocene Derivatives. In: *Organometallics*, 2007, nr. 26, p. 2414-2419.
152. Toma S., Sališová M., Solčániová E. Electrophilic substitutions on some ferrocenyl analogues of chalcones an unusual reaction caused by the high stability of the α -ferrocenylmethyl carbenium ion. In: *J. Organomet. Chem.*, 1975, nr. 90, p. 335-341.
153. Solčániová E., Toma S., Fiedlerová A. Investigation of substituent effects on the ^1H and ^{13}C NMR spectra of ferrocene analogues of chalcones. In: *Org. Magn. Reson.*, 1980, nr. 14, p. 181-185.
154. Gyömöre Á., Csámpai A. Synthesis and structure of planar chiral Ferroceno [*d*]pyridazinones, the first representatives of a novel class of fused metallocenes. In: *J. Organomet. Chem.*, 2011, nr. 696, p. 1626-1631.
155. Kröhnke F. The Specific Synthesis of Pyridines and Oligopyridines. In: *Synthesis*, 1976, p. 1-24.
156. Constable E.C. et al. Complexes containing ferrocenyl groups as redox spectators; synthesis, molecular structure and co-ordination behaviour of 4'-ferrocenyl-2,2':6',2''-terpyridine. In: *J. Chem. Soc., Dalton Trans.*, 1994, p. 645-650.
157. Braterman P., Song J.-I., Peacock R. Electronic absorption spectra of the iron(II) complexes of 2,2'-bipyridine, 2,2'-bipyrimidine, 1,10-phenanthroline, and 2,2':6',2''-terpyridine and their reduction products. In: *Inorg. Chem.*, 1992, nr. 31, p. 555-559.
158. Maciejewski A. et al. Determination of ferrocene triplet lifetime by measuring $T_1 \rightarrow T_1$ energy transfer to phenylosazone-D-glucose. In: *Chem. Phys. Lett.*, 1988, nr. 153, p. 227-232.
159. Constable E.C. et al. Development of supramolecular structure through alkylation of pendant pyridyl functionality. In: *J. Chem. Soc., Dalton Trans.*, 2000, p. 2219-2228.
160. Wood C. J. et al. Novel triphenylamine-modified ruthenium(II) terpyridine complexes for nickel oxide-based cathodic dye-sensitized solar cells. In: *RSC Adv.*, 2014, nr. 4, p. 5782-5791.
161. Shujian Q. et al. Synthesis and Fluorescence Properties of 5,7-Diphenylquinoline and 2,5,7-Triphenylquinoline Derived from m-Terphenylamine. In: *Molecules*, 2007, nr. 12, p. 988-996.
162. Xiang J.-N. et al. An efficient approach to the synthesis of 1,3-diaryl-1,2,3,4-[4H]-tetrahydronaphthalene-2-carboxylic acids. In: *Bioorg. Med. Chem.*, 1998, nr. 6, p. 695-700.

163. Brian Farlow et al. Synthesis, x-ray structural determination and coordination chemistry of 4'-ferrocenyl-2,2':6',2''-terpyridine. In: *Polyhedron*, 1993, nr. 12 (23), p. 2891-2894.
164. Lin Li et al. Synthesis, characterization and crystal structure of 6-ferrocenyl-2,4-dihydroxy-2,4-di(pyridine-2-yl) cyclohexanecarbonyl ferrocene. In: *Transition Met Chem*, 2008, nr. 33, p. 85-89.
165. Pappalardo S. et al. Synthesis and Complexation Studies of Regioisomers and Conformational Isomers of p-tert-Butylcalix[4]arene Bearing Pyridine or Pyridine N-Oxide Pendant Groups at the Lower Rim. In: *J. Org. Chem.*, 1995, nr. 60 (14), p. 4576-4584.
166. Gütllich P., Bill E., Trautwein A.X. *Mössbauer Spectroscopy and Transition Metal Chemistry*. Berlin: Springer – Verlag, 2011, XV. 569 p.
167. Pingheng Z. et al. Temperature Dependence of the Mössbauer Effect on Prussian Blue Nanowires. In: *Hyperfine Interactions*, 2002, nr. 142, p. 601-606.
168. Korecz L. et al. The Mössbauer investigation of some derivatives of ferrocenes. In: *Inorganica Chimica Acta*, 1974, nr. 9, p. 209-212.
169. Clemance M.C., Roberts R.M.G., Silver J. Mössbauer studies on ferrocene complexes VIII. Diacetyl ferrocene-metal halide complexes. In: *Journal of Organometallic Chemistry*, 1983, nr. 247, p. 219-222.
170. England J. et al. Electronic Structures of the Electron Transfer Series $[M(\text{bpy})_3]^n$, $[M(\text{tpy})_2]^n$, and $[\text{Fe}(\text{bpy})_3]^n$ ($M = \text{Fe}, \text{Ru}$; $n = 3+, 2+, 1+, 0, 1-$): A Mössbauer Spectroscopic and DFT Study. In: *European Journal of Inorganic Chemistry*, 2012, p. 4605–4621.
171. Hofmeier H., Schubert U.S. Recent developments in the supramolecular chemistry of terpyridine–metal complexes. In: *Chemical Society Reviews*, 2004, nr. 33, p. 373-399.
172. Herber R.H. *Chemical Mössbauer Spectroscopy*. New York: Plenum Press, 1984, p. 199-216.
173. Ulrich S., Schubert H.H., Newkome G.R. *Modern Terpyridine Chemistry*. Weinheim: Wiley-VCH, 2006, p. 37-68.
174. Pound R.V., Rebka G.A. Variation with Temperature of the Energy of Recoil-Free Gamma Rays from Solids. In: *Physical Review Letters*, 1960, nr. 4 (6), p. 274-275.
175. Benniston A.C., Sirbu D. et al. Synthesis, molecular structure and properties of a ferrocene-based difluoropyrrolo-oxaborole derivative. In: *Eur. J. Inorg. Chem.*, 2014, nr. 36, p. 6212-6219.
176. Choi S.H. et al. X-ray diffraction, DFT, and spectroscopic study of N,N'-difluoroboryl-5-(2-thienyl)dipyrin and fluorescence studies of related dipyrromethanes, dipyrins and BF_2 -dipyrins and DFT conformational study of 5-(2-thienyl)dipyrin. In: *J. Chem. Crystallogr.*, 2007, nr. 37 (5), p. 315 -331.
177. Karolin J. et al. Fluorescence and Absorption Spectroscopic Properties of Dipyrrometheneboron Difluoride (BODIPY) Derivatives in Liquids, Lipid Membranes, and Proteins. In: *J. Am. Chem. Soc.*, 1994, nr. 116 (17), p. 7801-7806.

178. Frath D. et al. Fluorescent boron(III) iminocoumarins (Boricos). *Chem. Commun.*, 2013, nr. 49, p. 4908-4910.
179. Broering M., Krueger R., Kleeberg C. BF₂-Chelate Complexes of 6-(4-Iodophenyl)-2,3,4,8,9,10-hexamethyldipyrin and 2-(4-Iodobenzoyl)-3,4,5-trimethylpyrrole: Fluorescent Dyes with a Chemical Anchor Group. In: *Z. Anorg. Allg. Chem.*, 2008, nr. 634, p. 1555-1559.
180. Chen J. et al. Synthesis and spectroscopic properties of 2-ketopyrrole–BF₂ complexes: a new class of fluorescent dye. In: *Tetrahedron Lett.*, 2000, nr. 41, p. 2303-2307.
181. Yin X. et al. A highly sensitive viscosity probe based on ferrocene-BODIPY dyads. In: *Dalton Trans.*, 2010, nr. 39, p. 9929-9935.
182. Koszarna B., Butenschän H., Gryko D.T. The synthesis and properties of bis-1,1'-(porphyrinyl)ferrocenes. In: *Org. Biomol. Chem.*, 2005, 3, p. 2640-2645.
183. Xie X. Conformational dynamics of bis(BF₂)-2,2'-bidipyrins revealed by through-space ¹³C – ¹⁹F and ¹⁹F – ¹⁹F couplings. In: *Magn. Reson. Chem.*, 2009, nr. 47, p. 1024-1030.
184. Good M.L., Buttone J., Foyt D. Mössbauer spectroscopy of metal sandwich compounds. In: *Ann. N. Y. Acad. Sci.*, 1974, nr. 239, p. 193-207.
185. Neshvad G., Roberts R.M.G., Silver J. Mössbauer studies on ferrocene complexes : V. Protonation of ferrocenyl ketones. In: *J. Organomet. Chem.*, 1982, nr. 236, p. 349-358.
186. Wang M. et al. The Influence of Charge Transport and Recombination on the Performance of Dye-Sensitized Solar Cells. In: *ChemPhysChem*, 2009, nr. 10, p. 290-299.
187. Haque S.A. et al. Charge Separation versus Recombination in Dye-Sensitized Nanocrystalline Solar Cells: the Minimization of Kinetic Redundancy. In: *J. Am. Chem. Soc.*, 2005, nr. 127, p. 3456-3462.
188. Tian H. et al. A Triphenylamine Dye Model for the Study of Intramolecular Energy Transfer and Charge Transfer in Dye-Sensitized Solar Cells. In: *Adv. Funct. Mater.*, 2008, nr. 18, p. 3461-3468.
189. Richard L.W. et al. Electron Dynamics in Nanocrystalline ZnO and TiO₂ Films Probed by Potential Step Chronoamperometry and Transient Absorption Spectroscopy. In: *J. Phys. Chem. B*, 2002, nr. 106 (31), p. 7605-7613.
190. Narayanan S.J. et al. Synthesis of meso Ferrocenyl Porphyrins. In: *Synlett*, 2000, nr. 12, p. 1834-1836.
191. Nemykin V.N. et al. Long-Range Electronic Communication in Free-Basemeso-Poly(Ferrocenyl)-Containing Porphyrins. In: *Inorg. Chem.*, 2010, nr. 49, p. 7497-7509.
192. Slota R. et al. Structural and Molecular Characterization of meso-Substituted Zinc Porphyrins: A DFT Supported Study. In: *Molecules*, 2011, nr. 16, p. 9957-9971.
193. Nemykin V.N. and Hadt R.G. Interpretation of the UV–vis Spectra of themeso(Ferrocenyl)-Containing Porphyrins using a TDDFT Approach: Is Gouterman's Classic Four-Orbital Model Still in Play? In: *J. Phys. Chem. A*, 2010, nr. 114, p. 12062-12066.

194. Nemykin V.N. et al. Mixed-valence states formation in conformationally flexible metal-free 5,10,15,20-tetraferrocenylporphyrin and 5,10-bisferrocenyl-15,20-bisphenylporphyrin. In: Dalton Trans., 2007, 31, p. 3378-3389.
195. Gouterman M., Wagnière G. H. Spectra of porphyrins. In: J. Mol. Spectrosc., 1963, nr. 11, p. 108-127.
196. Nemykin V.N. et al. Electron-Transfer Processes in Metal-Free Tetraferrocenylporphyrin. Understanding Internal Interactions To Access Mixed-Valence States Potentially Useful for Quantum Cellular Automata. In: J. Am. Chem. Soc., 2009, nr. 131, p. 14969-14978.
197. Nemykin V.N. et al. Metal-free and transition-metal tetraferrocenylporphyrins part 1: synthesis, characterization, electronic structure, and conformational flexibility of neutral compounds. In: Dalton Trans., 2008, nr. 32, p. 4233-4246.
198. Closs G.L., Closs L.E. Negative Ions of Porphin Metal Complexes. In: J. Am. Chem. Soc., 1963, nr. 85, p. 818-819.
199. Benniston A.C., Harriman A., Li P. Bidirectional Electron Transfer in Molecular Tetrads. In: J. Am. Chem. Soc., 2010, nr. 132, p. 26-27.
200. Hart A.S. et al. Porphyrin-Sensitized Solar Cells: Effect of Carboxyl Anchor Group Orientation on the Cell Performance. In: ACS Appl. Mater. Interfaces, 2013, nr. 5 (11), p. 5314-5323.
201. Gibson E.A. et al. Cobalt Polypyridyl-Based Electrolytes for p-Type Dye-Sensitized Solar Cells. In: J. Phys. Chem. C, 2011, nr. 115, p. 9772-9779.
202. Feldt S.M. et al. Regeneration and recombination kinetics in cobalt polypyridine based dye-sensitized solar cells, explained using Marcus theory. In: Phys. Chem. Chem. Phys., 2013, nr. 15, p. 7087-7097.
203. Subhra S. et al. Selective four electron reduction of O₂ by an iron porphyrin electrocatalyst under fast and slow electron fluxes. In: Chem. Commun., 2012, nr. 48, p. 7631-7633.
204. Loim N.M., Abramova N.V., Sokolov V.I. Synthesis of 5,10,15,20-tetra(ruthenocenyl)porphyrin and 5,10,15,20-tetra(ferrocenyl)porphyrin. In: Mendelev Comm., 1996, p. 46-47.
205. Rohde G.T. et al. Long-range metal-metal coupling in transition-metal 5,10,15,20-tetraferrocenylporphyrins. In: New J. Chem., 2011, nr. 35, p. 1440-1448.
206. Regimol G., Padmanabhan M. Solvent effects on some new meso-aryl substituted octabromoporphyrins. Proc. In: Indian Acad. Sci. (Chem. Sci.), 2003, nr. 115 (4), p. 263-271.
207. Lanese J.G., Wilson G.S. Electrochemical Studies of Zinc Tetraphenylporphin. In: J. Electrochem. Soc., 1972, nr. 119 (8), 1039-1043.
208. Wilson G.S., Peychal-Heiling G. Electrochemical studies of tetraphenylporphin, tetraphenylchlorin, and tetraphenylbacteriochlorin. In: Anal. Chem., 1971, nr. 43 (4), p. 550-556.
209. Fourmond V. et al. H₂ Evolution and Molecular Electrocatalysts: Determination of Overpotentials and Effect of Homoconjugation. In: Inorg. Chem., 2010, nr. 49, p. 10338-10347.

210. Krattinger B., Callot H.J. The first stable monocyclic phlorin free base. Preparation and X-ray structure determination of 5,21-dihydro-5,10,15,20,22-pentaphenylporphyrin (N-phenyl-meso-tetraphenylphlorin). In: Chem. Commun., 1996, p. 1341-1342.
211. Inhoffen H.H. et al. Zur weiteren Kenntnis des Chlorophylls und des Hämins, XII. Elektrochemische Reduktionen an Porphyrinen und Chlorinen, IV. In: Justus Liebigs Annalen der Chemie, 1967, nr.704 (1), p. 188-207.
212. Witte L., Fuhrhop J.-H. Darstellung und Reaktivität sterisch überladener Porphyrine. In: Angewandte Chemie, 1975, nr. 87 (10), p. 387-388.
213. Fourmond V. et al. A nickel-manganese catalyst as a biomimic of the active site of NiFe hydrogenases: a combined electrocatalytic and DFT mechanistic study. In: Energy Environ. Sci., 2011, nr. 4, p. 2417-2427.
214. Bonfantini E.E. et al. Efficient synthesis of free-base 2-formyl-5,10,15,20-tetraarylporphyrins, their reduction and conversion to[(porphyrin-2-yl)methyl]phosphonium salts. In: J. Porphyrins Phthalocyanines, 2002, nr. 6, p. 708-719.
215. Dolomanov O.V. et al. OLEX2: a complete structure solution, refinement and analysis program. In: J. Appl. Cryst., 2009, 42, p. 339-341.
216. Sheldrick G.M. A short history of SHELX. Acta Cryst., 2008, A64, p. 112-122.
217. Prisecaru I. WMOSS4 Mössbauer Spectral Analysis Software, www.wmoss.org, 2009-2013.
218. M. J. Frisch et al. Gaussian 03, Gaussian Inc., Wallingford CT, 2004.
219. Fröhlich F.G.R. et al. Novel access to chiral 1,1'-disubstituted ferrocene derivatives via double stereoselective cyanohydrin synthesis exploiting the hydroxynitrile lyase from *Hevea brasiliensis*. In: Tetrahedron Asymmetry, 2003, nr. 14, p. 355-362.
220. Rodríguez-Cendejas C.G., Liebeskind L.S., Peña-Cabrera E. Synthesis of arylferrocenylketones. In: Archive for Organic Chemistry, 2005, p. 250-265.
221. Ikeda T. et al. A preliminary step toward molecular spring driven by cooperative guest binding. In: Tetrahedron Lett., 2009, nr. 50, p. 2006-2009.
222. Crosby I.T., Geoffrey A.P., Justin A.R. Synthesis of Succinimidoalkyl benzaldehyde Analogues: Potential Bifunctional Linkers for Bioconjugation. In: Aust. J. Chem. 2008, nr. 61, p. 138-143.
223. Charlotte W., Paul W., Stephen J.H. Acid-catalysed synthesis and deprotection of dimethyl acetals in a miniaturised electroosmotic flow reactor. In: Tetrahedron, 2005, nr. 61, p. 5209-5217.

THE LIST OF PUBLICATIONS LINKED TO THE THESIS

Chapters in books:

Turta, C.; Duca, G.; Marin, I.; **Sirbu, D.** Chapter 3: Electrochemical Solar Cells Based on Pigments. In: *Management of Water Quality in Moldova*, SPRINGER, Series: *Water Science and Technology Library*, 2014, Vol. 69, p. 48-59.

Articles in scientific journals:

- in international journals rated ISI and SCOPUS:
 - **Sirbu, D.**; Turta, C.; Benniston, A. C.; Abou-Chahine, F.; Lemmetyinen, H.; Tkachenko, N. V.; Woodd, C.; Gibson, E. Synthesis and properties of a meso tris-ferrocene appended zinc(II) porphyrin and a critical evaluation of its dye sensitised solar cell (DSSC) performance. In: **RSC Advances**, 2014, V. 4 (43), p. 22733-22742
 - Benniston, A.C.; **Sirbu, D.**; Turta, C.; Probert, M.R.; Clegg, W. Synthesis, molecular structure and properties of a ferrocene-based difluoropyrrolo-oxaborole derivative. In: **Eur. J. Inorg. Chem.**, 2014, V. 36, p. 6212-6219.
 - Benniston, A.C.; **Sirbu, D.**; Turta, C.; Probert, M.R.; Clegg, W. A simple method for desymmetrizing 1,1'-ferrocenedicarboxaldehyde. In: **Tetrahedron Letters**, 2014, V. 55 (28), p. 3777-3780
 - **Sirbu, D.**; Turta, C.; Gibson, E.A.; Benniston, A.C. The Ferrocene Effect: Enhanced Electrocatalytic Hydrogen Production using meso-Tetra ferrocenyl porphyrin Palladium (II) and Copper (II) Complexes. In: **Dalton Transactions**, 2015. Advance Article.
- in journals from the National Register of profile journals:
 - **Sirbu, D.** Temperature dependence of ^{57}Fe -mössbauer spectra for a $\text{Fe}_{\text{Fc}}^{\text{II}} - \text{Fe}_{\text{tpy}}^{\text{II}} - \text{Fe}_{\text{Fc}}^{\text{II}}$ trinuclear system. In: **Chemistry Journal of Moldova. General, Industrial and Ecological Chemistry**, 2015, nr. 10 (1), p. 61-66.

Abstracts on scientific conferences:

1. **Sîrbu, D.** Sinteza și caracterizarea 5,10,15,20-tetra(ferocenil) porfirinatului de paladiu(II). In: Conferința Internațională a Tinerilor Cercetători, edition IX. Chișinău: Free International University of Moldova, 11 November 2011, p. 65;
2. Turtă, C.; **Sîrbu, D.**; Benniston, A.C. Uv-vis and redox chemistry of copper 5,10,15,20-tetra(ferrocenyl) porphyrin. In: The V International Conference-Symposium "Ecological Chemistry 2012". Chișinău: Academy of Sciences of Moldova, 2-3 March 2012, p. 137-138;
3. **Sîrbu, D.**; Barbă, A.; Gorincioi, E. Synthesis and NMR-characterisation of the novel 5,10-bisferrocenyl-15,20-bis(4-methoxybenzoyl) porphyrin. In: The XVII-th Conference "Physical Methods in Coordination and Supramolecular Chemistry". Chișinău: Institute of Chemistry of ASM, 24-26 October 2012, p. 188.
4. **Sirbu, D.** Synthesis and characterisation of the novel zinc(II)-5,10,15-trisferrocenyl-20-(4-carboxyphenyl) porphyrin. In: The VII National conference on chemistry and nanomaterials of young scientists, PhD and students with the international participation "Mendeleev-2013". St. Petersburg: Saint Petersburg State University, 2-5 April 2013, H-12.
5. **Sirbu, D.**; Turta, C.; Benniston, A.C. Synthesis and structure 1,1'-bis-(dipyrrromethane) ferocene. In: Integration through research and innovation. Chișinău: Moldova State University, 26-28 September 2013, p. 94-95.
6. **Sirbu, D.** Introducing ferrocene in dye-sensitizers for solar cell applications. In: Symposium & Young-Researcher-Meeting: Current Challenges in Supramolecular Artificial Photosynthesis. Poster and oral presentation. Jena, Germany: Friedrich Schiller University, 09-13 March 2014.
7. **Sirbu, D.**; Gorincioi, E. New Polychiralic asymmetrically 1,1'-disubstituted ferrocene ligand with multiple coordination sites. In: The Intern. Conf. dedicated to the 55th anniversary from foundation of the Institute of Chemistry of the ASM. Chișinău: Institute of Chemistry of ASM, 28-30 Mai 2014, p. 137.

ANNEXES

Annexe 1. The photocurrent action spectrum for NiO solar cell modified with **RTF**(PF₆)₂.

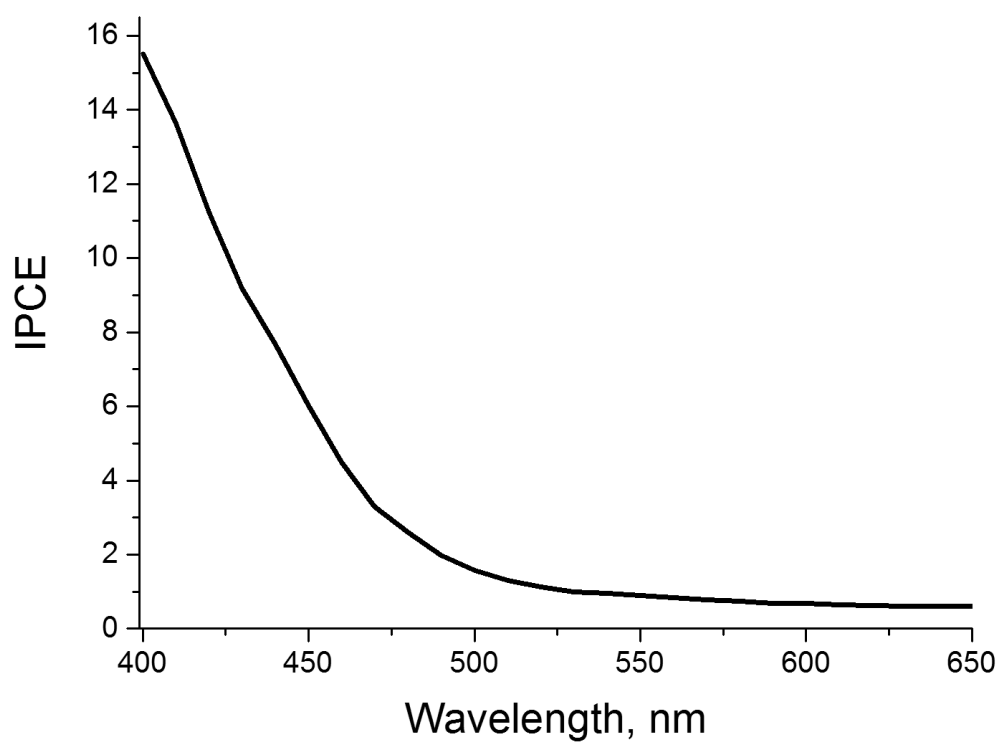


Fig. A1. The photocurrent action spectrum for NiO solar cell modified with **RTF**(PF₆)₂.

Annexe 2. NMR spectra and partial assignment for **2.6**.

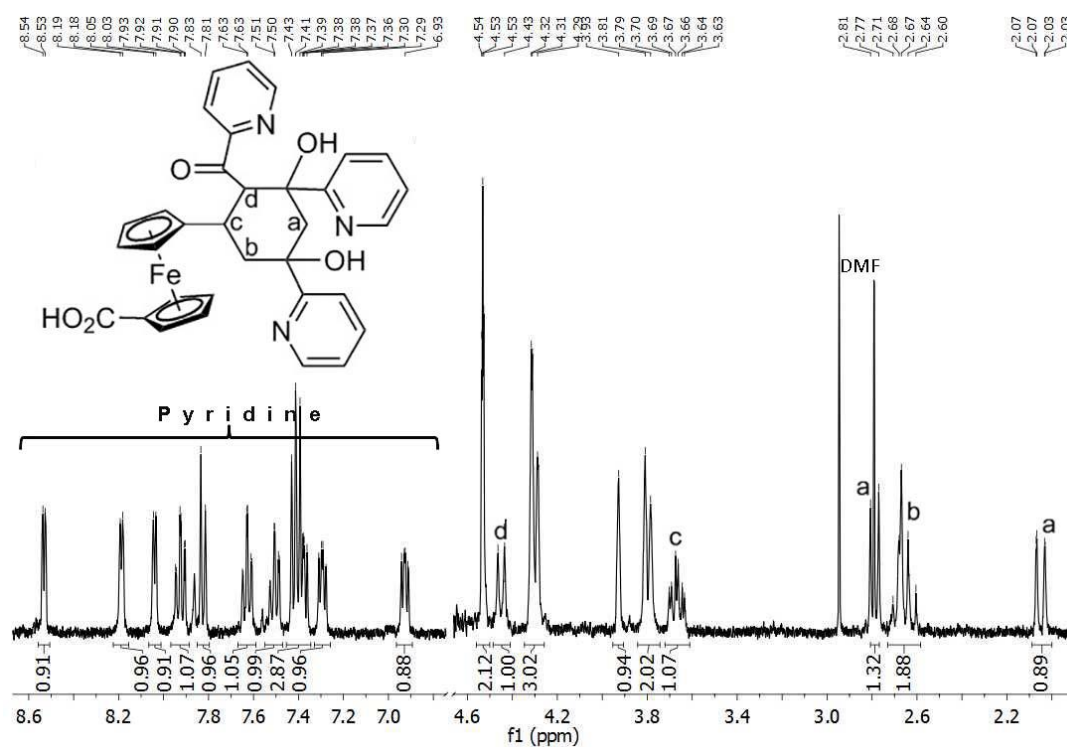


Fig. A2.1. Selected partial 400 MHz ¹H-NMR spectrum and partial assignment for **2.6**.

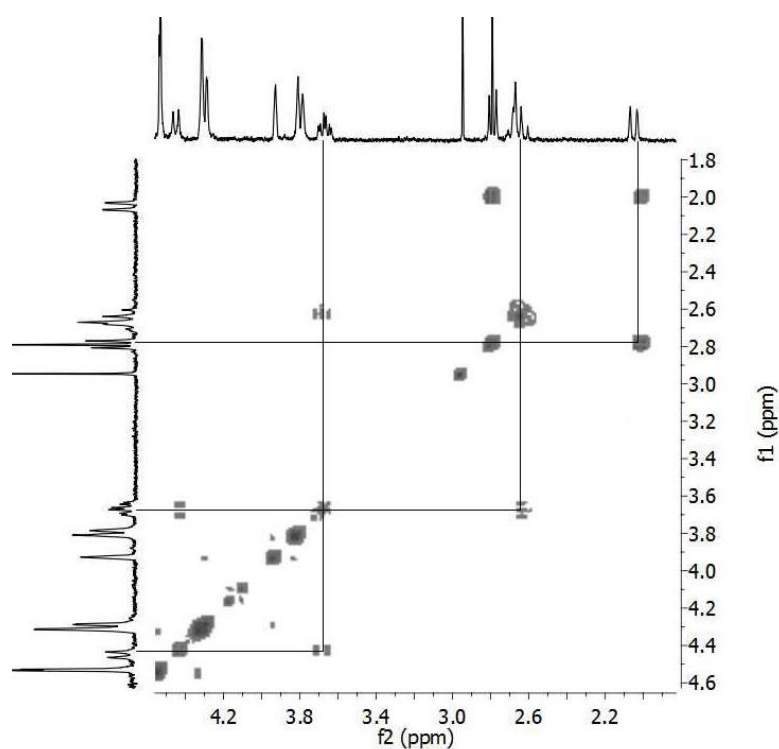


Fig. A2.2. Selected partial 400 MHz COSY45°-NMR spectrum for **2.6** showing the cyclohexane ring centred ¹H-¹H interaction.

Annexe 3. DFT calculated energy minimized structures and molecular orbitals for **FBF**.

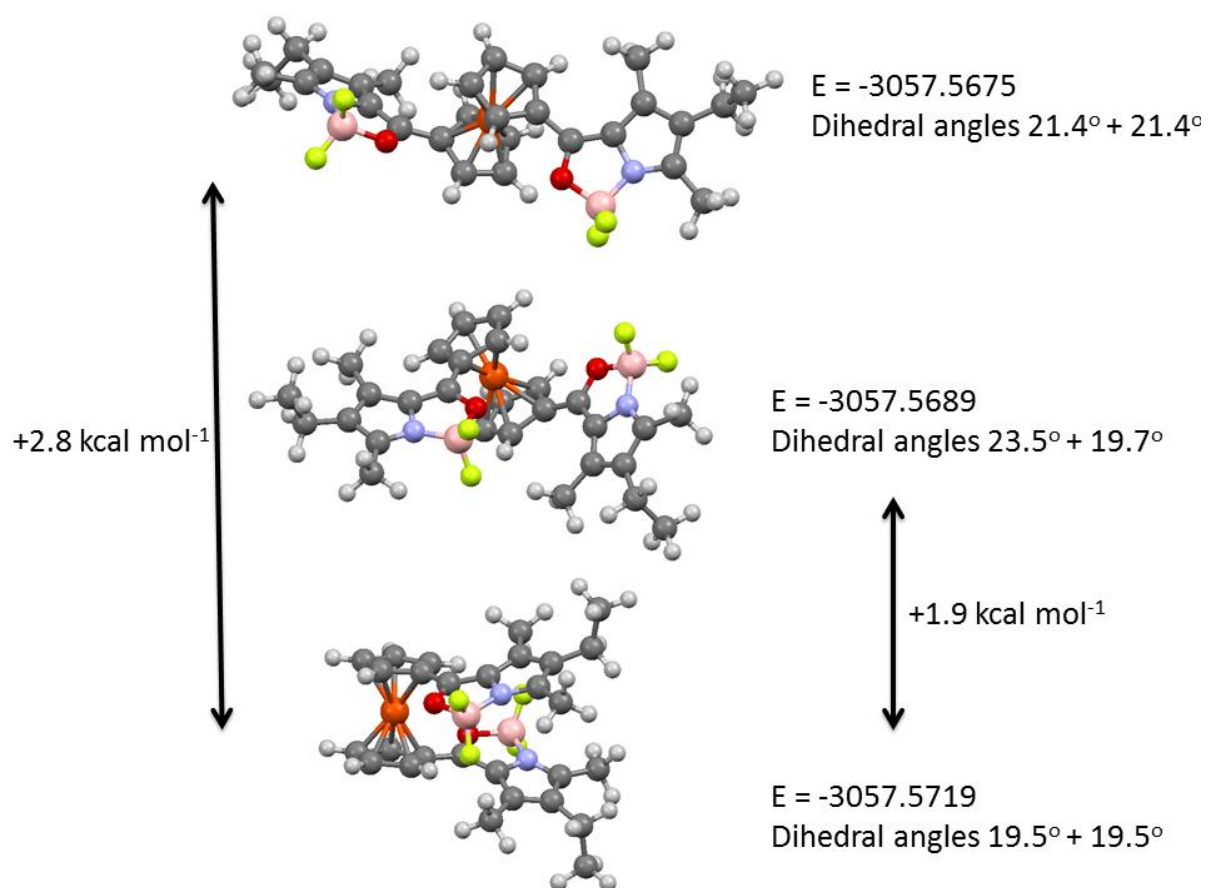


Fig. A3.1. DFT calculated energy minimized structures for **FBF**, their energies and dihedral angles.

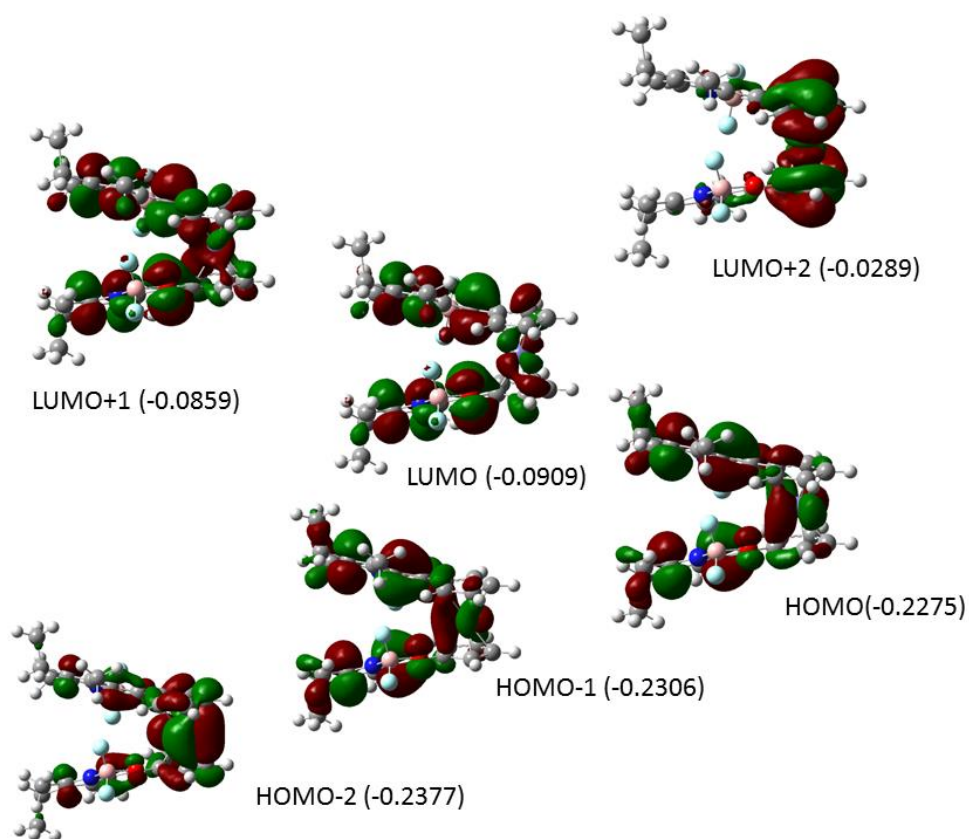


Fig. A3.2. DFT calculated molecular orbitals pictures for **FBF** in an eclipsed conformer.

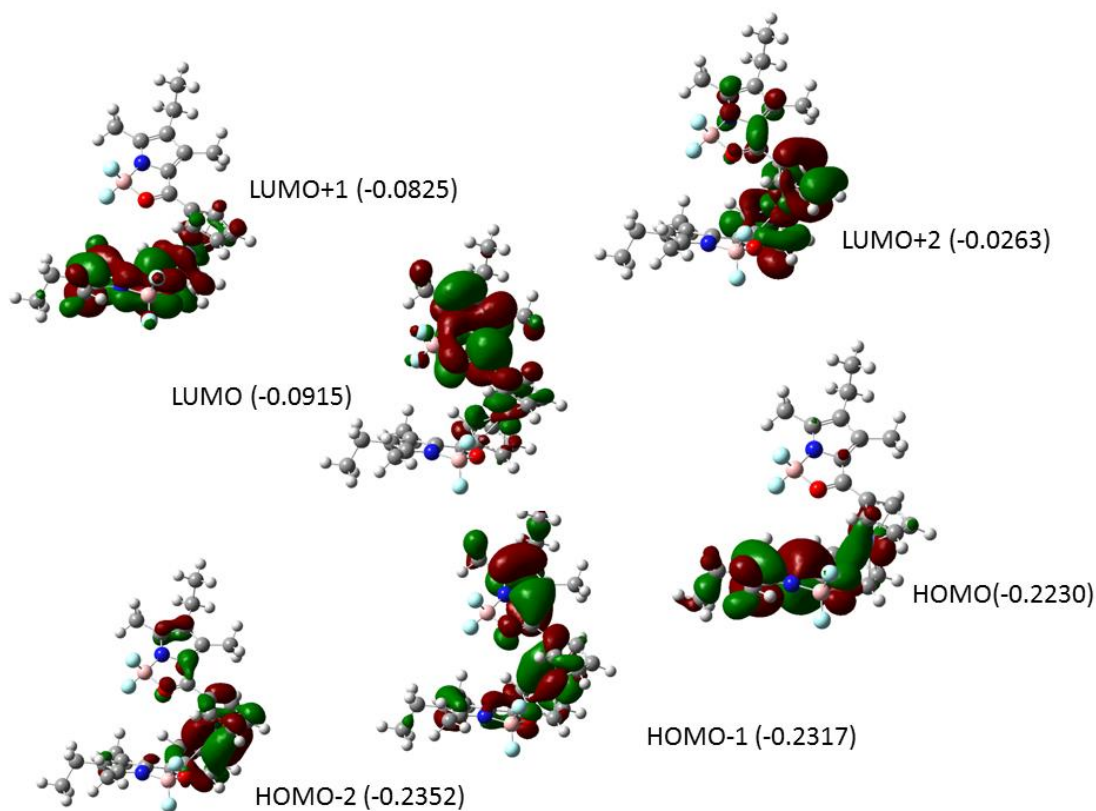


Fig. A3.3. DFT calculated molecular orbitals pictures for **FBF** in an open conformer.

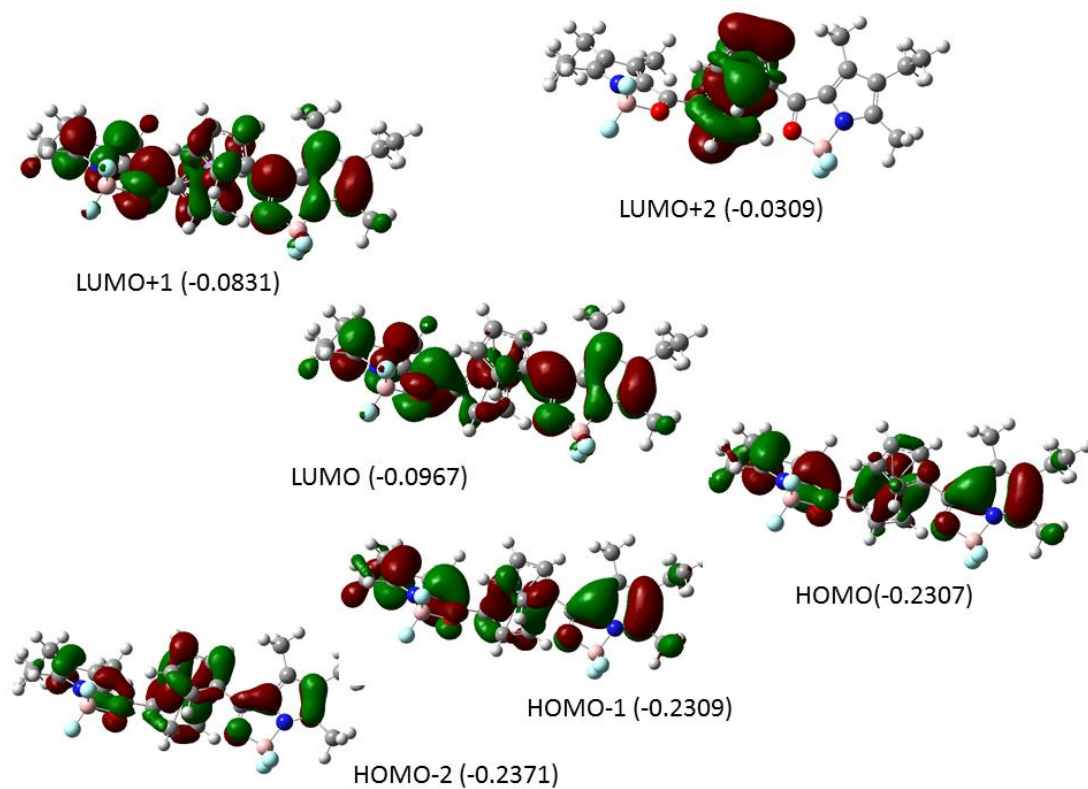


Fig. A3.4. DFT calculated molecular orbitals pictures for **FBF** in a staggered conformer.

Annexe 4. Cyclic voltammogram recorded for **FBF** in acetonitrile.

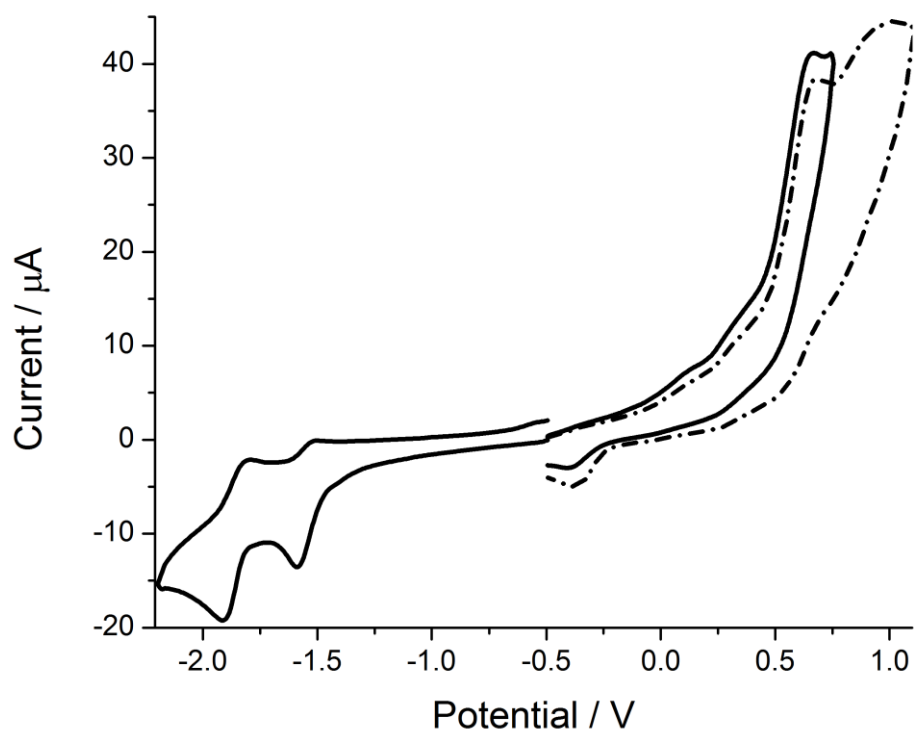


Fig. A4. Cyclic voltammogram recorded for **FBF** in acetonitrile containing 0.2 M TBATFB.
Scan rate = 100 mV s^{-1} .

Annexe 5. DFT calculated molecular orbitals for **2** using the X-ray determined structure.

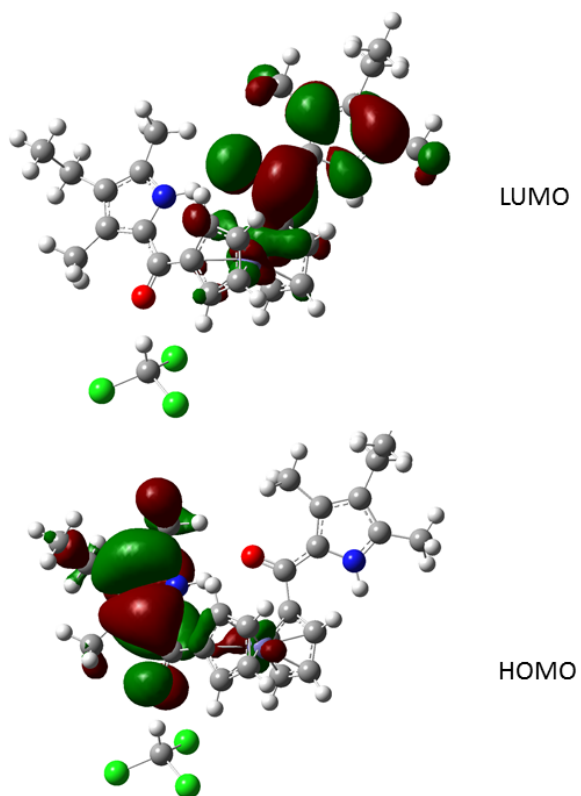


Fig. A5. DFT calculated molecular orbitals pictures for **2**, using the X-ray determined structure.

Annexe 6. ^1H -NMR spectrum in CDCl_3 with peaks assignment for **3.5**.

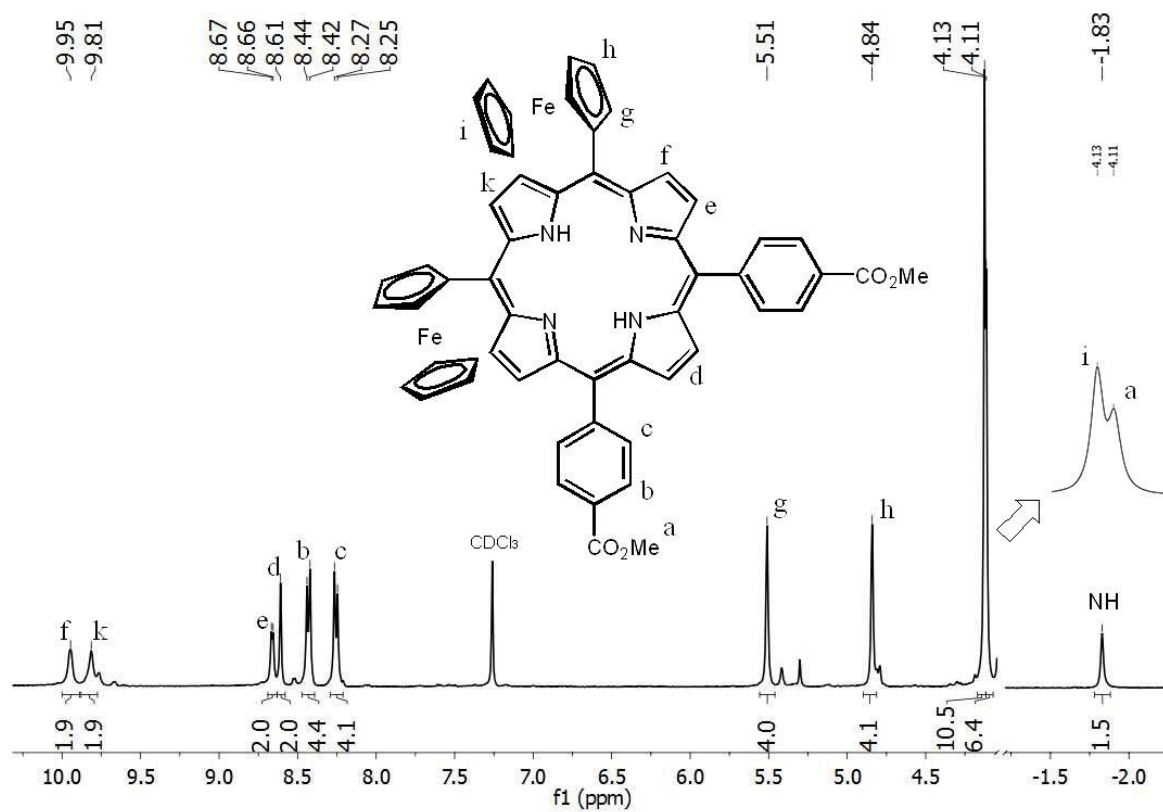


Fig. A6. Selected partial 400 MHz ^1H -NMR spectrum in CDCl_3 with peaks assignment for **3.5**.

Annexe 7. NMR spectra for **F3P**.

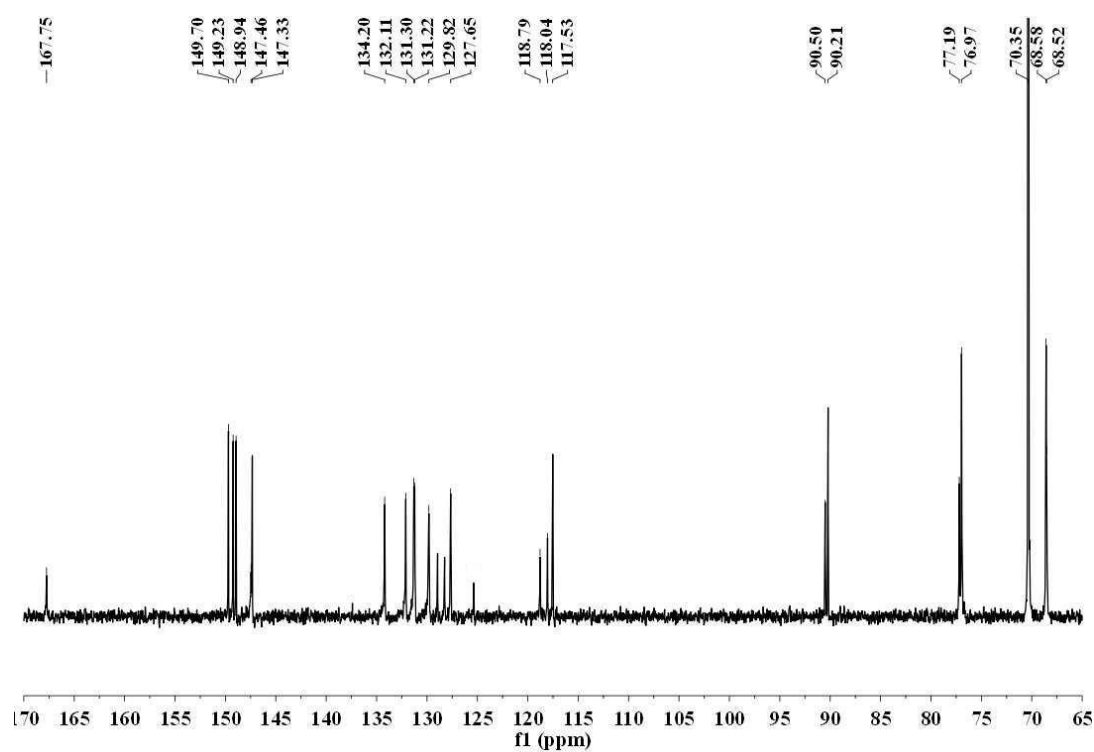


Fig. A7.1. $^{13}\text{C}\{^1\text{H}\}$ NMR spectrum for **F3P** in DMSO-d_6 .

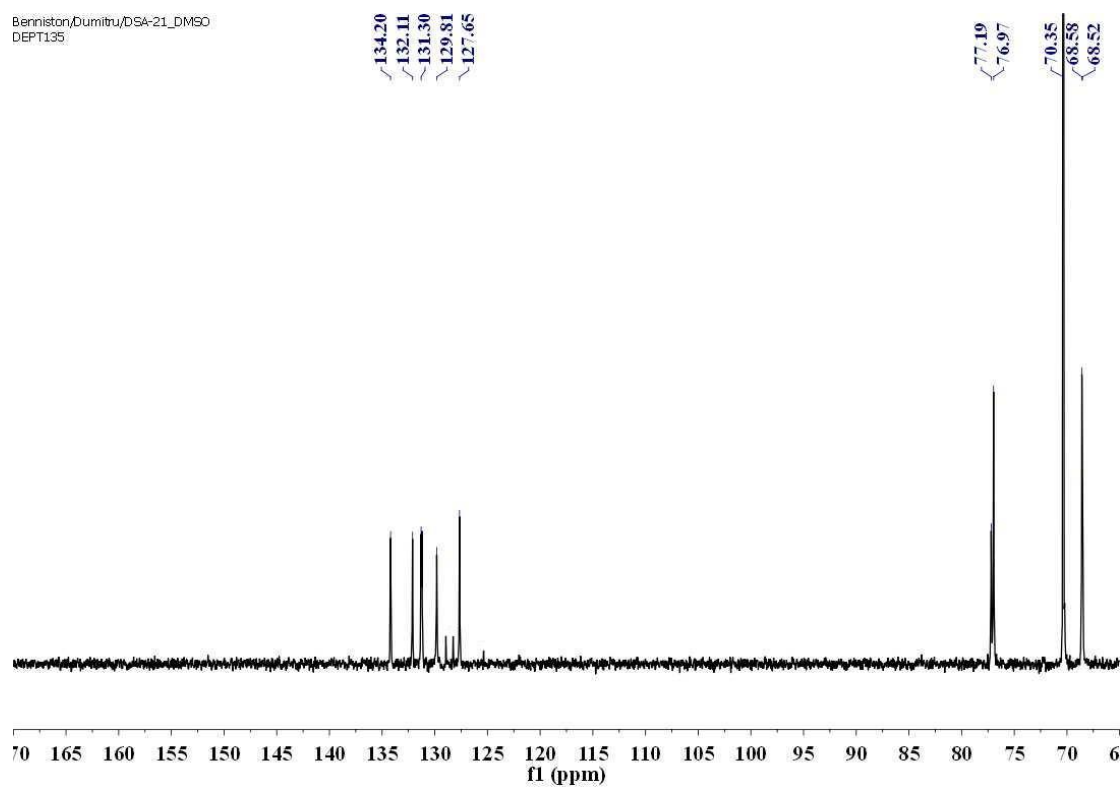


Fig. A7.2. DEPT-135 NMR spectrum for **F3P** in DMSO-d_6 .

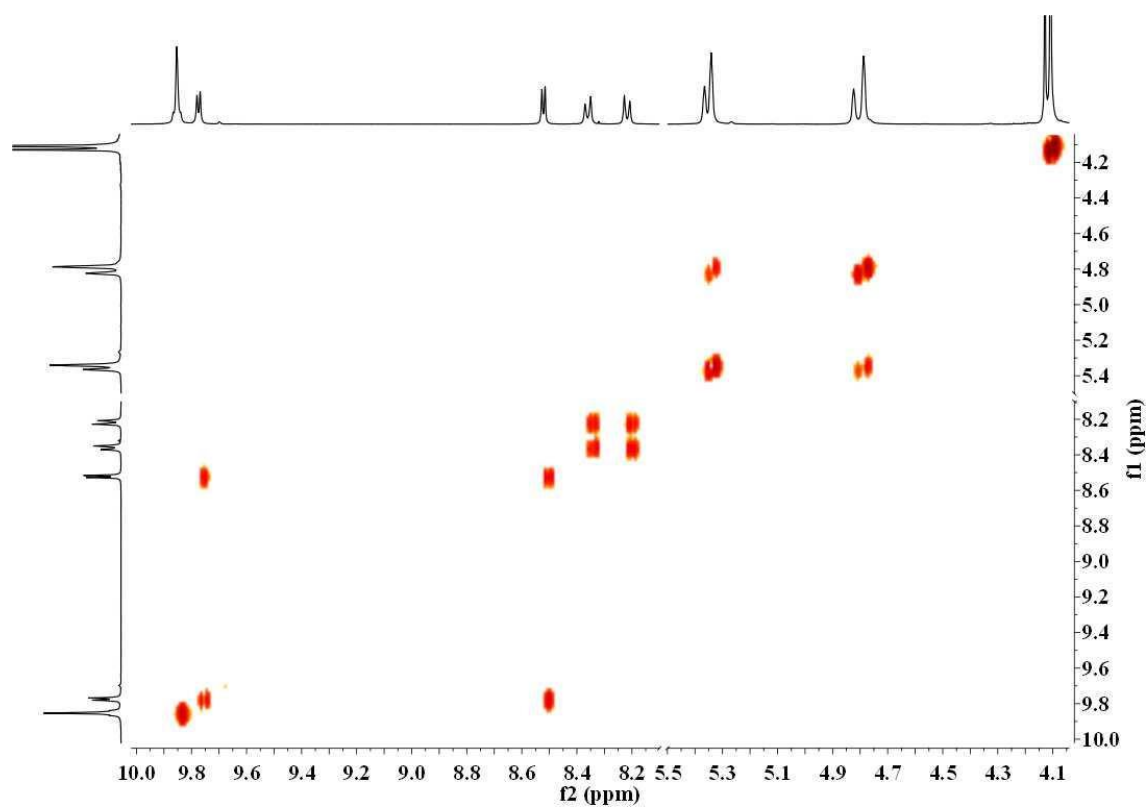


Fig. A7.3. COSY-45 NMR spectrum for **F3P** in DMSO- d_6 .

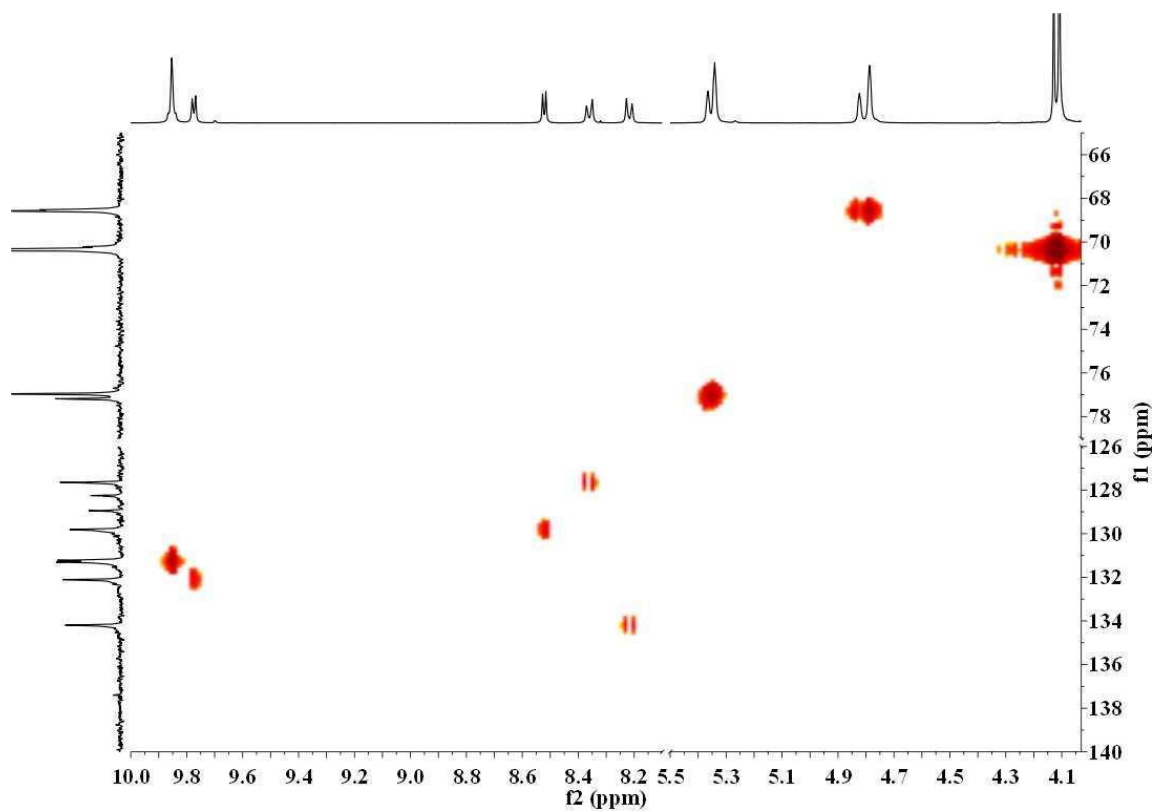


Fig. A7.4. HMQC NMR spectrum for **F3P** in DMSO- d_6 .

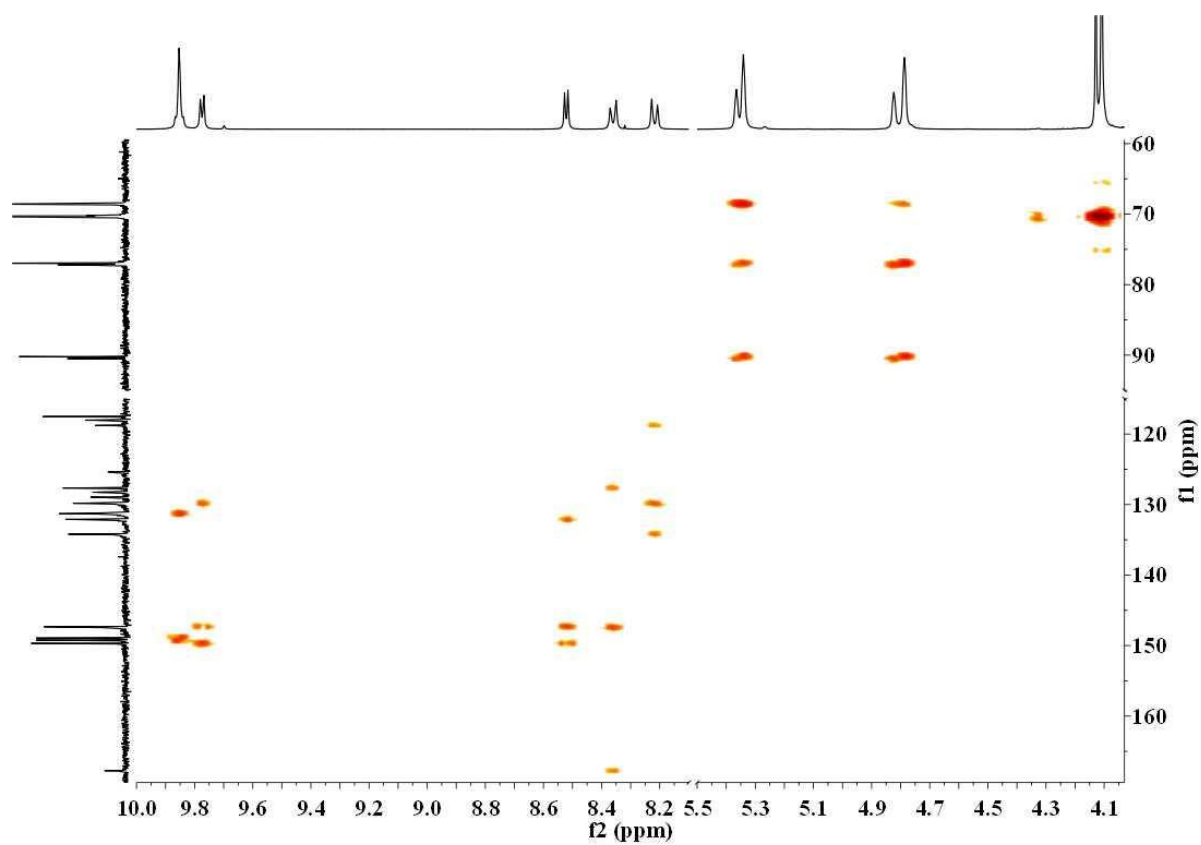


Fig. A7.5. HMBC NMR spectrum for **F3P** in DMSO-d₆.

Annexe 8. Computer calculated structures for **F3P** showing the bow in the porphyrin ring.

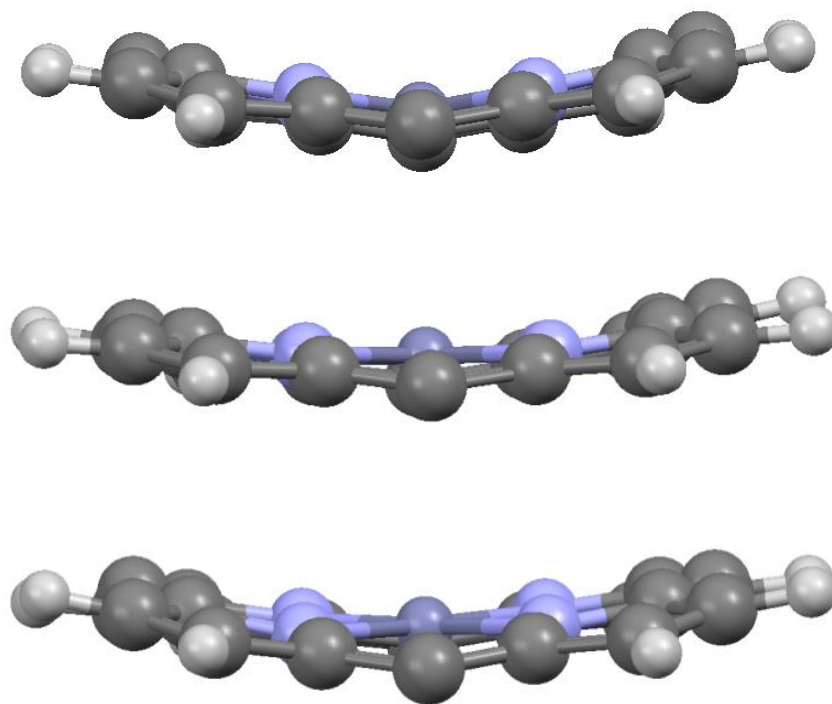


Fig. A8. Computer calculated structures for **F3P** showing the bow in the porphyrin ring. Top B3LYP (3-21G*), middle B3LYP (LanL2DZ), bottom B3PW91 (6-31G(d)). *meso*-Groups are omitted for clarity.

Annexe 9. Selected molecular orbitals for **F3P** calculated by DFT method.

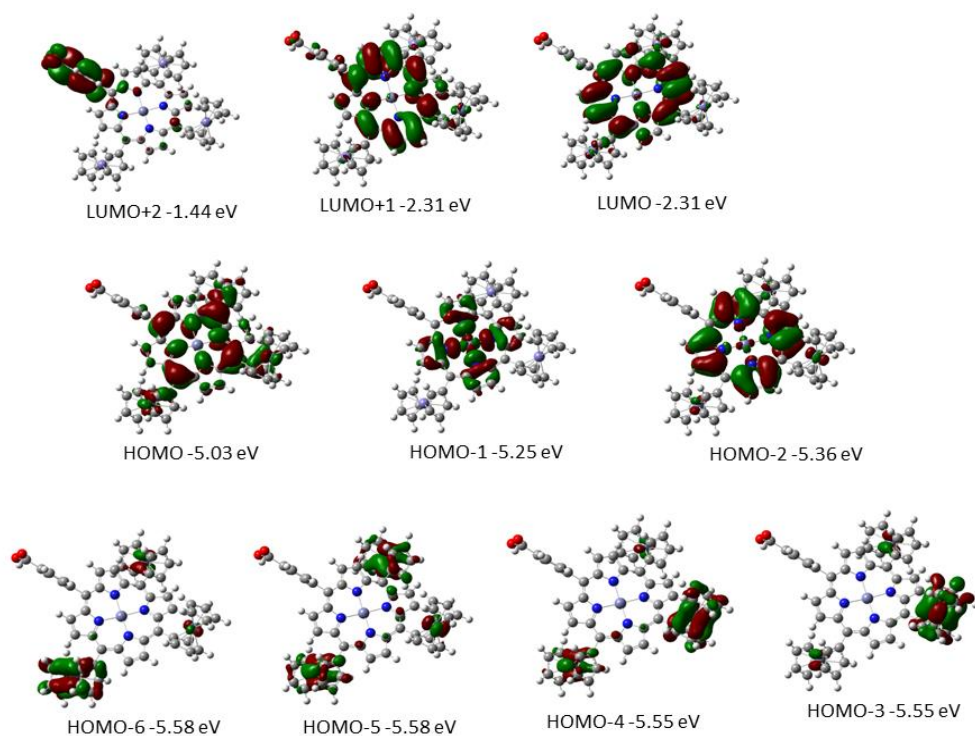


Fig. A9.1. Selected molecular orbitals pictures for **F3P** calculated by DFT (B3LYP) and using the 3-21G* basis set.

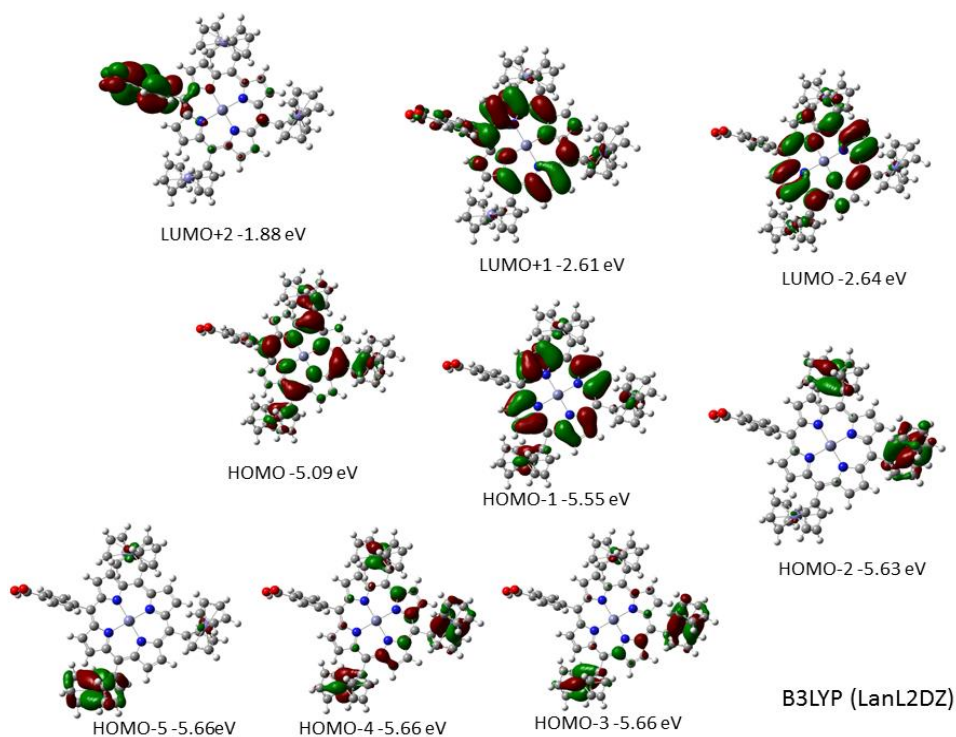


Fig. A9.2. Selected molecular orbitals pictures for **F3P** calculated by DFT (B3LYP) and using the LanL2DZ basis set.

Annexe 10. Time resolved transient absorption spectra of **F3P** attached to TiO_2 .

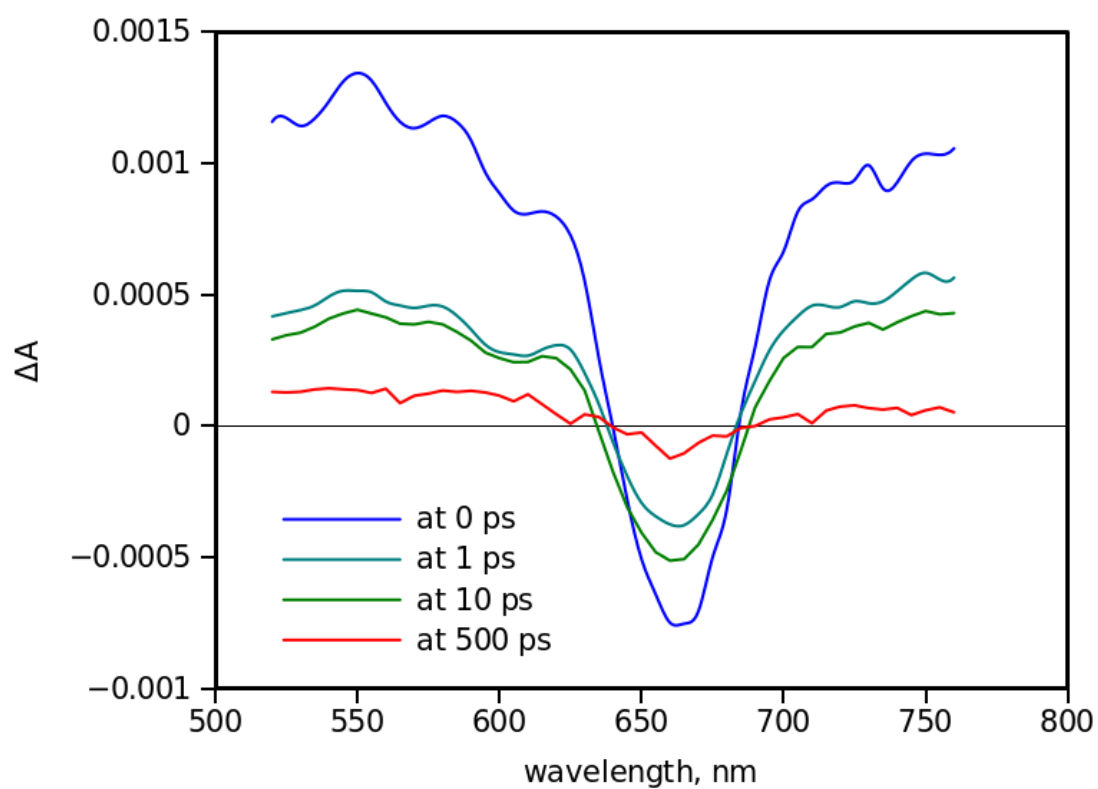


Fig. A10. Time resolved transient absorption spectra of **F3P** attached to TiO_2 .

Annexe 11. Decay component spectra for **ZnTPP** supported on TiO₂.

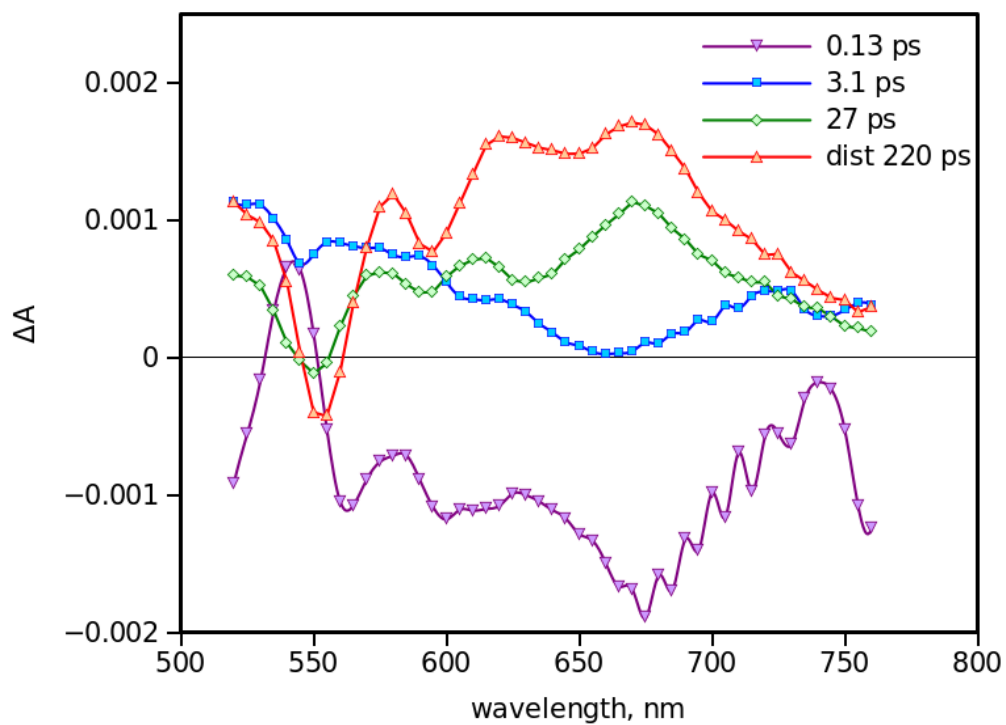


Fig. A11. Decay component spectra for **ZnTPP** supported on TiO₂.

Excitation wavelength is 550 nm.

Annexe 12. Cyclic voltammogram recorded for **PdTFP** in DCM.

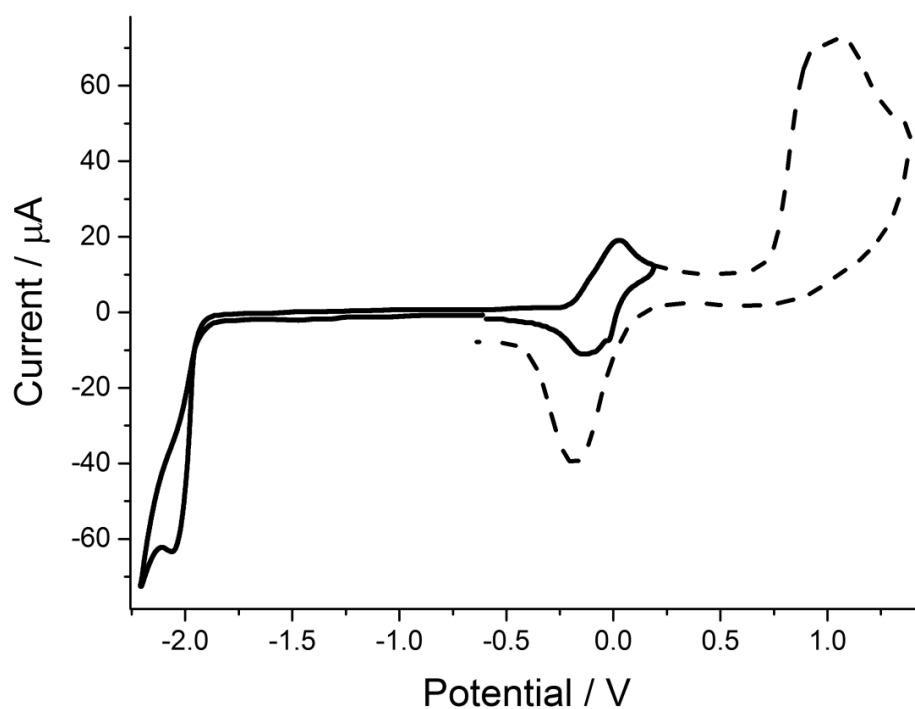


Fig. A12. Cyclic voltammogram recorded for **PdTFP** in DCM containing 0.2 M TBABF₄ vs Fc⁺/Fc. The dashed line shows the additional irreversible oxidation peak when the potential window was increased.

Annexe 13. Selected cyclic voltamograms for **NiTFP** (1.0 mM) at a glassy carbon electrode in dry DMF in the presence of increasing quantities of TFA.

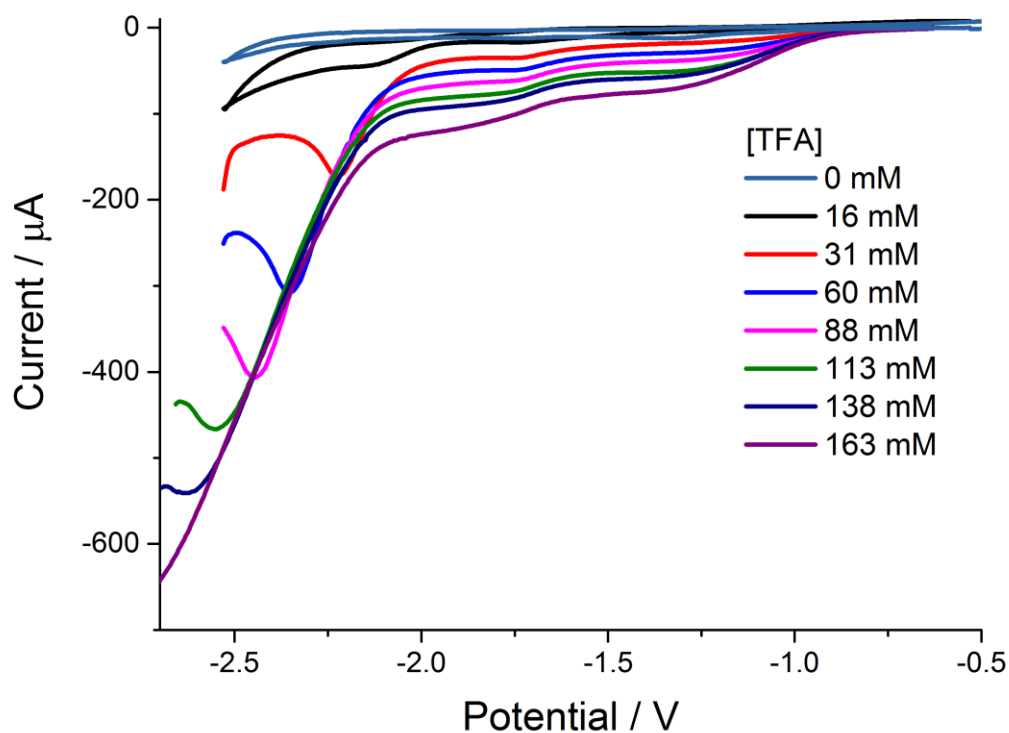


Fig. A13. Selected cyclic voltamograms for **NiTFP** (1.0 mM) at a glassy carbon electrode in dry DMF in the presence of increasing quantities of TFA. Voltammograms show that the addition of acid leads to the appearance of an irreversible wave of increasing amplitude corresponding to the reduction of TFA catalyzed by the complex. Conditions: $T = 298\text{ K}$, scan rate = 100 mV s^{-1} .

Supporting electrolyte: 0.2 M TBABF₄.

Annexe 14. Electrocatalytic hydrogen production vs time and charge vs time by applying -1.5 V vs SCE to a glassy carbon electrode in sol. of DMF containing 50 mM TFA and 0.1 mM **PdTFP**.

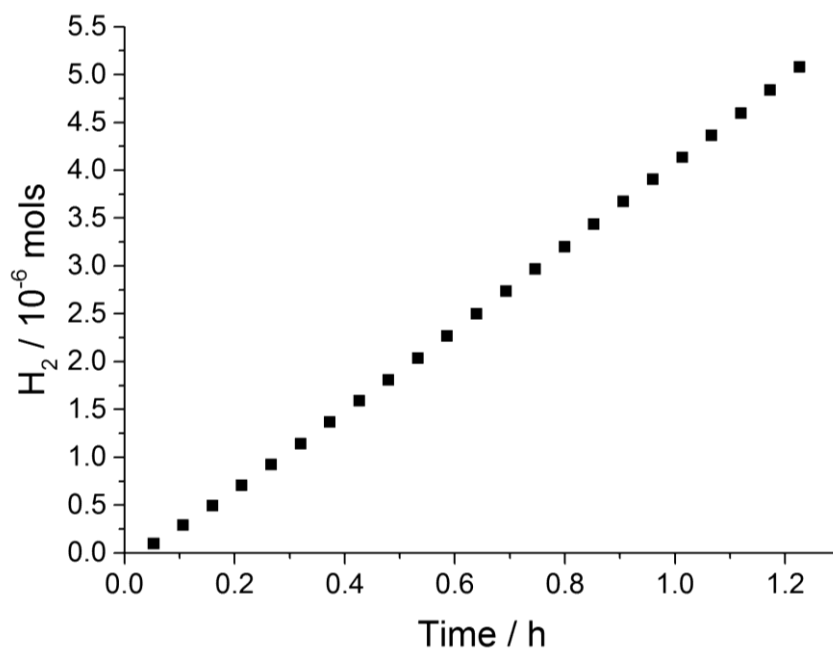


Fig. A14.1. Electrocatalytic hydrogen production vs time by applying -1.5 V vs SCE to a glassy carbon electrode in 0.1 M TBABF₄ sol. of DMF containing 50 mM TFA and 0.1 mM **PdTFP**.

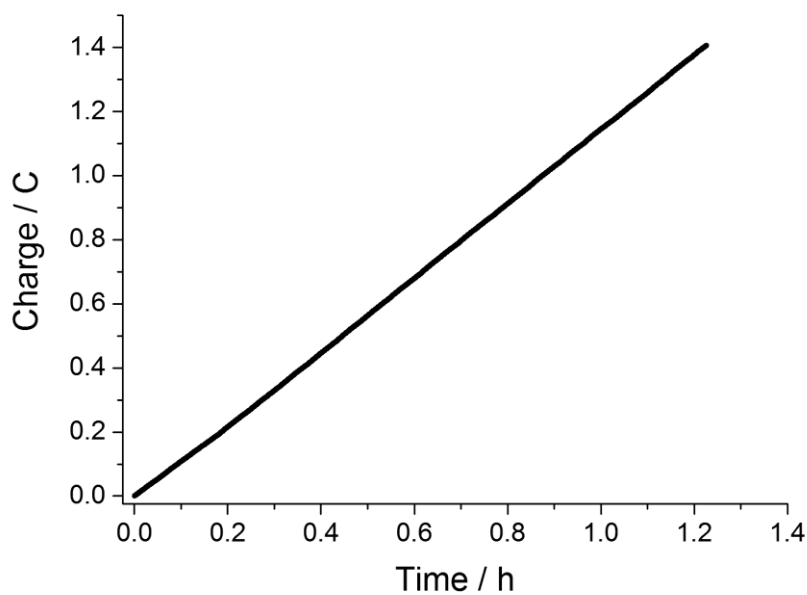


Fig. A14.2. Charge vs time by applying -1.5 V vs SCE to a glassy carbon electrode in 0.1 M TBABF₄ sol. of DMF containing 50 mM TFA and 0.1 mM **PdTFP**.


DECLARATION ON THE ASSUMPTION OF RESPONSIBILITY

I, the undersigned, Sîrbu Dumitru, declare on my own responsibility that the materials presented in the thesis are the result of my own research and scientific achievements. I realize that otherwise will suffer the consequences in accordance with the legislation in force.

Sîrbu Dumitru

Date 24.07.2015

Signature



CURRICULUM VITAE

Sîrbu Dumitru

Date of birth:

29 August, 1987

Address

**Institute of Chemistry
of the Academy of Sciences of Moldova,
str. Academiei 3, Chişinău,
Republic of Moldova. MD-2028**

Phone Nr.

(+373 22) 73-97-22

E-mail:

sirbudyma@gmail.com

EDUCATION DEGREES

**2010 -
present**

University of the Academy of Sciences of Moldova / Institute of Chemistry of the Academy of Sciences of Moldova, Chişinău, Republic of Moldova
PhD Student.

Scientific Supervisor: Acad., Dr. Hab. Turtă Constantin,
Scientific co-Supervisor: Prof., Dr. Andrew Benniston

2008-2010

University of the Academy of Sciences of Moldova, Chişinău, Republic of Moldova
Master's Degree in Chemistry Specialisation in Inorganic Chemistry
Dissertation Title: The synthesis and study of organic and inorganic dyes containing Fe group metals
Scientific Supervisor: Acad., Dr. Hab. Turtă Constantin

2005-2008

Moldova State University, Chişinău, Republic of Moldova, Undergraduate degree in Chemistry
Department Chemistry and Chemical Technology, Specialisation in Organic Chemistry
Dissertation title: The study of methods for synthesis of 3-(2-phenyl)- 1-(4-isothiocyanate-phenyl)-2-propan-1-one
Scientific Supervisor: Prof., Dr. Hab. Barbă Nicanor

GRANTS, SCHOLARSHIPS, AWARDS

2009

Merit scholarship awarded by Moldovan Government

2010-2011

National Grant : Synthesis and study of new photocatalysts for water splitting

2012-2013

National Grant : Synthesis and study of photosensitizer based on furancarboxylic acid, porphyrins, quinolinepyridine and imidazole.

2010-2013

MARIE CURIE FP7-PEOPLE-2009-IRSES GRANT Nr. 246902:
Photocatalytic Cluster Complexes for Artificial Photosynthesis Applications

2013

“Governmental Nominal Scholarship” - 2013

2013-2014

Scholarship in the framework of NATIONAL SCHOLARSHIP PROGRAMME of WORLD FEDERATION OF SCIENTISTS

2014

Second prize “The best young researcher of 2014 from Institute of Chemistry of AŞM”

2012-2016

CMST COST Action CM1202 Supramolecular photocatalytic water splitting (PERSPECT-H2O)

2015

AŞM Award “For valuable scientific achievements of young scientists”

AREA OF SCIENTIFIC INTERESTS

Synthesis	Organic, Inorganic, Organometallic and Materials Chemistry
Study	IR, NMR, Mass, Mossbauer, UV-Vis and transient absorption spectroscopies, X-ray diffraction analysis, Cyclic Voltammetry, Spectroelectrochemistry
Application	Dye Sensitized Solar Cells, Artificial Photosynthesis, Hydrogen Production

PUBLICATIONS

- Sirbu D., Marin I. Synthesis and IR, NMR characterisation of new *p*-(N,N-diphenylamino) chalcones. In: *Chemistry Journal of Moldova. General, Industrial and Ecological Chemistry*, 2011, 6 (1), p. 86-89. (B-grade journal, UIF 0.135)
- Sirbu D., Turta C., Benniston A.C., Abou-Chahine F., Lemmetyinen H., Tkachenko N.V., Woodd C., Gibson E. Synthesis and properties of a meso tris-ferrocene appended zinc(II) porphyrin and a critical evaluation of its dye sensitised solar cell (DSSC) performance. In: *RSC Advances*, 2014, 4 (43), p. 22733-22742. DOI: 10.1039/c4ra03105a. (IF 3.84)
- Benniston A.C., Sirbu D., Turta C., Probert M.R., Clegg W. Synthesis, molecular structure and properties of a ferrocene-based difluoropyrrolo-oxaborole derivative. In: *Eur. J. Inorg. Chem.*, 2014, 36, p. 6212–6219. DOI:10.1002/ejic.201402752. (IF 2.942).
- Benniston A.C., Sirbu D., Turta C., Probert M.R., Clegg W. A simple method for desymmetrizing 1,1'-ferrocenedicarboxaldehyde. In: *Tetrahedron Letters*, 2014, 55 (28), p. 3777-3780. DOI: 10.1016/j.tetlet.2014.05.040. (IF 2.379).
- Sirbu D. Temperature dependence of ^{57}Fe -mössbauer spectra for a $\text{Fe}_{\text{Fc}}^{\text{II}} - \text{Fe}_{\text{tpy}}^{\text{II}} - \text{Fe}_{\text{Fc}}^{\text{II}}$ trinuclear system. In: *Chemistry Journal of Moldova. General, Industrial and Ecological Chemistry*, 2015, 10 (1), p. 84-88. (B-grade journal, UIF 0.135)
- Turta C., Duca G., Marin I., Sirbu D. Chapter 3: Electrochemical solar cells based on pigments. In: *Management of Water Quality in Moldova*, SPRINGER, Series: *Water Science and Technology Library*, 2014, Vol. 69, p. 35-59. DOI: 10.1007/978-3-319-02708-1. ISSN 0921-092X, ISBN 928-3-319-02707-4.
- Iacob M., Sirbu D., Tugui C., Stiubianu G.T., Sacarescu L., Cozan V., Zelenáková A., Čížmár E., Feher A., Cazacu M. Superparamagnetic amorphous iron oxide nanowires self-assembled into ordered layered structures. In: *RSC Adv.*, 2015, Accepted Manuscript. DOI: 10.1039/C5RA10469F (IF 3.84)
- Sirbu D., Turta C., Gibson E.A., Benniston A.C. The ferrocene effect: enhanced electrocatalytic hydrogen production using meso-tetraferrocenyl porphyrin palladium (II) and copper (II) complexes. In: *Dalton Trans.*, 2015, Accepted Manuscript. DOI: 10.1039/C5DT02191J (IF 4.197)

LANGUAGES

Romanian – native	Russian – native
English - fluent (speaking, reading, writing)	French – basic (speaking, reading, writing)

Acknowledgements

This thesis would not be possible without all sorts of mentorship, assistance, friendship, and support from many important individuals.

First and foremost I want to express my deepest gratitude to my advisor, Academician Turtă Constantin. It has been an honour to be his Ph.D. student and I would like to dedicate this work to the memory of Prof. Constantin Turta. I appreciate the way he supported and motivated my research and thank him for allowing me to grow as a research scientist.

I would especially like to thank Professor Andrew Benniston for guiding me in the world of contemporary science. I appreciate all his contributions of time, ideas, and funding to make my experience in the Molecular Photonics Laboratory productive and stimulating.

I am very grateful to Dr Elizabeth Gibson for the chance to work in her group at Nottingham and Newcastle Universities. The results obtained during these secondments were of a great help for thesis and publication of papers.

I would also like to thank Professor Mangalagiu Ionel for the possibility to improve my knowledge and abilities in organic synthesis, during my stay in the Organic and Biochemistry Department of “A. I. Cuza” University.

Alexander von Humboldt Foundation and Professor Arion Vladimir are thanked for providing equipment necessary to finish this dissertation. Professors Sergiu Şova, Michael R. Probert, William Clegg, Fawzi Abou-Chahine, Helge Lemmetyinen, Nikolai V. Tkachenko and Alic Barbă, Elena Gorincioi, Christopher Wood, Gareth Summers are thanked for help with performing various studies of compounds and analysis of results.

I would also like to acknowledge the help of all past and present members of the Laboratory of Bioinorganic Chemistry and Nanocomposites and the Laboratory of Molecular Photonics.

I thank the Institute of Chemistry and Newcastle University for financial support. FP7-PEOPLE-2009-IRSES grant (246902) and CMST COST Action CM1202 are thanked for funding to cover the exchange of researchers. World Federation of Scientists is thanked for a scholarship in the framework of the National Scholarship Programme. The EPSRC UK National Mass Spectrometry Facility at Swansea University is also thanked for collecting mass spectra of compounds. Diamond Light Source is thanked for access to synchrotron facilities.

Last but not the least, I would like to thank my family for support, patience and immeasurable help offered during these endless years of challenging work.